Universidade de Aveiro Departamento de Física
2011

Nelson de Jesus Cordeiro Muga

Efeitos da Polarização em Sistemas de Comunicação por Fibras Óticas

Polarization Effects in Fiber-Optic Communication Systems

Nelson de Jesus Cordeiro Muga

Efeitos da Polarização em Sistemas de Comunicação por Fibras Óticas

Polarization Effects in Fiber-Optic Communication Systems

Tese apresentada à Universidade de Aveiro para cumprimento dos requisitos necessários à obtenção do grau de Doutor em Engenharia Física, realizada sob a orientação científica do Doutor Armando Humberto Moreira Nolasco Pinto, Professor Auxiliar do Departamento de Eletrónica, Telecomunicações e Informática da Universidade de Aveiro, e coorientação do Doutor Mário Fernando dos Santos Ferreira, Professor Associado com Agregação do Departamento de Física da Universidade de Aveiro

Apoio financeiro da Fundação para a Ciência e a Tecnologia através da bolsa SFRH/BD/28275/2006.

FCT Fundação para a Ciência e a Tecnologia
MINISTÉRIO DA CIÊNCIA, TECNOLOGIA E ENSINO SUPERIOR Portugal

o júri / the jury

presidente / president

Doutor Paulo Jorge dos Santos Gonçalves Ferreira
Professor Catedrático da Universidade de Aveiro

vogais / examiners committee

Doutor Mário Fernando dos Santos Ferreira
Professor Associado com Agregação da Universidade de Aveiro (Coorientador)

Doutor Adolfo da Visitação Tregeira Cartaxo
Professor Associado com Agregação do Instituto Superior Técnico da Universidade Técnica de Lisboa

Doutor José Manuel Marques Martins de Almeida
Professor Associado com Agregação da Universidade de Trás-os-Montes e Alto Douro

Doutor Henrique Manuel de Castro Faria Salgado
Professor Associado da Faculdade de Engenharia da Universidade do Porto

Doutor Armando Humberto Moreira Nolasco Pinto
Professor Auxiliar da Universidade de Aveiro (Orientador)

agradecimentos / acknowledgements

Queria endereçar as minhas primeiras palavras de agradecimento ao meu orientador, o Professor Doutor Armando Nolasco Pinto, e ao meu coorientador, o Professor Doutor Mário Fernando dos Santos Ferreira. Ao Professor Doutor Armando Nolasco Pinto, agradeço o facto de ter aceitado orientar-me cientificamente neste Doutoramento, e, de um modo muito especial, agradeço também toda a sua atenção, acompanhamento e constante motivação, sem esquecer os seus sempre oportunos e inspiradores ensinamentos. Aos dois, agradeço as suas sugestões para a organização desta tese, o árduo trabalho de leitura e revisão do texto, bem como a sua participação na interpretação e discussão de todos os resultados aqui apresentados.

Aos meus colegas de grupo, a Doutora Meire Fugihara e os Mestres Nuno Alexandre Silva, Álvaro Almeida, Gil Fernandes e Steven Carneiro, agradeço as suas valiosas contribuições para o trabalho aqui apresentado, em particular as colaborações em trabalho de laboratório, assim como as intermináveis e sempre empolgantes discussões científicas.

Gostaria de agradecer também às seguintes instituições: à Universidade de Aveiro; ao Instituto de Telecomunicações, onde dispus de todas as condições técnicas, logísticas e humanas para a realização do trabalho apresentado nesta dissertação; à Fundação para a Ciência e a Tecnologia, que através da minha bolsa de doutoramento SFRH/BD/28275/2006 e dos projectos OSP-HNLF, ref. PTDC/EEA-TEL/105254/2008, e QuantPrivTel, ref. PTDC/EEA-TEL/103402/2008, possibilitou a realização deste trabalho.

Uma palavra especial a todos os meus colegas e amigos do grupo de comunicações óticas do Instituto de Telecomunicações, cujo apoio, camaradagem e amizade em muito contribuíram para o bom desenrolar deste meu desafio.

À minha família, por tudo.

A todos, um sentido obrigado.

Nelson Muga

Palavras Chave

Fibra ótica, polarização da luz, espalhamento da polarização, controladores de polarização, dispersão dos modos de polarização, amplificação Raman, controlo da polarização totalmente ótico, distribuição de chaves quânticas

Resumo

Nesta tese realizamos uma análise detalhada do processo de espalhamento do estado de polarização (SOP) da luz, obtido através da concatenação de vários controladores de polarização (PCs) baseados no enrolamento de fibra ótica. É proposto um emulador de dispersão dos modos de polarização (PMD), construído através da concatenação de PCs e fibras que mantêm a polarização, capaz de gerar corretamente a estatística da PMD de primeira e segunda ordens.

Analisamos ainda a copropagação de dois feixes de luz em fibras de elevada birrefringência. A evolução ao longo da fibra do SOP relativo entre os dois feixes de luz é modelada através da definição do parâmetro grau de copolarização. O modelo é validado experimentalmente, explorando a dependência na polarização do efeito de mistura de quatro ondas em fibras de elevada birrefringência.

Estudamos também a interação sinal ruído mediada pelo efeito de Kerr em fibras óticas. É derivado um modelo que descreve o ruído gerado pela emissão espontânea amplificada em sistemas com ganho de Raman distribuído. Mostramos que a estatística do ruído varia com a distância de propagação e com a potência do sinal, e que para distâncias superiores a 120 km e potências do sinal maiores que 6 mW esta deixa de ser descrita por uma distribuição Gaussiana.

Analisamos o processo de controlo totalmente ótico da polarização baseado no efeito de espalhamento de Raman estimulado. Através do mapeamento do grau de polarização (DOP), mostramos que a amplificação preferencial de uma componente do sinal permite uma atração do SOP num intervalo de comprimentos de onda igual a 60 nm. A eficiência do processo é mais elevada em torno do comprimento de onda de ganho de Raman máximo, onde existe um intervalo de 15 nm para o qual o DOP tem valores praticamente constantes.

Finalmente, fazemos um estudo do controlo do SOP em sistemas de distribuição de chaves quânticas (QKD) com codificação na polarização. É derivado um modelo que permite estimar a taxa de erro quântica em sistemas de QKD com esquemas de controlo do SOP baseados na multiplexagem no comprimento de onda e na multiplexagem no domínio temporal.

Key words

Optical fiber, light polarization, polarization scattering, polarization controllers, polarization-mode dispersion, Raman amplification, all-optical polarization control, quantum key distribution

Abstract

In this thesis we perform a detailed analysis of the state of polarization (SOP) of light scattering process using a concatenation of fiber-coil based polarization controllers (PCs). We propose a polarization-mode dispersion (PMD) emulator, built through the concatenation of fiber-coil based PCs and polarization-maintaining fibers (PMFs), capable of generate accurate first- and second-order PMD statistics.

We analyze the co-propagation of two optical waves inside a high-birefringence fiber. The evolution along the fiber of the relative SOP between the two signals is modeled by the definition of the degree of co-polarization parameter. We validate the model for the degree of co-polarization experimentally, exploring the polarization dependence of the four-wave mixing effect into a fiber with high birefringence.

We also study the interaction between signal and noise mediated by Kerr effect in optical fibers. A model accurately describing amplified spontaneous emission noise in systems with distributed Raman gain is derived. We show that the noise statistics depends on the propagation distance and on the signal power, and that for distances longer than 120 km and signal powers higher than 6 mW it deviates significatively from the Gaussian distribution.

We explore the all-optical polarization control process based on the stimulated Raman scattering effect. Mapping parameters like the degree of polarization (DOP), we show that the preferred amplification of one particular polarization component of the signal allows a polarization pulling over a wavelength range of 60 nm. The efficiency of the process is higher close to the maximum Raman gain wavelength, where the DOP is roughly constant for a wavelength range of 15 nm.

Finally, we study the polarization control in quantum key distribution (QKD) systems with polarization encoding. A model for the quantum bit error rate estimation in QKD systems with time-division multiplexing and wavelength-division multiplexing based polarization control schemes is derived.

"*O mistério das cousas? Sei lá o que é mistério!*
O único mistério é haver quem pense no mistério."
O Guardador de Rebanhos
Alberto Caeiro

À Ana.

À Victória.

Contents

List of Acronyms

Notation	Description
ACF	Autocorrelation Function
ASE	Amplified Spontaneous Emission
BER	Bit-Error Rate
CD	Chromatic Dispersion
CW	Continuous Wave
DGD	Differential Group Delay
DMUX	Optical De-Multiplexer
DOP	Degree of Polarization
EDFA	Erbium-Doped Fiber Amplifier
EPC	Electronic Polarization Controller
FWHM	Full Width at Half Maximum
FWM	Four-Wave Mixing
HiBi	High-Birefringence
HWP	Half-Wave Plate
IM/DD	Intensity Modulation with Direct Detection
LCP	Left Circular Polarization
LHP	Linear Horizontal Polarization
LVP	Linear Vertical Polarization
MUX	Optical Multiplexer
MZI	Mach–Zehnder Interferometer
NDF	Normalized Deviation Factor
NLSE	Nonlinear Schrödinger Equation
NRZ	NonReturn-to-Zero

Notation	Description
OOK	on-off-keying
OSA	Optical Spectrum Analyzer
PBS	Polarization Beam Splitter
PC	Polarization Controller
PCD	Polarization-dependent Chromatic Dispersion
pdf	probability density function
PDG	Polarization-Dependent Gain
PDL	Polarization-Dependent Losses
PDM	Polarization-Division Multiplexing
PMD	Polarization-Mode Dispersion
PMF	Polarization-Maintaining Fiber
PSP	Principal State of Polarization
QBER	Quantum Bit Error Rate
QKD	Quantum Key Distribution
QWP	Quarter-Wave Plate
RCP	Right Circular polarization
rSOP	relative State of Polarization
RZ	Return-to-Zero
SOP	State of Polarization
SPDM	Single-Photon Detector Module
SRS	Stimulated Raman Scattering
SSFM	Split-Step Fourier Method
SSMF	Standard Single-Mode Fiber
TDM	Time-Division Multiplexing
VOA	Variable Optical Attenuator
WDM	Wavelength-Division Multiplexing

Note: Each acronym is defined the first time it appears in a Chapter.

List of Figures

List of Tables

List of Symbols

Symbol	Designation
α	Fiber losses coefficient
$\vec{b}$	Ratio between the birefringence vector $\vec{\beta}$ and the angular frequency ω
β	Propagation constant
$\vec{\beta}$	Local birefringence vector
$\vec{\beta}_{\text{circ}}$	Birefringence vector describing circular birefringence
$\vec{\beta}_{\text{lin}}$	Birefringence vector describing linear birefringence
β_i	Birefringence vector components (with $i = 1, 2, 3$)
β_ω	First-order derivative of β with respect to ω; Group velocity inverse
$\beta_{\omega\omega}$	Second-order derivative of β with respect to ω; Group velocity dispersion coefficient
β_x	Propagation constant along x axis
β_y	Propagation constant along y axis
c	Light speed in vacuum (299792458 ms^{-1})
D	Chromatic dispersion parameter
$\hat{D}$	Split-step fourier method linear operator
D_p	Polarization-mode dispersion coefficient
δ_{ij}	*Kronecker Delta* symbol
$\delta(x)$	*Dirac Delta* function
$\Delta\beta$	Difference between propagation constants of the principal axis; Local birefringence vector modulus
$\Delta\beta_\omega$	First-order derivative of $\Delta\beta$ with respect to ω;
$\Delta\lambda$	Wavelength separation
Δn	Modal refractive indices difference
$\Delta\omega$	Frequency separation
$\Delta\omega_c$	Correlation bandwidth
$\Delta\tau$	Differential group delay; First-order PMD vector modulus
$\langle\Delta\tau\rangle$	Mean differential group delay
$\Delta\tau_\omega$	Magnitude of the second-order PMD vector component parallel to $\vec{\tau}$
$\Delta\tau_{\text{rms}}$	Root mean square of $\Delta\tau$
Δt	Time delay
$\Delta\phi_{\text{NL}}$	Nonlinear phase shift

$\det(\mathbf{A})$	Determinant of a matrix $\mathbf{A}$
$\overrightarrow{E}$	Electric field vector
$f_{\parallel}$	Degree of co-polarization for the parallel scheme
$f_{\perp}$	Degree of co-polarization for the orthogonal scheme
f_n	Langevin noise source
f_r	Fraction of nonlinearity that arises from the delayed Raman response
f_{rep}	Pulse rate
$F_T\{\}$	Fourier transform
$F_T^{-1}\{\}$	Inverse Fourier transform
$\mathbf{F}$	PC matrix (QWP - HWP - QWP)
$\digamma_n$	Optical noise added discretely at each step of the SSFM
γ	Nonlinear coeficient
g_{af}	Afterpulse characteristic constant
g_R	Raman gain coefficient
$h_R(t)$	Raman response function
$\text{Im}[\,]$	Imaginary part of the argument
$\|J\rangle$	Jones Vector
k_B	Boltzmann constant
L_B	Beat length
L_C	Correlation length
L_D	Dispersion length
L_{eff}	Effective length
λ	Wavelength
λ_0	Wavelength in vacuum
$\mathbf{M}_{\lambda/4}$	QWP Mueller matrix
$\mathbf{M}_{\lambda/2}$	HWP Mueller matrix
n	Refractive index
$\hat{N}$	Split-step fourier method nonlinear operator
$\langle n \rangle$	Mean number of photons per pulse
$\langle n_g \rangle$	Mean number of reference photons per pulse leakage to data detector
$\langle n_r \rangle$	Mean number of reference photons per pulse
n_{sp}	Spontaneous scattering factor
η_{det}	Single-photon detector module efficiency
$\hat{p}$	PMD vector orientation (parallel to slow PSP)
P_{af}	Error probability due to afterpulses
P_{click}	Single-photon detector module click probability
P_{dc}	Dark count probability
p_{fACF}	Error probability due to polarization decorrelation in frequency domain
p_{ij}	Photo-elastic silica tensor
P_{leak}	Probability of photons leakage
$\hat{p}_{\omega}$	Depolarization of the PSPs
$\hat{p}_{\text{PSP}}^{\text{in}}$	Input PSPs
$\hat{p}_{\text{PSP}}^{\text{out}}$	Output PSPs
p_{SOP}	Error probability due to feedback SOP control

p_{tACF}	Error probability due to polarization decorrelation in time domain
$\mathrm{QBER}_{\mathrm{af}}$	QBER due to afterpulses
$\mathrm{QBER}_{\mathrm{dc}}$	QBER due to dark counts
$\mathrm{QBER}_{\mathrm{fACF}}$	QBER due to p_{fACF}
$\mathrm{QBER}_{\mathrm{leak}}$	QBER due to p_{leak}
$\mathrm{QBER}_{\mathrm{SOP}}$	QBER due to p_{SOP}
$\mathrm{QBER}_{\mathrm{tACF}}$	QBER due to p_{tACF}
R_{af}	Error rate due to afterpulses
R_{dc}	Error rate due to dark counts
$\mathrm{Re}[\,]$	Real part of the argument
R_{error}	Total error rate in a QKD system
R_{fACF}	Error rate due to p_{fACF}
R_{leak}	Error rate due to p_{leak}
R_{raw}	Rate of raw keying in a QKD system
R_{sift}	Rate in QKD system after sifting
R_{SOP}	Error rate due to p_{SOP}
R_{tACF}	Error rate due to p_{tACF}
$\mathbf{R}_x$	Rotation matrix of a PMF
$\lvert s\rangle$	Jones *ket* vector
$\langle s\rvert$	Jones *bra* vector
$\vec{S}$	Stokes vector
S_i	Stokes parameters (with $i = 0, 1, 2, 3$)
$\hat{s}$	Normalized Stokes vector
s_i	Normalized Stokes vector components (with $i = 1, 2, 3$).
$\boldsymbol{\sigma}_i$	Pauli matrices (with $i = 0, 1, 2, 3$)
$\vec{\sigma}$	Pauli vector
T_{af}	Time difference between reference pulse arrival and data gate opening
t_{link}	Transmission efficiency
T_{rep}	Repetition period ($1/f_{\mathrm{rep}}$)
τ_λ	Polarization-dependent chromatic dispersion
$\vec{\tau}$	First-order PMD vector
$\vec{\tau}_\omega$	Second-order PMD vector
$\tau_{\omega i}$	Second-order PMD vector coordinates (with $i = 1, 2, 3$)
$\vec{\tau}_{\omega\parallel}$	Second-order PMD vector component parallel to $\vec{\tau}$
$\vec{\tau}_{\omega\perp}$	Second-order PMD vector component perpendicular to $\vec{\tau}$
$\mathrm{Tr}(\mathbf{A})$	Trace of a matrix $\mathbf{A}$
$\mathbf{U}$	Jones matrix
ω	Angular frequency
$\vec{W}^{\mathrm{NL}}$	Nonlinear polarization rotation vector

Chapter 1

Introduction

Polarization effects in fiber-optic communication systems are usually related to fiber birefringence [1]. It is well known that standard single-mode fibers (SSMFs) support two orthogonally-polarized modes [2]. These two modes have almost the same propagation constant, i.e., they travel at the same velocity [3]. When light encounters any sort of perturbation or asymmetry within the fiber, it results very easy for optical energy to transfer from one of these modes to the other. For sufficiently long fibers, such perturbations or asymmetries lead to random polarization rotation, polarization-mode coupling, and polarization-mode dispersion (PMD) [4–7]. The stochastic behavior of the polarization evolution in optical fibers is undesirable, since, most of the times, it deteriorates the performance of the communication system [8]. Random polarization rotation can be overcome by using polarization-maintaining fibers (PMFs). This kind of fibers are engineered in such a way that the two orthogonally-polarized modes are forced to have different propagation constants, i.e., they travel at different velocities [9]. The velocity mismatch makes it very difficult for optical energy to cross-couple, which means that the state of polarization (SOP) of the transmitted light is preserved if initially it was aligned with one of the principal axes of the fiber. However, although suitable for laboratorial environments, this kind of fibers are cost-prohibitive for long-haul applications.

The following section presents an overview of the studies on polarization effects in fiber-optic communication systems. A deep review of the state-of-the-art of the various subjects analyzed in this thesis can be found at the Introduction of the respective Chapter.

1.1 Polarization in Fiber-Optic Communications

Light polarization in optical fibers began to receive special attention in the context of coherent optical communication systems [10]. In the 1980s, coherent detection presented some potential gains over the direct detection on-off-keying (OOK), and it was under investigation world-wide during several years. Coherent detection systems required that both phase and polarization of the received signal and the local oscillator were matched [11]. In order to solve the polarization matching problem, a large number of works have focused on the so-called endless SOP control [12, 13]. Such polarization

control schemes aimed to match the time varying SOP of the incoming signal with that of the local oscillator [14]. The first polarization controllers relied on the elasto-optic properties of silica by introducing controlled squeezing [15–18], or bending of the fiber itself [19]. Subsequently, other devices were proposed based on electro-optics crystals [20], Faraday rotators [12], and liquid crystals [21, 22]. Nevertheless, none of the early proposals covered the issue of endless control demanded by coherent receivers. The first proposals for endless control used rotatable waveplates [23], while the desire to avoid bulk optics led to ingenious techniques that enabled continuous rotation of fiber loops without introducing twists. Several other endless control schemes have been proposed and implemented, overcoming the finite range limitation of many transducers [24, 25]. However, the invention of erbium-doped fiber amplifiers (EDFAs) in the 1990s, in conjugation with the technical difficulties inherent to coherent receivers, contributed to an interruption on the research activities in coherent optical communication systems for nearly 20 years. As a consequence, the polarization control research applied to coherent detection also suffered an interruption for several years.

Optical amplification represented an important advance for optical communication systems, overcoming the main limitations imposed by electric regeneration, and allowing for the development of long-distance fiber-optic systems [26]. At that time, the EDFA emerged as the technology of choice, mainly because the optical pump powers required for Raman amplification were significantly higher than that for EDFA. In the 1990s, PMD becomes a limiting factor for intensity modulation with direct detection (IM/DD) lightwave systems designed to operate over long distances at high bit rates [8, 27, 28]. In its simplest manifestation, PMD splits a signal between the fast and the slow axes in an optical fiber and, at the same time, higher-orders of PMD induce signal depolarization and polarization-dependent chromatic dispersion (PCD) [6]. At high bit rates, these effects can lead to important transmission penalties. Since PMD is a stochastic phenomenon, the induced penalties change randomly over distance and time as the ambient temperature and other environmental parameters change [29]. The rapid stride toward high-speed transmission at 40 Gb/s and beyond has stimulated extensive research efforts on PMD. The investigations addressing this topic can be roughly divided into three broad areas. The first area covered the fundamental understanding of the PMD effect and its impact on optical transmission systems. The statistical nature of PMD [30], the development of PMD emulators [31–33], and the mixture of PMD with other impairments, e.g., polarization-dependent losses (PDL) [34] and nonlinearity [35], were largely discussed. The analysis of the tolerance of different modulation formats to PMD effects also received a great attention [8, 36, 37]. It was shown that return-to-zero (RZ) pulses perform better than nonreturn-to-zero (NRZ) because the energy is more confined to the center of the bit-slot in the RZ case. While the performance of RZ modulation is better for PMD-uncompensated systems, it was also shown that the effectiveness of PMD compensation is higher for NRZ data. The reason is that modulation formats with smaller duty cycle tend to have larger bandwidth and therefore they are more sensitive to high-order PMD [8]. Notice that the impairments in PMD compensated systems are mainly caused by high-order PMD. In general, the smaller the bandwidth of the modulation formats, the more improvement of PMD tolerance can be obtained after PMD compensation [37].

The second area, addressing the PMD measurement issue, was important both for gaining an increased understanding of the phenomenon and for compensation [38, 39]. Finally, the last area of research was related with PMD compensation, where both optical and electronic techniques were proposed [40, 41]. For instance, first-order PMD can be compensated by using a polarization controller (PC) and a variable time delay. Higher-orders PMD require more complex compensators with a large number of degrees of freedom. On the other hand, electronic methods are based on tapped delay lines and delayed decision techniques at the receiver to infer the transmitted signal [42, 43]. However, the problem for PMD compensation of multiple wavelengths is still an issue.

The advance of semiconductor pump laser engineering in the late 1990s, lead to the development of suitable high-power pumps, renewing the interest on Raman amplification. In fact, it was shown that Raman amplification presents some attractive features when compared with other optical amplification solutions, namely the EDFAs [44–46]. The possibility to adjust the gain profile by combining multiple pump wavelengths and the improved noise figure are among them [44, 45]. The polarization-dependence of the Raman gain affects the performance of Raman amplifiers in different ways [45]. As stated above, fluctuating birefringence of optical fibers changes the SOP of any optical field in a random fashion leading to PMD. It was shown that PMD reduces the average Raman gain and introduces signal fluctuations because of random changes in the relative angle between the pump and signal SOPs [47]. Such signal fluctuations can be quite large, depending on the value of the PMD parameter. It was also shown that fluctuations are larger in the case of forward pumping but can be reduced to less than 1% by use of backward pumping [47]. The concept of polarization-dependent gain (PDG) is a straightforward way to quantify the PMD effects in Raman amplifiers. This quantity is defined as the difference between the maximum and the minimum values of gain realized while varying the SOP of the input signal [48]. The analytical models describing the PDG statistics show that the mean PDG as well as PDG fluctuations are reduced by approximately a factor of 30 in the case of backward pumping [49]. Since the PDG effect is undesirable in a real telecom systems, the pump SOP is usually scrambled before launched into the fiber.

The increasing demand for bandwidth is rapidly pushing the capacity of actual optical communication systems to its limits [50]. The combination of advanced modulation formats, coherent detection and digital signal processing has emerged as a favorable solution for future high-speed optical communication systems, providing new capabilities that were not possible without the detection of the phase and amplitude of the optical signal [51, 52]. Recent fiber capacity records were established using advanced modulation formats, with significant focus on four-dimensional optimized formats (i.e., those using both quadratures and both polarization components of the electromagnetic field) [53]. Spectrally-efficient optical communication systems employ polarization-division multiplexing (PDM) as a practical solution, doubling in that way the capacity of a fiber link [54, 55]. The use of both polarizations to transmit information means that PMD remains a critically important channel characteristic that needs to be continuously reexamined in actual and future optical communication systems.

The polarization-encoded quantum key distribution (QKD) systems installed in tele-

com optical fibers are also affected by residual birefringence [56]. Changes and instability in the single photons SOP becomes a significant obstacle to the implementation of these systems. Notice that polarization encoding requires a perfect alignment between Alice and Bob's polarizers during the period of exchanging quantum bits [57] (in QKD, Alice and Bob are the conventional names of the sender and receiver, respectively). Since QKD systems aim to assure an unconditional secure distribution of secret keys between two parties, the influence of the SOP compensation system on the quantum channel should be avoided or, at least, minimized. That means that the traditional SOP control schemes used in classical communication systems are, normally, unsuitable to QKD systems. In order to make polarization encoding feasible, new several polarization control techniques were proposed [58–63].

1.2 Thesis Outlook

The following Chapters present an analysis of polarization effects in fiber-optic communication systems. This thesis is constituted by eight Chapters, organized as follows.

Chapter 2 introduces the Jones and Stokes formalisms used to trace the polarization of an electromagnetic wave into an optical fiber and other optical elements. The two formalisms are used to define the birefringence vector, as well as the first- and second-order PMD vectors and respective statistics.

Chapter 3 deals with the subject of polarization scattering and its application for PMD emulation [64–66]. After deriving a theoretical model for the SOP random distribution over the Poincaré sphere, the numerical results obtained for different PC configurations are presented. Those results are applied into the characterization of PMD emulators based on PMFs and fiber-coil based PCs.

Chapter 4 analyzes the polarization effects in fibers with high birefringence [67–72]. The degree of co-polarization is defined as a function of polarization orientation and ellipticity of the two input signals, considering two different input polarization schemes. The degree of co-polarization model is experimentally validated in a long-distance regime through measurements of the efficiency of the four-wave mixing (FWM) process into a high-birefringence (HiBi) fiber.

Chapter 5 regards the issue of amplified spontaneous emission (ASE) noise in Raman amplification [73–76]. The derived ASE model is validated through experimental results, and used to study the interaction between signal and noise mediated by the Kerr effect for different propagation regimes. The noise statistic is characterized through the calculation of high-order statistical moments.

Chapter 6 is devoted to the all-optical polarization control process using stimulated Raman scattering (SRS) [77]. It is shown that by copropagating a pump wave with a weak signal, the signal SOP can suffer an effective pulling process over a wide wavelength range. Parameters like the signal degree of polarization (DOP), the mean angle between the output signal SOP and the output pump SOP, the mean gain and its standard deviation are mapped for the entire Raman gain bandwidth, in both undepleted and

depleted pump regimes.

Chapter 7 presents a model for quantum bit error rate (QBER) estimation in QKD systems with polarization encoding [78–80]. Both time-division multiplexing (TDM)- and wavelength-division multiplexing (WDM)-based SOP control schemes applied to polarization-encoded QKD systems are analyzed. The QBER expressions derived for each SOP control scheme account for intrinsic impairments, like the fiber PMD and losses, as well as for limitative technical aspects, like the single-photon detector dark counts, after pulse detections, or the feedback SOP control performance.

Chapter 8 overviews the developed work, summarizes the main conclusions, and presents suggestions for future work.

1.3 Main Achievements

In the author opinion, the most important results reported in this thesis are the following:

- Proposal of a new method to uniformly scatter the light SOP over the Poincaré sphere [64–66]. The SOP scattering is obtained through the concatenation of fiber-coil based PCs, and can be applied to the construction of PMD emulators [64].

- Description of the relative SOP between two waves inside an HiBi fiber [70]. It is shown that for some distance and wavelength separation regimes, launching two signals into a HiBi fiber with orthogonal polarizations can result in a highest degree of co-polarization when compared with the initially parallel SOPs scheme [71, 72]. This result can be used for implementation and optimization or of new all-optical signal processing devices [67–69].

- Modeling of the interaction between signal and noise mediated by the Kerr effect in optical fibers, and characterization of the induced noise statistics changes [73, 75, 76]. It is shown that for some particular signal power and distance regimes, the noise statistics can deviate significatively from the Gaussian distribution [74].

- Characterization of a new technique for all-optical polarization control based on Raman amplification [77]. The preferred amplification of one particular polarization component of the signal allows the polarization pulling of an unpolarized signal over a wavelength range of 60 nm around the Raman gain peak. Due to the broadband effectiveness of this effect, this technique can be exploited into the development of next-generation optical regenerators.

- Modeling of the QBER in polarization-encoded QKD systems with dynamic SOP control [78]. The TDM-based SOP control scheme was identified as the most efficient SOP control solution for QKD systems with polarization encoding, when compared with the WDM-based SOP control scheme [79, 80].

1.4 List of Publications

The work accomplished during the elaboration of this thesis resulted in 9 papers published in internationally peer reviewed journals and 16 conference proceedings. The publications are listed bellow.

1.4.1 Journal Articles

9. N. J. Muga, M. F. Ferreira, and A. N. Pinto, "Broadband polarization pulling using Raman amplification," *Opt. Express*, vol. 19, no. 19, pp. 18707–18712, 2011.

8. N. A. Silva, N. J. Muga, A. N. Pinto, "Evolution of first-order sidebands from multiple FWM processes in HiBi optical fibers," *Opt. Commun.*, vol. 284, no. 3, pp. 3408–3415, 2011.

7. N. J. Muga, M. F. Ferreira, and A. N. Pinto, "QBER estimation in QKD systems with polarization encoding," *IEEE/OSA J. Lightwave Technol.*, vol. 29, no. 3, pp. 355–361, 2011.

6. N. J. Muga, N. A. Silva, M. F. Ferreira, and A. N. Pinto, "Evolution of the degree of co-polarization in high-birefringence fibers," *Opt. Commun.*, vol. 283, no. 10, pp. 2125–2132, 2010.

5. N. A. Silva, N. J. Muga, and A. N. Pinto, "Effective nonlinear parameter measurement using FWM in optical fibers in a low power regime," *IEEE J. Quantum Electron.*, vol. 46, no. 3, pp. 285–291, 2010.

4. N. A. Silva, N. J. Muga, and A. N. Pinto. "Influence of the stimulated Raman scattering on the four-wave mixing process in birefringent fibers," *IEEE/OSA J. Lightwave Technol.*, vol. 27, no. 22, pp. 4979–4988, 2009.

3. N. J. Muga, M. C. Fugihara, M. F. Ferreira, and A. N. Pinto, "Non-Gaussian ASE noise in Raman amplification systems," *IEEE/OSA J. Lightwave Technol.*, vol. 27, no. 16, pp. 3389–3398, 2009.

2. N. J. Muga, A. N. Pinto, and M. F. Ferreira, "Polarization scattering property of cascaded polarization controllers," *ETRI Trans.*, vol. 29, no. 6, pp. 838–840, 2007.

1. N. J. Muga, A. N. Pinto, M. F. Ferreira, and J. R. F. da Rocha, "Uniform polarization scattering with fiber-coil based polarization controllers," *IEEE/OSA J. Lightwave Technol.*, vol. 24, no. 11, pp. 3932–3943, 2006.

1.4.2 National and International Conferences

16. Á. J. Almeida, L. M. Martins, N. A. Silva, N. J. Muga, and A. N. Pinto, "Correlated Photon-Pair Generation in a Highly Nonlinear Fiber Using Spontaneous FWM," in *Proc Symp. on Enabling Optical Networks - SEON*, Aveiro, Portugal, 2011.

15. A. N. Pinto, Á. J. Almeida, N. A. Silva, N. J. Muga, and L. M. Martins, "Optical Quantum Communications: An Experimental Approach," in *Proc International Conference on Applications of Optics and Photonics - AOP2011*, Braga, Portugal, 2011.

14. Á. J. Almeida, N. A. Silva, N. J. Muga, and A. N. Pinto, "Single-Photon Source Using Stimulated FWM in Optical Fibers for Quantum Communication," in *Proc International Conference on Applications of Optics and Photonics - AOP2011*, Braga, Portugal, 2011.

13. N. J. Muga, Á. J. Almeida, M. F. Ferreira, and A. N. Pinto, "Optimization of polarization control schemes for QKD systems," in *Proc International Conference on Applications of Optics and Photonics - AOP2011*, Braga, Portugal, 2011.

12. Á. J. Almeida, S. R. Carneiro, N. A. Silva, N. J. Muga, and A. N. Pinto, "Polarization-entangled photon pairs using spontaneous four-wave mixing in a fiber loop," in *Proc Conf. on Telecommunications - ConfTele*, Lisboa, Portugal, vol. 1, pp. 11, 2011.

11. N. J. Muga, Á. J. Almeida, M. F. Ferreira, and A. N. Pinto, "Critical Issues in Polarization Encoded Quantum Key Distribution Systems," in *Proc Conf. on Telecommunications - ConfTele*, Lisboa, Portugal, vol. 1, pp. 11, 2011.

10. Á. J. Almeida, S. R. Carneiro, N. A. Silva, N. J. Muga, and A. N. Pinto, "Time coincidence of entangled photon pairs using spontaneous four-wave mixing in a fiber loop," in *Proc Symp. on Enabling Optical Networks - SEON*, Porto, Portugal, June, 2010.

9. N. J. Muga, N. A. Silva, M. F. Ferreira, and A. N. Pinto, "Generalized Analysis of the Polarization Evolution in High-Birefringence Fibers," in *Proc International Conf. on Transparent Networks – ICTON*, Munich, Germany, Mo.P.2, June/July, 2010.

8. N. J. Muga, N. A. Silva, M. F. Ferreira, and A. N. Pinto, "Relative State-of-Polarization in High-Birefringence Fibers," in *Proc European Conf. on Networks and Optical Communications and Conf. on Optical Cabling and Infrastructure - NOC/OC*, Faro, Portugal, vol. 1, pp. 121–126, June, 2010.

7. N. A. Silva, N. J. Muga, and A. N. Pinto, "Measurement of the Effective Nonlinear Parameter Using FWM in Random Polarization Optical Fibers," in *Proc European Conf. on Networks and Optical Communications and Conf. on Optical Cabling and Infrastructure - NOC/OC*, Faro, Portugal, vol. 1, pp. 185–190, June, 2010.

6. Á. J. Almeida, N. A. Silva, N. J. Muga, and A. N. Pinto, "Fiber-Optical Communication System Using Polarization-encoding Photons," in *Proc European Conf. on Networks and Optical Communications and Conf. on Optical Cabling and Infrastructure - NOC/OC*, Faro, Portugal, vol. 1, pp. 127–132, June, 2010.

5. N. J. Muga, M. C. F. Fugihara, M. F. Ferreira, and A. N. Pinto, "Non-White Noise Generation Method for ASE Noise Simulation in Systems with Raman Amplification," in *Proc International Conf. on Transparent Optical Networks - ICTON*, Ponta Delgada - Azores, Portugal, vol. 1, pp. WeA1.6, June, 2009.

4. N. J. Muga, M.C.F. Fugihara, M. F. Ferreira, and A. N. Pinto, "ASE Noise Simulation in Raman Amplification Systems," in *Proc Conf. on Telecommunications - ConfTele*, Santa Maria da Feira, Portugal, vol. 1, pp. 347–350, May, 2009.

3. N. A. Silva, N. J. Muga, and A. N. Pinto, "Single-Photon Generation,", in *Proc Conf. on Telecommunications - ConfTele*, Santa Maria da Feira, Portugal, vol. 1, pp. 35, May, 2009.

2. N. J. Muga, M. C. F. Fugihara, M. F. Ferreira, and A. N. Pinto, "Modeling of ASE Noise in Broadband Systems with Raman Amplification," in *Proc Symp. on Enabling Optical Networks - SEON*, Porto, Portugal, pp. 145–146, June, 2008.

1. N. J. Muga, A. N. Pinto, and M. F. Ferreira, "Polarization Controller: Angles Configuration and Scattering Properties," in *Proc Conf. on Telecommunications - ConfTele*, Peniche, Portugal, vol. IM.1, pp. 243–246, May, 2007.

References

[1] S. Rashleigh, "Origins and control of polarization effects in single-mode fibers," *IEEE/OSA J. Lightwave Technol.*, vol. 1, no. 2, pp. 312–331, Jun. 1983.

[2] G. P. Agrawal, *Nonlinear Fiber Optics, 4rd ed.* Academic Press, San Diego, USA, 2007.

[3] M. F. Ferreira, *Nonlinear Effects in Optical Fibers.* John Wiley & Sons, Inc, 2011.

[4] C. D. Poole and R. E. Wagner, "Phenomenological approach to polarization dispersion in longe-single mode fibres," *Electron. Lett.*, vol. 22, pp. 1029–1031, 1986.

[5] P. K. A. Wai and C. R. Menyuk, "Polarization mode dispersion, decorrelation, and diffusion in optical fibers with randomly varying birefringence," *IEEE/OSA J. Lightwave Technol.*, vol. 14, no. 2, pp. 148–157, 1996.

[6] H. Kogelnik, R. M. Jopson, and L. E. Nelson, *Optical Fiber Telecommunications IVb.* Academic Press, San Diego, 2002, ch. 15, pp. 725–861.

[7] J. P. Gordon and H. Kogelnik, "PMD fundamentals: Polarization mode dispersion in optical fibers," *PNAS*, vol. 97, no. 9, pp. 4541–4550, 2000.

[8] H. Sunnerud, M. Karlsson, C. Xie, and P. Andrekson, "Polarization-mode dispersion in high-speed fiber-optic transmission systems," *IEEE/OSA J. Lightwave Technol.*, vol. 12, no. 1, pp. 50–52, Dec. 2002.

[9] J. Noda, K. Okamoto, and Y. Sasaki, "Polarization-maintaining fibers and their applications," *IEEE/OSA J. Lightwave Technol.*, vol. 4, no. 8, pp. 1071–1089, Aug. 1986.

[10] T. Okoshi, "Recent advances in coherent optical fiber communication systems," *IEEE/OSA J. Lightwave Technol.*, vol. 5, no. 1, pp. 44–52, 1987.

[11] G. P. Agrawal, *Lightwave Technology: Telecommunication Systems.* John Wiley & Sons, New Jersey, USA, 2005.

[12] T. Okoshi, Y. H. Cheng, and K. Kikuchi, "New polarization control scheme for optical heterodyne receiver using two faraday rotators," *Electron. Lett.*, vol. 21, no. 18, pp. 787–788, 1985.

[13] N. G. Walker and G. R. Walker, "Polarization control for coherent communications," *IEEE/OSA J. Lightwave Technol.*, vol. 8, no. 3, pp. 438–458, 1990.

[14] R. Noe, H. Rodler, A. Ebberg, G. Gaukel, B. Noll, J. Wittmann, and F. Auracher, "Comparison of polarization handling methods in coherent optical systems," *IEEE/OSA J. Lightwave Technol.*, vol. 9, no. 10, pp. 1353–1366, Oct. 1991.

[15] R. Ulrich, "Polarization stabilization on single-mode fibers," *Appl. Phys. Lett.*, vol. 35, no. 11, pp. 840–842, 1979.

[16] H. Honmou, S. Yamazaky, K. Emura, R. Ishikawa, I. Mito, M. Shikada, and K. Minemura, "Stabilisation of heterodyne receiver sensitivity with automatic polarisation control system," *Electron. Lett.*, vol. 22, no. 22, pp. 1181–1182, 1986.

[17] M. Johnson, "In-line fiber-optical polarization transformer," *App. Opt.*, vol. 18, no. 9, pp. 1288–1289, 1979.

[18] P. Granestrand and L. Thylen, "Active stabilization of polarization on a single-mode fiber," *Electron. Lett.*, vol. 20, no. 9, pp. 365–366, 1984.

[19] H. C. Lefevre, "Single-mode fibre fractional wave devices and polarization controllers," *Electron. Lett.*, vol. 16, no. 20, pp. 778–780, 1980.

[20] Y. Kidoh, "Polarization control on output of single-mode optical fibers," *J. Quantum Electron.*, vol. 17, no. 6, pp. 991–994, 1981.

[21] W. L. Barnes, "2 × 2 optical fiber polarization switch and polarization controller," *Electron. Lett.*, vol. 24, no. 23, pp. 1427–1429, 1988.

[22] A. Siddiqui and H. Sherief, "Liquid crystal polarisation controller for use in fiber communication systems," in *Proc. OFC '89*, Houston, USA, Feb. 1989.

[23] T. Imai, K. Nosu, and H. Yamaguchi, "Optical polarisation control utilising an optical heterodyne detection scheme," *Electron. Lett.*, vol. 21, no. 2, pp. 52–53, 17 1985.

[24] T. Okoshi, "Polarization-state control schemes for heterodyne or homodyne optical fiber communications," *IEEE/OSA J. Lightwave Technol.*, vol. 3, no. 6, pp. 1232–1237, 1985.

[25] R. Noe, H. Heidrich, and D. Hoffmann, "Endless polarization control systems for coherent optics," *IEEE/OSA J. Lightwave Technol.*, vol. 6, no. 7, pp. 1199–1208, Jul. 1988.

[26] G. P. Agrawal, *Fiber-Optic Communication Systems, 3rd edition.* John Wiley & Sons, New York, USA, 2002.

[27] C. D. Poole and J. Nagel, *Polarization effects in lightwave systems - Optical Fiber Telecommunications.* Academic Press, San Diego, 1997, vol. IIIa, ch. 6, pp. 114–161.

[28] L. Nelson, M. Karlsson, and D. Chowdhury, "Guest editorial special issue on polarization-mode dispersion," *IEEE/OSA J. Lightwave Technol.*, vol. 22, no. 4, pp. 951–952, Apr. 2004.

[29] M. Karlsson, J. Brentel, and P. Andrekson, "Long-term measurement of PMD and polarization drift in installed fibers," *IEEE/OSA J. Lightwave Technol.*, vol. 18, no. 7, pp. 941–951, Jul. 2000.

[30] G. J. Foschini, L. E. Nelson, R. M. Jopson, and H. Kogelnik, "Probability densities of second-order polarization mode dispersion including polarization dependent chromatic fiber dispersion," *IEEE Photonics Technol. Lett.*, vol. 12, no. 3, pp. 293–295, 2000.

[31] I. T. Lima, R. Khosravani, P. Ebrahimi, E. Ibragimov, C. R.Menyuk, and A. E. Willner, "Comparison of polarization mode dispersion emulators," *IEEE/OSA J. Lightwave Technol.*, vol. 19, no. 12, pp. 1872–1881, 2001.

[32] N. J. Muga, A. N. Pinto, and M. Ferreira, "The development of a PMD emulator," in *ConfTele 2005, Tomar*, 2005.

[33] N. J. Muga, "Dispersão dos Modos de Polarização em Fibras Ópticas," Master's thesis, Universidade de Aveiro, 2006.

[34] C. Vinegoni, M. Karlsson, M. Petersson, and H. Sunnerud, "The statistics of polarization-dependent loss in a recirculating loop," *IEEE/OSA J. Lightwave Technol.*, vol. 22, no. 4, pp. 968–976, 2004.

[35] Q. Lin and G. Agrawal, "Vector theory of cross-phase modulation: role of nonlinear polarization rotation," *IEEE J. Quantum Electron.*, vol. 40, no. 7, pp. 958–964, Jul. 2004.

[36] H. Sunnerud, M. Karlsson, and P. Andrekson, "A comparison between NRZ and RZ data formats with respect to PMD-induced system degradation," *IEEE Photonics Technol. Lett.*, vol. 13, no. 5, pp. 448–450, May 2001.

[37] C. Xie, L. Moller, H. Haunstein, and S. Hunsche, "Comparison of system tolerance to polarization-mode dispersion between different modulation formats," *IEEE Photonics Technol. Lett.*, vol. 15, no. 8, pp. 1168–1170, Aug. 2003.

[38] A. Galtarossa and L. Palmieri, "Spatially resolved PMD measurements," *IEEE/OSA J. Lightwave Technol.*, vol. 22, no. 4, pp. 1103–1115, April 2004.

[39] N. Cyr, H. Chen, and G. Schinn, "Random-Scrambling Tunable POTDR for Distributed Measurement of Cumulative PMD," *IEEE/OSA J. Lightwave Technol.*, vol. 27, no. 18, pp. 4164–4174, Sept. 2009.

[40] H. Sunnerud, C. Xie, M. Karlsson, R. Samuelsson, and P. Andrekson, "A comparison between different PMD compensation techniques," *IEEE/OSA J. Lightwave Technol.*, vol. 20, no. 3, pp. 368–378, Mar. 2002.

[41] M. Ferreira, A. Pinto, P. André, N. Muga, J. Machado, R. Nogueira, S. Latas, and J. da Rocha, "Polarization mode dispersion in high-speed optical communication systems," *Fiber Integrated Opt.*, vol. 24, pp. 261–285, 2005.

[42] F. Buchali and H. Bulow, "Adaptive PMD compensation by electrical and optical techniques," *IEEE/OSA J. Lightwave Technol.*, vol. 22, no. 4, pp. 1116–1126, April 2004.

[43] H. F. Haunstein, W. Sauer-Greff, A. Dittrich, K. Sticht, and R. Urbansky, "Principles for electronic equalization of polarization-mode dispersion," *IEEE/OSA J. Lightwave Technol.*, vol. 22, no. 4, pp. 1169–1182, Apr. 2004.

[44] M. Islam, "Raman amplifiers for telecommunications," *IEEE J. Sel. Top. Quantum Electron.*, vol. 8, no. 3, pp. 548–559, 2002.

[45] C. Headley III and G. P. Agrawal, *Raman Amplification in Fiber Optical communication Systems.* Academic Press, EUA, 2004.

[46] J. Bromage, "Raman amplification for fiber communications systems," *IEEE/OSA J. Lightwave Technol.*, vol. 22, no. 1, pp. 79–93, Jan. 2004.

[47] Q. Lin and G. P. Agrawal, "Polarization mode dispersion-induced fluctuations during Raman amplifications in optical fibers," *Opt. Lett.*, vol. 27, no. 24, pp. 2194–2196, Dec. 2002.

[48] J. N. Damask, *Polarization optics in telecomunications.* Springer, New York, EUA, 2005.

[49] Q. Lin and G. P. Agrawal, "Statistics of polarization dependent gain in fiber-based Raman amplifiers," *Opt. Lett.*, vol. 28, pp. 227–229, Aug. 2003.

[50] R.-J. Essiambre, G. Kramer, P. Winzer, G. Foschini, and B. Goebel, "Capacity limits of optical fiber networks," *IEEE/OSA J. Lightwave Technol.*, vol. 28, no. 4, pp. 662–701, Feb. 2010.

[51] E. Ip, A. P. T. Lau, D. J. F. Barros, and J. M. Kahn, "Coherent detection in optical fiber systems," *Opt. Express*, vol. 16, no. 2, pp. 753–791, Jan. 2008.

[52] S. Savory, "Digital coherent optical receivers: Algorithms and subsystems," *IEEE J. Sel. Top. Quantum Electron.*, vol. 16, no. 5, pp. 1164–1179, 2010.

[53] X. Zhou, J. Yu, M.-F. Huang, Y. Shao, T. Wang, L. Nelson, P. Magill, M. Birk, P. Borel, D. Peckham, R. Lingle, and B. Zhu, "64-Tb/s, 8 b/s/Hz, PDM-36QAM Transmission Over 320 km Using Both Pre- and Post-Transmission Digital Signal Processing," *IEEE/OSA J. Lightwave Technol.*, vol. 29, no. 4, pp. 571–577, Feb. 2011.

[54] F. Yaman and G. Li, "Nonlinear impairment compensation for polarization-division multiplexed WDM transmission using digital backward propagation," *IEEE Photonics Technol. Lett.*, vol. 2, no. 5, pp. 816–832, Oct. 2010.

[55] L. E. Nelson, X. Zhou, N. M. Suibhne, A. D. Ellis, and P. Magill, "Experimental comparison of coherent polarization-switched QPSK to polarization-multiplexed QPSK for 10 × 100 km WDM transmission," *Opt. Express*, vol. 19, no. 11, pp. 10 849–10 856, May 2011.

[56] N. Gisin, G. Ribordy, W. Tittel, and H. Zbinden, "Quantum cryptography," *Rev. Mod. Phys.*, vol. 74, no. 1, pp. 145–195, Mar. 2002.

[57] H. Zbinden, N. Gisin, B. Huttner, A. Muller, and W. Tittel, "Practical aspects of quantum cryptographic key distribution," *J. Cryptology*, vol. 13, no. 2, pp. 207–220, Dec. 2000.

[58] J. Chen, G. Wu, Y. Li, E. Wu, and H. Zeng, "Active polarization stabilization in optical fibers suitable for quantum key distribution," *Opt. Express*, vol. 15, no. 26, pp. 17 928–17 936, 2007.

[59] P. Cheng-Zhi, Z. Jun, Y. Dong, G. Wei-Bo, M. Huai-Xin, H. Yin, H.-P. Zeng, Y. Tao, W. Xiang-Bin, and P. Jian-Wei, "Experimental long-distance decoy-state quantum key distribution based on polarization encoding," *Phys. Rev. Lett.*, vol. 98, no. 1, p. 010505, Jan. 2007.

[60] G. B. Xavier, G. V. de Faria, G. P. T. ao, and J. P. von der Weid, "Full polarization control for fiber optical quantum communication systems using polarization encoding," *Opt. Express*, vol. 16, no. 3, pp. 1867–1873, 2008.

[61] A. Poppe, "Method and device for readjusting a polarization drift," *United States Patent, no. US2008/0310856 A1*, Dec. 2008.

[62] J. Chen, G. Wu, L. Xu, X. Gu, E. Wu, and H. Zeng, "Stable quantum key distribution with active polarization control based on time-division multiplexing," *New J. Phys.*, vol. 11, no. 6, pp. 17 928–17 936, 2009.

[63] G. B. Xavier, N. Walenta, G. V. de Faria, G. P. Temporão, N. Gisin, H. Zbinden, and J. P. von der Weid, "Experimental polarization encoded quantum key distribution over optical fibres with real-time continuous birefringence compensation," *New J. Phys.*, vol. 11, no. 4, p. 045015, 2009.

[64] N. J. Muga, A. N. Pinto, M. Ferreira, and J. R. F. da Rocha, "Uniform polarization scattering with fiber-coil based polarization controllers," *IEEE/OSA J. Lightwave Technol.*, vol. 24, no. 11, pp. 3932–3943, 2006.

[65] N. J. Muga, A. N. Pinto, and M. Ferreira, "Polarization scattering property of cascaded polarization controllers," *ETRI Trans.*, vol. 29, no. 6, pp. 838–840, 2007.

[66] N. J. Muga, A. N. Pinto, and M. Ferreira, "Polarization controller: Angles configuration and scattering properties," in *Proc Conf. on Telecommunications - ConfTele2007*, vol. IM.1, Peniche, Portugal, May 2007, pp. 243–246.

[67] N. A. Silva, N. J. Muga, and A. N. Pinto, "Influence of the stimulated Raman scattering on the four-wave mixing process in birefringent fibers," *IEEE/OSA J. Lightwave Technol.*, vol. 27, no. 22, pp. 4979–4988, Nov. 2009.

[68] N. A. Silva, N. J. Muga, and A. N. Pinto, "Effective nonlinear parameter measurement using FWM in optical fibers in a low power regime," *IEEE J. Quantum Electron.*, vol. 46, no. 3, pp. 285–291, 2010.

[69] N. A. Silva, N. J. Muga, and A. N. Pinto, "Evolution of first-order sidebands from multiple FWM processes in HiBi optical fibers," *Opt. Commun.*, vol. 284, no. 13, pp. 3408–3415, 2011.

[70] N. J. Muga, N. A. Silva, M. Ferreira, and A. N. Pinto, "Evolution of the degree of copolarization in high-birefringence fibers," *Opt. Commun.*, vol. 283, no. 10, pp. 2125–2132, 2010.

[71] N. J. Muga, N. A. Silva, M. Ferreira, and A. N. Pinto, "Generalized analysis of the polarization evolution in high-birefringence fibers," in *Proc International Conf. on Transparent Networks – ICTON*, vol. Mo.P.2, Munich, Germany, Jun. 2010.

[72] N. J. Muga, N. A. Silva, M. Ferreira, and A. N. Pinto, "Relative state-of-polarization in high-birefringence fibers," in *Proc European Conf. on Networks and Optical Communications and Conf. on Optical Cabling and Infrastructure - NOC/OC*, vol. 1, Faro, Portugal, Jun. 2010, pp. 121–126.

[73] N. J. Muga, M. C. Fugihara, Mário F. S. Ferreira, and A. N. Pinto, "Modeling of ASE noise in broadband systems with Raman amplification," in *Proc Symp. on Enabling Optical Networks - SEON*, Porto, Portugal, Jul. 2008, pp. 145–146.

[74] N. J. Muga, M. C. Fugihara, Mário F. S. Ferreira, and A. N. Pinto, "Non-Gaussian ASE noise in Raman amplification systems," *IEEE/OSA J. Lightwave Technol.*, vol. 27, no. 16, pp. 3389–3398, 2009.

[75] N. J. Muga, M. C. Fugihara, Mário F. S. Ferreira, and A. N. Pinto, "Non-white noise generation method for ASE noise simulation in systems with Raman amplification," in *International Conf. on Transparent Optical Networks - ICTON*, vol. 1, Ponta Delgada - Azores, Portugal, Jun. 2009, p. WeA1.6.

[76] N. J. Muga, M. C. Fugihara, Mário F. S. Ferreira, and A. N. Pinto, "ASE noise simulation in Raman amplification systems," in *Proc Conf. on Telecommunications - ConfTele2009*, vol. 1, Santa Maria da Feira, Portugal, May 2009, pp. 347–350.

[77] N. J. Muga, M. F. S. Ferreira, and A. N. Pinto, "Broadband polarization pulling using Raman amplification," *Opt. Express*, vol. 19, no. 19, pp. 18 707–18 712, Sept. 2011.

[78] N. J. Muga, Mário F. S. Ferreira, and A. N. Pinto, "QBER estimation in QKD systems with polarization encoding," *IEEE/OSA J. Lightwave Technol.*, vol. 29, no. 3, pp. 355–361, 2011.

[79] N. J. Muga, Á. J. Almeida, M. Ferreira, and A. N. Pinto, "Critical issues in polarization encoded quantum key distribution systems," in *Proc EUROCON2011 and 8ª Conf. on Telecommunications - ConfTele2011*, vol. 1, Lisboa, Portugal, May 2011, pp. 11–11.

[80] N. J. Muga, Á. J. Almeida, M. Ferreira, and A. N. Pinto, "Optimization of polarization control schemes for QKD systems," in *International Conference on Applications of Optics and Photonics - AOP2011*, vol. 1, Braga, Portugal, Apr. 2011.

Chapter 2

Polarization and Optical Fibers

The analysis of polarization effects in optical fiber communication systems requires a detailed description of fiber birefringence as well as a robust tool to represent the state of polarization (SOP) of a light wave. In this chapter, we introduce the two widely used polarization representation formalisms, the Jones and the Stokes formalisms. Besides that, we also introduce the optical birefringence effect present in optical fibers, whose random evolution in time and space domains leads to polarization-mode dispersion (PMD). After defining the PMD vector and its main properties, we present the first- and second-order PMD statistics. We finish this chapter by presenting the time and frequency autocorrelation functions (ACFs) of both SOP and PMD vectors.

2.1 Polarization Representation

The SOP of light wave is defined by the orientation of the electric field vector $\overrightarrow{E}(x, y, z, t)$, whose components are dependent on both the position (x, y, z) and time t. For a given position z inside an optical fiber, the electrical field vector can be represented as [1]

$$\overrightarrow{E}(x, y, z, t) = \mathrm{Re}\left[\left(F_x(x, y)A_x(z, t)\,\hat{x} + F_y(x, y)A_y(z, t)\,\hat{y}\right)\, e^{i(\beta z - \omega_0 t)}\right], \qquad (2.1)$$

where Re[ ] means real part of the argument, $F_x(x, y)$ and $F_y(x, y)$ are the spatial distributions of the two fundamental modes oriented along the axes x and y, respectively, $A_x(z, t)$ and $A_y(z, t)$ are the field complex amplitudes, and β is the propagation constant at the carrier angular frequency ω_0. Functions $F_x(x, y)$ and $F_y(x, y)$ are z-independent and are normalized in order to make the field power equal to $|A_x(z, t)|^2 + |A_y(z, t)|^2$.

2.1.1 Jones Formalism

The Jones formalism uses the two field complex amplitudes to define a 2D vector, well-known as Jones vector, whose components are complex values [2]. This vector charac-

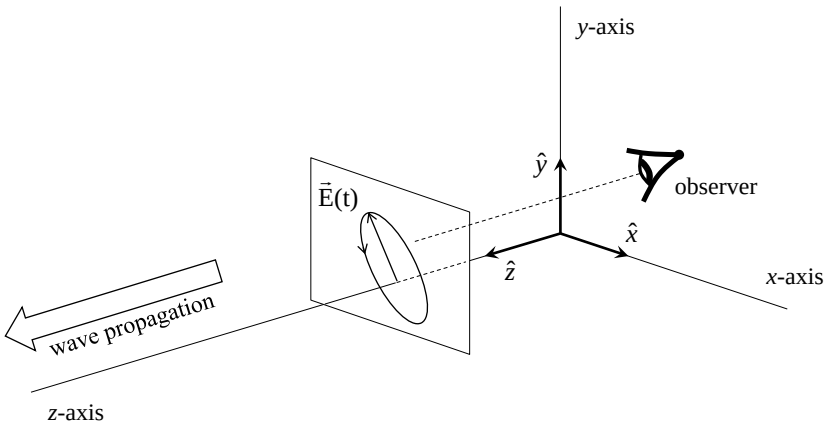

Figure 2.1: Schematic representation of the motion of an elliptically-polarized electric field in the plane perpendicular to the propagation direction.

terizes the intensity, the phase, and the state of polarization of a monochromatic light wave, and can be written as

$$|J\rangle = \begin{bmatrix} A_x \\ A_y \end{bmatrix}, \tag{2.2}$$

whose components represent the envelopes of the electric field along the horizontal and vertical linear SOPs, respectively, see Fig. 2.1. These are the two most common SOPs used to define the basis of the Jones vectors, although others SOPs pairs, e.g. left circular polarization (LCP) and right circular polarization (RCP), can also be considered [3]. The normalized version of (2.2) is the so-called Jones ket vector

$$|s\rangle = \begin{bmatrix} a_x \\ a_y \end{bmatrix} = \frac{1}{\sqrt{|A_x|^2 + |A_y|^2}} \begin{bmatrix} A_x \\ A_y \end{bmatrix} = \begin{bmatrix} s_x e^{i\varphi_x} \\ s_y e^{i\varphi_y} \end{bmatrix}, \tag{2.3}$$

where s_x (s_y) and φ_x (φ_y) are the magnitude and phase of the complex amplitude a_x (a_y), respectively. In this formalism, the bra $\langle s|$ indicates the corresponding complex conjugate row vector, given by $\langle s| = [s_x e^{-i\varphi_x}, s_y e^{-i\varphi_y}]$, with $\langle s|\, s\rangle = 1$. For instance, the ket $[\cos\theta, \sin\theta]^t$ represents a linearly polarized wave at an angle θ, measured in relation to the x axis. Notice that the normalized Jones vector representation of the SOP of light is not unique since, for instance, both Jones ket vectors $[1, 0]^t$ and $[i, 0]^t$ represent a linear horizontal polarization. Considering $s_x = s_y$ and $\varphi_y - \varphi_x = \pi/2$, with $\varphi_x = 0$, the x and y components of the real part of $|s\rangle\, e^{i(\beta z - \omega_0 t)}$ at $z = 0$ are given by

$$\mathcal{E}_x(t) = \frac{1}{\sqrt{2}} \cos(-\omega_0 t) \tag{2.4}$$

and

$$\mathcal{E}_y(t) = \frac{1}{\sqrt{2}} \cos(-\omega_0 t + \pi/2), \tag{2.5}$$

respectively. The instantaneous electric field vector represented by (2.4) and (2.5) traces out a circular locus in space, and has a clockwise sense of rotation when it is viewed along the axis of propagation (the observer is placed behind the light source [4], see Fig. 2.1). In this case, we say that the wave is right-handed circularly polarized and the corresponding Jones ket vector can be given by $1/\sqrt{2}\,[1, i]^t$. If the field vector has a counterclockwise sense of rotation, the wave is said to be left-handed circularly polarized, and Jones ket vector is given by $1/\sqrt{2}\,[1, -i]^t$. An extended list of SOP representations in the Jones space is presented in Appendix A.

The transmission through an optic element, e.g., an optical fiber or a phase retarder, is represented in the Jones space by a complex 2×2 transmission matrix $\mathbf{T}$. An output SOP $|t\rangle$ is related to the input SOP as

$$|t\rangle = \mathbf{T}\,|s\rangle = \exp(i\phi_0)\mathbf{U}\,|s\rangle\,, \tag{2.6}$$

where the real part of ϕ_0 is related with the isotropic phase term, while the imaginary part represents the isotropic loss or gain, and $\mathbf{U}$ is the so-called Jones matrix. If the optical element has no polarization-dependent losses (PDL) then $\mathbf{U}$ is unitary, with det($\mathbf{U}$)=1. A general unitary matrix can be written as [5]

$$\mathbf{U} = \begin{bmatrix} e^{i\zeta}\cos\kappa & -e^{i\varrho}\sin\kappa \\ e^{-i\varrho}\sin\kappa & e^{-i\zeta}\cos\kappa \end{bmatrix}, \tag{2.7}$$

where the two phases, given by ζ and ϱ, and the amplitude, given by κ, represent the three independent variables of the matrix.

2.1.2 Stokes Formalism

In 1852, Sir George Gabriel Stokes showed that the light polarization behavior could be represented in terms of physical observables [6]. He found that any polarization could be completely described by four measurable quantities, now known as the Stokes polarization parameters [7, 8]. Unlike Jones vectors, the Stokes parameters are real-valued and can represent both full or partially polarized light [9]. In case of fully polarized light, the Stokes parameters can be obtained from the elements of the Jones vector as follows [5]

$$S_0 = \langle J|\,\boldsymbol{\sigma}_0\,|J\rangle = A_x A_x^* + A_y A_y^*, \tag{2.8}$$
$$S_1 = \langle J|\,\boldsymbol{\sigma}_1\,|J\rangle = A_x A_x^* - A_y A_y^*, \tag{2.9}$$
$$S_2 = \langle J|\,\boldsymbol{\sigma}_2\,|J\rangle = A_x A_y^* + A_x^* A_y, \tag{2.10}$$
$$S_3 = \langle J|\,\boldsymbol{\sigma}_3\,|J\rangle = i(A_x A_y^* - A_x^* A_y), \tag{2.11}$$

where

$$\boldsymbol{\sigma}_0 = \begin{bmatrix} 1 & 0 \\ 0 & 1 \end{bmatrix}, \tag{2.12}$$

is the identity Pauli matrix, and

$$\boldsymbol{\sigma}_1 = \begin{bmatrix} 1 & 0 \\ 0 & -1 \end{bmatrix}, \quad \boldsymbol{\sigma}_2 = \begin{bmatrix} 0 & 1 \\ 1 & 0 \end{bmatrix}, \quad \boldsymbol{\sigma}_3 = \begin{bmatrix} 0 & -i \\ i & 0 \end{bmatrix}, \tag{2.13}$$

are the Pauli spin matrices. The parameters S_0, S_1, S_2, and S_3 are observables of light wave: S_0 describes the total power of the optical beam; the parameter S_1 describes the difference between the emerging powers obtained when an optical beam is made to pass through a linear polarizer aligned with the x axis and a linear polarizer aligned with the y axis, i.e, it gives the preponderance of linear horizontal polarization (LHP) light over linear vertical polarization (LVP) light; the parameter S_2 describes the difference between the emerging powers obtained when an optical beam is made to pass through a linear polarizer making an angle of 45° with x axis and a linear polarizer making an angle of $-45°$ with x axis, i.e., it gives the preponderance of $+45°$ linear polarized light over $-45°$ linear polarized light; the parameter S_3 describes the difference between the emerging powers obtained when an optical beam is made to pass through a right-circular polarizer and a left-circular polarizer, i.e., it gives the preponderance of RCP light over LCP light. The last three parameters can be used to define the Stokes vector [10],

$$\vec{S} = \begin{bmatrix} S_1 \\ S_2 \\ S_3 \end{bmatrix}, \tag{2.14}$$

whose length represents the intensity of the polarized component of the light. For a fully polarized beam, the length of the Stokes vector equals the parameter S_0, i.e., $S_0 = |\vec{S}|$. In such cases, the SOP is characterized by the normalized Stokes vector, a 3D unitary vector defined as $\hat{s} = \vec{S}/|\vec{S}|$ [11]. The normalized Stokes vector corresponding to the Jones ket $|s\rangle$ can be obtained using the Pauli matrices represented in (2.13) [12]

$$\begin{bmatrix} s_1 \\ s_2 \\ s_3 \end{bmatrix} = \begin{bmatrix} \langle s|\boldsymbol{\sigma}_1|s\rangle \\ \langle s|\boldsymbol{\sigma}_2|s\rangle \\ \langle s|\boldsymbol{\sigma}_3|s\rangle \end{bmatrix}, \tag{2.15}$$

or more concisely,

$$\hat{s} = \langle s|\vec{\sigma}|s\rangle, \tag{2.16}$$

where $\vec{\sigma}$ is the Pauli spin vector [12], defined as

$$\vec{\sigma} = \begin{bmatrix} \boldsymbol{\sigma}_1 \\ \boldsymbol{\sigma}_2 \\ \boldsymbol{\sigma}_3 \end{bmatrix}. \tag{2.17}$$

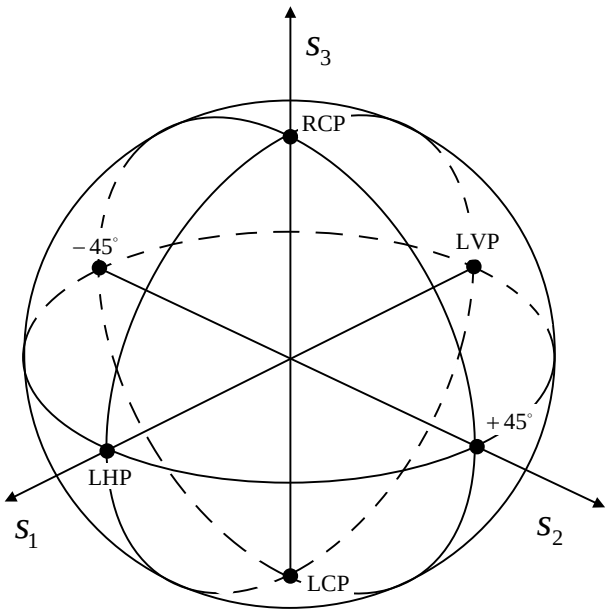

Figure 2.2: The Stokes space representation of all possible SOPs form the so-called Poincaré sphere: LHP – linear horizontal polarization; LVP – linear vertical polarization; +45° – linear polarization at +45°; −45° – linear polarization at −45°; RCP – right circular polarization; LCP – left circular polarization.

The normalized Stokes vectors $[1,0,0]^t$ and $[-1,0,0]^t$ represent the LHP and LVP states, respectively, whereas $[0,0,1]^t$ and $[0,0,-1]^t$ represent the RCP and LCP states. An extended list of SOP representations in the Jones space is presented in Appendix A. The all possible normalized Stokes vectors form the surface of a unit sphere known as the Poincaré sphere [5], see Fig. 2.2. Linear SOPs are plotted along the equator, and circular SOPs are plotted at the poles (north for RCP, and south for LCP) [12]. Elliptical SOPs are plotted elsewhere on the surface of the Poincaré sphere.

The transmission through an optic element is mathematically represented in the Stokes space by a real 3×3 or 4×4 Mueller matrix ($\mathbf{R}$ and $\mathbf{M}$, respectively). If the transmission element does not present PDL or polarization-dependent gain (PDG), the Mueller matrix is 3×3, otherwise the optical element must be modeled as a 4×4 matrix. Therefore, transformation of an input normalized Stokes vector $\hat{s}$ in an output Stokes vector $\hat{t}$ is calculated analogously to (2.6), i.e.,

$$\hat{t} = \mathbf{R}\hat{s}, \tag{2.18}$$

where $\mathbf{R}$ is the 3×3 Mueller matrix. In this case, the Mueller matrix is also called the rotation matrix since only the orientation of Stokes vector is changed. If both the SOP and intensity are changed the Stokes parameters at the output $\mathcal{S}_o = [S_0, S_1, S_2, S_3]^t$ are

related to the input Stokes parameters $\mathcal{S}_i = [S_0, S_1, S_2, S_3]^t$ by the equation

$$\mathcal{S}_o = \mathbf{M}\mathcal{S}_i. \tag{2.19}$$

The connection between Jones and Mueller matrices uses the Pauli matrices defined in (2.12) and (2.13), and can be calculated through the following expression [5, 13]

$$M_{i+1,j+1} = \frac{1}{2}\mathrm{Tr}(\mathbf{U}\sigma_j\mathbf{U}^\dagger\sigma_i), \tag{2.20}$$

where $M_{i+1,j+1}$ represents the component $(i+1, j+1)$ of the 4×4 Mueller matrix, with i, j=0,1,2 or 3, Tr is the trace operator, and † means the conjugate transpose. Using the previous equation, we obtain the 3×3 Mueller matrix corresponding to the general unitary Jones matrix presented in (2.7)

$$\mathbf{R}=\begin{bmatrix} \cos 2\kappa & -\cos(\zeta-\varrho)\sin 2\kappa & -\sin(\zeta-\varrho)\sin 2\kappa \\ \cos(\zeta+\varrho)\sin 2\kappa & \cos 2\zeta\cos^2\kappa-\cos 2\varrho\sin^2\kappa & \sin 2\zeta\cos^2\kappa+\sin 2\varrho\sin^2\kappa \\ -\sin(\zeta+\varrho)\sin 2\kappa & -\sin 2\zeta\cos^2\kappa+\sin 2\varrho\sin^2\kappa & \cos 2\zeta\cos^2\kappa+\cos 2\varrho\sin^2\kappa \end{bmatrix}, \tag{2.21}$$

where the components $R_{i,j}$ are given by $M_{i+1,j+1}$, with i, j=1,2 and 3, and $\det(\mathbf{R})$=1.

2.1.3 Degree of Polarization

As stated above, Stokes parameters describe not only the completely polarized light but also unpolarized or partially polarized light. Unpolarized light is represented as

$$\mathcal{S}_{\text{unp}} = \begin{bmatrix} S_0 \\ 0 \\ 0 \\ 0 \end{bmatrix}, \tag{2.22}$$

where S_0 is the first Stokes parameter, representing the total intensity. On the other hand, partially polarized light can be seen as a mixing of completely polarized light and unpolarized light, and is represented as

$$\mathcal{S} = \begin{bmatrix} S_0 \\ S_1 \\ S_2 \\ S_3 \end{bmatrix} = (1-\text{DOP}) \begin{bmatrix} S_0 \\ 0 \\ 0 \\ 0 \end{bmatrix} + \text{DOP} \begin{bmatrix} S_0 \\ S_1 \\ S_2 \\ S_3 \end{bmatrix}, \tag{2.23}$$

where DOP $\in [0, 1]$ is called the degree of polarization (DOP). The DOP of a light beam is the ratio of the intensity of the polarized light to the total intensity of the light beam,

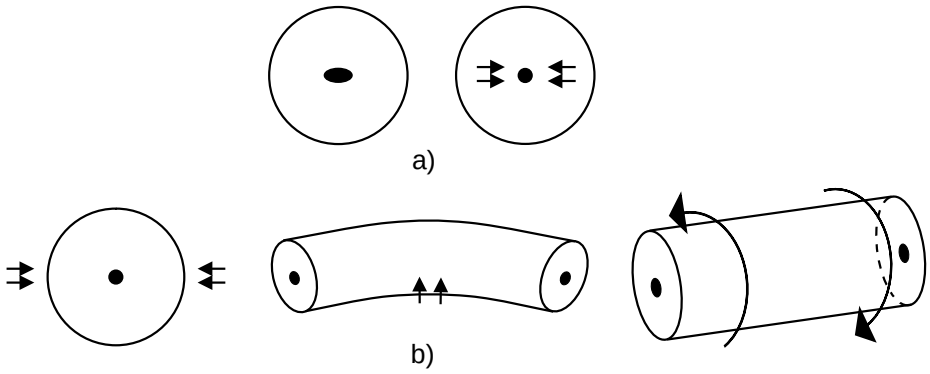

Figure 2.3: Different kind of birefringence mechanisms that can be found in a SSMF: a) – intrinsic mechanisms; b) – extrinsic mechanisms.

and can be expressed in terms of the four Stokes parameters as follows

$$\mathrm{DOP} = \frac{\sqrt{{S_1}^2 + {S_2}^2 + {S_3}^2}}{S_0}. \tag{2.24}$$

With this definition, completely polarized light has a DOP equal to 1, while unpolarized light has a DOP equal to 0. For light partially polarized the DOP takes values between 0 and 1. We have $S_0^2 \geq S_1^2 + S_2^2 + S_3^2$, being $S_0^2 = S_1^2 + S_2^2 + S_3^2$ for completely polarized light and $S_0^2 > S_1^2 + S_2^2 + S_3^2$ for unpolarized or partially polarized light [14].

2.2 Fiber-Optic Birefringence

Birefringence arises in standard single-mode fibers (SSMFs) due to loss of circular symmetry [15]. Such loss of symmetry may result either from a non-circular geometry of the fiber core or from other mechanisms associated with the material anisotropy, likewise asymmetric stresses. In practice, both factors are present in SSMFs.

The mechanisms leading to anisotropy can be divided into two groups: intrinsic and extrinsic. Intrinsic mechanisms are related with the manufacturing process and are a permanent feature of the fiber. The non-circular geometry of the core and non-symmetrical stress field in the glass around the core are two examples (see Fig. 2.3–a)). Birefringence can also be created in a fiber subjected to external forces in handling or cabling. Figure. 2.3–b) shows three examples of the so-called extrinsic mechanisms: lateral stress, bending, and twisting. Due to the extrinsic mechanisms, fiber birefringence will change randomly over the time, reflecting the environmental conditions. This effect is responsible to the stochastic behavior of PMD.

2.2.1 Birefringence Vector

A generalized representation of the local fiber birefringence is obtained by using the eigenvalues and eigenvectors of the transmission matrix. A small piece of SSMF can be described by a unitary matrix like the one presented in (2.7). In such cases, the eigenvalues of the transmission matrix are complex exponentials that have unit magnitude and they are conjugates of one another [5]. Hence, the eigenvalue equation can be written as

$$\mathbf{U}\,|s_\pm\rangle = e^{\pm i\varphi}\,|s_\pm\rangle\,, \tag{2.25}$$

where φ is a phase, and $|s_+\rangle$ and $|s_-\rangle$ are the eigenvectors of $\mathbf{U}$, corresponding to the eigenvalues $e^{i\varphi}$ and $e^{-i\varphi}$, respectively. The eigenvectors form an orthogonal basis, i.e., $\langle s_-|\, s_+\rangle = 0$, and physically they represent two orthogonal propagation modes. By definition, if the input SOP is given by $|s_\pm\rangle$, then $\mathbf{U}$ does not change the polarization, only a phase is introduced. Notice that for each pair of eigenvectors, $|s_\pm\rangle$, there are a corresponding pair of vectors, $\hat{p}_\pm$, in the Stokes space. In this space, orthogonal polarizations have a dot product equal to -1, which means that $\hat{p}_- \cdot \hat{p}_+ = -1$.

By making $\kappa = 0$ in the general unitary transmission matrix presented in (2.7), we obtain the following matrix

$$\mathbf{U} = \begin{bmatrix} e^{i\zeta} & 0 \\ 0 & e^{-i\zeta} \end{bmatrix}, \tag{2.26}$$

whose eigenvalues are given by $e^{\pm i\zeta}$. The corresponding eigenvectors can be calculated using the eigenvalues and substituting (2.26) into (2.25). We obtain the Jones vectors $|s_+\rangle = [1,0]^t$ and $|s_-\rangle = [0,1]^t$, respectively. By using (2.16), we find the corresponding eigenvectors in the Stokes space: $\hat{p}_+ = [1,0,0]^t$ and $\hat{p}_- = [-1,0,0]^t$, respectively. This example describes a piece of fiber with linear birefringence, whose principal propagation modes are oriented along x and y, respectively, and $\zeta = z\Delta\beta/2$, where $\Delta\beta$ represents the difference between the propagation constants of the slow and fast principal propagation modes, β_x and β_y, respectively, [16]

$$\Delta\beta = \beta_x - \beta_y = \frac{\omega\Delta n}{c}, \tag{2.27}$$

with Δn representing the modal refractive indices difference. Notice that in order to account for the linear birefringence in (2.1), the complex amplitudes $A_x(z,t)$ and $A_y(z,t)$ should be replaced by

$$A_x(z,t)\, e^{i\frac{\Delta\beta}{2}z}, \tag{2.28}$$

and

$$A_y(z,t)\, e^{-i\frac{\Delta\beta}{2}z}, \tag{2.29}$$

respectively.

A second unitary matrix example is found by setting $\zeta = \varrho = 0$ in (2.7). In this case, the following matrix is obtained

$$\mathbf{U} = \begin{bmatrix} \cos\kappa & -\sin\kappa \\ \sin\kappa & \cos\kappa \end{bmatrix}. \tag{2.30}$$

The eigenvalues of (2.30) are $e^{\pm i\kappa}$. In this case, the eigenvectors corresponding to $e^{\pm i\kappa}$ are $|s_+\rangle = 1/\sqrt{(2)}[1, -i]^t$ and $|s_-\rangle = 1/\sqrt{(2)}[1, i]^t$, respectively. Using again (2.16), we find the corresponding eigenvectors in the Stokes space: $\hat{p}_+ = [0, 0, -1]^t$ and $\hat{p}_- = [0, 0, 1]^t$, respectively. Since the eigenvectors correspond to circular polarizations, we verify that this case is physically related with a fiber with circular birefringence. That means that the two orthogonal SOPs RCP and LCP remain unchanged along the propagation into a fiber with this king of birefringence.

Results presented above are useful to understand the definition of the birefringence vector in the Stokes space. The birefringence vector is usually defined as a 3D Stokes vector [17, 18],

$$\vec{\beta} = \frac{2\varphi}{z}\,\hat{p}_+, \tag{2.31}$$

where the magnitude, $2\varphi/z$, represents the phase retardation per unit of length between two signals propagated in each one of the eigenvectors of the system. The orientation of the birefringence vector, $\hat{p}_+$, is given by the direction on the Stokes space of the eigenvector $|s_+\rangle$, corresponding to the slow principal propagation mode. The birefringence vector for the system represented by (2.26) (a piece of fiber with linear birefringence) will be $\vec{\beta} = [\Delta\beta, 0, 0]^t$. Note that the vector $\vec{\beta}$ only characterizes the local birefringence [19], i.e., it is assumed that the fiber characteristics are z-independent and this is only true for a small piece of fiber. The analysis presented above shows that the two first components, β_1 and β_2, parameterize the linear birefringence, while the third component β_3 parameterizes the circular birefringence. A general birefringence vector $\vec{\beta} = [\beta_1, \beta_2, \beta_3]^t$ can always be expressed as a sum of two vectors

$$\vec{\beta} = \vec{\beta}_{\text{lin}} + \vec{\beta}_{\text{circ}} = \begin{bmatrix} \beta_1 \\ \beta_2 \\ 0 \end{bmatrix} + \begin{bmatrix} 0 \\ 0 \\ \beta_3 \end{bmatrix}, \tag{2.32}$$

which physically means the coexistence of a linear, $\vec{\beta}_{\text{lin}}$, and a circular, $\vec{\beta}_{\text{circ}}$, birefringence in the same piece of optical fiber. These two particular birefringences can be induced by lateral stresses and twisting, respectively. If both linear and circular birefringences are present, the total birefringence is called as elliptic. In such cases, there are two elliptical SOPs that will propagate unchanged through the fiber.

The local birefringence vector determines how the SOP evolves inside a small piece of fiber. The evolution of the Stokes vector $\hat{s}$, with the distance, z, is governed by the

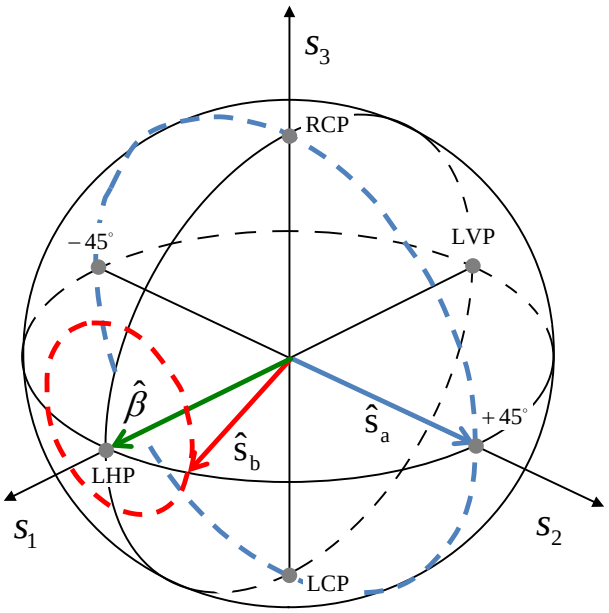

Figure 2.4: Poincaré sphere representation of the SOP evolution with the distance due to fiber linear birefringence $\vec{\beta}$, represented in the figure as a green arrow. Blue and red dash lines represent the SOP evolution of two input Stokes vectors, $\hat{s}_a$ and $\hat{s}_b$, respectively.

following equation [20, 21],

$$\frac{\partial \hat{s}}{\partial z} = \vec{\beta} \times \hat{s}. \tag{2.33}$$

Assuming that a signal linearly polarized at +45° is launched into a small piece of fiber, whose constant linear birefringence is characterized by the particular vector $\vec{\beta} = [1, 0, 0]^t$, then the SOP will evolve cyclically with the distance [22, 23]: it starts as linear at +45°, evolves to elliptical, circular, elliptical, and becomes linear at −45°. The polarization evolution on the Poincaré sphere of two signals with input SOPs equal to $\hat{s}_a$ and $\hat{s}_b$ is schematically represented in Fig. 2.4.

2.2.2 Beat Length

After traveling a length L_B, the SOPs return to the original linear polarizations. This characteristic length, L_B, is referred to as the beat length of the fiber, and can be used as an alternative measure of the fiber birefringence [24]. The beat length can written as a function of the refractive indices difference,

$$L_B = \frac{2\pi}{\Delta\beta} = \frac{\lambda}{\Delta n}, \tag{2.34}$$

where λ represents the wavelength [24]. Typically, fibers installed in the field in the 1990s present beat lengths on the order of tens meters [24], which corresponds to refractive

indices difference of $\sim 10^{-7}$. Nowadays, SSMFs are manufactured with beat length on the order of hundreds of meters, whereas high-birefringence (HiBi) fibers, developed specially to control the polarization, have beat lengths on the order of the millimeters [25].

2.2.3 Differential Group Delay

The differential phase velocity represented in (2.27) is accompanied by a difference in the local group velocities. That means that a signal propagated along the two principal axes will arrive at the fiber output at different time instants. This time delay is called as the differential group delay (DGD), $\Delta\tau$, and characterizes the time-domain manifestation of PMD. The DGD per unit length can be obtained by taking the frequency derivative of (2.27) [16],

$$\frac{\Delta\tau}{L} \equiv \frac{d}{d\omega}\Delta\beta, \tag{2.35}$$

which gives

$$\frac{\Delta\tau}{L} = \frac{\Delta n}{c} + \frac{\omega}{c}\frac{d\Delta n}{d\omega}. \tag{2.36}$$

Note that the linear length dependence of $\Delta\tau$ applies only for short fiber lengths, where the birefringence vector is assumed to be constant.

2.3 Polarization-Mode Dispersion

For long fibers, the birefringence is no longer uniform, and both magnitude and orientation of the birefringence vector evolve randomly. In fact, long fibers are usually modeled by the concatenation of randomly coupled uniform birefringence sections of fibers [26]. When a signal is launched into a birefringent fiber segment, the fast and slow polarization modes have different time arrivals. Besides that, they will decompose into both the fast and slow modes of the next segment, leading to polarization-mode coupling. Due to this coupling, the DGD of each fiber segment may either add or subtract from the total DGD, which means that the DGD does not accumulated linearly with the fiber length. In such case, fiber is in the so-called long regime.

2.3.1 Correlation Length

In order to identify if a fiber is in a short or long regime, a parameter called the correlation length L_C was introduced [15, 16, 27]. The definition of this characteristic length considers the evolution of the polarizations as a function of the length in an ensemble of fibers submitted to statistically equivalent perturbations. Therefore, assuming a fixed input polarization, it is expected that for a large distance all the polarizations have the same probability to be observed. The correlation length is defined as the distance for which

the ensemble average powers polarized along the axis y, $\langle P_y \rangle$, and the ensemble average powers polarized along the axis x, $\langle P_x \rangle$, obeys the following relation [27]

$$\frac{\langle P_x(L_C) \rangle - \langle P_y(L_C) \rangle}{P_{\text{Total}}} = \frac{1}{e^2}, \tag{2.37}$$

where P_{Total} represents the total power launched at the fiber input, polarized along the x axis. Using this definition, we have $\langle P_x \rangle = P_{\text{Total}}$ and $\langle P_y \rangle = 0$ at the fiber input, while $< P_x > \approx < P_y > \approx P_{\text{Total}}/2$ for $L \gg L_C$.

Fibers whose length is small compared to correlation length are in the regime of short distances. In such case, the transmission does not present stochastic properties, and it is usually assumed that the DGD increases linearly with distance. In the case of fibers whose length is large when compared with L_C, they are in a long-distance regime and it is usually assumed that the DGD grows with the square root of the distance [26]. The growth of DGD with the distance can be elegantly represented for both regimes by the following expression [26, 28],

$$\left\langle \Delta\tau^2 \right\rangle = 2 \left(\Delta\beta_\omega\right)^2 L_C^2 \left(e^{-L/L_C} - \frac{L}{L_C} - 1 \right), \tag{2.38}$$

where $\Delta\beta_\omega = \partial\Delta\beta/\partial\omega$. Then, for short distances such that $L \ll L_C$, the root mean square of the DGD, $\Delta\tau_{\text{rms}} \equiv \sqrt{\langle \Delta\tau^2 \rangle}$, simplifies to

$$\Delta\tau_{\text{rms}} \simeq \Delta\beta_\omega L, \tag{2.39}$$

which is in good agreement with (2.35). For long fiber distances, i.e., $L \gg L_c$, the $\Delta\tau_{\text{rms}}$ is approximately given by

$$\Delta\tau_{\text{rms}} \simeq \Delta\beta_\omega \sqrt{2 L_c L} \equiv D_p \sqrt{L}, \tag{2.40}$$

where D_p is the PMD parameter, having unities of ps/km$^{1/2}$. Fibers installed during the 1980s have large PMD such that $D_p > 0.1$ ps/km$^{1/2}$. In contrast, recent fibers are designed to have low PMD, and typically $D_p < 0.1$ ps/km$^{1/2}$. As we are going to show in the next subsection, the mean DGD can be calculated from (2.40) by using the relationship between the mean DGD, $\langle \Delta\tau \rangle$, and the mean square DGD, $\langle \Delta\tau^2 \rangle$, of a Maxwellian distribution.

2.3.2 Principal States of Polarization

As mentioned above, fibers of transmission systems are generally in a long-distance regime. That means that the intensity and orientation of birefringence have a random evolution along the fiber [29]. This fact makes the description of the light wave propagation complex, particularly due to polarization-mode coupling. However, it was shown that one can still find two orthogonal SOPs at the fiber input, $\hat{p}^{\text{in}}_{\text{PSP}\pm}$, that result in two

ortogonal output SOPs, $\hat{p}^{\text{out}}_{\text{PSP}\pm}$, frequency independent to first-order [22], i.e.,

$$\lim_{\Delta\omega\to 0} \frac{\hat{p}^{\text{out}}_{\text{PSP}\pm}(\omega+\Delta\omega) - \hat{p}^{\text{out}}_{\text{PSP}\pm}(\omega)}{\Delta\omega} \to \vec{0} \tag{2.41}$$

This pair of SOPs are referred to as principal states of polarization (PSPs) [22]. Notice, however, that these states are not eigenstates of the transmission matrix $\mathbf{R}$ since the output PSPs are generally not the same as the input PSPs.

2.3.3 PMD Vector

The PSP model can be used to characterize the fiber PMD through the definition of a 3D vector in the Stokes space. This vector describes the dependence of the output SOP on the signal frequency, and is given by [12]

$$\vec{\tau} = \Delta\tau\hat{p}, \tag{2.42}$$

where the magnitude, $\Delta\tau$, represents the DGD between the two PSPs, and $\hat{p}$ is a unitary vector oriented along the slow output PSP. When represented in the Stokes space, the PMD vector is therefore at 180° from $-\hat{p}$, that represents the fast PSP. An alternative definition of the PMD vector can be found in the literature [16, 22]; in such description the magnitude is also given by $\Delta\tau$, nevertheless the vector orientation is defined in a left-circular Stokes space (in such space, LCP corresponds to $s_3 = 1$).

The dynamic evolution of PMD with distance is obtained by relating the PMD vector $\vec{\tau}$ with the local birefringence vector $\vec{\beta}$. In order to achieve that, we use the equation describing the Stokes vector rotations due to local birefringence, given by (2.33), and the equation governing the dependence of the output SOP on the signal frequency. This last equation can be written as [30],

$$\frac{\partial\hat{s}}{\partial\omega} = \vec{\tau}\times\hat{s}. \tag{2.43}$$

The geometric interpretation of (2.43) is as follows: by tuning the frequency ω of the incoming signal, the Stokes vector $\hat{s}$, representing the SOP at certain distance, suffers a rotation with rate $\Delta\tau$ around the axis defined by the vector $\vec{\tau}$. From (2.43), we also realize that when $\hat{s}$ is parallel to $\vec{\tau}$ the output SOP remains unchanged. This is in good agreement with the definition of the PSP model presented above. Basically, equations (2.33) and (2.43) describe, respectively, the spatial evolution of polarization for a particular frequency and the evolution of polarization with the frequency at a particular fiber point. Notice, however, that the birefringence vector is related with the local fiber properties, while the PMD vector accounts for the entire fiber characteristics.

Performing the differentiation of (2.33) with respect to frequency ω and (2.43) with respect to distance z, we obtain, respectively,

$$\frac{\partial^2\hat{s}}{\partial\omega\partial z} = \frac{\partial}{\partial\omega}\left(\vec{\beta}\times\hat{s}\right) = \frac{\partial\vec{\beta}}{\partial\omega}\times\hat{s} + \vec{\beta}\times(\vec{\tau}\times\hat{s}), \tag{2.44}$$

and

$$\frac{\partial^2 \hat{s}}{\partial z \partial \omega} = \frac{\partial}{\partial z}(\vec{\tau} \times \hat{s}) = \frac{\partial \vec{\tau}}{\partial z} \times \hat{s} + \vec{\tau} \times (\vec{\beta} \times \hat{s}). \tag{2.45}$$

By combining the two previous equations, we obtain a single equation relating the birefringence, the PMD, and the SOP vectors

$$\frac{\partial \vec{\tau}}{\partial z} \times \hat{s} = \frac{\partial \vec{\beta}}{\partial \omega} \times \hat{s} - \vec{\tau} \times (\vec{\beta} \times \hat{s}) + \vec{\beta} \times (\vec{\tau} \times \hat{s}). \tag{2.46}$$

At this point, it is usually assumed that the Euclidian metric can be used to describe operations over the vector $\hat{s}$, whose space is the Poincaré sphere. Therefore, using the following cross product identity [12]

$$\vec{a} \times (\vec{b} \times \vec{c}) = \vec{b}(\vec{a} \cdot \vec{c}) - \vec{c}(\vec{a} \cdot \vec{b}), \tag{2.47}$$

the expression present in (2.46) can be simplified to

$$\frac{\partial \vec{\tau}}{\partial z} \times \hat{s} = \frac{\partial \vec{\beta}}{\partial \omega} \times \hat{s} + \vec{\tau}(\vec{\beta} \cdot \hat{s}) - \vec{\beta}(\vec{\tau} \cdot \hat{s}). \tag{2.48}$$

The PMD dynamical equation is finally obtained by using again (2.47) into the last two terms of the right hand side of (2.48), which gives

$$\frac{\partial \vec{\tau}}{\partial z} = \frac{\partial \vec{\beta}}{\partial \omega} + \vec{\beta} \times \vec{\tau}. \tag{2.49}$$

The modulus of the first term on the right hand side represents the intrinsic PMD at a given position z, with units s/m. This equation states that the PMD grows, as one moves down the fiber through a small section, by rotating the existing PMD about the local birefringence vector $\vec{\beta}$ and adding the intrinsic PMD to the result.

2.3.4 Higher-Order PMD

The PMD vector changes with frequency can be accounted by using a Taylor series expansion around the carrier frequency [26, 31],

$$\vec{\tau}(\omega_0 + \Delta\omega) = \vec{\tau}(\omega_0) + \frac{d\vec{\tau}}{d\omega}(\omega_0)\Delta\omega + \cdots \tag{2.50}$$

Second-order PMD vector is obtained by differentiating (2.42) with respect to the frequency [32]

$$\frac{d\vec{\tau}}{d\omega} = \vec{\tau}_\omega = \Delta\tau_\omega \hat{p} + \Delta\tau \hat{p}_\omega, \tag{2.51}$$

where the subscript ω indicates differentiation. Equation (2.51) shows that second-order PMD vector has a first term parallel to first-order PMD vector, $\vec{\tau}_{\omega\parallel} = \Delta\tau_\omega \hat{p}$, and a

second term orthogonal to first-order PMD vector, $\vec{\tau}_{\omega\perp} = \Delta\tau\hat{p}_\omega$. The term $\vec{\tau}_{\omega\perp}$ accounts for the rotation of the PSP due to frequency changes. The modulus of the first term, $\Delta\tau_\omega$, characterizes the dependence of the DGD on the frequency, leading to polarization-dependent chromatic dispersion (PCD) [33, 34]. Chromatic dispersion (CD) is usually quantified by the dispersion parameter D [35]

$$D = \frac{d\beta_\omega}{d\lambda} = -\frac{2\pi c}{\lambda^2}\frac{d\beta_\omega}{d\omega}, \tag{2.52}$$

where $\beta_\omega = d\beta/d\omega$ is the inverse of the group velocity. If we multiply (2.52) by a given distance L, the amount of CD due to PMD can be written as

$$\tau_\lambda = -\frac{2\pi c}{\lambda^2}\left(\frac{1}{2}\Delta\tau_\omega\right) = \frac{1}{2}\frac{d\Delta\tau}{d\lambda}, \tag{2.53}$$

with unities ps/nm. The factor 1/2 present in (2.53) means that only one half of the time delay between PSP is considered. Therefore, the effective CD of a fiber with PMD is

$$(DL)_{\text{eff}} = DL \pm \tau_\lambda, \tag{2.54}$$

where the + and − signals are associated with the propagation through the slow and fast PSPs.

The dynamic equation of second-order PMD vector can be obtained by differentiating (2.49) with respect to the frequency

$$\frac{\partial\vec{\tau}_\omega}{\partial z} \equiv \frac{\partial}{\partial\omega}\left(\frac{\partial\vec{\tau}}{\partial z}\right), \tag{2.55}$$

which gives

$$\frac{\partial\vec{\tau}_\omega}{\partial z} = \frac{\partial^2\vec{\beta}}{\partial\omega^2} + \frac{\partial\vec{\beta}}{\partial\omega}\times\vec{\tau} + \vec{\beta}\times\vec{\tau}_\omega. \tag{2.56}$$

This equation describes the evolution of $\vec{\tau}_\omega$ with the distance, showing that the evolution of the second-order PMD vector is more complex when compared with the first-order PMD vector.

2.3.5 Probability Density Functions

In this subsection we present the analytical expressions of first- and second-order PMD probability density function (pdfs). These functions provide a statistical description of PMD changes in frequency and time domains. The PMD statistics have a single scaling factor, the mean DGD of the fiber, and the first- and second-order PMD vectors, $\vec{\tau}$ and $\vec{\tau}_\omega$, respectively, depend on each other. That means that by knowing the mean DGD of a particular fiber link, we have access to all the information about the statistical behavior of PMD.

The magnitude of first-order PMD vector, $|\vec{\tau}| \equiv \Delta\tau$, is described by a Maxwellian

distribution [21, 36]

$$p_{\Delta\tau}(x) = \frac{8}{\pi^2\langle\Delta\tau\rangle}\left(\frac{2x}{\langle\Delta\tau\rangle}\right)^2 e^{-\frac{1}{\pi}\left(\frac{2x}{\langle\Delta\tau\rangle}\right)^2}, \tag{2.57}$$

where $x \in [0;+\infty[$. This function is well-known to characterize the distribution of the magnitude of the sum of 3D vectors having random orientation and length. Using (2.57), we can calculate the probability of $\Delta\tau$ exceeding a particular value. For instance, the probability of $\Delta\tau/\langle\Delta\tau\rangle$ be greater than 3.7 is 1.3×10^{-7} [37]. In other words, if the mean DGD equals 10 ps, then 99.99999% of the time, the DGD will be smaller than 37 ps. These events are extremely important since they can result in PMD-induced outages [38]. The relation between the mean and the mean square values for a Maxwellian distribution is given by the expression [39]

$$\langle\Delta\tau^2\rangle = \frac{3\pi}{8}\langle\Delta\tau\rangle^2. \tag{2.58}$$

Each components of the PMD vector, τ_i, with $i = 1, 2, 3$, is statistically represented by a zero-mean Gaussian distribution [26]

$$p_{\tau_i}(x) = \frac{2}{\pi\langle\Delta\tau\rangle}\, e^{-\frac{1}{\pi}\left(\frac{2x}{\langle\Delta\tau\rangle}\right)^2}, \tag{2.59}$$

where $x \in]-\infty;+\infty[$.

The components of second-order PMD vector $\tau_{\omega i}$ also have a mean value equal to zero. The respective pdf is given by [40],

$$p_{\tau_{\omega i}}(x) = \frac{4}{\pi\langle\Delta\tau\rangle^2}\,\operatorname{sech}\left(\frac{4x}{\langle\Delta\tau\rangle^2}\right), \tag{2.60}$$

with $x \in]-\infty;+\infty[$, which means that the components of second-order PMD vector are shaped like the soliton amplitude [41].

The magnitude of the second-order PMD vector, $|\vec{\tau}_\omega|$, is given by [42],

$$p_{|\vec{\tau}_\omega|}(x) = \frac{8}{\pi\langle\Delta\tau\rangle^2}\,\frac{4x}{\langle\Delta\tau\rangle^2}\,\tanh\left(\frac{4x}{\langle\Delta\tau\rangle^2}\right)\operatorname{sech}\left(\frac{4x}{\langle\Delta\tau\rangle^2}\right), \tag{2.61}$$

where $x \in [0;+\infty[$. The mean value of $p_{|\vec{\tau}_\omega|}(x)$ is $\frac{2\mathrm{G}}{\pi}\,\langle\Delta\tau\rangle^2$, where G is the Catalan's constant (G = 0.915965...).

Equation (2.51) shows that second-order PMD vector results from the sum of two orthogonal vectors. The first one is parallel to $\vec{\tau}$, and is related with the PCD. Its

magnitude, $\Delta\tau_\omega$, has a pdf given by [40]

$$p_{\Delta\tau_\omega}(x) = \frac{2}{\langle\Delta\tau\rangle^2}\ \mathrm{sech}^2\left(\frac{4x}{\langle\Delta\tau\rangle^2}\right), \tag{2.62}$$

with $x \in]-\infty;+\infty[$. The second-order quantity $\hat{p}_\omega$ characterizes the depolarization of the PSPs and the respective pdf is given by the following expression [40]

$$p_{|\hat{p}_\omega|}(x) = x\left(\frac{24}{\pi\langle\Delta\tau\rangle^2}\right)\int_0^\infty d\beta \frac{\sinh^{2/3}\beta}{\sqrt{\beta}\ \cosh^{5/2}\beta}\ {}_1F_1\left(\frac{5}{2};1;\frac{x^2 4\beta}{\pi\langle\Delta\tau\rangle^2}\tanh\beta\right) \tag{2.63}$$

where ${}_1F_1(-;-;-)$ is the standard hypergeometric function [43].

2.4 SOP and PMD Drifts

As stated in Section 2.2, fiber birefringence changes randomly over time, reflecting the environmental conditions like the air temperature or the wind velocity. That random behavior affects two distinct things: first, the drift of the SOP vector; and second, the drift of the PMD vector [44]. In general, the rate of these drifts are much slower than the transmission data rate [38].

Several experimental studies carried out on PMD temporal dynamics showed a significant variation of correlation times. It was shown that for spools of fiber in a laboratory environment, the correlation time can take values of about 30 minutes on 31.6 km of fiber [21], and 3 hours on a fiber with 10 km [45]. On the other hand, DGD variations on a 48 km aerial cable exhibited time scales ranging from 5 to 90 minutes, depending the air temperature rate of change [46]. For submarine cables, a DGD correlation time of about 1 hour was observed on a 119 km cable [47], and PMD changes with a period of about 2 months were observed on a 62 km fiber optic cable [48]. Finally, on buried fibers, correlation times of at least 20 minutes (on a 17 km optical fiber) [49], one to two hours (on a 48.8 km optical fiber) [46], 3 and 5.7 days (on a 127 km optical fiber) [44], and 19 hours (on a 114 km optical fiber) [50] have been reported. This considerable variation of correlation times demonstrates how the installation scheme impacts the temporal behavior of PMD. Since temperature variations are known to cause PMD variations, cables in a thermally stable environment (e.g., submarine cable) will have long correlation times, whereas cables that experience diurnal temperature variations (e.g., aerial cables and buried cables with above-ground segments) will have correlation times less than 24 hours. Cables in an unstable thermal and mechanical environment (e.g., aerial cables) will have correlation times dependent on both temperature and wind conditions.

In terms of frequency, when fibers are in a long regime and the input signal frequency is largely tuned, both SOP and PMD vectors will also change. Note that the PSPs are defined assuming small frequency changes; for such small frequency changes, the PMD vector remains approximately fixed and the SOP vector evolves cyclically with frequency. Nevertheless, for large frequency tunings the orientation of the PSPs will change, and

therefore the SOP and PMD vectors will present a random drift in the frequency domain, analogously to the time domain.

Next subsection presents the analytical expressions for the ACFs of PMD and SOP vectors in the time and frequency domains.

2.4.1 SOP Vector

The ACFs describing the Stokes vector $\hat{s}$ drifts in time and frequency domains are presented in reference [44]. In a mathematical point of view, these two functions can be defined as

$$g_{\hat{s}}(t_1, t_2, \omega_1, \omega_2) = E[\hat{s}(t_1, \omega_1) \cdot \hat{s}(t_2, \omega_2)], \tag{2.64}$$

that is the expectation of the dot product of two SOP vectors at different instants (t_1 and t_2) and/or frequencies (ω_1 and ω_2). Derivations of these ACFs are based on a discrete model of the fiber, where the fiber is modeled as a concatenation of birefringence sections having a constant birefringence vector. Then, a statistical average over the all possible birefringence vector orientations is performed. Final expressions are obtained by considering a continuous fiber limit, i.e., by keeping the total DGD constant while the number of elements approaches infinity.

Considering the particular case $\omega_1 = \omega_2 = \omega$, the correlation between the SOP vector at different instants is given by [44]

$$\langle \hat{s}(t_1, \omega) \cdot \hat{s}(t_2, \omega) \rangle = \exp\left(-\frac{|\Delta t|}{t_d}\right), \tag{2.65}$$

where $\Delta t = t_2 - t_1$ is the temporal separation, and t_d represents the typical drift time. It was shown that this characteristic time depends on the PMD coefficient as $t_d = 2t_0/(3\omega^2 D_p^2 z)$, where t_0 represents the drift time of the index difference between the fast and slow fiber axes [44]. This result shows that fibers with higher PMD values will present higher drifts on the output SOP.

The ACF in the frequency domain is obtained for the special case $t_1 = t_2 = t$. In such case, the ACF depends solely on the frequency difference, $\Delta\omega = \omega_1 - \omega_2$, and is given by,

$$\langle \hat{s}(t, \omega_1) \cdot \hat{s}(t, \omega_2) \rangle = \exp\left(-\frac{\langle \Delta\tau^2 \rangle \Delta\omega^2}{3}\right). \tag{2.66}$$

This function tells how large, on average, a frequency separation is necessary for two signal SOPs become statistically uncorrelated. The correlation bandwidth $\Delta\omega_c$ of two SOP vectors can be defined as

$$\Delta\omega_c = \int_{-\infty}^{\infty} \frac{\langle \hat{s}(t, \omega_1) \cdot \hat{s}(t, \omega_2) \rangle}{g_{\hat{s}}(t, \Delta\omega = 0)} d\Delta\omega. \tag{2.67}$$

Therefore, using (2.66) into (2.67), we obtain the correlation bandwidth as a function of the mean DGD, $\Delta\omega_c = 2\sqrt{2}/\langle \Delta\tau \rangle$.

2.4.2 PMD Vector

The ACFs describing the PMD vector drifts in time and frequency domains are presented in [44] and [39, 51], respectively. These functions are obtained following a similar method of that used for the polarization vector. In this case, the ACFs are defined as

$$g_{\vec{\tau}}(t_1, t_2, \omega_1, \omega_2) = E[\vec{\tau}(t_1, \omega_1) \cdot \vec{\tau}(t_2, \omega_2)], \tag{2.68}$$

that is the expectation of the dot product of two PMD vectors at different instants (t_1 and t_2) and/or frequencies (ω_1 and ω_2).

Considering the particular case $\omega_1 = \omega_2 = \omega$, the ACF of the PMD vector is given by [44]

$$\langle \vec{\tau}(t_1, \omega) \cdot \vec{\tau}(t_2, \omega) \rangle = \langle \Delta\tau^2 \rangle \frac{1 - \exp\left(-\dfrac{|\Delta t|}{t_d}\right)}{\dfrac{|\Delta t|}{t_d}}. \tag{2.69}$$

The ACF in the frequency domain is obtained for the special case $t_1 = t_2 = t$, and assumes the following form [39, 51],

$$\langle \vec{\tau}(t, \omega_1) \cdot \vec{\tau}(t, \omega_2) \rangle = 3 \, \frac{1 - \exp\left(-\dfrac{\langle \Delta\tau^2 \rangle \Delta\omega^2}{3}\right)}{\Delta\omega^2}. \tag{2.70}$$

Equation (2.70) shows that the correlation between two PMD vectors decreases quadratically with the frequency separation. The correlation bandwidth $\Delta\omega_c$ of the PMD vectors is calculated using (2.70) into (2.67). In this case, we obtain the value $\Delta\omega_c = 4\sqrt{2}/\langle \Delta\tau \rangle$, i.e., twice the bandwidth of the SOP vector (see (2.67)).

References

[1] G. P. Agrawal, *Lightwave Technology: Telecommunication Systems.* John Wiley & Sons, New Jersey, USA, 2005.

[2] R. C. Jones, "A new calculus for the treatment of optical systems," *J. Opt. Soc. Am.*, vol. 31, no. 7, pp. 488–493, Jul. 1941.

[3] G. P. Agrawal, *Nonlinear Fiber Optics, 4rd ed.* Academic Press, San Diego, USA, 2007.

[4] C. A. Balanis, *Advanced Engineering Electromagnetics,.* Wiley, San Diego, USA, 1989.

[5] J. N. Damask, *Polarization optics in telecomunications.* Springer, New York, EUA, 2005.

[6] G. G. Stokes, "On the composition and resolution of streams of polarized light from different sources," *Trans. Cambridge Phil. Soc.*, vol. 9, p. 399, 1852.

[7] M. J. Walker, "Matrix calculus and the Stokes parameters of polarized radiation," *Am. J. Phys.*, vol. 22, no. 4, pp. 170–174, 1954.

[8] W. S. Bickel and W. M. Bailey, "Stokes vectors, Mueller matrices, and polarized scattered light," *Am. J. Phys.*, vol. 53, no. 5, pp. 468–478, 1985.

[9] D. Goldstein, *Polarized Light, Second edition.* CRC Press, New York, EUA, 2003.

[10] S. G. Evangelides Jr., L. F. Mollenauer, J. P. Gordon, and N. S. Bergano, "Polarization multiplexing with solitons," *IEEE/OSA J. Lightwave Technol.*, vol. 10, pp. 28–35, 1992.

[11] N. Akhmediev and J. M. Soto-Crespo, "Dynamics of solitonlike pulse propagation in birefringent optical fibers," *Phys. Rev. E*, vol. 49, no. 6, pp. 5742–5754, Jun. 1994.

[12] J. P. Gordon and H. Kogelnik, "PMD fundamentals: Polarization mode dispersion in optical fibers," *PNAS*, vol. 97, no. 9, pp. 4541–4550, 2000.

[13] F. L. Roy-Brehonnet and B. L. Jeune, "Utilization of Mueller matrix formalism to obtain optical targets depolarization and polarization properties," *Prog. Quant. Electr.*, vol. 21, no. 2, pp. 109–151, 1997.

[14] E. Collet, *Field Guide to Polarization.* SPIE Press, Washington, USA, 2005.

[15] H. Kogelnik, R. M. Jopson, and L. E. Nelson, *Optical Fiber Telecommunications IVb.* Academic Press, San Diego, 2002, ch. 15, pp. 725–861.

[16] C. D. Poole and J. Nagel, *Polarization effects in lightwave systems - Optical Fiber Telecommunications.* Academic Press, San Diego, 1997, vol. IIIa, ch. 6, pp. 114–161.

[17] T. Wanner, B. S. Marks, C. R. Menyuk, and J. Zweck, "Polarization decorrelation in optical fibers with randomly varying elliptical birefringence," *Opt. Lett.*, vol. 28, no. 19, pp. 1799–1801, Oct. 2003.

[18] A. Galtarossa, L. Palmieri, M. Schiano, and T. Tambosso, "Measurement of birefringence correlation length in long, single-mode fibers," *Opt. Lett.*, vol. 26, no. 13, pp. 962–964, Jul. 2001.

[19] W. Eickhoff, Y. Yen, and R. Ulrich, "Wavelength dependence of birefringence in single-mode fiber," *Appl. Opt.*, vol. 20, no. 19, pp. 3428–3435, Oct 1981.

[20] B. Daino, G. Gregori, and S. Wabnitz, "New all-optical devices based on third-order nonlinearity of birefringent fibers," *Opt. Lett.*, vol. 11, no. 1, pp. 42–44, Jan. 1986.

[21] C. D. Poole, J. H. Winters, and J. A. Nagel, "Dinamical equation for polarization dispersion," *Opt. Lett.*, vol. 16, no. 6, pp. 372–374, 1991.

[22] C. D. Poole and R. E. Wagner, "Phenomenological approach to polarization dispersion in longe-single mode fibres," *Electron. Lett.*, vol. 22, pp. 1029–1031, 1986.

[23] N. J. Muga, N. A. Silva, M. Ferreira, and A. N. Pinto, "Evolution of the degree of copolarization in high-birefringence fibers," *Opt. Commun.*, vol. 283, no. 10, pp. 2125–2132, 2010.

[24] A. Galtarossa, L. Palmieri, A. Pizzinat, M. Schiano, and T. .Tambosso, "Measurement of local beat length and differential group delay in installed single-mode fibers," *IEEE/OSA J. Lightwave Technol.*, vol. 18, pp. 1389–1394, 2000.

[25] J. Noda, K. Okamoto, and Y. Sasaki, "Polarization-maintaining fibers and their applications," *IEEE/OSA J. Lightwave Technol.*, vol. 4, no. 8, pp. 1071–1089, Aug. 1986.

[26] G. J. Foschini and C. D. Poole, "Statistical theory of polarization dispersion in single mode fibers," *IEEE/OSA J. Lightwave Technol.*, vol. 9, no. 11, pp. 1449–1456, 1991.

[27] I. P. Kaminow, "Polarization in optical fibers," *Quantum Electron.*, vol. 17, pp. 15–22, 1981.

[28] P. K. A. Wai and C. R. Menyuk, "Polarization mode dispersion, decorrelation, and diffusion in optical fibers with randomly varying birefringence," *IEEE/OSA J. Lightwave Technol.*, vol. 14, no. 2, pp. 148–157, 1996.

[29] N. J. Muga, A. N. Pinto, and M. Ferreira, "Efeitos estocásticos da polarização em fibras ópticas," in *14ª Conferência Nacional de Física*, Porto, Portugal, 2005.

[30] C. D. Poole, N. S. Bergano, and R. E. Wagner, "Polarization dispersion and principal states in a 147-km undersea lightwave cable," *IEEE/OSA J. Lightwave Technol.*, vol. 6, no. 7, pp. 1185–1190, 1988.

[31] H. Bullow, "System outage probability due to first-and second-order PMD," *IEEE Photonics Technol. Lett.*, vol. 10, no. 5, pp. 696–698, 1998.

[32] L. Nelson, R. Jopson, H. Kogelnik, and G. Foschini, "Measurement of depolarization and scaling associated with second-order polarization mode dispersion in optical fibers," *IEEE Photonics Technol. Lett.*, vol. 11, no. 12, pp. 1614–1616, Dec. 1999.

[33] C. D. Poole and C. R. Giles, "Polarization dependent pulse compression and broadening due to polarization dispersion in dispersion shifted fiber," *Opt. Lett.*, vol. 13, no. 2, pp. 155–157, 1988.

[34] G. J. Foschini, R. M. Jopson, L. E. Nelson, and H. Kogelnik, "The statistics of PMD-induced chromatic fiber dispersion," *IEEE/OSA J. Lightwave Technol.*, vol. 17, no. 9, pp. 1560–1565, 1999.

[35] G. P. Agrawal, *Nonlinear Fiber Optics, 3rd ed.* Academic Press, San Diego, USA, 2001.

[36] F. Curti, B. Daino, G. D. Marchis, and F. Matera, "Satistical treatment of the evolution of the principal states of polarization in single-mode fibers," *IEEE/OSA J. Lightwave Technol.*, vol. 8, no. 8, pp. 1162–1166, 1990.

[37] C. Allen, P. Kondamuri, D. Richards, and D. Hague, "Measured temporal and spectral PMD characteristics and their implications for network-level mitigation approaches," *IEEE/OSA J. Lightwave Technol.*, vol. 21, no. 1, pp. 79–86, Jan. 2003.

[38] H. Kogelnik and P. Winzer, "PMD outage probabilities revisited," in *Optical Fiber Communication and the National Fiber Optic Engineers Conference, 2007. OFC/NFOEC 2007. Conference on*, Mar. 2007, pp. 1–3.

[39] M. Karlsson and J. Brentel, "Autocorrelation function of the polarization-mode dispersion vector," *Opt. Lett.*, vol. 24, no. 14, pp. 939–941, 1999.

[40] G. J. Foschini, L. E. Nelson, R. M. Jopson, and H. Kogelnik, "Probability densities of second-order polarization mode dispersion including polarization dependent chromatic fiber dispersion," *IEEE Photonics Technol. Lett.*, vol. 12, no. 3, pp. 293–295, 2000.

[41] A. N. Pinto, "Análise e optimização de sitemas de comunicação ópticos baseados em solitões," Ph.D. dissertation, Universidade de Aveiro, 1999.

[42] G. Foschini, L. Nelson, R. Jopson, and H. Kogelnik, "Statistics of second-order PMD depolarization," *IEEE/OSA J. Lightwave Technol.*, vol. 19, no. 12, pp. 1882–1886, Dec. 2001.

[43] G. Arfken, *Mathematical Methods for Physicists, 3rd ed.* Academic Press, 1985, ch. 13.5, pp. 748–752.

[44] M. Karlsson, J. Brentel, and P. Andrekson, "Long-term measurement of PMD and polarization drift in installed fibers," *IEEE/OSA J. Lightwave Technol.*, vol. 18, no. 7, pp. 941–951, Jul. 2000.

[45] S. Bahsoun, J. Nagel, and C. Poole, "Measurements of temporal variations in fiber transfer characteristics to 20 GHz due to polarization-mode dispersion," in *Proc. ECOC1990*, 1990, pp. 1003–1006.

[46] J. Cameron, L. Chen, X. Bao, and J. Stears, "Time evolution of polarization mode dispersion in optical fibers," *IEEE Photonics Technol. Lett.*, vol. 10, no. 9, pp. 1265–1267, Sept. 1998.

[47] T. Takahashi, T. Imai, and M. Aiki, "Time evolution of polarisation mode dispersion in 120 km installed optical submarine cable," *Electron. Lett.*, vol. 29, no. 18, pp. 1605–1606, Sept. 1993.

[48] T. Kawazawa and Y. Namihira, "Long-term polarization-mode-dispersion measurement of installed optical submarine cable," in *Proc. OFC1994*, 1994, pp. 228–229.

[49] C. De Angelis, A. Galtarossa, G. Gianello, F. Matera, and M. Schiano, "Time evolution of polarization mode dispersion in long terrestrial links," *IEEE/OSA J. Lightwave Technol.*, vol. 10, no. 5, pp. 552–555, May 1992.

[50] J. A. Nagel, M. W. Chbat, L. D. Garrett, J. P. Soigne, N. A. Weaver, B. M. Desthieux, H. Bulow, A. R. McCormick, and R. M. Derosier, "Long-term PMD mitigation at 10 Gb/s and time dynamics over high-PMD installed fiber," in *Proc. ECOC2000*, vol. II(4.2.1), 200, pp. 31–32.

[51] M. Shtaif, A. Mecozzi, and J. Nagel, "Mean-square magnitude of all orders of polarization mode dispersion and the relation with the bandwidth of the principal states," *IEEE Photonics Technol. Lett.*, vol. 12, no. 1, pp. 53–55, Jan. 2000.

Chapter 3

Polarization Scattering and PMD Emulation

A detailed analysis of the state of polarization (SOP) scattering and polarization-mode dispersion (PMD) emulation processes is presented in this Chapter. We start by presenting the main characteristics of a fiber-coil based polarization controller (PC). The mathematical method developed to this device allows a deterministic calculation of its configuration, i.e., the three waveplate angles, in order to transform between any two SOPs. Afterwards, we analyze the SOP scattering process, showing that a uniform SOP scattering over the Poincaré sphere can be achieved through the concatenation of fiber-coil based PCs. An approach to PMD emulation based on the previously analyzed PCs is presented at the end of this Chapter. Good first- and second-order PMD statistics are obtained through the concatenation of polarization-maintaining fibers (PMFs) and scattering sections comprised by the concatenation of several fiber-coil based SOP controllers.

3.1 Introduction

The first polarization control schemes used in fiber-optic communication systems were based on the elasto-optic properties of silica, by means of controlled squeezing [1–4], or bending of the fiber itself [5]. Subsequently, other devices were proposed based on electro-optics crystals [6], Faraday rotators [7] and liquid crystals [8, 9]. Nevertheless, still now the most common PC, at least in laboratorial systems, is the fiber-coil based PC. The fiber-coil based PC uses the elasto-optic properties of silica fibers in order to control the output SOP. The low cost, easy handling and the ability to transform between any two SOPs are the main reasons for the widespread use of this PC device. The first PC device using fiber-coils was presented by Lefevre in 1980 [5], and it was patented three years later in 1983 [10].

The fiber-coil based device is equivalent to a fractional waveplate of classical optics. In [5] it is shown how to use a combination of fiber-coils in order to control the polarization inside a single-mode fiber. In the proposed scheme, the fiber was looped into

three coils to create three independent fractional waveplates: two quarter-wave plates (QWPs) and one half-wave plate (HWP). The first QWP transforms the input SOP into a linear polarization. The HWP rotates the angle of the linear polarization, and the last QWP transforms the linear polarization into the desired SOP. This device became known as QWP-HWP-QWP fiber-coil based PC and this configuration is still now prevalent, although other schemes have been proposed [11].

In the late 1980s the studies related with PCs were mainly driven by the need of controlling the SOP in optical receivers for coherent optical transmission systems. A good overview of the work done during that time can be found in [12]. With the advent of Erbium-Doped Fiber Amplifier (EDFA) the coherent systems became less attractive and the number of publications related with PCs also decreased. More recently, the study of polarization effects in optical fibers became quite intense in connection with the problem of PMD, which strongly limits the reach of high-speed optical communication systems.

The statistical nature of the PMD effect makes difficult to assess PMD compensators. If we use an installed communication system to perform such assessment, very long times will be required in order to evaluate the compensator over a significant range of differential group delay (DGD) values [13, 14]. An accurate assess of PMD compensators is only possible with a PMD emulator system, with the ability to quickly cycle through different DGD values. PMD emulators allow a fast and versatile access to all possible DGD values, in particular low probability DGD values. Besides that, the first- and second-order PMD statistics produced by the emulator should follow the PMD statistics of real fibers, presented in Chapter 2.

PMD emulators are usually constructed by the concatenation of several birefringence elements. The birefringence elements can be sections of PMF, birefringence crystals, or other devices able to provide a DGD between the two orthogonal polarization axes. The polarization-mode coupling is then obtained by rotating the orientation of the principal axes of each birefringent section, or by placing a polarization scrambler between sections. Here, we show that the fiber-coil based PCs can be applied to generate the required SOP scattering [15, 16]. Furthermore, we show the feasibility of building a PMD emulator based on the concatenation of PMFs and scattering sections comprised by the concatenation of several fiber-coil based SOP controllers.

3.1.1 The Physics of a Fiber-Coil Based PC

In standard single-mode fibers (SSMFs) the birefringence arises from the loss of circular symmetry of the core or by mechanical stress through the elasto-optic effect (see Section 2.2). When a fiber is bent, as shown in Fig. 3.1, the birefringence is mainly due to mechanical stress [17]. The dominant stress component takes place along the z direction. Nevertheless, it does not contribute directly to the birefringence as it is an odd function of y (is a tensile stress for $y < 0$ and a compressive stress for $y > 0$, across the "$x - y$" plane), whereas the electromagnetic modes functions are even functions [18]. In fact, the birefringence arises due to the lateral stress in the x and y directions. Lateral stresses

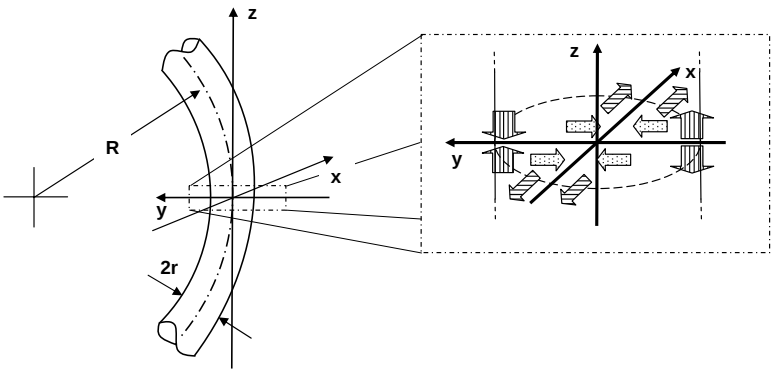

Figure 3.1: A bent fiber and its principal mechanical stresses. The fiber birefringence arises due to the lateral stress in the x and y directions.

induce changes in the fiber refractive indices along the x and y axes of the fiber due to the elasto-optic properties of the silica. These changes are given, respectively, by [5]

$$\Delta n_x = \frac{n^3}{4}(p_{12} - \nu p_{12} - \nu p_{11}) \left(\frac{r}{R}\right)^2, \tag{3.1}$$

and

$$\Delta n_y = \frac{n^3}{4}(p_{11} - 2\nu p_{12}) \left(\frac{r}{R}\right)^2, \tag{3.2}$$

where ν is the Poisson's ratio, p_{11} and p_{12} are two terms of the fiber material photo-elasto tensor, r and R are, respectively, the fiber and the curvature radius, see Fig. 3.1. If we define Δn as the refractive index difference between the fast and slow axis, we obtain

$$\Delta n = -a \left(\frac{r}{R}\right)^2, \tag{3.3}$$

with $a \simeq 0.133$ [5], for silica fibers. Although the refractive index difference is small, it can produce a considerable phase delay over a distance correspondent to a large number of wavelengths. In fact, by coiling the fiber with a small number of turns with a few centimeters of radius, it is possible to obtain an optical phase difference of π, $\pi/2$ or $\pi/4$ (i.e., $\lambda/2$, $\lambda/4$, $\lambda/8$... λ/m devices). For m equal to 2 and 4 we obtain a HWP and QWP, respectively.

Using (3.3) we can derive an expression for the coil radius as a function of the optical path difference, λ/m, and the number of turns, N, [5],

$$R(\lambda/m, N) = 2\pi a r^2 \frac{N}{\lambda/m}. \tag{3.4}$$

With (3.4), it is possible to design a device equivalent to a waveplate of classical optics, i.e., a device with a fixed phase retardation and retardation axes orientation changeable.

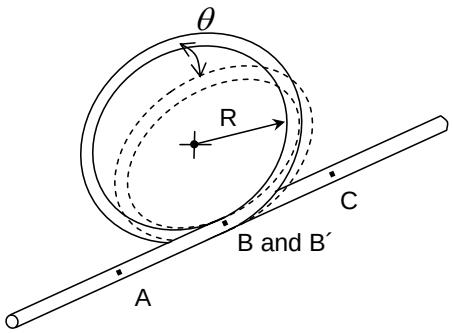

Figure 3.2: Schematic representation of a fiber-coil based waveplate. Points A and C are fixed in a lab coordinate system, while points B and B' are fixed in a coordinate system solidary with the fiber-coil.

In order to control the light SOP using a fiber-coil we must be able to rotate the waveplate retardation axes with relation to the SOP of the incident light. Such rotation can be made through the setup presented in Fig. 3.2. The setup comprises a fiber-coil with a radius R, where the points A and C remain fixed. When the coil plane is rotated through an angle θ a twist effect is present in the fiber segments AB and B'C. Such effect reduces the rotation angle to an effective rotation angle equal to $(1-t)\theta$, where t is the twist effect coefficient [5]. However, according with [18], the coefficient t takes a small value for silica fibers, approximately equal to 0.08, making the effective rotation angle almost equal to the physical rotation angle.

In conclusion, a fiber-coil can be seen as a classical waveplate where the phase delay is fixed and the principal axes orientation are changeable.

3.1.2 A Mathematical Model for the Fiber-Coil Based PC

A QWP allows to convert any input SOP into a linear SOP and vice versa, and a HWP allows to change between any two linear SOPs. To transform an arbitrary input SOP into an also arbitrary output SOP, the QWP-HWP-QWP waveplates combination is the most commonly used [5]. In the following, a method to deterministically calculate the QWP-HWP-QWP PC configuration (i.e., the three waveplate angles) for a given input and output SOP is presented.

If we have an input SOP and we aim to generate another SOP at the PC output we must select the correct configuration angles $(\theta_1, \theta_2, \theta_3)$, see Fig. 3.3. The SOP at the input and output of the PC can be written, respectively, as the Stokes vectors,

$$\hat{s}_i = [(s_1)_i, (s_2)_i, (s_3)_i]^t, \tag{3.5}$$

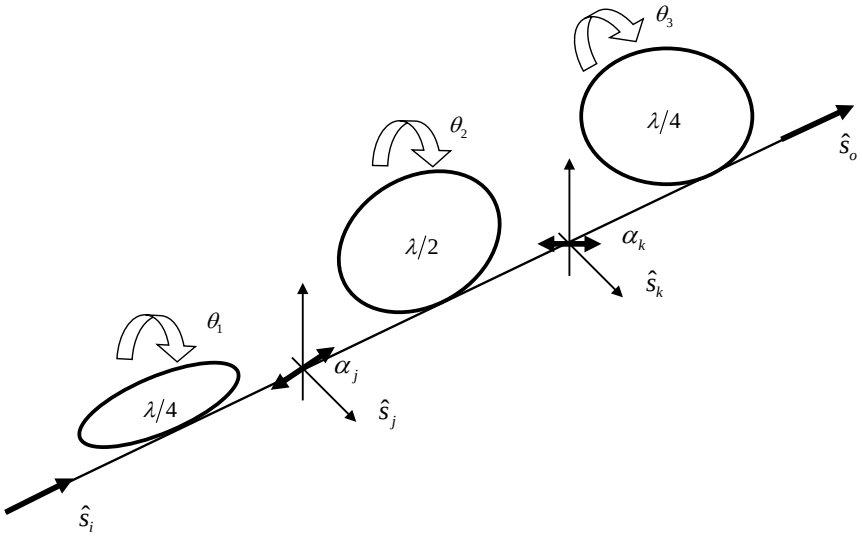

Figure 3.3: Schematic representation of a fiber-coil based PC, comprised by the concatenation of two QWPs and one HWP. The three waveplate angles, θ_1, θ_2, and θ_3, fully characterize the PC configuration.

and

$$\hat{s}_o = [(s_1)_o, (s_2)_o, (s_3)_o]^t, \tag{3.6}$$

where t indicates the transpose. In the same way, the SOP after the QWP and the HWP can be written, respectively, as, $\hat{s}_j = [(s_1)_j, (s_2)_j, (s_3)_j]^t$ and $\hat{s}_k = [(s_1)_k, (s_2)_k, (s_3)_k]^t$. Therefore, after going through the first QWP the SOP is given by

$$\hat{s}_j = \mathbf{R}(\theta_1)\mathbf{M}_{\lambda/4}\mathbf{R}(-\theta_1)\hat{s}_i, \tag{3.7}$$

where θ_1 is the angle of the first waveplate, $\mathbf{M}_{\lambda/4}$ is the QWP matrix and $\mathbf{R}$ is the rotation matrix of the waveplate. In the Stokes space, $\mathbf{M}_{\lambda/4}$ and $\mathbf{R}$ matrices are given by

$$\mathbf{M}_{\lambda/4} = \begin{bmatrix} 1 & 0 & 0 \\ 0 & 0 & -1 \\ 0 & 1 & 0 \end{bmatrix}, \tag{3.8}$$

and

$$\mathbf{R} = \begin{bmatrix} \cos(2\theta) & -\sin(2\theta) & 0 \\ \sin(2\theta) & \cos(2\theta) & 0 \\ 0 & 0 & 1 \end{bmatrix}, \tag{3.9}$$

respectively.

Using (3.8) and (3.9) into (3.7), we obtain the following expression for the Stokes

vector at the output of the first waveplate

$$\hat{s}_j = \begin{bmatrix} (s_1)_i \cos^2(2\theta_1) + (s_2)_i \cos(2\theta_1)\sin(2\theta_1) + (s_3)_i \sin(2\theta_1) \\ (s_1)_i \cos(2\theta_1)\sin(2\theta_1) + (s_2)_i \sin^2(2\theta_1) - (s_3)_i \cos(2\theta_1) \\ (s_2)_i \cos(2\theta_1) - (s_1)_i \sin(2\theta_1) \end{bmatrix}. \tag{3.10}$$

In order to transform the input SOP, $\hat{s}_i$, into a linear SOP, $\hat{s}_j$, we must choose for the first plate (QWP) an angle θ_1, such that the third component of (3.10) vanishes. Therefore θ_1 is given by

$$\theta_1 = \frac{1}{2}\arctan\left(\frac{(s_2)_i}{(s_1)_i}\right). \tag{3.11}$$

Under this condition, $\hat{s}_j$ can be written as

$$\hat{s}_j = [X, Y, 0]^t, \tag{3.12}$$

where X and Y are the two non-null Stokes parameters at the input of the second plate (HWP), which are respectively given by

$$X = (s_1)_i \cos^2(2\theta_1) + (s_2)_i \cos(2\theta_1)\sin(2\theta_1) + (s_3)_i \sin(2\theta_1), \tag{3.13}$$

and

$$Y = (s_1)_i \cos(2\theta_1)\sin(2\theta_1) + (s_2)_i \sin^2(2\theta_1) - (s_3)_i \cos(2\theta_1). \tag{3.14}$$

Light after the first plate, $\hat{s}_j$, presents a linear SOP. The second plate will transform the linear SOP into another linear SOP, $\hat{s}_k$, given by

$$\hat{s}_k = [W, Z, 0]^t, \tag{3.15}$$

where W and Z are functions of the desired final SOP, $\hat{s}_o$. The linear SOPs, $\hat{s}_j$ and $\hat{s}_k$, can be characterized by their respective polarization plane angles α_j and α_k. In the first case, the angle α_j depends on the input SOP and is given by

$$\alpha_j = \frac{1}{2}\arctan\left(\frac{Y}{X}\right), \tag{3.16}$$

while in the second case, the angle α_k depends on the output SOP and is given by

$$\alpha_k = \frac{1}{2}\arctan\left(\frac{Z}{W}\right). \tag{3.17}$$

Considering the situation where $\theta_2 = 0$, the $\hat{s}_k$ vector is obtained by multiplying the $\mathbf{M}_{\lambda/2}$ matrix,

$$\mathbf{M}_{\lambda/2} = \begin{bmatrix} 1 & 0 & 0 \\ 0 & -1 & 0 \\ 0 & 0 & -1 \end{bmatrix}, \tag{3.18}$$

with $\hat{s}_j$. In such case, the following linear SOP is obtained

$$\hat{s}_k = [X, -Y, 0]^t. \tag{3.19}$$

From (3.19) we observe that when $\theta_2 = 0$ the output angle is just the inverse of the input angle, $\alpha_k = -\alpha_j$. It is also known that by rotating the HWP of an angle θ induces a rotation in the linear polarization of an angle 2θ [5]. Hence the polarization plane angle of the light at the output of the second fiber-coil is given by

$$\alpha_k = -\alpha_j + 2\theta_2. \tag{3.20}$$

At this stage, using equations (3.16) and (3.17) into (3.20), the following waveplate angle θ_2 is obtained

$$\theta_2 = \frac{1}{4}\left[\arctan\left(\frac{Y}{X}\right) + \arctan\left(\frac{Z}{W}\right)\right]. \tag{3.21}$$

Note that θ_2 is a function of both input and output SOPs, $\hat{s}_i$ and $\hat{s}_o$, respectively. The angle of the third waveplate, W and Z are determined using an equation analogous to (3.7),

$$\hat{s}_o = \mathbf{R}(\theta_3)\mathbf{M}_{\lambda/4}\mathbf{R}(-\theta_3)\hat{s}_k. \tag{3.22}$$

Using again the matrices $\mathbf{M}_{\lambda/4}$ and $\mathbf{R}$, given by (3.8) and (3.9), respectively, we obtain the following expression for the Stokes vector at the output of the PC

$$\begin{bmatrix} (s_1)_o \\ (s_2)_o \\ (s_3)_o \end{bmatrix} = \begin{bmatrix} W\cos^2(2\theta_3) + Z\cos(2\theta_3)\sin(2\theta_3) \\ W\cos(2\theta_3)\sin(2\theta_3) + Z\sin^2(2\theta_3) \\ Z\cos(2\theta_3) - W\sin(2\theta_3) \end{bmatrix}. \tag{3.23}$$

From (3.23), and knowing $(s_1)_o$ and $(s_2)_o$, we find the angle of the second QWP

$$\theta_3 = \frac{1}{2}\arctan\left(\frac{(s_2)_o}{(s_1)_o}\right). \tag{3.24}$$

With the help of (3.24), and with the knowledge of $(s_3)_o$, we find the expressions

$$W = (s_1)_o\cos^2(2\theta_3) + (s_2)_o\cos(2\theta_3)\sin(2\theta_3) - (s_3)_o\sin(2\theta_3), \tag{3.25}$$

and

$$Z = (s_1)_o\cos(2\theta_3)\sin(2\theta_3) + (s_2)_o\sin^2(2\theta_3) - (s_3)_o\cos(2\theta_3), \tag{3.26}$$

for W and Z, respectively.

In conclusion, equations (3.11), (3.21) and (3.24), in conjugation with (3.5), (3.6), (3.13), (3.14), (3.25) and (3.26), allow us to calculate the three waveplate angles needed to transform between any two SOPs.

Like each individual waveplate, the fiber-coil based PC can also be represented by a Mueller matrix, resulting from the concatenation of the waveplate matrices. Therefore

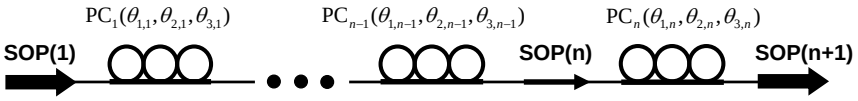

Figure 3.4: Schematic representation of n concatenated PCs that can be used to generate a random SOP scattering over the Poincaré sphere. Each event of the scattering system is characterized by a set of 3×n angles.

the matrix $\mathbf{F}$ that describes the PC is given by

$$\mathbf{F}(\theta_1, \theta_2, \theta_3) = \mathbf{R}(\theta_3)\mathbf{M}_{\lambda/4}\mathbf{R}(-\theta_3)\mathbf{R}(\theta_2)\mathbf{M}_{\lambda/2}\mathbf{R}(-\theta_2)\mathbf{R}(\theta_1)\mathbf{M}_{\lambda/4}\mathbf{R}(-\theta_1). \tag{3.27}$$

Matrix $\mathbf{F}$ can be used to calculate the output SOP, $\hat{s}_o$, given the input SOP, $\hat{s}_i$, and the three configuration angles (θ_1, θ_2 and θ_3).

3.2 SOP Scattering Process

The results presented above can be used to test the ability to uniformly scatter an input SOP over the Poincaré sphere with a system resulting from the concatenation of several fiber-coil based PCs. This system is schematically represented in Fig. 3.4. A device, or a concatenation of devices, with the ability to produce a uniform SOP scatter over the Poincaré sphere can be useful for instance in the development of PMD emulators. Indeed, some authors have proposed PMD emulators based on pieces of polarization maintaining fibers interconnected with uniform scattering devices [19, 20].

The scattering uniformity is evaluated through the calculation of the statistics of each component of the Stokes vector. If we have a uniform distribution of points over the Poincaré sphere, each Stokes vector component, s_i, has a mean value equal to zero, variance 1/3 and uniform distribution between -1 and 1 (Appendix B presents a detailed derivation of this result). The approach used to investigate the evolution of the polarization scattering, namely the variance convergence to 1/3 of our device, was inspired in the Marcuse analysis of two rotation matrices [21].

3.2.1 Theoretical Derivation

As shown in Fig. 3.4, the output signal of a PC is used as the input of the next PC. The SOP statistics at the end of each PC is evaluated and compared with the desired uniform distribution. The number of concatenated elements is increased in order to improve the scattering uniformity. Therefore, the SOP at the n^{th} PC output is related with the SOP

at the n^{th} PC input by the following expression,

$$\begin{bmatrix} (s_1)_{n+1} \\ (s_2)_{n+1} \\ (s_3)_{n+1} \end{bmatrix} = \mathbf{F}_n(\theta_{1,n}, \theta_{2,n}, \theta_{3,n}) \begin{bmatrix} (s_1)_n \\ (s_2)_n \\ (s_3)_n \end{bmatrix}, \tag{3.28}$$

with $\mathbf{F}_n(\theta_{1,n}, \theta_{2,n}, \theta_{3,n})$ given by (3.27). Index n was introduced in $\mathbf{F}_n(\theta_{1,n}, \theta_{2,n}, \theta_{3,n})$ in order to make clear that the matrix $\mathbf{F}$ and the angles θ_1, θ_2 and θ_3 refer to the n^{th} PC. In (3.28), $(s_i)_n$ represents the i component of the Stokes vector at the input of the n^{th} PC.

We are going to assume that the PC angles are randomly changed following a uniform distribution within the range $\left[-m\frac{\pi}{4}; m\frac{\pi}{4}\right]$, with $m = 1,2,3...$. We are also going to assume that the change is independent between the angles of the same PC and between the angles of different PCs. Therefore, the average value of the $\mathbf{F}$ matrix elements, f_{ij}, will be equal for all the PCs and will be hereafter designated simply by $\langle f_{ij} \rangle$. The mean value of each Stokes parameter at the output of the n^{th} PC, $\langle (s_i)_{n+1} \rangle$, is given by

$$\begin{bmatrix} \langle (s_1)_{n+1} \rangle \\ \langle (s_2)_{n+1} \rangle \\ \langle (s_3)_{n+1} \rangle \end{bmatrix} = \begin{bmatrix} \langle f_{11} \rangle & \langle f_{12} \rangle & \langle f_{13} \rangle \\ \langle f_{21} \rangle & \langle f_{22} \rangle & \langle f_{23} \rangle \\ \langle f_{31} \rangle & \langle f_{32} \rangle & \langle f_{33} \rangle \end{bmatrix} \begin{bmatrix} \langle (s_1)_n \rangle \\ \langle (s_2)_n \rangle \\ \langle (s_3)_n \rangle \end{bmatrix}. \tag{3.29}$$

Note that the n index was dropped in the matrix coefficients of (3.29), because all the PCs are statistically equivalents. In (3.29), the mean value $\langle f_{11} \rangle$, for instance, is calculated by

$$\langle f_{11} \rangle = \int_{-m\frac{\pi}{4}}^{m\frac{\pi}{4}} \int_{-m\frac{\pi}{4}}^{m\frac{\pi}{4}} \int_{-m\frac{\pi}{4}}^{m\frac{\pi}{4}} p_\theta^3 f_{11} d\theta_1 d\theta_2 d\theta_3, \tag{3.30}$$

where p_θ is the probability density function for each waveplate angle and f_{11} is obtained directly from (3.27) and is given by

$$\begin{aligned} f_{11} =& 2\cos^2(2\theta_1)\cos^2(2\theta_3)\cos^2(2\theta_2) + 2\cos^2(2\theta_1)\cos(2\theta_2)\cos(2\theta_3)\sin(2\theta_3)\sin(2\theta_2) \\ & - \cos^2(2\theta_1)\cos^2(2\theta_3) + 2\cos(2\theta_1)\sin(2\theta_1)\sin(2\theta_2)\cos^2(2\theta_3)\cos(2\theta_2) \\ & + \cos(2\theta_1)\sin(2\theta_1)\cos(2\theta_3)\sin(2\theta_3) + \sin(2\theta_3)\sin(2\theta_1) \\ & - 2\cos(2\theta_1)\sin(2\theta_1)\cos(2\theta_3)\sin(2\theta_3)\cos^2(2\theta_2). \end{aligned} \tag{3.31}$$

Assuming a uniform distribution between $-m\frac{\pi}{4}$ and $m\frac{\pi}{4}$ for the configuration angles, the probability density function is given by $p_\theta = 2/(m\pi)$. Using this value into the nine triple integrals similar to (3.30) we find that

$$\langle f_{ij} \rangle_{\theta_i \in \left[-m\frac{\pi}{4}; m\frac{\pi}{4}\right]} = \delta_{2i}\delta_{2j}\delta_{1(-1)^{m-1}} \left(\frac{2}{m\pi}\right)^2, \tag{3.32}$$

where δ_{ij} is the Kronecker delta. In contrast with the other matrix elements, $\langle f_{22} \rangle$ only

vanishes for particular waveplate angle ranges, that is, if m is an even number. For odd values of m, $\langle f_{22} \rangle$ does not vanish, but converges to zero as m increases. In order to analyze the statistics of the system resulting from the concatenation of several PCs, we use (3.32) into (3.31), which is subsequently applied iteratively for an arbitrary initial SOP, $\hat{s}_1 = [(s_1)_1, (s_2)_1, (s_3)_1]^T$. Then, the mean values of the Stokes vector components at the end of the n^{th} PC, $\langle \hat{s}_{n+1} \rangle$, are obtained:

$$\left[\begin{array}{c} \langle (s_1)_{n+1} \rangle \\ \langle (s_2)_{n+1} \rangle \\ \langle (s_3)_{n+1} \rangle \end{array}\right]_{\theta_i \in \left[-m\frac{\pi}{4}; m\frac{\pi}{4}\right]} = \delta_{1(-1)^{m-1}} A \left[\begin{array}{c} 0 \\ 1 \\ 0 \end{array}\right] + \delta_{n0} B \left[\begin{array}{c} 0 \\ 1 \\ 0 \end{array}\right], \tag{3.33}$$

where coefficients A and B are given by

$$A = (s_2)_1 \frac{1}{\left(\frac{(m\pi)^2}{4}\right)^n}, \tag{3.34}$$

and

$$B = 1 - \delta_{1(-1)^{m-1}} \frac{4}{(m\pi)^2}. \tag{3.35}$$

Previous equations show that first and third Stokes vector components have always a null average, whereas the second component depends on both m and n values. This second component vanishes if m is an even number and converges to zero (as n and m increase) if m is an odd number.

In order to calculate the variance of each Stokes vector component we need to calculate the mean square value of $(s_i)_{n+1}$. Squaring each component of (3.28), the following equation is obtained,

$$\left[\begin{array}{c} (s_1)^2_{n+1} \\ (s_2)^2_{n+1} \\ (s_3)^2_{n+1} \end{array}\right] = \left[\begin{array}{l} f^2_{11,n}\,(s_1)^2_n + f^2_{12,n}\,(s_2)^2_n + f^2_{13,n}\,(s_3)^2_n + 2\sum\limits_{i,j=1(i\neq j)}^{3} f_{1i,n}\, f_{1j,n}\,(s_i)_n (s_j)_n \\ f^2_{21,n}\,(s_1)^2_n + f^2_{22,n}\,(s_2)^2_n + f^2_{23,n}\,(s_3)^2_n + 2\sum\limits_{i,j=1(i\neq j)}^{3} f_{2i,n}\, f_{2j,n}\,(s_i)_n (s_j)_n \\ f^2_{31,n}\,(s_1)^2_n + f^2_{32,n}\,(s_2)^2_n + f^2_{33,n}\,(s_3)^2_n + 2\sum\limits_{i,j=1(i\neq j)}^{3} f_{3i,n}\, f_{3j,n}\,(s_i)_n (s_j)_n \end{array}\right]. \tag{3.36}$$

Considering the statistical independence of $(s_i)_n$, and f_{ij}, the mean values $\left\langle (s_i)^2_{n+1} \right\rangle$ can

be written as

$$\begin{bmatrix}\left\langle (s_1)^2_{n+1}\right\rangle \\ \left\langle (s_2)^2_{n+1}\right\rangle \\ \left\langle (s_3)^2_{n+1}\right\rangle\end{bmatrix}=\begin{bmatrix}\left\langle f^2_{11}\right\rangle \left\langle (s_1)^2_n\right\rangle + \left\langle f^2_{12}\right\rangle \left\langle (s_2)^2_n\right\rangle + \left\langle f^2_{13}\right\rangle \left\langle (s_3)^2_n\right\rangle + 2\sum_{i,j=1(i\neq j)}^{3}\langle f_{1i}f_{1j}\rangle \langle (s_i)_n(s_j)_n\rangle \\ \left\langle f^2_{21}\right\rangle \left\langle (s_1)^2_n\right\rangle + \left\langle f^2_{22}\right\rangle \left\langle (s_2)^2_n\right\rangle + \left\langle f^2_{23}\right\rangle \left\langle (s_3)^2_n\right\rangle + 2\sum_{i,j=1(i\neq j)}^{3}\langle f_{2i}f_{2j}\rangle \langle (s_i)_n(s_j)_n\rangle \\ \left\langle f^2_{31}\right\rangle \left\langle (s_1)^2_n\right\rangle + \left\langle f^2_{32}\right\rangle \left\langle (s_2)^2_n\right\rangle + \left\langle f^2_{33}\right\rangle \left\langle (s_3)^2_n\right\rangle + 2\sum_{i,j=1(i\neq j)}^{3}\langle f_{3i}f_{3j}\rangle \langle (s_i)_n(s_j)_n\rangle\end{bmatrix}. \tag{3.37}$$

The mean values $\langle f_{ki}f_{kj}\rangle$ are evaluated using an equation analogous to (3.30),

$$\langle f_{ki}f_{kj}\rangle = \int_{-m\frac{\pi}{4}}^{m\frac{\pi}{4}}\int_{-m\frac{\pi}{4}}^{m\frac{\pi}{4}}\int_{-m\frac{\pi}{4}}^{m\frac{\pi}{4}} p_\theta^3 f_{ki}f_{kj}d\theta_1 d\theta_2 d\theta_3, \tag{3.38}$$

where f_{ki} and f_{kj} are directly obtained from (3.27), and $p_\theta = 2/(m\pi)$. After calculating the triple integral we reach the conclusion that $\langle f_{ki}f_{kj}\rangle = 0$ when $i \neq j$. Using this result and calculating the values for the case $i = j$ the following expression is obtained,

$$\begin{bmatrix}\left\langle (s_1)^2_{n+1}\right\rangle \\ \left\langle (s_2)^2_{n+1}\right\rangle \\ \left\langle (s_3)^2_{n+1}\right\rangle\end{bmatrix} = \begin{bmatrix}3/8 & 3/8 & 1/4 \\ 3/8 & 3/8 & 1/4 \\ 1/4 & 1/4 & 1/2\end{bmatrix}\begin{bmatrix}\langle (s_1)^2_n\rangle \\ \langle (s_2)^2_n\rangle \\ \langle (s_3)^2_n\rangle\end{bmatrix}. \tag{3.39}$$

Equation (3.39) gives a relation between the mean square values of Stokes vector components at the input and output of the n^{th} PC. By using (3.39) iteratively and considering an initial SOP $\hat{s}_1 = [(s_1)_1, (s_2)_1, (s_3)_1]^t$, the following expression is found

$$\begin{bmatrix}\left\langle (s_1)^2_{n+1}\right\rangle \\ \left\langle (s_2)^2_{n+1}\right\rangle \\ \left\langle (s_3)^2_{n+1}\right\rangle\end{bmatrix} = \frac{1}{3}\begin{bmatrix}1\\1\\1\end{bmatrix} + \frac{a}{4^n}\begin{bmatrix}1\\1\\-2\end{bmatrix} + \delta_{n0}b\begin{bmatrix}1\\-1\\0\end{bmatrix}, \tag{3.40}$$

where coefficients a and b, given by

$$a = \frac{1}{2}\left(\frac{1}{3} - (s_3)^2_1\right), \tag{3.41}$$

and

$$b = \frac{1}{2}\left((s_1)^2_1 - (s_2)^2_1\right), \tag{3.42}$$

are functions of the input SOP, $\hat{s}_1$. In contrast with the mean values, we verify that the mean square values of the three Stokes vector components are no more dependent on the waveplate angle range. We also verify that the mean square of each component of the

Stokes vector converges to the 1/3 value with a factor $a/4^n$. Indeed, from (3.41) we can say that SOPs with the same modulus of $(s_3)_1$ have the same convergence rate (note that these SOP domains depict a circumference in the Poincaré sphere parallel to the $s_3 = 0$ plane) and that the convergence rate decreases with the increase of the modulus of a. The parameter a becomes null when $(s_3)_1^2 = 1/3$, which means that, independently of the number of PCs, $\hat{s}_1 = \left[(s_1)_1, (s_2)_1, \pm(1/3)^{1/2}\right]^t$ is a special initial SOP. In fact, with this initial SOP the mean square values of the Stokes parameters reach the 1/3 value right after the first PC.

The variance of $(s_i)_{n+1}$ can be easily calculated by subtracting the square of (3.33) to (3.40). In the cases of Stokes vector components with null mean, the respective variance is simply described by (3.40).

3.2.2 Numerical Simulations

We are going to present some numerical results in terms of SOP scattering, considering the model resulting from the concatenation of several PCs. Using a particular initial SOP, we analyze the statistics of the scattered output SOPs. We show how the selected number of PCs and waveplate angle range affects the statistics of the distribution.

The analytical model presented above shows clearly that the number of PCs should enhance the scattering properties. In Fig. 3.5–a) are represented 5000 Stokes vectors, obtained at the end of a single PC, considering the same input SOP $\hat{s}_1 = [0, 0, 1]^t$ and varying the configuration angles uniformly between $-\pi$ and π, i.e., using $m = 4$. Points are not uniformly distributed over the Poincaré sphere and histograms presented in Figs. 3.5–b), 3.5–c) and 3.5–d) show clearly that the three Stokes vector components have non uniform distributions within the range -1 to 1. From Figs. 3.5–b), 3.5–c) and 3.5–d) we conclude that each Stokes vector component presents a null mean, which is in good agreement with (3.33). Using (3.40), the mean square values for the case considered in Fig. 3.5 are

$$\begin{bmatrix} \langle (s_1)_2^2 \rangle \\ \langle (s_2)_2^2 \rangle \\ \langle (s_3)_2^2 \rangle \end{bmatrix} = \begin{bmatrix} 1/4 \\ 1/4 \\ 1/4 \end{bmatrix}. \tag{3.43}$$

Figure 3.6–a) shows the evolution of the mean squares with the number of samples used in the simulation. A quick convergence to the theoretical values, given by (3.43), is observed. These results confirm that a system resulting from only one PC is unable to produce a uniform distribution of SOPs over the Poincaré sphere. Although not presented here, we repeated the numerical simulations and observed that with one PC the output Stokes parameters mean square values are strongly dependent of the initial SOP. Besides that, we have used three different input SOPs, with equal third Stokes vector component modulus ($|(s_3)_1|$), and three similar distributions were obtained. This result is in good agreement with the $|(s_3)_1|$ parameter degeneration present in (3.40).

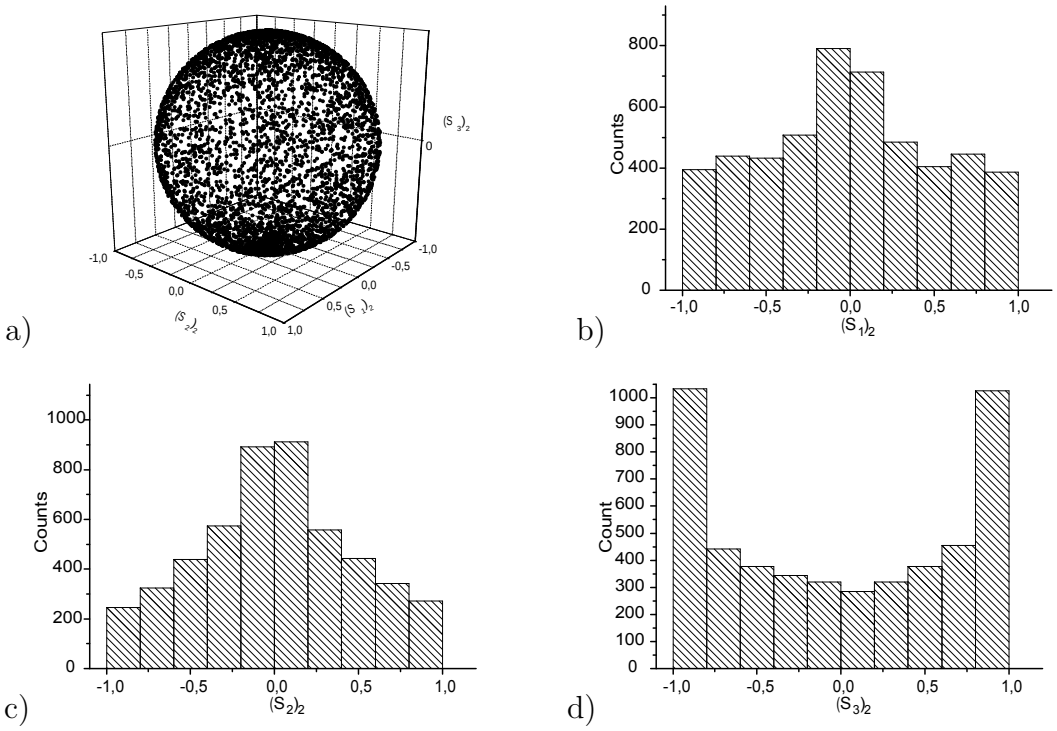

Figure 3.5: Results using $n = 1$, $m = 4$, and initial SOP $\hat{s}_1 = [0, 0, 1]^t$: a) - Poincaré sphere representation of the output SOPs; b) – the $(s_1)_2$ histogram; c) – the $(s_2)_2$ histogram; d) – the $(s_3)_2$ histogram.

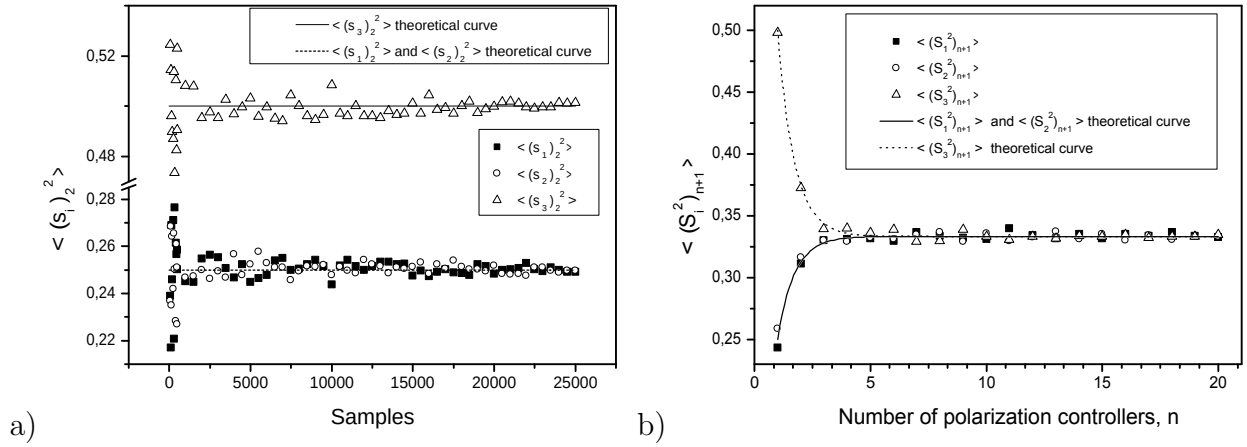

Figure 3.6: a) – Mean square of the Stokes parameters as a function of the samples number, considering $n = 1$, $m = 4$ and $\hat{s}_1 = [0, 0, 1]^t$. b) – Mean square of the Stokes parameters as a function of n, considering $m = 4$, and initial SOP $\hat{s}_1 = [0, 0, 1]^t$. Numerical and theoretical values are represented as symbols and lines, respectively.

Figure 3.7–a) represents 5000 Stokes vectors resulting from the scattering of an input SOP $\hat{s}_1 = [0, 0, 1]^t$. The scattering system was comprised by the concatenation of 20 PCs,

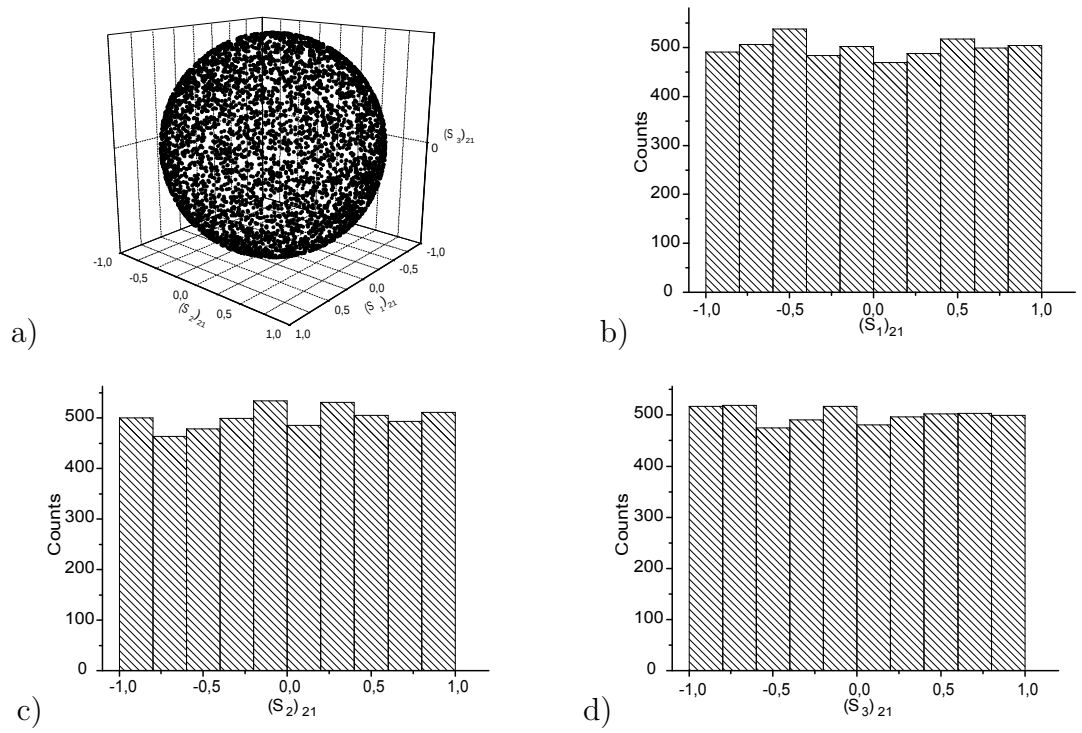

Figure 3.7: Results using $n = 20$, $m = 4$, and initial SOP $\hat{s}_1 = [0, 0, 1]^t$: a) – Poincaré sphere representation of the output SOP; b) – the $(s_1)_{21}$ histogram; c) – the $(s_2)_{21}$ histogram; d) – the $(s_3)_{21}$ histogram.

whose waveplates were uniformly changed between $-\pi$ and π, i.e., we used $m = 4$. In this case, SOPs seems to be uniformly distributed over the Poincaré sphere. Furthermore, Figs. 3.7–b), 3.7–c) and 3.7–d) show that the three Stokes parameters are uniformly distributed between -1 and 1. According with (3.40), for large values of n, the mean value of s_1^2, s_2^2 and s_3^2 converges to 1/3, independently of the input SOP. We present in Fig. 3.6–b) the mean squares of the Stokes parameters as a function of the PC number n, considering $m = 4$ and the same particular input SOP, $\hat{s}_1 = [0, 0, 1]^t$. Numerical and analytical data are represented as symbols and lines, respectively. As expected, all mean squares values quickly converge to the 1/3 value, with a good agreement between the numerical results and (3.40).

We also have analyzed the influence of the waveplate angle range parameter, m, on the uniformity of the scattering [16]. In order to do that, we calculated a normalized deviation factor (NDF) for each Stokes vector component with respect to an ideal uniform

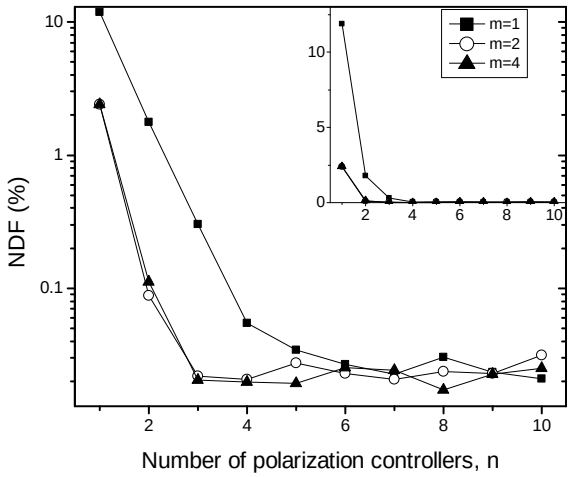

Figure 3.8: Sum of the three Stokes vector component distribution NDFs as a function of the number of PCs, considering different waveplate angle ranges.

distribution. The NDF is defined as [16, 19]

$$\mathrm{NDF} = \sum_{i=1}^{N_c} \left| \frac{p_{\mathrm{Em}}(x_i)\delta x - \int_{x_i-\frac{\delta x}{2}}^{x_i+\frac{\delta x}{2}} p_{\mathrm{Te}}(x)dx}{\int_{x_i-\frac{\delta x}{2}}^{x_i+\frac{\delta x}{2}} p_{\mathrm{Te}}(x)dx} \right|^2, \tag{3.44}$$

where $p_{\mathrm{Em}}(x_i)$ is the simulated probability density function (pdf) for each Stokes vector component, $p_{\mathrm{Te}}(x_i)$ is the pdf of a vector component corresponding to a uniform distribution of points over the Poincaré sphere, δx is the bin width of the histogram, x_i is the center position of the i^{th} bin, and N_c is the number of bins composing the histogram.

Figure 3.8 presents the sum of the three Stokes vector component distribution NDFs as a function of the number of concatenated PCs, for different values of m and input SOP $\hat{s}_1 = [0, 0, 1]^t$. Results show that for a small number of PCs, up to six, a significant NDF improvement is observed if the waveplate angle range is increased from $m = 1$ to $m = 2$. Nevertheless, increasing the range from $m = 2$ to $m = 4$ no changes are observed in the statistics. This can be explained by the periodicity of the waveplate angle properties. For six or more concatenated PCs the angle range becomes no more relevant since the uniformity degree of the obtained distributions is similar for the different m values.

3.3 PMD Emulation

For testing purposes, it is impractical to wait until a high-PMD effect occurs naturally in a real system, and PMD emulators are sometimes used to create such occurrences [14, 22]. We consider in this Section an application of the uniform polarization scattering using fiber-coil based PCs to PMD emulation. A real fiber is usually modeled by the con-

catenation of randomly coupled linear birefringence sections. In the same way, a device to emulate fiber PMD may be constructed by the concatenation of several birefringence elements [23]. These birefringence elements may be sections of PMF, birefringence crystals, or other device that provides a DGD between the two orthogonal polarization axes. PMD emulators can be classified into five main groups [24]:

- *Emulators with fixed orientation sections* - This kind of emulators result from the concatenation of several PMF sections spliced at fixed angles [19, 25]. These emulators have been used in polarization analyzer tests, and comparison of different PMD measurement devices and techniques. A rigorous statistic analysis of their results was only made theoretically. A computational simulation of an emulator with 15 equal-length PMF sections, spliced randomly, has generated a DGD distribution well described by a Maxwellian distribution [19]. The main limitation of these emulators is that, in order to obtain different PMD emulator states, wide wavelength sweeps are required.

- *Emulators with uniform scattering of polarization* - These emulators are obtained by placing polarization scramblers between PMF sections to uniformly scatter the SOP over the Poincaré sphere. Emulators comprised by the concatenation of three, five and ten PMF sections (with random lengths) were presented in [19]. Results showed that only with ten or more PMF sections the pdf of the DGD is well fitted by a Maxwellian distribution. Similar results were obtained in [26], using all the PMF sections with the same length.

- *Emulators with rotatable sections* - In this case, the birefringent sections are randomly rotated relatively to each other. An emulator with twelve equal-length yttrium ortho-vanadate (YVO4) birefringent crystals, mounted into twelve independent and motorized rotation stages placed in cascade, was presented in [27]. Aspheric lenses couple light to and from the input and output fibers. The collimated beam between the input and the output passes through over all crystals. First- and higher-order PMD have been generated. However, all moving parts can affect emulator properties like stability or durability. Two PMD emulators, with 3 and 15 PMF sections coupled with rotatable connectors, have also been constructed [28]. Using such kind of emulators, different fiber realizations are obtained (at a particular wavelength) by randomly rotating the connectors. Results showed that only with 15 PMF sections the emulator is able to generate DGD values in good agreement with the Maxwellian distribution. The 15 PMF sections emulator exhibited also good results in terms of autocorrelation function (ACF) of the PMD vector. An average level of 10% correlation remains between well-spaced wavelengths.

- *Emulators with tunable birefringence* - Although the reasonable results exhibited by the two previous emulator types, they still present some issues, like cumbrously, relatively high losses, or an insufficient automatic control. An emulator with tunable birefringent sections, exploiting the temperature sensitivity of PMF, was presented in [29]. Thirty sections of PMFs were fusion spliced together at 45^{o} angles. Applying voltages, micro heaters thermally tune the birefringence of each DGD section.

This emulator exhibited reasonable results: first-order PMD was well fitted with a Maxwellian distribution, and the measured second-order PMD only differs from expected theoretical distribution in the low probability tail; The ACF was higher residual correlation value, 20%, comparatively with the 15 PMF sections connected with rotatable connectors emulator described above (that presented only 10% of residual correlation). A possible way to solve these two issues is to increase the number of PMF sections. The main advantages of this compact emulator are the low insertion losses, electronic control, no moving parts, negligible polarization-dependent losses (PDL), and no internal reflections.

- *Emulators with tunable statistics* - The emulator with tunable statistics presented in [30] makes use of three programmable DGD elements separated by two fiber-squeezer-based PCs. The DGD elements consist of several birefringent crystals, whose lengths increase in a binary series. They are separated by electrically driven polarization switches that can be programmed in order to generate a desired DGD value [31]. Varying the DGD of each element according to a Maxwellian distribution with average $\langle\Delta\tau\rangle$, and uniformly scattering the polarization between sections, a Maxwellian distribution with average $\sqrt{3}\langle\Delta\tau\rangle$ is yield at the emulator output. Experimental results showed an accurate tunability of the PMD statistics. The first-order PMD values are well fitted by a Maxwellian, however, the mean of second-order PMD is about 30% lower than the expected for a real fiber. Simulation results reveal that only with fifteen or more DGD elements it is possible to obtain an ACF with residual correlation values lower than 10% [32]. Thus, one limitation of this emulator is that it would require more DGD elements in order to accurately emulate the statistics of second-order PMD and to exhibit reasonable residual correlation values. Nevertheless, features like stability and repeatability are well achieved. Another advantage of this emulator is the possibility of being used to experimentally employ the powerful technique of importance sample to quickly generate extremely low probability events [30].

We consider a system composed of several PMFs with one or more PCs between adjacent PMFs to scatter the light polarization. Each PMF can be described by the following matrix [19],

$$\mathbf{R}_x = \begin{bmatrix} 1 & 0 & 0 \\ 0 & \cos(2\phi) & -\sin(2\phi) \\ 0 & \sin(2\phi) & \cos(2\phi) \end{bmatrix} \tag{3.45}$$

where $\phi = \omega\Delta\tau_s$ is the birefringence-induced phase mismatch directly related with the differential group delay (DGD) of the PMF, $\Delta\tau_s$, and ω is the angular frequency of the light. The polarization scattering between PMFs can be modeled as

$$\mathbf{R}_s = \prod_{n=1}^{m} \mathbf{F}_n(\theta_{1,n}, \theta_{2,n}, \theta_{3,n}), \tag{3.46}$$

where $\mathbf{F}$ is given by (3.27) and m is number of PCs used to scatter the light polarization.

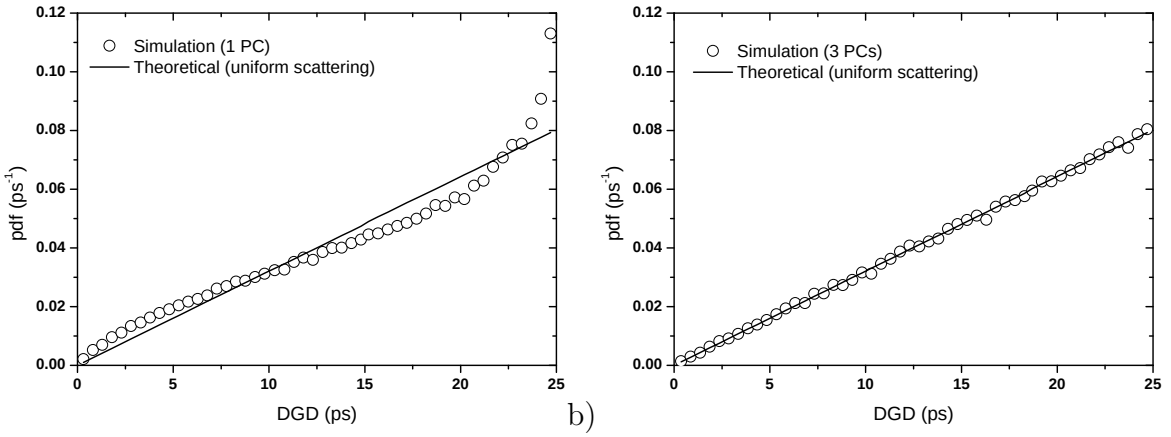

Figure 3.9: Probability density function for the DGD in a system with two equal-length PMFs using between them a) – one, and b) – three PCs to scatter the light polarization. Solid lines represent the theoretical values assuming uniform scattering, given by equation (3.47), and marks represent values from the numerical simulation.

3.3.1 System with Two PMFs

In order to assess the effect of the polarization scattering uniformity we simulated a system resulting from the concatenation of two PMFs, with DGD equal to 12 ps, and with a polarization scattering section between PMFs. After that, we calculated the magnitude of the PMD vector. The polarization scattering section comprises a concatenation of several PCs. The magnitude of the resulting first-order PMD vector (the DGD) was obtained using the matrices presented in (3.45) and (3.46), and the well known concatenation rule of PMD vectors [33, 34]. Simulation results are presented in Fig. 3.9. Two cases were considered: in the first one, the scattering is performed using only one PC, see Fig. 3.9–a), and in the second one, three PCs were used to perform the scattering, see Fig. 3.9–b). For each case, 10^5 realizations were performed. Note that each realization is related with an ensemble of three angles, θ_1, θ_2 and θ_3, randomly chosen for each PC. The angles are uniformly distributed between $-\pi$ and π and are statistically independents.

Assuming two PMFs with an ideal uniform polarization scattering between them, Djupsjöbacka [26] has proven that the pdf for the magnitude of the resulting first-order PMD vector, $\Delta\tau$, is given by,

$$f(\Delta\tau) = \frac{\Delta\tau}{2\Delta\tau_s^2}, \quad \Delta\tau \in [0, 2\Delta\tau_s], \tag{3.47}$$

where $\Delta\tau_s$ is the DGD of each single PMF. Comparing our simulation results with (3.47), represented in Fig. 3.9 as a solid line, we observe that as the number of PCs used to scatter the polarization increases, the simulation points are closer to the expected theoretical value. We can say that the three PCs used in the simulation depicted in Fig. 3.9–b) provide a uniform polarization scattering over the Poincaré sphere. This result corroborates

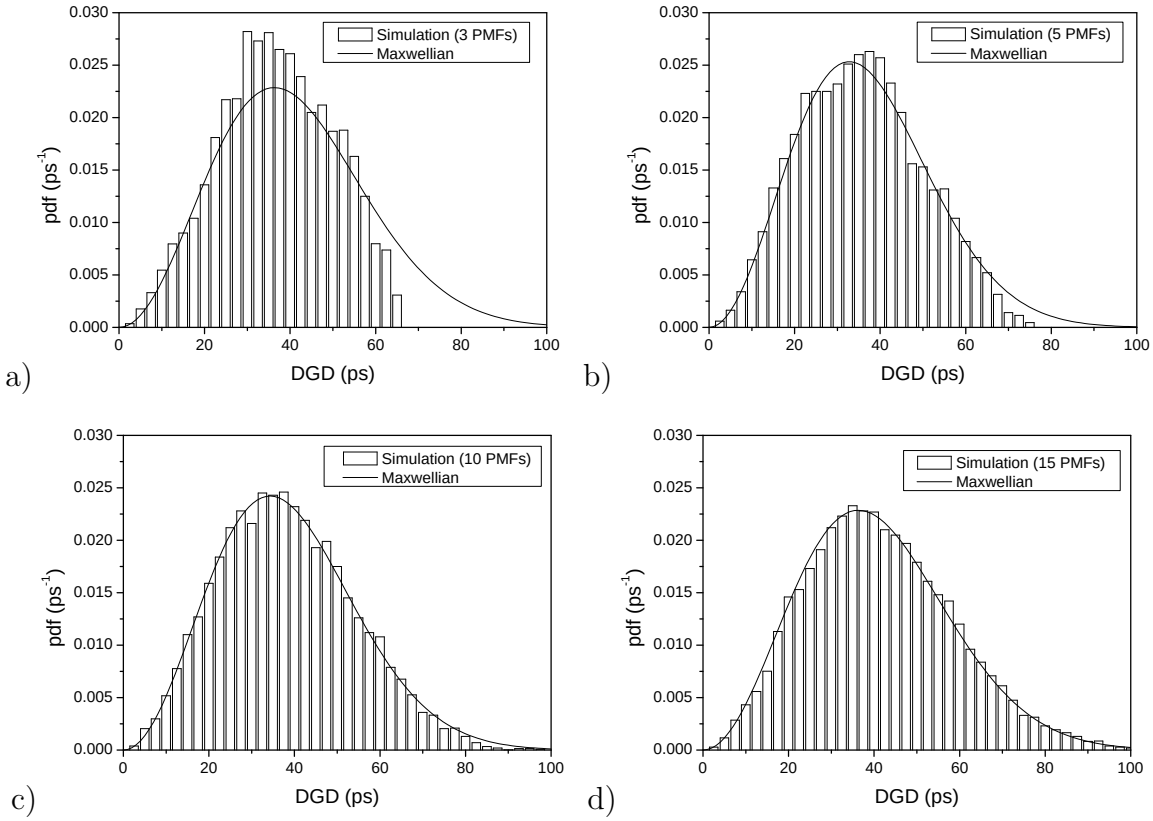

Figure 3.10: Probability density functions of the first-order PMD vector obtained from a system with: a) – three; b) – five; c) – ten; and d) – fifteen PMFs. The Maxwellian distribution is represented as a solid line.

the one obtained in the last Section, where we have shown that the uniformity of the polarization scattering increases with the number of PCs.

3.3.2 Emulator Based on PMFs and Fiber-Coil Based PCs

We investigate in this subsection the ability to produce accurate first- and second-order PMD statistics, using the concatenation of PMFs and fiber-coil based PCs. We are going to use n PMFs and $n-1$ polarization scattering sections. In a first stage, between PMFs is placed a light scattering section comprising three PCs. As we saw previously, this number of PCs produces a quite good uniform scattering over the Poincaré sphere. PMD vectors were simulated using the Mueller Matrix Method with a 0.025 nm step and a 0.0083 nm interleave step [35, 36]. We considered 120 different wavelengths and for each wavelength 250 statistically independent combinations for the PCs configuration angles were applied. The length of PMFs was obtained from a Gaussian distribution with mean L_m and standard deviation equal to 20%. The mean length was chosen in order to generate a DGD distribution with mean value around 41 ps.

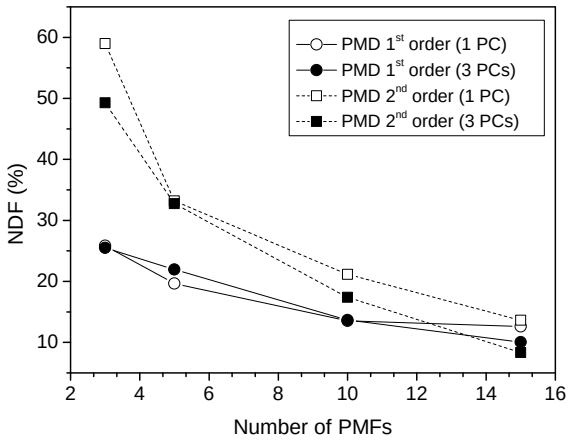

Figure 3.11: Normalized deviation factor for first- and second-order PMD as a function of the number of PMFs. All represented points result from polarization scattering sections composed of 3 PCs.

.

The pdfs of first-order PMD, obtained for systems with three, five, ten and fifteen PMF sections are shown in Figs. 3.10–a), 3.10–b), 3.10–c) and 3.10–d), respectively. In Figs. 3.10–a) and 3.10–b) we observe that both three and five PMFs are insufficient to mimic the theoretical distribution of the first-order PMD, i.e. a Maxwellian [37]. On the other hand, Figs. 3.10–c) and 3.10–d) show that a system with ten and more PMFs can reproduce a large range of first-order PMD values with a statistic close to the Maxwellian distribution, including the tail distribution.

The deviations of the first- and second-order PMD vectors were calculated by using the NDF defined in (3.44). Figure 3.11 shows the NDF of the first- and second-order PMD, for the cases where the scattering sections comprise one and three PCs, as a function of the number of PMFs. In a global analysis, results show that as the number of PMFs increases the NDF parameter decreases, which is in good agreement with previous results presented in literature [19]. For fixed number of PMFs, a statistical improvement is in general also observed when a more uniform distribution is performed, i.e., when using three PCs instead of just one PC. Nevertheless, the number of PMFs seems to be a more critical parameter when accurate PMD statistics are required.

Figure 3.12 represents the pdfs for the emulator with fifteen PMFs, with a polarization scattering between PMFs using one and three PCs (represented as blue circles and black empty squares, respectively) . The magnitude of the first-order PMD vector is represented in Fig. 3.12–a). The magnitude and one component of the second-order PMD vector $\vec{\tau}_\omega$ are represented in Figs. 3.12–b) and 3.12–c), respectively. The second-order PMD component associated with the polarization dependent chromatic dispersion (PCD) [38] is represented in Fig. 3.12–d). The Maxwellian correspondent to the first-order pdf, represented in Fig. 3.12–a) as a solid line, has a mean value equal to 41 ps. The remain theoretical pdfs, also represented as solid lines, are plotted with the fit parameter equal

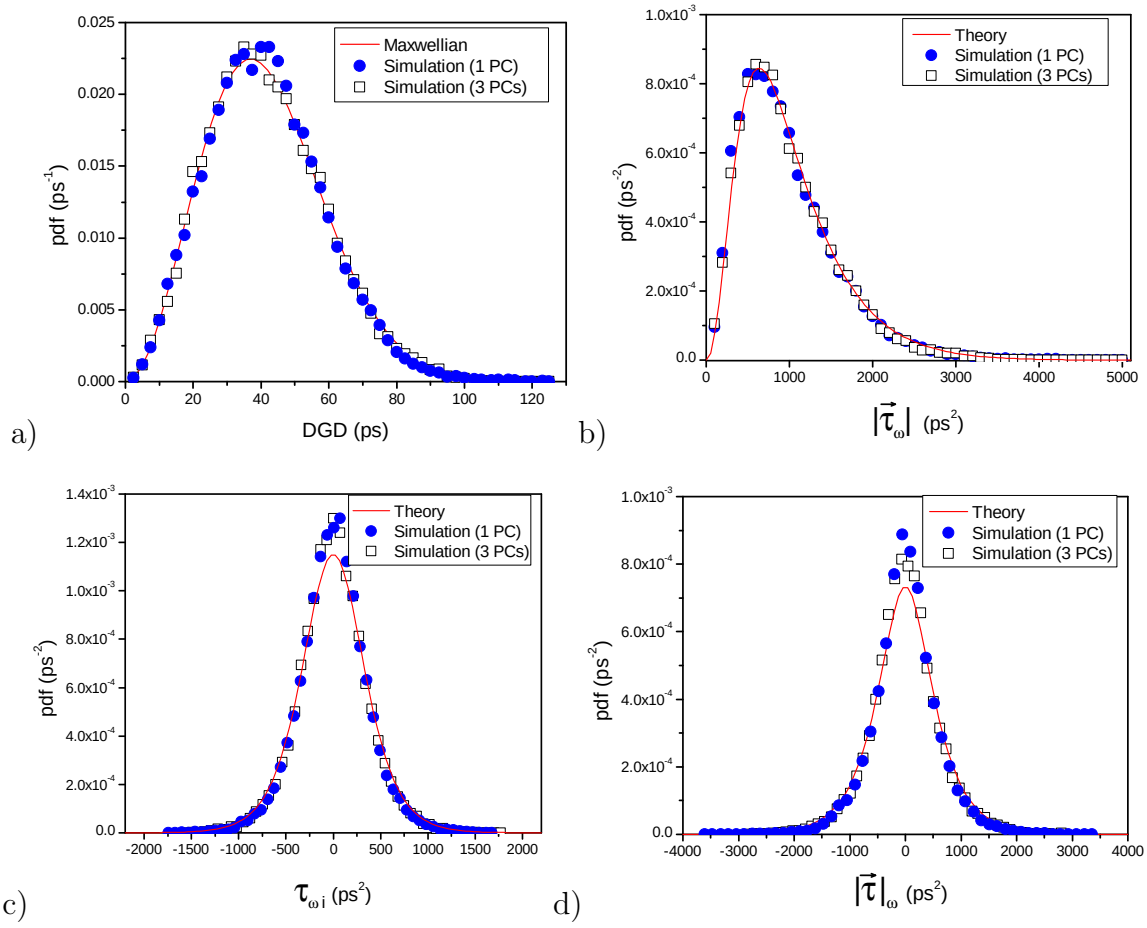

Figure 3.12: First- and second-order PMD functions of an emulator with fifteen sections: a) – first-order PMD; b) – magnitude of the second-order PMD vector; c) – a component of the second-order PMD vector; d) – second-order component associated with PCD.

to the mean value of 41 ps. For both cases, polarization scattering with one and three PCs, the simulation results are in good agreement with the theory. Using these results, in conjugation with those presented in Fig. 3.11, we conclude that a large number of PMFs should be considered in an emulator design and that the uniformity of the polarization scattering is a less relevant factor.

3.4 Summary

In this Chapter, a model for the fiber-coil based PC was introduced. The proposed model can be used to deterministically calculate the PC configuration, i.e., the three waveplate angles, in order to transform the polarization between any two SOPs.

Furthermore, we presented an analytical expression for the variance of the Stokes parameters when several fiber-coil based PCs are concatenated in order to scatter a given

input SOP. This expression was extensively confirmed with simulation data. Results showed that a uniform polarization scattering is obtained through the concatenation of at least three PCs, and randomly changing the configuration of the waveplate PC angles between $-\pi/2$ and $\pi/2$. In terms of waveplate angles range, we showed that for six or more concatenated PCs, the uniformity degree of the obtained distributions is independent of m.

An application of the polarization scattering to PMD emulation was also proposed. The first- and second-order PMD statistics can be accurately generated when fifteen PMFs are interconnected with fourteen polarization scattering sections (comprised by the concatenation of several fiber-coil based PCs). We also showed that for a high number of polarization scattering sections the number of PCs used in each section to scatter the light polarization becomes less decisive to the accuracy of the generated statistics.

References

[1] R. Ulrich, "Polarization stabilization on single-mode fibers," *Appl. Phys. Lett.*, vol. 35, no. 11, pp. 840–842, 1979.

[2] H. Honmou, S. Yamazaky, K. Emura, R. Ishikawa, I. Mito, M. Shikada, and K. Minemura, "Stabilisation of heterodyne receiver sensitivity with automatic polarisation control system," *Electron. Lett.*, vol. 22, no. 22, pp. 1181–1182, 1986.

[3] M. Johnson, "In-line fiber-optical polarization transformer," *App. Opt.*, vol. 18, no. 9, pp. 1288–1289, 1979.

[4] P. Granestrand and L. Thylen, "Active stabilization of polarization on a single-mode fiber," *Electron. Lett.*, vol. 20, no. 9, pp. 365–366, 1984.

[5] H. C. Lefevre, "Single-mode fibre fractional wave devices and polarization controllers," *Electron. Lett.*, vol. 16, no. 20, pp. 778–780, 1980.

[6] Y. Kidoh, "Polarization control on output of single-mode optical fibers," *J. Quantum Electron.*, vol. 17, no. 6, pp. 991–994, 1981.

[7] T. Okoshi, Y. H. Cheng, and K. Kikuchi, "New polarization control scheme for optical heterodyne receiver using two faraday rotators," *Electron. Lett.*, vol. 21, no. 18, pp. 787–788, 1985.

[8] W. L. Barnes, "2 × 2 optical fiber polarization switch and polarization controller," *Electron. Lett.*, vol. 24, no. 23, pp. 1427–1429, 1988.

[9] A. Siddiqui and H. Sherief, "Liquid crystal polarisation controller for use in fiber communication systems," in *Proc. OFC '89*, Houston, USA, Feb. 1989.

[10] H. C. LeFevre, "Fiber optic polarization controller," *United States Patent, no. 4,389,090*, 1983.

[11] B. G. Koehler and J. E. Bowers, "In-line single-mode fiber polarization controllers at 1500, 1300 and 630 nm," *Appl. Optics*, vol. 24, no. 3, pp. 349–353, 1985.

[12] N. G. Walker and G. R. Walker, "Polarization control for coherent communications," *IEEE/OSA J. Lightwave Technol.*, vol. 8, no. 3, pp. 438–458, 1990.

[13] M. Boroditsky, M. Brodsky, N. Frigo, P. Magill, C. Antonelli, and A. Mecozzi, "Outage probabilities for fiber routes with finite number of degrees of freedom," *IEEE Photonics Technol. Lett.*, vol. 17, no. 2, pp. 345–347, Feb. 2005.

[14] S. Wang, A. Weiner, S. H. Foo, D. Bownass, M. Moyer, M. O'Sullivan, M. Birk, and M. Boroditsky, "PMD tolerance testing of a commercial communication system using a spectral polarimeter," *IEEE/OSA J. Lightwave Technol.*, vol. 24, no. 11, pp. 4120–4126, Nov. 2006.

[15] N. J. Muga, A. N. Pinto, M. Ferreira, and J. R. F. da Rocha, "Uniform polarization scattering with fiber-coil based polarization controllers," *IEEE/OSA J. Lightwave Technol.*, vol. 24, no. 11, pp. 3932–3943, 2006.

[16] N. J. Muga, A. N. Pinto, and M. Ferreira, "Polarization scattering property of cascaded polarization controllers," *ETRI Trans.*, vol. 29, no. 6, pp. 838–840, 2007.

[17] R. Ulrich, S. C. Rashleigh, and W. Eickhoff, "Bending-induced birefringence in single mode fibers," *Opt. Lett.*, vol. 5, no. 6, pp. 273–275, 1980.

[18] R. Ulrich and A. Simon, "Polarization optics of twisted single-mode fibers," *Appl. Optics*, vol. 18, no. 13, pp. 2241–2251, 1979.

[19] I. T. Lima, R. Khosravani, P. Ebrahimi, E. Ibragimov, C. R.Menyuk, and A. E. Willner, "Comparison of polarization mode dispersion emulators," *IEEE/OSA J. Lightwave Technol.*, vol. 19, no. 12, pp. 1872–1881, 2001.

[20] Y. K. Lizé, L. Palmer, N. Godbout, S. Lacroix, and R. Kashyap, "Scalable polarization-mode dispersion emulator with proper first- and second-order statistics," *IEEE Photonics Technol. Lett.*, vol. 17, no. 11, pp. 2451–2453, 2005.

[21] D. Marcuse, C. R. Menyuk, and P. K. Wai, "Application of the Manakov - PMD equation to studies of signal propagation in optical fibers with randomly varying birefringence," *IEEE/OSA J. Lightwave Technol.*, vol. 15, no. 9, pp. 1735–1746, 1997.

[22] N. J. Muga, A. N. Pinto, and M. Ferreira, "Efeitos estocásticos da polarização em fibras ópticas," in *14ª Conferência Nacional de Física*, Porto, Portugal, 2005.

[23] A. E. Willner and M. C. Hauer, "PMD emulation," *Venice Summer School on Polarization Mode Dispersion, Venice Italy, 24-26 June*, 2002.

[24] N. J. Muga, A. N. Pinto, and M. Ferreira, "The development of a PMD emulator," in *ConfTele 2005, Tomar*, 2005.

[25] C. H. Prola, J. A. P. da Silva, A. O. D. Forno, R. Passy, J. P. Weid, and N. Gisin, "Autocorrelation function for polarization mode dispersion emulators with rotators," *IEEE Photonics Technology Letters*, vol. 9, no. 6, pp. 842–844, 1997.

[26] A. Djupsjöbacka, "Comparison of polarization mode dispersion emulators," *IEEE/OSA J. Lightwave Technol.*, vol. 19, no. 12, pp. 1872–1881, 2001.

[27] J. N. Damask, "A programmable polarization-mode dispersion emulator for systematic testing of 10 Gb/s PMD compensators," *OSA Optical Fiber Communication Tech. Dig.*, vol. ThB3, 2000.

[28] R. Khosravani, I. T. L. Jr., E. I. P Ebrahimi and, A. E. Willner, and C. R. Menyuk, "Time and frequency domain characteristics of polarization-mode dispersion emulators," *IEEE Photonics Technol. Lett.*, vol. 13, no. 2, pp. 127–129, 1997.

[29] M. C. Hauer, E. R. L. Q. Yu, C. H. Lin, A. A. Au, and A. E. W. H. P. Lee, "Electrically controllable all-fiber PMD emulator using a compact array of thin-film microheaters," *IEEE/OSA J. Lightwave Technol.*, vol. 22, no. 4, pp. 1059–1065, 2004.

[30] L. Yan, M. C. Hauera, Y. Shi, X. S. Yao, P. Ebrahimi, Y. Wang, A. E. Willner, and W. L. Kath, "Polarization-mode-dispersion emulator using variable differential-group-delay (DGD) elements and its use for experimental importance sampling," *IEEE/OSA J. Lightwave Technol.*, vol. 22, no. 4, pp. 1051–1058, 2004.

[31] L. Yan, C. Yhe, G. Yang, L. Lin, Z. Chen, Y. Q. Shi, A. E. Willner, and X. S. Yao, "Programmable group-delay module using binary polarization switching," *IEEE/OSA J. Lightwave Technol.*, vol. 21, no. 7, pp. 1676–1684, 2003.

[32] J. H. Lee, M. Kim, and Y. C. Chung, "Statistical PMD emulator using variable DGD elements," *IEEE Photonics Technol. Lett.*, vol. 15, no. 1, pp. 54–56, 2003.

[33] N. Gisin and J. P. Pellaux, "Polarization Mode Dispersion: time versus frequency domains," *Opt. Commun.*, vol. 89, pp. 316–323, 1992.

[34] J. P. Gordon and H. Kogelnik, "PMD fundamentals: Polarization mode dispersion in optical fibers," *PNAS*, vol. 97, no. 9, pp. 4541–4550, 2000.

[35] R. M. Jopson, L. E. Nelson, and H. Kogelnik, "Measurement of second-order polarization-mode dispersion vectors in optical fibers," *IEEE Photonics Technol. Lett.*, vol. 11, no. 9, pp. 1153–1155, 1999.

[36] N. J. Muga, "Dispersão dos Modos de Polarização em Fibras Ópticas," Master's thesis, Universidade de Aveiro, 2006.

[37] F. Curti, B. Daino, G. D. Marchis, and F. Matera, "Satistical treatment of the evolution of the principal states of polarization in single-mode fibers," *IEEE/OSA J. Lightwave Technol.*, vol. 8, no. 8, pp. 1162–1166, 1990.

[38] G. J. Foschini, L. E. Nelson, R. M. Jopson, and H. Kogelnik, "Probability densities of second-order polarization mode dispersion including polarization dependent chromatic fiber dispersion," *IEEE Photonics Technol. Lett.*, vol. 12, no. 3, pp. 293–295, 2000.

Chapter 4

Degree of Co-Polarization in High-Birefringence Fibers

In this chapter, we analyze the case of two continuous waves (CWs) at different wavelengths copropagating inside a high-birefringence (HiBi) fiber. An analytical model accurately describing the evolution of the relative state of polarization (rSOP) between the two signals is derived. We define and calculate the degree of co-polarization as a function of polarization orientation and ellipticity of the two input signals, considering two different input polarization schemes. In the first scheme, the input signals have the same polarization, while in the second scheme, the input signals have orthogonal polarizations. It is shown that for small fiber lengths or narrow wavelength separations, launching the two signals with orthogonal polarizations can lead a higher degree of co-polarization along the propagation; for large wavelength separations or long distances, the degree of co-polarization for the parallel scheme is always equal or higher than the one for the orthogonal case. The degree of co-polarization model is compared with theoretical and experimental four-wave mixing (FWM) results obtained into a dispersion-shifted HiBi fiber.

4.1 Introduction

Physical effects involving more than one optical signal, like stimulated FWM or stimulated Raman scattering (SRS), tend to be dependent on the rSOP along the propagation [1–4]. We showed previously that when two optical signals at different wavelengths are co-propagated inside a standard single-mode fiber, the rSOP changes randomly due to the fiber residual birefringence [5–8]. The stochastic behavior of the polarization evolution in optical fibers are generally undesirable since it can deteriorate the performance of the communication system.

Polarization-maintaining fibers (PMFs) with refractive indices difference higher than 10^{-5} are usually named as HiBi fibers [9]. This kind of fibers avoid random changes of the state of polarization (SOP) [9, 10] and, consequently, of the rSOP. In recent years, several new applications have been proposed based on HiBi fibers. For instance,

the writing of Bragg gratings in HiBi fibers are used to produce inline fiber polarization dependent sensors [11, 12], polarization-mode dispersion (PMD) compensators [13–15], or all-optical processing devices [16]. Several PMD emulators, based on the concatenation of HiBi fibers, were also proposed in the literature [17–19]. A novel design for polarization-independent single-pump fiber-optic parametric amplifiers using the concatenation of two pieces of HiBi fibers was also proposed in [20]. These kind of fibers have also been used to generate polarization-entangled photons pairs in the 1550 nm telecom band [21, 22].

In general, the evolution of the SOP in birefringent fibers requires a simultaneous consideration of both linear and nonlinear birefringence [23–26]. The nonlinear birefringence can induce nonlinear polarization evolution and polarization instabilities [2, 25, 27], making more complex the analysis of the SOP dynamics in this kind of fibers. Nevertheless, the nonlinear contribution to the SOP evolution is significantly different for weakly and strongly birefringence fibers [25, 26]. In the case of HiBi fibers, the input power needed to observe nonlinear birefringence is of the order of hundreds of watts [26, 27], making nonlinear birefringence negligible for most applications in this fibers. The main properties of the PMF, including some discussions of their early applications, were reported in several papers [28–30]. A detailed description of the nonlinear pulse propagation in such kind of fibers is presented in [31].

The dependence of the FWM efficiency on the rSOP of all the optical signals involved in the process makes birefringence to play an important role on the overall performance of parametric amplifiers [1, 4]. It is well-known that for isotropic fibers, the polarization dependence of the signal gain can be minimized using two orthogonal pumps [32]. Nevertheless, this result can differ for fibers with birefringence [33, 34]. In this context, the FWM process inside fibers with constant, random and spun birefringence was analyzed in several theoretical and experimental works [20, 35–37], considering both the single and dual pump configurations. An interesting result is that the random birefringence presented in non-HiBi fibers can itself mitigate the signal polarization dependencies associated with the intrinsic birefringence if orthogonal pumps are used [38].

Here, we analyze the dynamics of the rSOP between two signals at different wavelengths copropagating into a HiBi fiber for two different input polarization schemes. It is shown that, for narrow wavelength separations, launching the signals into the fiber with orthogonal SOPs can result in a higher degree of co-polarization compared with the case of initial parallel SOPs. We validate experimentally part of the theoretical results through measurements of the efficiency of the FWM process in a dispersion-shifted HiBi fiber, showing that our model is able to describe the evolution of the new waves, generated by FWM.

4.2 SOP Evolution in HiBi Fibers

Optical signal propagation in a HiBi fiber induces different phase changes on the field components polarized along the two principal axes. Depending on the power and propagation distance regimes, the nonlinear birefringence can give important contributions to the total phase change experimented by the optical signal along propagation [25, 26, 39].

In our approach we assume that the changes in the SOP are exclusively governed by linear birefringence, neglecting in this way the nonlinear polarization rotation [40]. The validity of this approach is discussed later in Section 4.4.

Using the Jones-vector notation [41, 42], the evolution of the total field $|A\rangle = [a_x, a_y]^t$, where a_x and a_y are the envelopes of the electric field polarized along $\hat{x}$ and $\hat{y}$, respectively, can be written as [20]

$$|A(z,t)\rangle = \exp\left[i\left(\frac{1}{2}\vec{\beta}\cdot\vec{\sigma}\right)z\right]|A(0,t)\rangle, \tag{4.1}$$

where $|A(0,t)\rangle$ represents the input field, $\vec{\sigma}$ is the Pauli spin vector, defined in (2.17), and $\vec{\beta}$ is the birefringence vector, defined in (2.31). The magnitude of the birefringence vector can be written in terms of wavelengths as

$$\Delta\beta = \frac{2\pi\Delta n}{\lambda_0}, \tag{4.2}$$

where Δn is the difference between the fast and slow refractive indices of the fiber, and λ_0 is the wavelength of the signal in vacuum. However, the analysis of the evolution of the SOP becomes straightforward by writing (4.1) in the Stokes space [42]. As stated in Chapter 2, the SOPs are represented in this space by the Stokes vector, $\hat{s}(z)$, that can be calculated from the Jones vector $|A(z)\rangle$ by using the relation presented in (2.16). Since we are assuming a linear birefringence with the slow propagation mode aligned with $\hat{x}$, the birefringence vector can be written as

$$\vec{\beta} = \begin{bmatrix} \Delta\beta \\ 0 \\ 0 \end{bmatrix}. \tag{4.3}$$

Therefore, using (4.1) and (2.17) in (2.16), and performing some spin vector calculus (see [42, chap. 2]), the evolution of the SOP can be described as

$$s_1(z) = s_1(0), \tag{4.4}$$
$$s_2(z) = s_2(0)\cos\phi(z) + s_3(0)\sin\phi(z), \tag{4.5}$$
$$s_3(z) = -s_2(0)\sin\phi(z) + s_3(0)\cos\phi(z), \tag{4.6}$$

where s_k, with $k = 1$, 2 and 3, are the three components of the Stokes vector $\hat{s}(z)$,

$$\hat{s}(0) = [s_1(0), s_2(0), s_3(0)]^t \tag{4.7}$$

is the Stokes vector at $z = 0$, and $\phi(z)$ is the linear phase shift, which is given by

$$\phi(z) = \frac{2\pi z\Delta n}{\lambda_0}. \tag{4.8}$$

As we are assuming that signals are completely polarized, the Stokes vector is a unit

vector, i.e., $s_1^2 + s_2^2 + s_3^2 = 1$. The evolution of the SOP given by (4.4)–(4.6) can be represented explicitly as an unitary rotation on the Stokes space

$$\hat{s}(z) = \mathbf{M}(z)\hat{s}(0), \tag{4.9}$$

where the Mueller matrix $\mathbf{M}(z)$ is given by

$$\mathbf{M}(z) = \begin{bmatrix} 1 & 0 & 0 \\ 0 & \cos\phi(z) & \sin\phi(z) \\ 0 & -\sin\phi(z) & \cos\phi(z) \end{bmatrix}. \tag{4.10}$$

When a signal is propagated inside a fiber with constant birefringence, the respective Stokes vector $\hat{s}(z)$ depicts on the Poincaré sphere a rotation of the initial SOP over the axis $\hat{s}_1$ by an angle ϕ, given by (4.8) [43]. Note that the SOP is only maintained along the propagation when the input polarization is aligned with one of the principal axes, i.e., $s_1(0) = 1$ or $s_1(0) = -1$. On the other hand, we observe that $s_1(z)$ is constant along the propagation. That means that no power exchange between the two principal axes of the fiber is observed, which is a consequence of neglecting the nonlinear polarization rotation.

4.3 SOP Evolution and Degree of Co-polarization

The analysis of the evolution of the rSOP between two signals at wavelengths λ_s and λ_p, with polarizations $\hat{s}_s$ and $\hat{s}_p$, respectively, into a HiBi fiber, is performed considering two particular schemes for their input SOPs. These two cases are schematically represented in Fig. 4.1: a) In the parallel scheme, signals have the same polarization, with its ellipsis major axis making an angle $\theta/2$ with the slow axis, and ellipticity $\varepsilon/2$. b) In the orthogonal scheme, signals have orthogonal polarizations, with the ellipsis major axes making an angle $\theta/2$ with the slow and fast axis, and ellipticity $\varepsilon/2$. The respective Stokes vectors are

$$\hat{s}_{s,\parallel}(0) = \hat{s}_{p,\parallel}(0) = \begin{bmatrix} \cos\varepsilon\cos\theta \\ \cos\varepsilon\sin\theta \\ \sin\varepsilon \end{bmatrix}, \tag{4.11}$$

for the parallel case, and

$$\hat{s}_{s,\perp}(0) = -\hat{s}_{p,\perp}(0) = \begin{bmatrix} \cos\varepsilon\cos\theta \\ \cos\varepsilon\sin\theta \\ \sin\varepsilon \end{bmatrix}, \tag{4.12}$$

for the orthogonal case.

We define the degree of co-polarization between two optical signals inside an optical fiber as the mean value of the dot product of the respective Stokes vectors along the

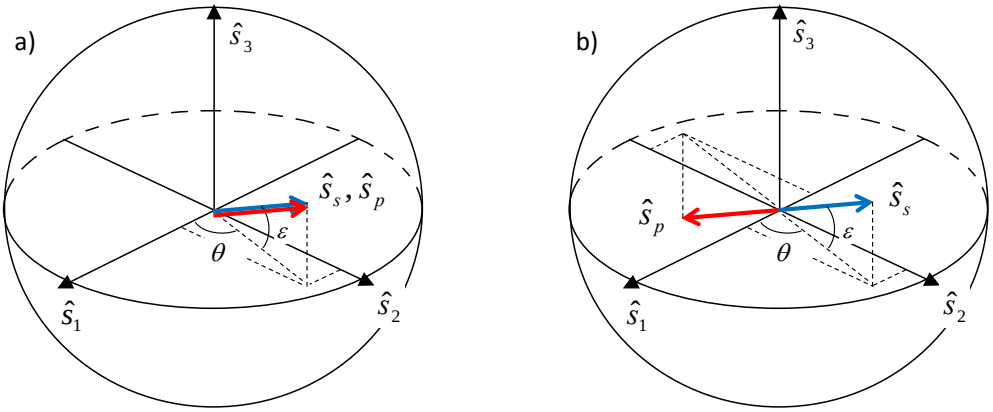

Figure 4.1: Poincaré sphere representation of the two considered schemes for the input SOPs used to calculate the degree of co-polarization into a HiBi fiber: a) – parallel scheme, the input SOPs $\hat{s}_p(0)$ and $\hat{s}_s(0)$ are parallel; b) – orthogonal scheme, the input SOPs $\hat{s}_p(0)$ and $\hat{s}_s(0)$ are orthogonal.

fiber length [44]. The dot product in the Stokes space has already been used elsewhere to quantify the efficiency of polarization-dependent effects [2]. Using this definition, the degree of co-polarization can be written as

$$f(\theta, \varepsilon, L) = \frac{1}{L} \int_0^L \hat{s}_s(z) \cdot \hat{s}_p(z) dz, \tag{4.13}$$

where L is the total propagation distance. With this definition, the function $f(\theta, \varepsilon, L)$ takes the value 1 when the two signals are always co-polarized, and -1 when the two signals remain always orthogonally polarized along the fiber propagation. Notice that the dot product of two orthogonal SOPs is equal to -1 in the Stokes space, in contrast with the 2D Jones space, where the result is by definition equal to 0 [41]. Assuming that the evolution of each signal is governed by (4.9), equation (4.13) can be defined in terms of the Mueller matrices and input SOPs for the parallel and orthogonal schemes presented in Fig. 4.1 as

$$f_{\parallel}(\theta, \varepsilon, L) = \frac{1}{L} \int_0^L \left[\mathbf{M}_s(z) \hat{s}_{s,\parallel}(0)\right] \cdot \left[\mathbf{M}_p(z) \hat{s}_{p,\parallel}(0)\right] dz, \tag{4.14}$$

and

$$f_{\perp}(\theta, \varepsilon, L) = \frac{1}{L} \int_0^L \left[\mathbf{M}_s(z) \hat{s}_{s,\perp}(0)\right] \cdot \left[\mathbf{M}_p(z) \hat{s}_{p,\perp}(0)\right] dz, \tag{4.15}$$

respectively, where the matrices $\mathbf{M}_s(z)$ and $\mathbf{M}_p(z)$ are obtained from (4.10) considering $\lambda_0 = \lambda_s$ and $\lambda_0 = \lambda_p$, respectively. Using (4.10)–(4.12) in (4.14) and (4.15), we obtain

the following equations

$$f_{\parallel}(\theta,\varepsilon,L) = \cos^2\theta\cos^2\varepsilon + (1-\cos^2\theta\cos^2\varepsilon)\frac{1}{L}\int_0^L [\cos\phi_p(z)\cos\phi_s(z)+\sin\phi_p(z)\sin\phi_s(z)]\,dz, \quad (4.16)$$

and

$$f_{\perp}(\theta,\varepsilon,L) = -\cos^2\theta\cos^2\varepsilon - (1-\cos^2\theta\cos^2\varepsilon)\frac{1}{L}\int_0^L [\cos\phi_p(z)\cos\phi_s(z)+\sin\phi_p(z)\sin\phi_s(z)]\,dz, \quad (4.17)$$

where phases $\phi_s(z)$ and $\phi_p(z)$ are obtained from (4.8) considering $\lambda_0 = \lambda_s$, and $\lambda_0 = \lambda_p$, respectively. Solving the integral present in (4.16) and (4.17), we obtain the following solutions for the degree of co-polarization [44, 45],

$$f_{\parallel}(\theta,\varepsilon,\psi) = \cos^2\theta\cos^2\varepsilon + (1-\cos^2\theta\cos^2\varepsilon)\frac{\sin\psi}{\psi}, \quad (4.18)$$

and

$$f_{\perp}(\theta,\varepsilon,\psi) = -\cos^2\theta\cos^2\varepsilon - (1-\cos^2\theta\cos^2\varepsilon)\frac{\sin\psi}{\psi}, \quad (4.19)$$

corresponding to the parallel and orthogonal schemes, respectively. The parameter ψ is a function of the signal wavelengths, the difference between the fast and slow refractive indices, and the fiber length,

$$\psi = \frac{2\pi\Delta n L(\lambda_s-\lambda_p)}{\lambda_s\lambda_p}. \quad (4.20)$$

Considering only linear input SOPs, i.e., making $\varepsilon = 0$, equations (4.18) and (4.19) can be rewritten as

$$f_{\parallel}(\theta,\psi) = \cos^2\theta + \sin^2\theta\frac{\sin\psi}{\psi}, \quad (4.21)$$

and

$$f_{\perp}(\theta,\psi) = -\cos^2\theta - \sin^2\theta\frac{\sin\psi}{\psi}, \quad (4.22)$$

respectively.

Figure 4.2 shows the evolution of the degree of co-polarization as a function of the angle θ and parameter ψ, considering different ellipticity values: a) $\varepsilon = 0$; b) $\varepsilon = \pi/8$; c) $\varepsilon = \pi/4$; d) $\varepsilon = 3\pi/8$; and e) $\varepsilon = \pi/2$. Both cases of parallel and orthogonal input SOPs are represented in each plot. Results reveal a strong dependence of the degree of co-polarization on the ellipticity of the input SOPs. Notice that the particular cases of

linear SOPs, i.e. $\varepsilon = 0$, and circular SOPs, i.e. $\varepsilon = \pi/2$ are represented in Fig. 4.2–a) and Fig. 4.2–e), respectively. For linear input SOPs, we observe that when signals are launched in the principal states of polarization (PSPs), i.e. when $\theta = 0$ or $\theta = \pi$, the degree of co-polarization is independent of ψ. That means that polarization is maintained along the propagation and therefore $f(\theta, \varepsilon = 0, \psi)$ takes the value equal to 1 for parallel case, and the value equal to -1 for the orthogonal case. Nevertheless, for ellipticity values higher than zero (see Figs. 4.2–b), 4.2–c), 4.2–d), and 4.2–e)), the degree of co-polarization of signals launched in the PSPs will decrease and increase for the parallel and orthogonal schemes, respectively. This occurs because elliptical signals have a non-zero projection on both principal fiber axes, making the SOPs to evolve along the fiber propagation.

We can also observe in Fig. 4.2 that increasing the SOP ellipticity of the input signals, the degree of co-polarization exhibit a smaller range of values as a function of the orientation of the input polarization. On the other hand, the regions for which the degree of co-polarization can assume considerable higher values in the orthogonal scheme, when compared with the parallel one, increase. Note that these regions are achieved for small values of ψ, corresponding to small fiber distances or narrow wavelength separations. In order to better understand this regime, we can rewrite equation (4.20) as

$$\psi \simeq \frac{2\pi \Delta n L \Delta\lambda}{\lambda_c^2}, \tag{4.23}$$

where $\Delta\lambda = \lambda_s - \lambda_p$ is the wavelength separation between the two signals, and

$$\lambda_c = \frac{\lambda_s + \lambda_p}{2} \approx \lambda_p, \lambda_s, \tag{4.24}$$

is a central wavelength. Figure 4.3 shows the degree of co-polarization as a function of the angle θ and the wavelength separation $\Delta\lambda$, assuming input signal with $\varepsilon = 0$ launched into an optical fiber with the following parameters: length equal to 100 m, $\Delta n = 4 \times 10^{-4}$, and $\lambda_c = 1550$ nm. These particular values correspond to the experimental conditions presented in Section 4.4, where a commercial HiBi fiber (CORNING PM DS 15-U40A) is used. In this particular example, we confirm the presence of several domains in the plane "$\Delta\lambda - \theta$", for which the orthogonal scheme case presents a higher degree of co-polarization. These domains are represented in Fig. 4.4, where the $\Delta\lambda$ axis was extended to 0.5 nm. A relation between θ and the general parameter ψ, for which $f_\perp(\theta, \psi) > f_\parallel(\theta, \psi)$, can be found using (4.21) and (4.22),

$$\tan\theta < \frac{\psi}{\sin\psi}. \tag{4.25}$$

The size of these domains decreases when the separation between signals increases. On the other hand, we observe that the domains periodicity is related with the set of the

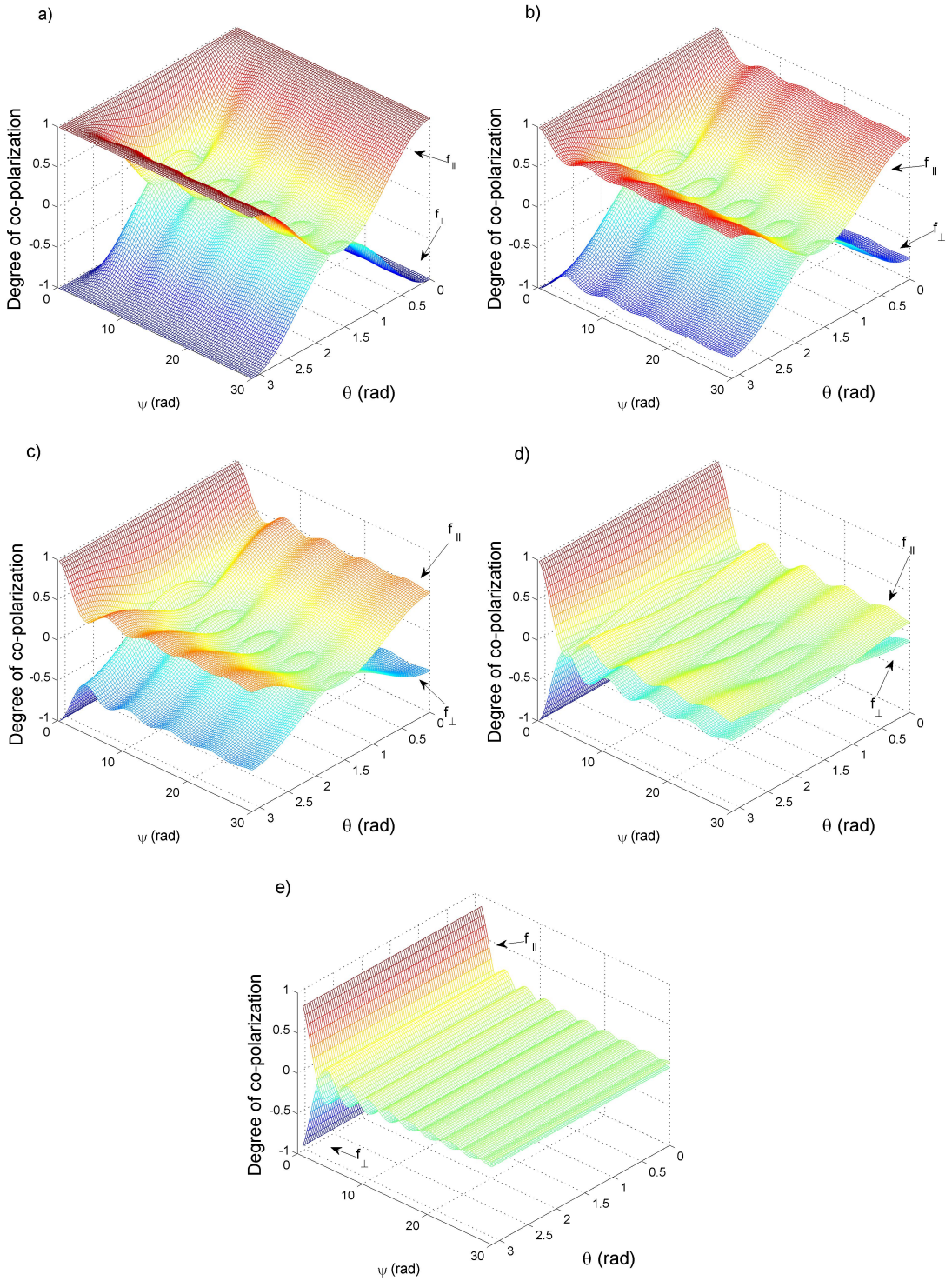

Figure 4.2: Degree of co-polarization as a function of the angle θ and parameter ψ, for different values of ellipticity: a) – $\varepsilon = 0$; b) – $\varepsilon = \pi/8$, c) – $\varepsilon = \pi/4$, d) – $\varepsilon = 3\pi/8$, e) – $\varepsilon = \pi/2$. Both parallel and orthogonal input SOP schemes are represented.

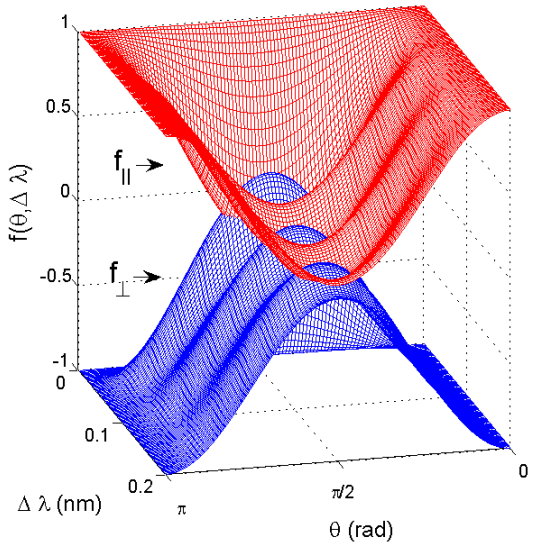

Figure 4.3: Degree of co-polarization between two signals when launched with parallel and orthogonal linear input SOPs ($\varepsilon = 0$), as a function of the input angle θ and the wavelength separation $\Delta\lambda$, for a HiBi fiber with length equal to 100 m, $\Delta n = 4 \times 10^{-4}$, and $\lambda_c = 1550$ nm.

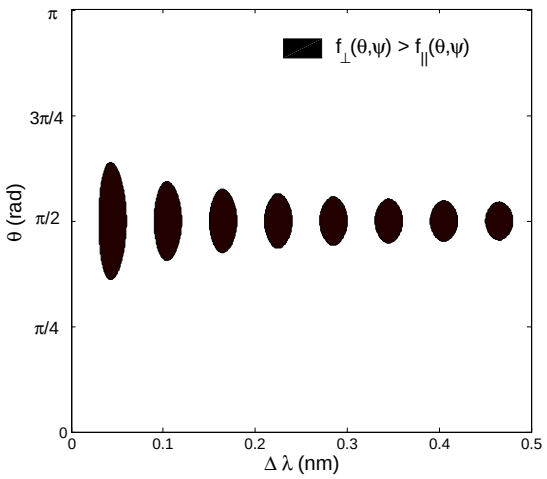

Figure 4.4: Domains in the plane "$\Delta\lambda - \theta$", for which the orthogonal case has a higher degree of co-polarization compared with the parallel one (see Fig. 4.3).

local extrema of the $\sin\psi/\psi$ function.

4.3.1 Long-Distance Limit

Results presented above (see Fig. 4.2) show that for high values of the parameter ψ the dependence of $f(\theta, \psi)$ on ψ decreases. In fact, considering the limit $\psi \to \infty$, equations (4.21) and (4.22) can be simplified. Note that in such limit the expression $\sin(\psi)/\psi$ will

vanish. Therefore, assuming $\psi \to \infty$, the degree of co-polarization expressions derived in the previous Section can be approximated by

$$f_{\parallel}(\theta, \varepsilon, \psi) \simeq f_{\parallel}(\theta, \varepsilon) = \cos^2\theta \cos^2\varepsilon, \tag{4.26}$$

for the parallel scheme, and by

$$f_{\perp}(\theta, \varepsilon, \psi) \simeq f_{\perp}(\theta, \varepsilon) = -\cos^2\theta \cos^2\varepsilon, \tag{4.27}$$

for the orthogonal scheme. These solutions show that in this limit the degree of co-polarization is only dependent on the input SOP. In the particular case of $\theta = \pi/2$, the degree of co-polarization will present the same value for both parallel and orthogonal input SOP schemes, i.e., $f_{\parallel}(\pi/2, \varepsilon) = f_{\perp}(\pi/2, \varepsilon) = 0$.

Using the definition of ψ given by (4.20), and assuming that $\psi \gg 1$, the regime for which (4.26) and (4.27) are valid can be explicitly defined as a function of the physical parameters as

$$L \gg \frac{L_{B,s} L_{B,p}}{2\pi(L_{B,s} - L_{B,p})}, \tag{4.28}$$

where $L_{B,s} = \lambda_s/\Delta n$ and $L_{B,p} = \lambda_p/\Delta n$ are the polarization beat lengths of the SOP for the wavelengths λ_s and λ_p, respectively.

Figure 4.5 shows the evolution of the degree of co-polarization with the distance for the case $\varepsilon = 0$ and $\theta = \pi/2$ rad, considering $\Delta n = 4 \times 10^{-4}$, and a wavelength separation $\Delta\lambda = 1.5$ nm (with $\lambda_c = 1550$ nm). For this particular case, the right hand side of (4.28) takes the value 0.64 m, which reveals that (4.26) and (4.27) start to become valid for relatively small fiber distances. In fact, the curves depicted in Fig. 4.5 show that, for fiber lengths longer than 13 m, the degree of co-polarization oscillates around zero with amplitudes lower than 5% of the absolute maximum value. Results also show that the two first distance ranges for which the degree of co-polarization in the orthogonal scheme is higher than the parallel scheme are from 2 to 4 meters and from 6 to 8 meters (see Fig. 4.5). In these two domains the degree of co-polarization for the orthogonal (parallel) schemes takes the maximum (minimum) values of 0.21 (-0.21) and 0.09 (-0.09). For the general case, the m^{th} domain can be found making $\sin\psi = 0$, which gives

$$L \in \left[(2m-1)\frac{\lambda_c^2}{2\Delta\lambda\Delta n} \,;\, (2m)\frac{\lambda_c^2}{2\Delta\lambda\Delta n} \right], \tag{4.29}$$

with m =1,2,3...

4.3.2 Empirical Analysis of the Long-Distance Limit

The long-distance analysis of the rSOP between two signals inside a HiBi fiber can be analyzed empirically using the evolution in the Poincaré sphere surface of the two Stokes

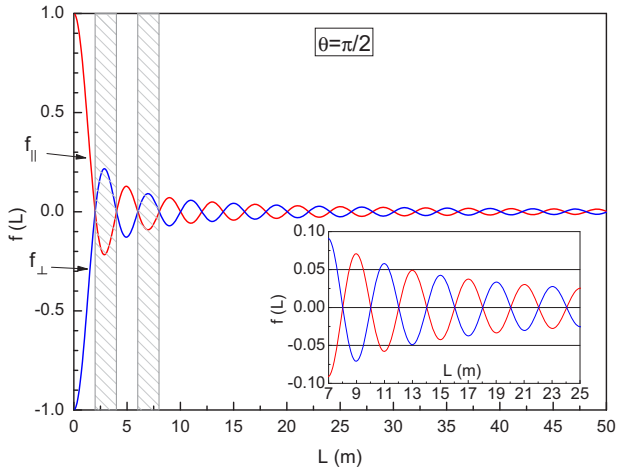

Figure 4.5: Degree of co-polarization as a function of the fiber length L, considering $\varepsilon = 0$, $\theta = \pi/2$ rad, and $\Delta\lambda = 1.5$ nm. Inset shows that for fiber lengths longer than 13 m the degree of co-polarization oscillates around zero, with amplitudes lower than 5% of the maximum value. Patterns show the two first distance ranges, $L \in [2; 4]$ and $[6; 8]$, for which $f_{\perp}(\theta = \pi/2, \varepsilon = 0, L) > f_{\parallel}(\theta = \pi/2, \varepsilon = 0, L)$.

vectors, $\hat{s}_p(z)$ and $\hat{s}_s(z)$. As presented in Section 4.2, the evolution of the SOP into a HiBi fiber depicts on the Poincaré sphere a rotation of the initial SOP over the axis $\hat{s}_1$ by an angle ϕ. That means that when (4.28) is satisfied, the two Stokes vectors perform a large number of rotations on the Poincaré sphere. In such case, the degree of co-polarization given by (4.26) and (4.27) can be obtained by the average of the *best* and *worst* orientations of the two vectors, i.e. the average of the higher and the smaller values of the dot product between $\hat{s}_p(z)$ and $\hat{s}_s(z)$,

$$\mathfrak{f}(\theta, \varepsilon) = \frac{1}{2}\left(\hat{s}_p(0) \cdot \hat{s}_s^{+} + \hat{s}_p(0) \cdot \hat{s}_s^{-}\right), \tag{4.30}$$

where $\hat{s}_s^{+}$ and $\hat{s}_s^{-}$ are the *best* and *worst* SOPs for the signal λ_s, given an initial SOP $\hat{s}_p(0)$ for the signal λ_p.

These two scenarios are schematically represented in Fig. 4.6, considering $\varepsilon = 0$. In the case of parallel input SOPs, see Fig. 4.6 a), the *best* case occurs when the two SOPs coincide, and the *worst* case occurs when the angle between $\hat{s}_p(z)$ and $\hat{s}_s(z)$ is equal to 2θ. Using (4.30), the degree of co-polarization for the parallel scheme can therefore be written as

$$\mathfrak{f}_{\parallel}(\theta, \varepsilon) = \frac{1}{2}\left(\begin{bmatrix} \cos\varepsilon\cos\theta \\ \cos\varepsilon\sin\theta \\ \sin\varepsilon \end{bmatrix}^{t} \begin{bmatrix} \cos\varepsilon\cos\theta \\ \cos\varepsilon\sin\theta \\ \sin\varepsilon \end{bmatrix} + \begin{bmatrix} \cos\varepsilon\cos\theta \\ \cos\varepsilon\sin\theta \\ \sin\varepsilon \end{bmatrix}^{t} \begin{bmatrix} \cos\varepsilon\cos\theta \\ -\cos\varepsilon\sin\theta \\ -\sin\varepsilon \end{bmatrix}\right), \tag{4.31}$$

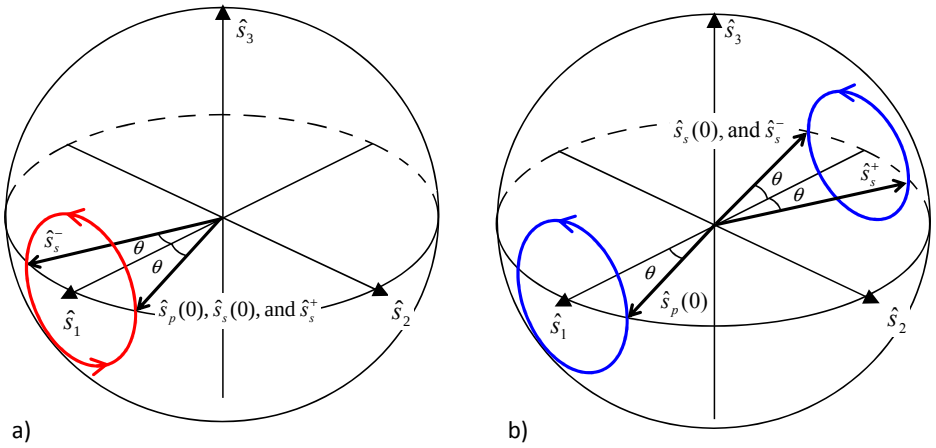

Figure 4.6: 3D Stokes space representation of the SOP evolution in the Poincaré sphere. The *best* and *worst* SOPs, $\hat{s}_s^+$ and $\hat{s}_s^-$, respectively, are represented for the a) – parallel and b) – orthogonal SOP schemes.

which gives

$$\mathfrak{f}_{\parallel}(\theta,\varepsilon) = \cos^2\theta\cos^2\varepsilon. \tag{4.32}$$

In the case of the orthogonal input SOPs, see Fig. 4.6 b), the *best* case occurs when the angle, in the Stokes space, between $\hat{s}_s(z)$ and $\hat{s}_p(z)$ is minimum, i.e. equal to the difference $\pi-2\theta$, and the *worst* case occurs when the $\hat{s}_s(z)$ and $\hat{s}_p(z)$ vectors have opposite orientations in the sphere. Therefore, the degree of co-polarization for the orthogonal scheme can be written as

$$\mathfrak{f}_{\perp}(\theta,\varepsilon) = \frac{1}{2}\left(\begin{bmatrix}\cos\varepsilon\cos\theta\\ \cos\varepsilon\sin\theta\\ \sin\varepsilon\end{bmatrix}^t\begin{bmatrix}-\cos\varepsilon\cos\theta\\ \cos\varepsilon\sin\theta\\ \sin\varepsilon\end{bmatrix} + \begin{bmatrix}\cos\varepsilon\cos\theta\\ \cos\varepsilon\sin\theta\\ \sin\varepsilon\end{bmatrix}^t\begin{bmatrix}-\cos\varepsilon\cos\theta\\ -\cos\varepsilon\sin\theta\\ -\sin\varepsilon\end{bmatrix}\right), \tag{4.33}$$

which gives

$$\mathfrak{f}_{\perp}(\theta,\varepsilon) = -\cos^2\theta\cos^2\varepsilon. \tag{4.34}$$

These results show that the empirical solutions, given by (4.32) and (4.34), coincide with the analytical solutions for the degree of co-polarization when the fiber length is much longer than the beating length between the SOPs of the two signals present in the fiber, i.e. when (4.28) is verified. Note that in the particular case $\theta=\pi/2$, for which the parallel and orthogonal schemes present the same degree of polarization, the Stokes vectors rotate in the "s_2-s_3" plane and therefore the *best* and *worst* cases for the parallel and orthogonal schemes coincide.

4.4 Degree of Co-Polarization and FWM Effect in HiBi Fibers

In this Section we use the FWM effect to validate our model for the degree of co-polarization. Experiments are based on the power measurements of two new waves generated by FWM as a function of the input SOP angle (with $\varepsilon = 0$). In order to generate measurable optical powers through FWM considering our experimental devices and fiber characteristics we cannot decrease the length of the fiber below to 100 m. This means that if we aim to validate the degree of co-polarization model in the short-distance regime we should be able to reduce the wavelength separation between signals. According with results presented in Figs. 4.3 and 4.4, for fiber lengths of 100 m we will need signal wavelengths separations shorter than 0.2 nm. Nevertheless, for these wavelength separations the new waves will be overlapped by the background spectra of our lasers (see Fig. 4.8). Therefore, the validation presented here refers only to the long-distance regime.

As aforementioned in Section 4.2, the model for the degree of co-polarization presented here neglects polarization changes due to nonlinear birefringence. In order to validate the use of such approach we can calculate the nonlinear phase shift contribution corresponding to the experimental conditions presented in this Section. Assuming the case of CW signals in a non-dispersive medium, the highest relative nonlinear phase shift between the two polarization components of signal propagated into a HiBi fiber is $\Delta\phi_{\mathrm{NL}} = \gamma P_0 L_{\mathrm{eff}}/3$ [25], where γ is the nonlinear coefficient, L_{eff} is the effective length and P_0 is the power of the CW signal launched into the fiber. Using the fiber parameters and the highest pump power value presented below, see Subsection 4.4.2, we find that $\Delta\phi_{\mathrm{NL}} \approx 4.0 \times 10^{-4}$ rad $\ll \pi$. This value shows a weak contribution of the nonlinear birefringence to the total phase shift, and assures that the linear birefringence approximation is valid in the experimental conditions used to test our theoretical model.

4.4.1 FWM Theory

The efficiency of the FWM process is highly dependent on the rSOP between the signals [2, 4, 25, 46]. The best efficiency is obtained when signals propagate with parallel SOPs, and the worst efficiency is obtained when signals propagate with orthogonal SOPs.

When two pumps are launched into the fiber, two new waves are generated through multiple FWM processes [25, 47–49]. Basically, these two new waves are related with three different FWM processes: two degenerate processes and one non-degenerate process [47]. Assuming that pumps have frequencies ω_p and ω_s, the frequency of the new waves are determined by the degenerate FWM processes,

$$2\omega_p \rightarrow \omega_s + \omega_4 \tag{4.35}$$

and

$$2\omega_s \rightarrow \omega_p + \omega_3. \tag{4.36}$$

In the first case, two photons of the first pump are used to generate one photon at the frequency of the second pump, ω_s, and another photon at the new frequency ω_4. In the second case, two photons of the second pump are used to generate one photon at the frequency of the first pump, ω_p, and another at the new frequency ω_3. The presence of the new waves in the fiber will stimulate a non-degenerate FWM process involving the two pumps: in this case, two photons, one from each pump, are combined to produce two photons at the new frequencies,

$$\omega_p + \omega_s \rightarrow \omega_3 + \omega_4. \tag{4.37}$$

The new wave generated at ω_3 will have a component polarized along the axis x, and another polarized along the axis y. Assuming that the waves at ω_p and ω_s have similar low powers (few miliwatts) and components polarized along the axis x, then the power of the new wave at ω_3 polarized along x is given by [32–34]

$$P_{3,x}(z) = \gamma^2 P_{p,x} P_{s,x}^2 \left(\frac{\sin(\delta z)}{\delta} \right)^2, \tag{4.38}$$

with

$$\delta = \frac{\beta(\omega_p) - 2\beta(\omega_s) + \beta(\omega_3) + \gamma(2P_{s,x} - P_{p,x})}{2}, \tag{4.39}$$

where γ is the nonlinear coefficient, $\beta(\omega_i)$ is the propagation constant at the frequency ω_i, and $P_{s,x}$ and $P_{p,x}$ are the input pump powers polarized along the x axis at the frequencies ω_s and ω_p, respectively. The power of the new wave at ω_4 can be obtained from (4.38) interchanging the subscripts s and p. Note that the total power at the new frequencies comprises the individual powers generated in both x and y axes, $P_3 = P_{3,x} + P_{3,y}$.

The input pump powers on the x and y axes, $P_{i,x}$ and $P_{i,y}$ (with $i = p, s$), are related with the total input pump power P_i through the angle between the input linear SOPs and the principal axes of the fiber $\theta/2$. Notice that we are only considering linear input SOPs, i.e., $\varepsilon = 0$ in (4.11) and (4.12). We obtain the relations

$$P_{p,x}(\theta) = P_p \cos^2\left(\frac{\theta}{2}\right), \tag{4.40}$$

$$P_{p,y}(\theta) = P_p \sin^2\left(\frac{\theta}{2}\right), \tag{4.41}$$

$$P_{s,x}(\theta) = P_s \cos^2\left(\frac{\theta}{2}\right), \tag{4.42}$$

$$P_{s,y}(\theta) = P_s \sin^2\left(\frac{\theta}{2}\right), \tag{4.43}$$

for the parallel scheme represented in Fig. 4.1 a), and the relations

$$P_{p,x}(\theta) = P_p \cos^2\left(\frac{\theta}{2}\right), \tag{4.44}$$

$$P_{p,y}(\theta) = P_p \sin^2\left(\frac{\theta}{2}\right), \tag{4.45}$$

$$P_{s,x}(\theta) = P_s \sin^2\left(\frac{\theta}{2}\right), \tag{4.46}$$

$$P_{s,y}(\theta) = P_s \cos^2\left(\frac{\theta}{2}\right), \tag{4.47}$$

for the orthogonal scheme represented in Fig. 4.1 b). The theoretical curves for the total power of new waves at ω_3 and ω_4 are compared with experimental results in Subsection 4.4.3. The dependence on the input SOP angle $\theta/2$ is explored for both parallel and orthogonal input SOP schemes.

4.4.2 Experimental Setup

The experimental setups used to perform the FWM measurements in the orthogonal and parallel schemes are schematically represented in Fig. 4.7–a) and 4.7–b), respectively. Two CW signals, at wavelengths $\lambda_p = 1549.32$ nm and $\lambda_s = 1550.91$ nm, are launched into a dispersion-shifted HiBi fiber, with parallel or orthogonal linear SOPs. The dispersion-shifted HiBi fiber has a length equal to 100 m, a minimum of chromatic dispersion at 1550 nm, a polarization beat length (at 1550 nm) equal to 3.8 mm, a nonlinear coefficient equal to 4.75 $W^{-1}km^{-1}$ and an attenuation coefficient equal to 0.5 dB/km.

In the parallel scheme, see Fig. 4.7–a), signals are made to pass through a polarization controller (PC) before being coupled at the optical multiplexer (MUX). The two PCs are used in order align both SOPs with the linear polarizer. A PMF is placed at the inline linear polarizer output in order to assure that the two signals are launched with parallel SOPs into the HiBi fiber. The angle between the linear SOPs and the slow axis of the fiber is tuned using a graduated rotatable key connector.

In the orthogonal scheme, see Fig. 4.7–b), signals are made to pass through a PC before being coupled at the polarization beam splitter (PBS). In this case, the two PCs align the SOPs with the two input ports of the PBS. At the PBS output, signals have orthogonal SOPs (whose stability is assured through a PMF connecting the PBS to the rotatable key connector), and the angle between the two linear SOPs and the slow and fast fiber axes is tuned using a graduated rotatable key connector. An optical spectrum analyzer (OSA) is used to measure the spectra of the new generated signals.

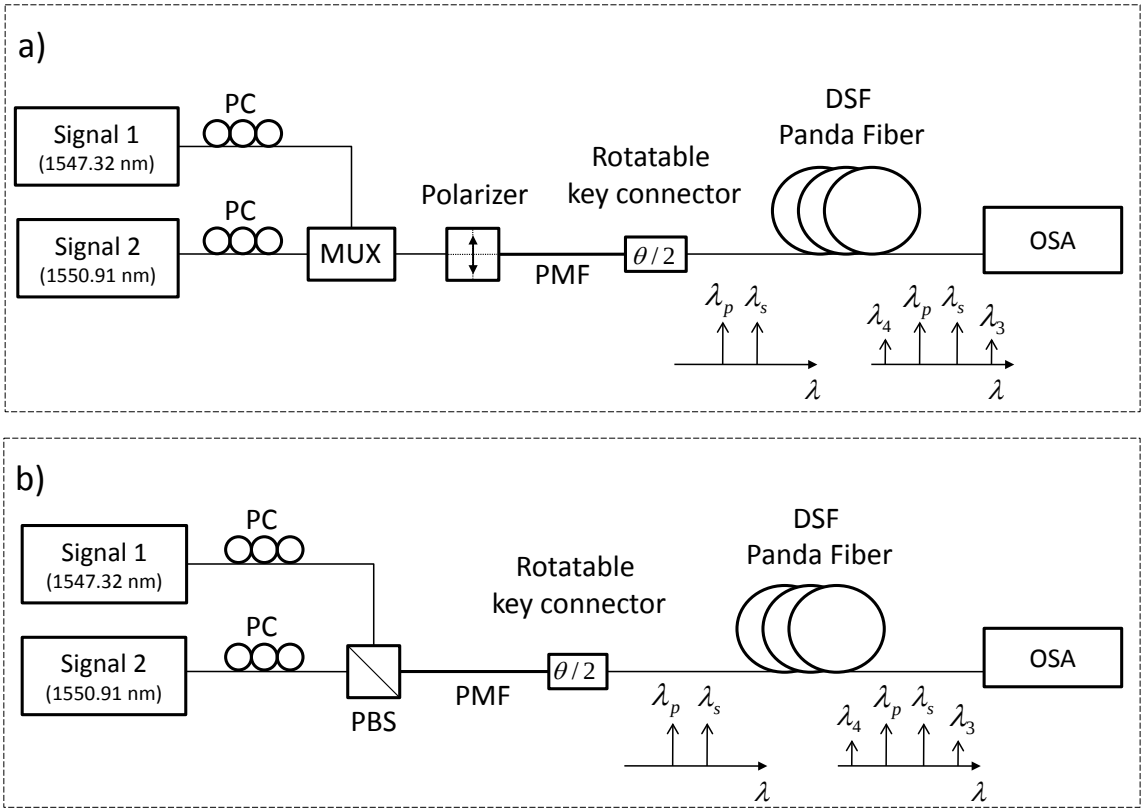

Figure 4.7: Experimental setups used to measure the power of the new waves generated into a dispersion-shifted HiBi fiber through FWM process. a) – Parallel scheme: the two input signals are combined by a MUX and made pass through a linear polarizer. b) – Orthogonal scheme: the two input signals are combined into a PBS. In both cases, the angle between the linear SOP and the slow axis of the fiber is tuned using a graduated rotatable key connector. Signals are detected in an optical spectrum analyzer (OSA).

4.4.3 Experimental Results

Since the efficiency of the FWM process depends on the rSOP, the power of the new waves at wavelengths λ_3 and λ_4 will be related with the adjustable angle $\theta/2$. Figure 4.8 shows four particular spectra obtained for the parallel and orthogonal schemes at angles $\theta/2$ equal to 0° and 45° (graphics up and down, respectively), with pump powers equal to $P_p = 2.36$ dBm and $P_s = 4.50$ dBm.

As expected by FWM theory presented above, two new waves are created at wavelengths $\lambda_4 = 1547.71$ nm and $\lambda_3 = 1552.52$ nm. The spectra show that for $\theta/2 = 0°$, the new waves are only present in the parallel scheme, see inset Fig. 4.8-up), while for $\theta/2 = 45°$ the new waves at λ_3 and λ_4 have similar powers in the parallel and orthogonal schemes, see inset Fig. 4.8-down). This result agrees with the model presented in Section 4.3 since for a long-distances regime, i.e. when (4.28) is verified, it predicts that for $\theta/2 = 45°$ the signals have the same degree of co-polarization, either when they are launched into the fiber with orthogonal or parallel SOPs. For $\theta/2 = 0°$, the signals are

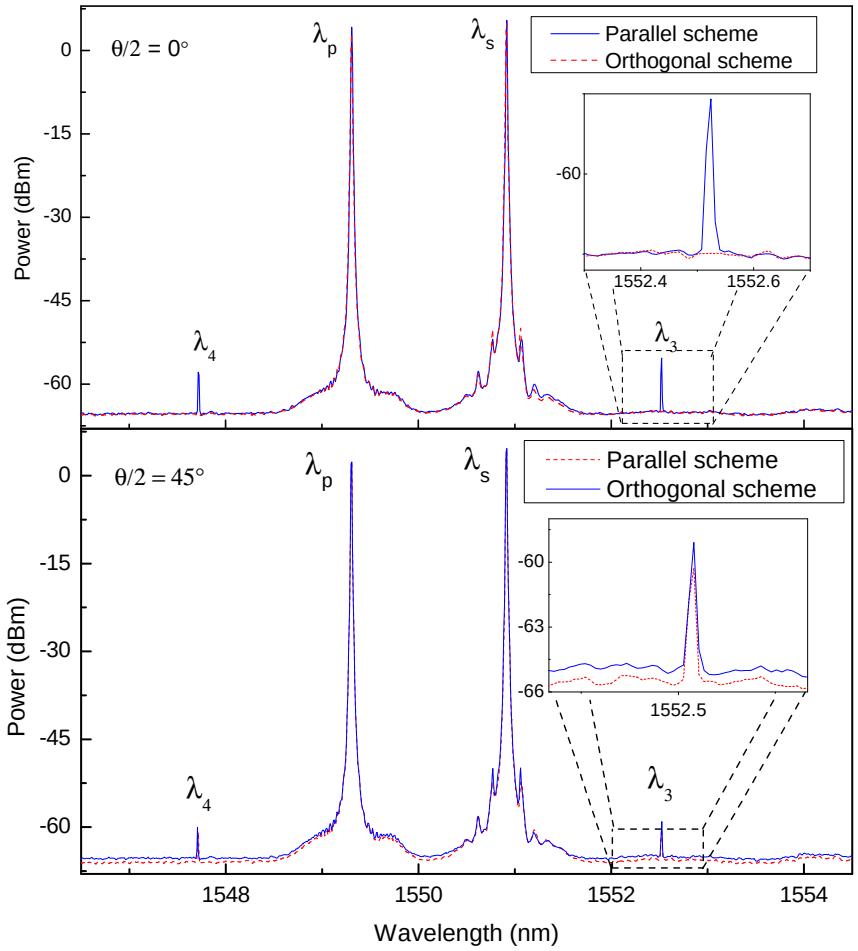

Figure 4.8: Experimental spectra of the new waves λ_3 and λ_4 generated through FWM effect into a dispersion-shifted HiBi fiber, obtained for the parallel and orthogonal schemes. Pump powers equal to $P_p = 2.36$ dBm and $P_s = 4.50$ dBm and angles between the input linear SOPs and PSPs equal to 0° and 45° (up and down, respectively). Inset shows the power of the new wave at wavelength λ_3 for both schemes.

propagated along the principal axis of the fiber, which means that the new waves will be generated with a maximum of efficiency in the parallel scheme, and with a minimum of efficiency in the orthogonal scheme.

The power of the new wavelengths, P_3 and P_4, were measured for different angles of the linear input SOPs. These experimental results are represented in Fig. 4.9–b) as symbols. We observe that the signal at λ_3 presents slightly higher power values with respect to λ_4 for the two polarization schemes. This behavior is related with the different input pump powers, P_p and P_s. The experimental values obtained for the power of the new waves, P_3 and P_4, are in good agreement with FWM theory given by (4.38), and represented in Fig. 4.9–b) as lines. Results also show that the variations of P_3 and P_4 with the input angle are strongly correlated with the degree of co-polarization, $f_{\|}(\theta, \varepsilon = 0)$

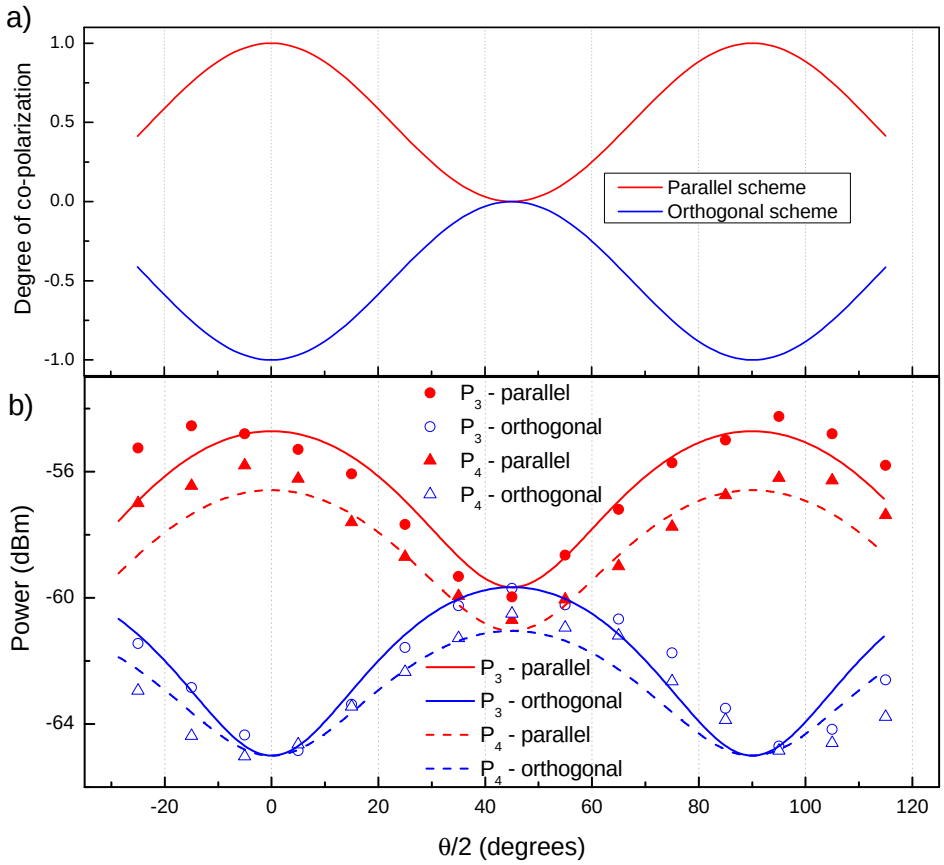

Figure 4.9: a) – Degree of co-polarization, $f_{\parallel}(\theta)$ and $f_{\perp}(\theta)$, as a function of the input linear SOP angle, $\theta/2$, for both the parallel and orthogonal schemes. b) – Power of the new waves at λ_3 and λ_4 generated by FWM, as a function of the input linear SOP angle, $\theta/2$, for both the parallel and orthogonal schemes: experimental data are represented as solid and empty symbols (parallel and orthogonal schemes, respectively), whereas theoretical FWM results are represented as solid and dashed lines (P_3 e P_4, respectively).

and $f_{\perp}(\theta, \varepsilon = 0)$, given by (4.26) and (4.27), respectively, and graphically represented in Fig. 4.9–a). For $\theta/2 = 0$ the signals are launched in the PSPs and propagate always parallel, in the parallel scheme, or always orthogonal, in the orthogonal scheme. This angle corresponds to the maximum and minimum power of the new waves for the parallel and orthogonal cases, respectively. In the orthogonal case, the minimum values of P_3 and P_4 are coincident with the OSA background level, whose value was added to theoretical curves represented in Fig. 4.9–b). With the increase of $\theta/2$, the two degrees of co-polarization approaches zero and, for $\theta/2 = 45^{\circ}$, the degree of co-polarization for both schemes is equal to zero ($f_{\parallel}(90^{\circ}, \varepsilon = 0) = f_{\perp}(90^{\circ}, \varepsilon = 0) = 0$). At this particular input angle, the power of the new waves are similar in both parallel and orthogonal schemes. For $\theta/2 = 90^{\circ}$, signals are launched again into the PSPs, with the slow and fast axes exchanged, and the results are similar to those obtained for $\theta/2 = 0^{\circ}$.

4.5 Summary

We have developed an analytical model that accurately describes the degree of co-polarization between two signals copropagating inside a HiBi fiber. We found that the degree of co-polarization for parallel and orthogonal input SOPs is described by symmetrical expressions. We also showed that for small fiber lengths or narrow wavelength separations, launching two signals into a HiBi fiber with orthogonal polarizations can result in a higher degree of co-polarization when compared with the input of parallel SOPs scheme.

On the other hand, a long-distance regime for which the degree of co-polarization for the parallel scheme is always equal or higher than that presented by the orthogonal case was identified. For waves propagating in this regime, the degree of co-polarization becomes only dependent on the angle of the input SOPs.

We have also experimentally validated our theoretical model in the long-distance regime using linear input SOPs for both parallel and orthogonal schemes. The measurements on the efficiency of the FWM process in a dispersion-shifted HiBi fiber, showed that our model is able to describe the power of the new waves as a function of the initial SOP angles.

With the recent developments on photonic crystal fibers, some new characteristics, such as highly nonlinear performance or optimized dispersion properties, become available. The results presented in this Chapter can be used in order to accurately understand the behavior of some polarization dependent physical effects in this kind of fibers. In particular, they could lead to implementation and optimization of new all-optical signal processing devices involving more than one signal.

References

[1] G. P. Agrawal, *Applications of Nonlinear Fiber Optics.* Academic Press, San Diego, USA, 2002.

[2] Q. Lin and G. P. Agrawal, "Vector theory of four-wave mixing: polarization effects in fiber-optic parametric amplifiers," *J. Opt. Soc. Am. B*, vol. 21, pp. 1216–1224, Jun. 2004.

[3] N. J. Muga, M. C. Fugihara, Mário F. S. Ferreira, and A. N. Pinto, "Non-Gaussian ASE noise in Raman amplification systems," *IEEE/OSA J. Lightwave Technol.*, vol. 27, no. 16, pp. 3389–3398, 2009.

[4] N. A. Silva, N. J. Muga, and A. N. Pinto, "Influence of the stimulated Raman scattering on the four-wave mixing process in birefringent fibers," *IEEE/OSA J. Lightwave Technol.*, vol. 27, no. 22, pp. 4979–4988, Nov. 2009.

[5] R. Ulrich, "Polarization stabilization on single-mode fibers," *Appl. Phys. Lett.*, vol. 35, no. 11, pp. 840–842, 1979.

[6] C. D. Poole, N. S. Bergano, and R. E. Wagner, "Polarization dispersion and principal states in a 147-km undersea lightwave cable," *IEEE/OSA J. Lightwave Technol.*, vol. 6, no. 7, pp. 1185–1190, 1988.

[7] P. K. A. Wai and C. R. Menyuk, "Polarization mode dispersion, decorrelation, and diffusion in optical fibers with randomly varying birefringence," *IEEE/OSA J. Lightwave Technol.*, vol. 14, no. 2, pp. 148–157, 1996.

[8] C. D. Poole and J. Nagel, *Polarization effects in lightwave systems - Optical Fiber Telecommunications.* Academic Press, San Diego, 1997, vol. IIIa, ch. 6, pp. 114–161.

[9] J. Noda, K. Okamoto, and Y. Sasaki, "Polarization-maintaining fibers and their applications," *IEEE/OSA J. Lightwave Technol.*, vol. 4, no. 8, pp. 1071–1089, Aug. 1986.

[10] S. Rashleigh, "Origins and control of polarization effects in single-mode fibers," *IEEE/OSA J. Lightwave Technol.*, vol. 1, no. 2, pp. 312–331, Jun. 1983.

[11] I. Abe, H. J. Kalinowski, O. Frazão, J. L. Santos, R. N. Nogueira, and J. L. Pinto, "Superimposed Bragg gratings in high-birefringence fibre optics: three-parameter simultaneous measurements," *Meas. Sci. Technol.*, vol. 15, pp. 1453–1457, 2004.

[12] P. Westbrook, K. Feder, P. Reyes, P. Steinvurzel, B. Eggleton, R. Ernst, L. Reith, and D. Gill, "Application of fiber Bragg grating filter/tap module to a wavelength-locked low-chirp directly-modulated 10 Gb/s RZ transmitter," in *Optical Fiber Communication Conference and Exhibit, 2002. OFC 2002*, Mar. 2002, pp. 680–682.

[13] S. Lee, R. Khosravani, J. Peng, V. Grubsky, D. Starodubov, A. Willner, and J. Feinberg, "Adjustable compensation of polarization mode dispersion using a high-birefringence nonlinearly chirped fiber Bragg grating," *IEEE Photonics Technol. Lett.*, vol. 11, no. 10, pp. 1277–1279, Oct. 1999.

[14] X. Dong, N. Ngo, P. Shum, J. H. Ng, X. Yang, G. Ning, and C. Lu, "Tunable compensation of first-order PMD using a high-birefringence linearly chirped fiber Bragg grating," *IEEE Photonics Technol. Lett.*, vol. 16, no. 3, pp. 846–848, Mar. 2004.

[15] M. Ferreira, A. Pinto, P. André, N. Muga, J. Machado, R. Nogueira, S. Latas, and J. da Rocha, "Polarization mode dispersion in high-speed optical communication systems," *Fiber Integrated Opt.*, vol. 24, pp. 261–285, 2005.

[16] R. Nogueira, A. Teixeira, J. Pinto, and J. Rocha, "Polarization-assisted OCDMA using fiber bragg gratings written in highly birefringent fibers," *IEEE Photonics Technol. Lett.*, vol. 18, no. 7, pp. 841–843, Jan. 2006.

[17] Y. K. Lizé, L. Palmer, N. Godbout, S. Lacroix, and R. Kashyap, "Scalable polarization-mode dispersion emulator with proper first- and second-order statistics," *IEEE Photonics Technol. Lett.*, vol. 17, no. 11, pp. 2451–2453, 2005.

[18] N. J. Muga, A. N. Pinto, and M. Ferreira, "The development of a PMD emulator," in *ConfTele 2005, Tomar*, 2005.

[19] N. J. Muga, A. N. Pinto, M. Ferreira, and J. R. F. da Rocha, "Uniform polarization scattering with fiber-coil based polarization controllers," *IEEE/OSA J. Lightwave Technol.*, vol. 24, no. 11, pp. 3932–3943, 2006.

[20] F. Yaman, Q. Lin, and G. Agrawal, "A novel design for polarization-independent single-pump fiber-optic parametric amplifiers," *IEEE Photonics Technol. Lett.*, vol. 18, no. 22, pp. 2335–2337, Nov. 2006.

[21] X. Li, P. L. Voss, J. E. Sharping, and P. Kumar, "Optical-Fiber Source of Polarization-Entangled Photons in the 1550 nm Telecom Band," *Phys. Rev. Lett.*, vol. 94, no. 5, p. 053601, Feb. 2005.

[22] Á. J. Almeida, S. R. Carneiro, N. A. Silva, N. J. Muga, and A. N. Pinto, "Polarization-entangled photon pairs using spontaneous four-wave mixing in a fiber loop," in *EUROCON2011 & CONFTELE2011, Lisbon, Portugal*, 2011.

[23] H. G. Winful, "Self-induced polarization changes in birefringent optical fibers," *Appl. Phys. Lett.*, vol. 47, no. 3, pp. 213–215, 1985.

[24] S. Wabnitz, "Spatial chaos in the polarization for a birefringent optical fiber with periodic coupling," *Phys. Rev. Lett.*, vol. 58, no. 14, pp. 1415–1418, Apr. 1987.

[25] G. P. Agrawal, *Nonlinear Fiber Optics, 4rd ed.* Academic Press, San Diego, USA, 2007.

[26] V. Kermène, M. Flores-Arias, J. Ares, A. Desfarges-Berthelemot, and A. Barthélémy, "Nonlinear polarization evolution: a numerical study of the coupling between main linear normal modes," *Opt. Commun.*, vol. 247, no. 1-3, pp. 195–203, 2005.

[27] Y. Barad and Y. Silberberg, "Polarization evolution and polarization instability of solitons in a birefringent optical fiber," *Phys. Rev. Lett.*, vol. 78, no. 17, pp. 3290–3293, Apr. 1997.

[28] N. Imoto, N. Yoshizawa, J. Sakai, and H. Tsuchiya, "Birefringence in single-mode optical fiber due to elliptical core deformation and stress anisotropy," *IEEE J. Quantum Electron.*, vol. 16, no. 11, pp. 1267–1271, Nov. 1980.

[29] I. P. Kaminow, "Polarization in optical fibers," *Quantum Electron.*, vol. 17, pp. 15–22, 1981.

[30] D. Payne, A. Barlow, and J. Hansen, "Development of low- and high-birefringence optical fibers," *IEEE J. Quantum Electron.*, vol. 18, no. 4, pp. 477–488, Apr. 1982.

[31] C. Menyuk, "Nonlinear pulse propagation in birefringent optical fibers," *IEEE J. Quantum Electron.*, vol. 23, no. 2, pp. 174–176, Feb. 1987.

[32] C. McKinstrie, H. Kogelnik, R. Jopson, S. Radic, and A. Kanaev, "Four-wave mixing in fibers with random birefringence," *Opt. Express*, vol. 12, no. 10, pp. 2033–2055, 2004.

[33] C. J. McKinstrie, H. Kogelnik, and L. Schenato, "Four-wave mixing in a rapidly-spun fiber," *Opt. Express*, vol. 14, no. 19, pp. 8516–8534, 2006.

[34] C. J. McKinstrie, S. Radic, and C. Xie, "Phase conjugation driven by orthogonal pump waves in birefringent fibers," *J. Opt. Soc. Am. B*, vol. 20, no. 7, pp. 1437–1446, 2003.

[35] K. Inoue, "Polarization effect on four-wave mixing efficiency in a single-mode fiber," *IEEE J. Quantum Electron.*, vol. 28, no. 4, pp. 883–894, Apr. 1992.

[36] P. Morgan and J. Liu, "Parametric four-photon mixing followed by stimulated Raman scattering with optical pulses in birefringent optical fibers," *IEEE J. Quantum Electron.*, vol. 27, no. 4, pp. 1011–1021, Apr. 1991.

[37] S. Trillo and S. Wabnitz, "Parametric and Raman amplification in birefringent fibers," *J. Opt. Soc. Am. B*, vol. 9, no. 7, pp. 1061–1082, 1992.

[38] K. Wong, M. Marhic, K. Uesaka, and L. Kazovsky, "Polarization-independent two-pump fiber optical parametric amplifier," *IEEE Photonics Technol. Lett.*, vol. 14, no. 7, pp. 911–913, Jul. 2002.

[39] B. Crosignani, S. Piazzolla, P. Spano, and P. D. Porto, "Direct measurement of the nonlinear phase shift between the orthogonally polarized states of a single-mode fiber," *Opt. Lett.*, vol. 10, no. 2, pp. 89–91, 1985.

[40] Q. Lin and G. Agrawal, "Vector theory of cross-phase modulation: role of nonlinear polarization rotation," *IEEE J. Quantum Electron.*, vol. 40, no. 7, pp. 958–964, Jul. 2004.

[41] J. P. Gordon and H. Kogelnik, "PMD fundamentals: Polarization mode dispersion in optical fibers," *PNAS*, vol. 97, no. 9, pp. 4541–4550, 2000.

[42] J. N. Damask, *Polarization optics in telecomunications.* Springer, New York, EUA, 2005.

[43] D. Goldstein, *Polarized Light, Second edition.* CRC Press, New York, EUA, 2003.

[44] N. J. Muga, N. A. Silva, M. Ferreira, and A. N. Pinto, "Evolution of the degree of co-polarization in high-birefringence fibers," *Opt. Commun.*, vol. 283, no. 10, pp. 2125–2132, 2010.

[45] N. J. Muga, N. A. Silva, M. Ferreira, and A. N. Pinto, "Generalized analysis of the polarization evolution in high-birefringence fibers," in *Proc International Conf. on Transparent Networks – ICTON*, vol. Mo.P.2, Munich, Germany, Jun. 2010.

[46] Q. Lin, F. Yaman, and G. P. Agrawal, "Photon-pair generation in optical fibers through four-wave mixing: Role of Raman scattering and pump polarization," *Phys. Rev. A*, vol. 75, no. 2, p. 023803, 2007.

[47] J. R. Thompson and R. Roy, "Multiple four-wave mixing process in an optical fiber," *Opt. Lett.*, vol. 16, no. 8, pp. 557–559, 1991.

[48] C. McKinstrie, S. Radic, and A. Chraplyvy, "Parametric amplifiers driven by two pump waves," *IEEE J. Sel. Top. Quantum Electron.*, vol. 8, no. 3, pp. 538–547, 2002.

[49] X.-M. Liu, "Theory and experiments for multiple four-wave-mixing processes with multi-frequency pumps in optical fibers," *Phys. Rev. A*, vol. 77, no. 4, p. 043818, Apr. 2008.

Chapter 5

Noise Statistics in Raman Amplifiers

A model describing the interaction between signal and noise mediated by the Kerr effect in optical fibers is proposed in this Chapter. We present and characterize a method able to generate non-white noise that is used in the numerical resolution of the nonlinear equation governing the evolution of the optical field. Numerical simulations are corroborated with experimental amplified spontaneous emission (ASE) power spectra obtained for various pump powers and fiber lengths. Furthermore, our model is used to study the noise statistics after propagation inside a fiber with Raman amplification. We show that the noise statistics deviates significatively from the Gaussian distribution if distances longer than 120 km and signal powers higher than 6 mW are considered.

5.1 Introduction

Due to the progressive generalization of broadband access, telecommunications transport networks capacity has been continuously increased [1]. This has been achieved by increasing the bit rate per channel and by increasing the number of optical channels per fiber [2]. In order to support those lightwave systems operating in the 1.55 μm region, optical amplifiers capable of providing uniform gain over broad bandwidths are required. In this context, Raman amplification presents some attractive features when compared with other optical amplification solutions [3–7]. The possibility to adjust the gain profile by combining multiple pump wavelengths and the improved noise figure are among them [3, 4].

Despite playing a key role in the installed optical communication systems, optical amplification is an intrinsic source of noise due to the ASE [8]. The noise has direct and multiple implications on the performance of optical communication systems: it degrades the signal-to-noise ratio [8] and induces timing jitter and frequency fluctuations [9–12]. Therefore an accurate description of the ASE noise is crucial to assess the performance of fiber-optic communication systems.

In general, simulation, analysis, design and optimization of optical Raman amplification systems are done through the resolution of a system of coupled differential equations

for the mean powers of all involved pumps and signals [13–17]. Several efficient algorithms were proposed in order to solve this system of equations [5, 18–20]. In this kind of analysis the entire spectral range is sliced into narrow bandwidths around discrete central frequencies, and the numerical treatment is performed considering the mean power within narrow spectral windows. When considered, noise is also treated in the mean power domain, likewise signals and pumps. The above mentioned theoretical models account for several physical effects: stimulated and spontaneous Raman scattering; Rayleigh scattering; pump-to-pump, pump-to-signal and signal-to-signal interactions. Nevertheless, even for moderate intensity fields, Kerr effect should also be considered in order to account for the nonlinear fiber response. However, such analysis requires the resolution of the coupled nonlinear Schrödinger equations (NLSEs) for both the pump and Stokes fields [21, 22].

Spontaneous Raman scattering is associated with the random vibrations of the silica molecules due to temperature [8]. The modeling of this effect can be done with the inclusion of a Langevin noise term into the wave equation [21, 23]. In [21] it is shown that this effect can be considered including a noise term into the third-order nonlinear polarization. This means that the coupled NLSEs are solved assuming the third-order nonlinear polarization as a sum of three distinct contributions: the Kerr polarization, the Raman polarization and a noise polarization [21]. Alternative approaches can be used to include the optical noise. For instance, in [24] it was studied the problem of adding the ASE noise at the end of each optical amplifier section. After amplification, independent Gaussian random variables are added to each spectral component. However, the noise shape and nonlinear noise-to-noise and noise-to-signal interaction inside the amplifier are ignored in these approaches.

The use of the NLSE to model the propagation inside the fiber amplifier permits the study of the interaction between signal and ASE noise mediated by the fiber nonlinearities. In particular, it is possible to assess the changes on the noise statistical properties. Several works on this topic were already reported, mainly concerning phase modulated systems, where the induced nonlinear phase noise is an important impairment of system performance [25–27]. In a recent work [28], the evolution of the noise statistics was analyzed considering the particular case of a zero memory nonlinear system. In such case, results showed that the Kerr nonlinearity induces deviations on the input statistics of the noise.

In this study, we analyze the ASE noise induced by spontaneous Raman scattering in broadband systems. The generalized NLSE is solved through the well-known split-step Fourier method (SSFM) [22] with a non-white noise term added to account for the gain profile. After an experimental validation of our ASE noise model, the noise statistics are characterized and it is observed that even for moderate distances and signal powers the noise statistics deviate considerably from the Gaussian distribution.

5.2 ASE Modeling and Simulation

5.2.1 Theoretical Modeling

The simplest scheme of Raman amplification in optical fibers is based on a single signal copropagating with a single pump. For this setting, the evolution along the fiber of the signal and pump average powers, P_s and P_p, respectively, can be described by the following coupled differential equations [22]

$$\frac{dP_s}{dz} = g_R(\Omega)P_p - \alpha_s P_s, \tag{5.1}$$

$$\frac{dP_p}{dz} = -\frac{\omega_p}{\omega} g_R(\Omega)P_p P_s - \alpha_p P_p, \tag{5.2}$$

where α_s and α_p are the fiber losses at the signal, ω, and pump, ω_p, frequencies, respectively, and $g_R(\Omega)$ is the Raman gain coefficient. Note that the frequency dependence of the Raman gain coefficient is defined in terms of the difference between pump and signal frequencies, $\Omega = \omega_p - \omega$, and that the frequency ratio ω_p/ω appears in (5.2) because the pump and signal photons have different energies.

The evolution of the optical field $A_s(z,t)$, which includes signal and noise, can be described by the following equation [29, 30],

$$\begin{aligned}\frac{\partial A_s(z,t)}{\partial z} = &\left(-i\frac{\beta_{\omega\omega}}{2}\frac{\partial^2}{\partial t^2} - \frac{1}{2}\alpha_s\right) A_s(z,t) \\ &+ i\gamma[|A_s(t,z)|^2 + (2-f_R)P_p(z)]A_s(z,t) \\ &+ i\gamma f_R P_p(z)\int_{-\infty}^{+\infty} h_R(t-t')A_s(t',z)\exp(-i\Omega_R(t-t'))dt' \\ &+ f_n(z,t),\end{aligned} \tag{5.3}$$

where $|A_s(z,t)|^2$ is the field power, $\beta_{\omega\omega} = \partial^2\beta/\partial\omega^2$ is the group velocity dispersion coefficient, γ is the nonlinear coefficient, f_R is the fraction of nonlinearity that arises from the delayed Raman response, Ω_R is the vibrational frequency of the molecules, which is assumed to be at peak of the Raman gain curve, $h_R(t)$ is the Raman response function, and $f_n(z,t)$ is a Langevin noise source [4].

The linear part of (5.3) includes dispersion and fiber losses, whereas the nonlinear part accounts for signal self-phase modulation, cross-phase modulation and Raman scattering. Note that the Raman gain is proportional to the imaginary part of the Raman response function, and is defined as

$$g_R(\Omega) = 2f_R\gamma\mathrm{Im}[\tilde{h}_R(\Omega)], \tag{5.4}$$

where $\tilde{h}_R(\Omega)$ is the Fourier transform of $h_R(t)$ and Im[ ] stands for the imaginary part [22]. The last term in (5.3), $f_n(z,t)$, represents mathematically the optical noise continuously added through spontaneous scattering.

The noise associated with the spontaneous Raman scattering processes is usually modeled as a white noise process with Gaussian statistics [4, 29]. Using this approximation, the noise represented by $f_n(z,t)$ vanishes on average,

$$\langle f_n(z,t)\rangle \ = 0, \tag{5.5}$$

and its autocorrelation function (ACF) is given by [4]

$$\langle f_n(z,t) f_n^*(z',t')\rangle = n_{\mathrm{sp}}\hbar\omega_0 g_R(\Omega_0) P_p(z)\delta(z-z')\delta(t-t'), \tag{5.6}$$

where ω_0 is the central frequency, $\hbar\omega_0$ is the mean photon energy, $\Omega_0 = \omega_p - \omega_0$ represents the Raman shift, i.e. the difference between pump and central frequencies, $\delta(z-z')$ and $\delta(t-t')$ are Dirac delta functions, and n_{sp} is the spontaneous-scattering factor, described by [7]

$$n_{\mathrm{sp}}(\Omega_0) = \frac{1}{1-\exp\left(\dfrac{-\hbar\Omega_0}{k_B T}\right)}, \tag{5.7}$$

where k_B is the Boltzmann constant and T is the absolute temperature of the fiber. The delta functions in (5.6) indicate that, at different positions and times, independent noise events occur.

5.2.2 ASE Simulation Using the Split-Step Fourier Method

The NLSE is usually solved using the SSFM [22]. Such method requires the division of the fiber into small steps. For each step, the approximated solution is calculated assuming that the linear and nonlinear effects act independently. Then, neglecting the noise term in (5.3), we can write

$$\frac{\partial A_s(z,t)}{\partial z} = \left(\hat{D} + \hat{N}\right) A_s(z,t), \tag{5.8}$$

where $\hat{D}$ and $\hat{N}$ are, respectively, the linear and nonlinear operators. Assuming that $A_s(z,t)$ varies little when compared with the time scale of the Raman response, and that near the gain peak the real part of $\tilde{h}_R(\Omega)$ vanishes, then the term containing the integral on (5.3) can be written as $1/2\, g_R(\Omega) P_p A_s$ [30]. Therefore, since the linear part of (5.3) is solved in the frequency domain, we can include the Raman gain term on $\hat{D}$, accounting in this way for the frequency dependence of the gain. The dispersive term of (5.3) can be written in the frequency domain by replacing the operator $\partial/\partial t$ by $-i\omega$, and therefore the operator $\hat{D}$ becomes

$$\hat{D}(\omega,z) = i\frac{\beta_{\omega\omega}}{2}\omega^2 + \frac{1}{2}g_R(\Omega)P_p(z) - \frac{1}{2}\alpha_s. \tag{5.9}$$

The operator $\hat{N}$ is given by

$$\hat{N}(t,z) = i\gamma \left[|A_s(z,t)|^2 + (2 - f_R)P_p(z) \right], \tag{5.10}$$

and operates in the time domain. Assuming a step Δz, the optical field at the position $z + \Delta z$ can be approximated by

$$A_s(z+\Delta z,t) \cong \exp\left(\frac{\Delta z}{2}\hat{D}\right) \times \exp\left[\int_z^{z+\Delta z} \hat{N}(z')dz'\right] \exp\left(\frac{\Delta z}{2}\hat{D}\right) A_s(z,t). \tag{5.11}$$

This solution is a second-order approximation, also called symmetrized SSFM, and has an error proportional to Δz^3 [22, 31].

In order to include the noise term, we add the noise discretely to the field. This means that the noise that is continuously created along a real fiber is approximated by a certain amount of noise, $F_n(z,t)$, that is added to the field at each simulation step of the SSFM. This approach reveals reasonable providing that the simulation step Δz is small. For small simulation steps the integral present in (5.11) can also be approximated by $\exp(\Delta z\hat{N})$. Using these approaches, the total optical field at the position $z + \Delta z$ can be written as follows

$$A_s(z+\Delta z,t) \cong \exp\left(\frac{\Delta z}{2}\hat{D}\right) \times \exp(\Delta z\hat{N}) \exp\left(\frac{\Delta z}{2}\hat{D}\right) A_s(z,t) + F_n(z,t). \tag{5.12}$$

However, the inclusion of the noise term in (5.12) reduces the computational efficiency of the SSFM. This occurs because when (5.12) is applied iteratively, the operation $\exp(\frac{\Delta z}{2}\hat{D})$ do not appear consecutively, therefore only the operator $\hat{N}$ can be applied over the whole step [22]. In order to make the method faster, the position where the noise is added was changed; we start by applying the operator $\hat{D}$ to $A_s(z,t)$ over a distance $\Delta z/2$, after we apply the operator $\hat{N}$ over the whole segment length Δz and, before applying again the operator $\hat{D}$, we add the ASE noise $F_n(z,t)$. Equation (5.12) is finally written as follows [32]

$$A_s(z+\Delta z,t) \cong \exp\left(\frac{\Delta z}{2}\hat{D}\right) \times \left[\exp(\Delta z\hat{N}) \exp\left(\frac{\Delta z}{2}\hat{D}\right) A_s(z,t) + F_n(z,t)\right]. \tag{5.13}$$

Note that if (5.13) is applied iteratively, the two consecutive operations $\exp(\frac{\Delta z}{2}\hat{D})$ can now be simply replaced by the single operation $\exp(\Delta z\hat{D})$. With this solution we are able to include the noise term on the SSFM, without reducing the numerical efficiency of the SSFM.

5.2.3 Non-White Noise Generation

Each spontaneous emission event can be considered independent, therefore $f_n(z,t)$ can be considered as a white Gaussian stochastic process. This means that both real and imaginary components of the field are Gaussian random variables, with variance given by (5.6). This model are quite suitable if the bandwidth of the simulation is small when compared with the amplifier bandwidth. Note that this approximation ignores the frequency dependence of $g_R(\Omega)$, since the delta function $\delta(t-t')$ on (5.6) implies a flat spectrum over all the considered bandwidth [33]. Nevertheless, if the $g_R(\Omega)$ dependence on the frequency is considered, then $f_n(z,t)$ cannot be defined as a white Gaussian noise process. In fact, this consideration becomes relevant for broad bandwidth simulations, where multiple signals at various frequencies are analyzed.

The noise added at each step is z dependent, due to the dependence on the pump power $P_p(z)$, and, at each position, it will be frequency shaped, due to the dependence on the gain profile $g_R(\Omega)$. In our method, the generation of this kind of noise follows three stages [34, 35]:

1. We start by generating a white Gaussian distribution of points, $F_n^w(z,t)$, with mean equal to zero, $\langle F_n^w(z,t)\rangle = 0$, (the superscript w indicates "white" noise). Assuming a finite bandwidth and a small step, the variance is calculated from the following expression

$$\sigma_0^2(z) = n_{\mathrm{sp}}(\Omega_0)\hbar\omega_0 g_R(\Omega_0)P_p(z)\Delta z B_{\mathrm{op}}, \tag{5.14}$$

   where $g_R(\Omega_0)$ is the Raman gain at the central signal frequency ω_0, Δz is the step used in the SSFM, and B_{op} is the optical bandwidth of our simulation.

2. In the second stage, we perform the Fourier transform of F_n^w, in order to obtain the spectrum of the previously generated distribution,

$$\widetilde{F}_n^w(z,\omega) = F_T\{F_n^w(z,t)\}, \tag{5.15}$$

   where $F_T\{\,\}$ denotes the Fourier-transform operation. At this point, the obtained spectrum is flat in the considered bandwidth. After that, the spectrum is multiplied by $\sigma_N(z,\omega)$, in order to obtain the desired spectrum profile, i.e. the $g_R(\Omega)$ profile,

$$\widetilde{F}_n^{\mathrm{nw}}(z,\omega) = \sigma_N(z,\omega)\widetilde{F}_n^w(z,\omega), \tag{5.16}$$

   where $\sigma_N(z,\omega)$, the normalized standard deviation, is just the ratio between the variances calculated at the frequency ω and central frequency, ω_0,

$$\sigma_N^2(z,\omega) = \frac{n_{\mathrm{sp}}(\Omega)\hbar\omega\, g_R(\Omega)P_p(z)\Delta z B_{\mathrm{op}}}{\sigma_0^2} \tag{5.17}$$

$$= \frac{n_{\mathrm{sp}}(\Omega)}{n_{\mathrm{sp}}(\Omega_0)}\frac{\omega\, g_R(\Omega)}{\omega_0 g_R(\Omega_0)}. \tag{5.18}$$

   In (5.16) the superscript nw indicates "non-white" noise.

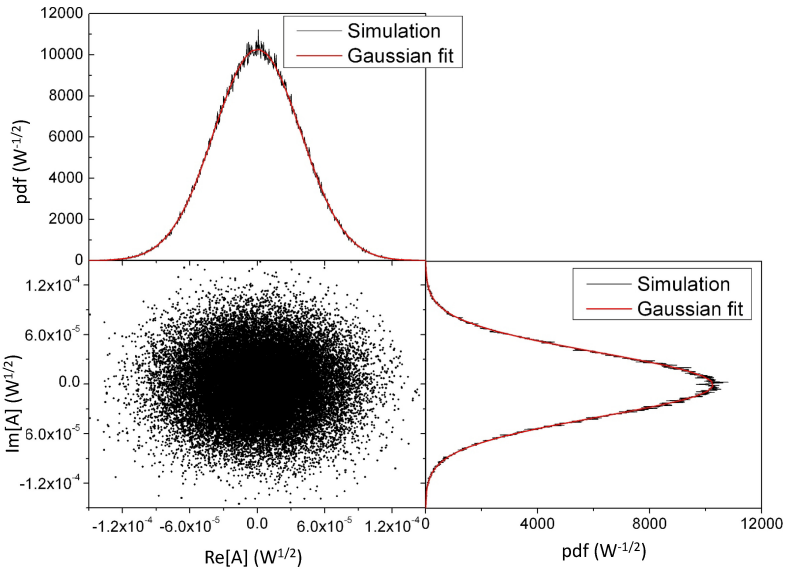

Figure 5.1: Complex representation of the non-white noise added at each step of the SSFM. The pdfs for the real and imaginary parts are compared with the respective Gaussian distribution fits.

3. Finally, in the third stage, the inverse Fourier transform is performed and a non-white noise, $F_n^{\mathrm{nw}}(z,t)$, is obtained in the time domain,

$$F_n^{\mathrm{nw}}(z,t) = F_T^{-1}\{\widetilde{F}_n^{\mathrm{nw}}(z,\omega)\}, \tag{5.19}$$

where $F_T^{-1}\{\,\}$ denotes the inverse Fourier-transform operation.

5.2.4 Non-White Noise Characterization

The non-white noise method presented above only changes the "color" of the noise. This means that the colored noise represented by (5.19) should present the initial distribution, i.e. a Gaussian distribution. Figure 5.1 shows an ensemble of noise samples generated by this method and represented in the 2D complex plane. The respective probability density function (pdfs) for the real and imaginary parts of the complex field are also shown in the same figure. Results show that the generated noise points are distributed around zero, and that the pdfs for the real and imaginary parts are well fitted by a Gaussian distribution with zero mean.

The reshape of the noise spectrum induces a broadening in of the ACF of the distribution [36]. In such cases, the variance distribution is no more governed by (5.6). Fig. 5.2 shows the autocorrelation of the distribution presented in Fig. 5.1. The autocorrelation function of a standard white noise distribution is also represented in the same figure as a green dashed line. The comparison between the two curves shows a broader ACF of the colorized noise, which indicates an increased correlation between samples of such

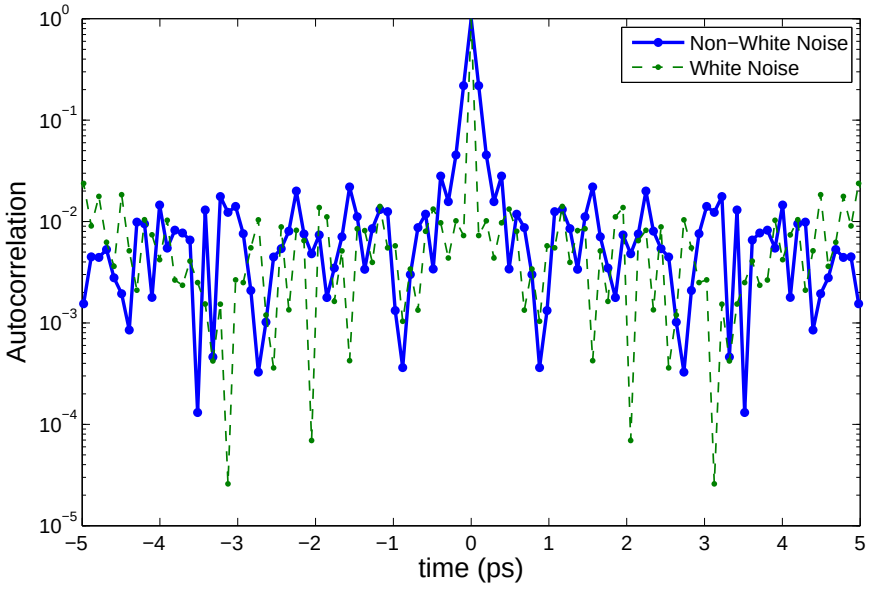

Figure 5.2: ACF for a white (dashed line) and non-white noise (solid line) distributions. The colorized noise presents a broader autocorrelation function, which indicates an increased correlation between samples of such distribution. The sample period used in the simulations was 0.1 ps.

distribution.

5.3 Experimental Validation

In order to validate the proposed ASE noise model, we have compared our simulation results with experimental ASE power spectra. Different fiber lengths and input pump powers were investigated.

5.3.1 Numerical Simulation

The simulation of the ASE noise was based on the numerically resolution of the NLSE version presented in (5.3), using the modified SSFM presented in Section 5.2. The following fiber parameters were considered in the simulations: step size equal to 80 m, nonlinear coefficient of 1.5 $\mathrm{W^{-1}km^{-1}}$, group velocity dispersion of -21.4 $\mathrm{ps^2/km}$, fiber losses of 0.23 dB/km, f_R equal to 0.18, and the Raman gain coefficient $g_R(\Omega)$ given by

$$g_R(\Omega) = \sum_{i=1}^{14} a_i \exp\left(-\frac{(\Omega - m_i)^2}{2\sigma_i^2}\right), \tag{5.20}$$

where a_i, m_i and σ_i represent, respectively, the amplitude, central position and root-mean-square width of the i^{th} Gaussian function. Table 5.1 shows the value of each

Table 5.1: Coefficient values of the 14 Gaussian functions used to describe the Raman gain profile $g_R(\Omega)$ inside a standard single-mode fiber.

Curve #	Parameters		
i	m_i [THz]	a_i [$\times 10^{-15}$(Wm)$^{-1}$]	σ_i [THz]
1	2.3008	10.1789	1.8685
2	5.0715	9.2341	2.0494
3	7.1173	9.2375	1.8139
4	8.5426	7.8260	1.4252
5	9.8932	2.8127	0.9069
6	11.8048	42.1553	2.1300
7	13.1447	22.7000	1.0470
8	13.9548	11.0000	0.4279
9	14.7000	30.0000	0.3500
10	15.3000	13.0000	0.1981
11	16.0006	7.8000	0.6294
12	17.5956	11.9000	0.7470
13	19.5722	9.4227	1.7894
14	23.3083	10.3140	0.7248

parameter used in the simulation to represent the frequency dependence of the Raman gain coefficient.

The curve of $g_R(\Omega)$, represented in Fig. 5.3, results from the fit of 14 Gaussian curves to experimental Raman gain values, following the procedure presented in [17]. These experimental values of $g_R(\Omega)$ were obtained through on/off gain measurements using the experimental setup schematically depicted in Fig. 5.4–b). Our simulation was centered around the maximum of the gain curve and $A_s(z=0,t) = 0$ and $P_p(z=0,t) = 100$ and 203 mW. The ASE noise power spectral density was obtained from the signal at the fiber output

$$S(\omega) = \frac{\widetilde{A}_s(\omega)\widetilde{A}_s^*(\omega)}{T_W}, \tag{5.21}$$

where $\widetilde{A}_s(\omega)$ is the Fourier transform of the output signal $A_s(t)$ and T_W is the time window considered in the simulation, which was 12.8 ns. The curves for the ASE noise power were obtained from the convolution of the ASE noise power density spectra through an ideal filter with bandwidth equal to 15 GHz, and are represented in Fig. 5.5 as solid lines.

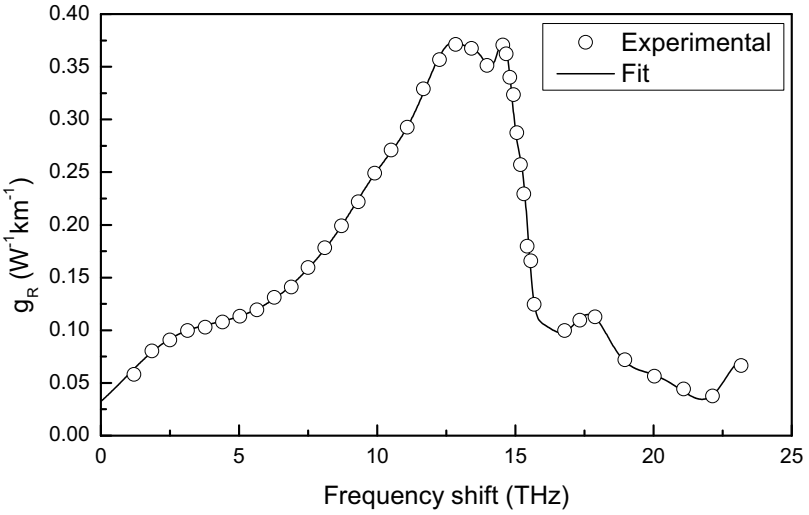

Figure 5.3: Raman gain coefficient as a function of the pump-signal frequency separation. Experimental points, represented as red circles, were obtained through on/off gain measurements. The solid curve results from the fit of 14 Gaussian curves, represented in (5.20), to the measured $g_R(\Omega)$ values.

5.3.2 Experimental Setup and Results

The setup used to perform the experimental ASE noise measurements comprises a semiconductor laser pump, a standard single-mode fiber (SSMF), and an optical spectrum analyzer (OSA), as schematically represented in Fig. 5.4–a). The laser pump was centered at 1470 nm and was propagated in the forward direction with two different continuous wave (CW) powers: 100 and 203 mW. The ASE noise was analyzed at the fiber end in the OSA, and its power spectra are represented in Fig. 5.5 as circles.

The comparison between the data depicted in Fig. 5.5 shows a good agreement between simulated and experimental results for the ASE noise at different propagation distances and for different pump powers. This agreement, which in some cases covers a range of almost 70 nm of the spectrum, i.e., all the simulated bandwidth, seems to be better when the pump power is equal to 203 mW. Since lower pump powers induce lower ASE powers, the reason for the observed mismatches could be related with the assumption, in our model, of an ideal pump spectrum. As shown in the inset of Fig. 5.4, the pump spectrum presents a non-zero background in the wavelength range 1530–1610 nm. Although, it should be noted that commercial Raman amplification systems use pump powers equal or higher than 203 mW.

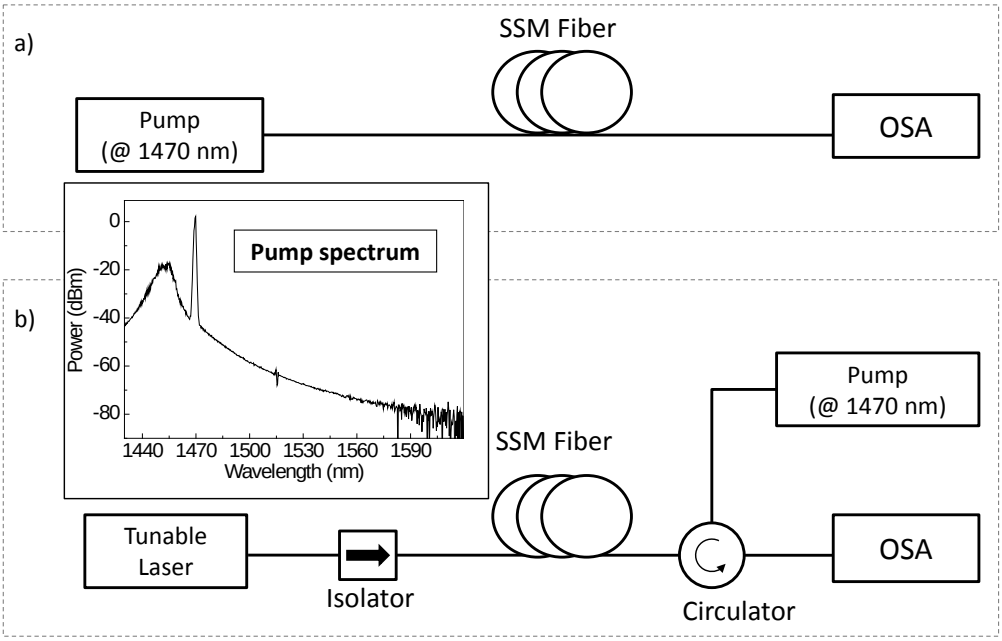

Figure 5.4: a) – Experimental setup used to measure the ASE noise. b) – Experimental setup used to perform measurements of the Raman gain coefficient. Inset shows the output pump laser spectrum, represented in a dBm scale, used in both cases.

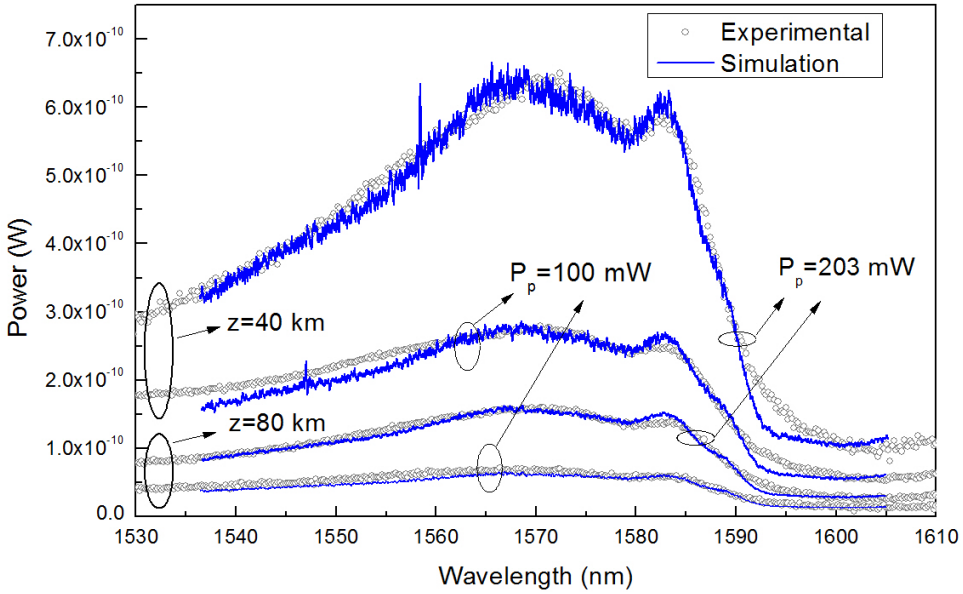

Figure 5.5: Experimental and simulated ASE power spectra for different fiber lengths (40 and 80 km) and input pump powers (100 and 203 mW). The Raman pump, centered at 1470 nm, was propagated in the forward direction.

5.4 Statistics Characterization

The knowledge of the noise statistics reveals to be important in the estimation of some performance key parameters in new high-speed optical communication systems [37]. Bit-

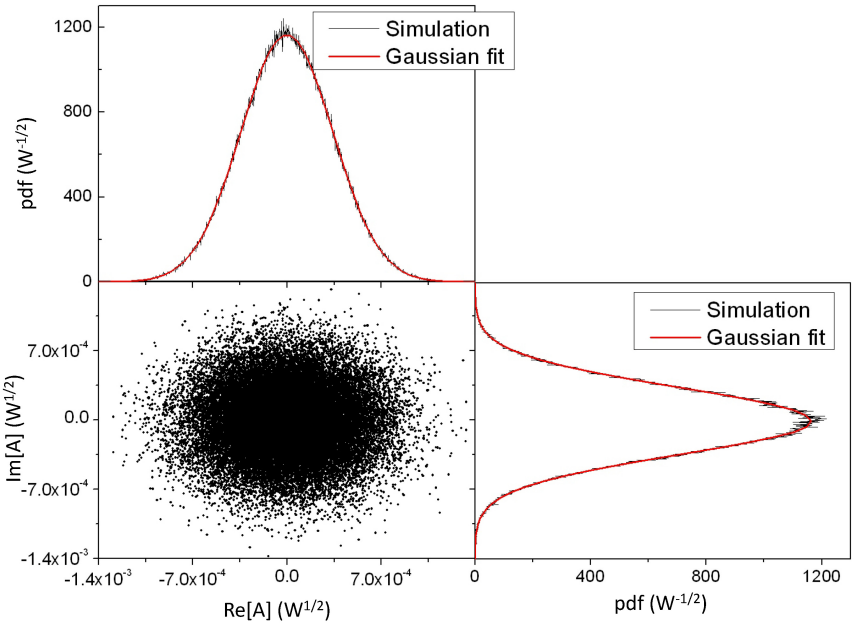

Figure 5.6: Complex representation of the noise after a propagation of 40 km of fiber. The pdfs for the real and imaginary parts are compared with the respective Gaussian distribution fits.

error rate (BER) is usually calculated assuming that the signal noise can be approximated by Gaussian distributions [22]. In this Chapter we show that the use of such approximation for ASE noise becomes inappropriate in some regimes. Using our model to generate the ASE noise, we have simulated the propagation of the noise for different scenarios. For each propagation distance, we have considered the propagation of the ASE noise alone, as well as the co-propagation of the ASE noise and a CW signal. Two different input signal powers were considered: 6 and 12 mW. In order to compensate for fiber losses along the propagation, a Raman pump, with a power equal to 350 mW and propagating in the forward direction, was introduced at each 40 km. In the following we show the noise statistics for three particular cases.

In the first case, we analyzed the statistics of the ASE noise, without any copropagating signal, after a propagation along 40 km of optical fiber. The propagation is governed by (5.3), which means that both dispersive and nonlinear physical effects are considered in the analysis. The complex representation of the noise and respective statistical pdfs are shown in Fig. 5.6. The results show that the real and imaginary parts of the electric field are well fitted by Gaussian distributions. That means that the Gaussian statistics of the noise added at each step do not undergo significant changes along the propagation due to fiber nonlinearities.

The second case corresponds to the co-propagation of the ASE noise and a CW signal with 12 mW of input power, for the same distance of the previous case, i.e., 40 km. Fig. 5.7 shows the field representation in the complex space, and their respective pdfs for

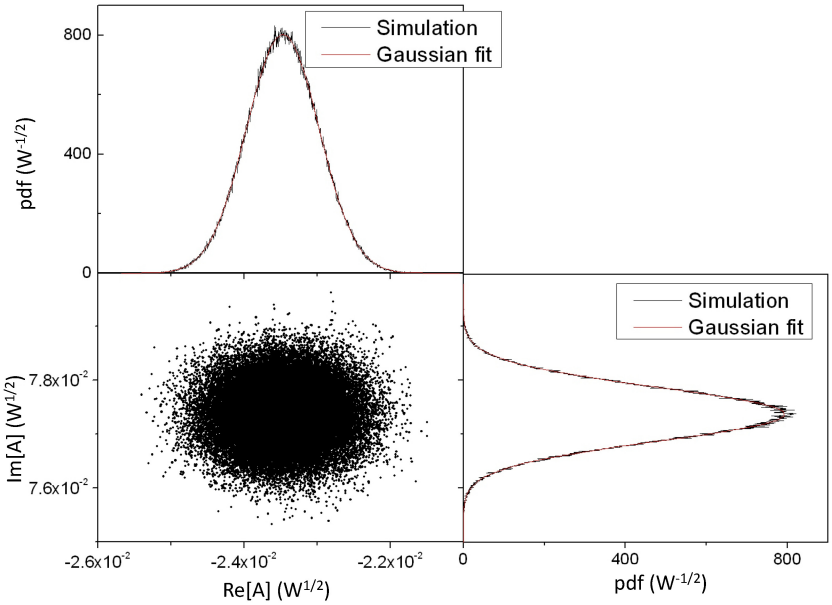

Figure 5.7: Complex representation of the noise resulting from the co-propagation of a signal (12 mW of power) and ASE over 40 km of fiber. The pdfs for the real and imaginary parts are compared with the respective Gaussian distribution fits.

the real and imaginary parts. We observe that the real and imaginary parts of the field are still well fitted by two Gaussian distributions. Since ASE noise is co-propagated with a CW signal, the two distributions present non-zero means.

The third case, whose statistics are represented in Fig. 5.8, corresponds to a propagation along 160 km, where the signal co-propagated with the ASE noise has an input power equal to 12 mW. In this case, in contrast with those presented above, the noise statistics result modified; the pdfs for the real and imaginary parts of the field deviate from the Gaussian shape, as observed in Fig. 5.8.

A detailed analysis of the probability distribution deviation from the Gaussian statistics involves the calculation of high-order statistical moments. Skewness and kurtosis measures are often used to describe the shape characteristics of probability distributions. These two well-known measures are functions of the high-order statistical moments, and are defined as [38]

$$\gamma_1 = \frac{\mu_3}{(\mu_2)^{3/2}}, \tag{5.22}$$

and

$$\gamma_2 = \frac{\mu_4}{(\mu_2)^2}, \tag{5.23}$$

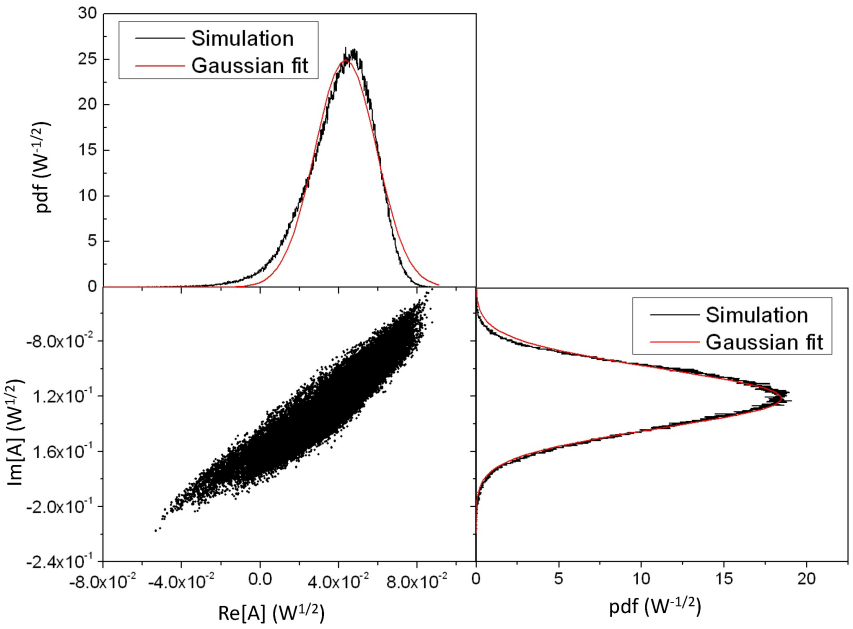

Figure 5.8: Complex representation of the noise resulting from the co-propagation of a signal (12 mW of power) and ASE over 160 km of fiber. The pdfs for the real and imaginary parts are compared with the respective Gaussian distribution fits.

respectively, where μ_i is the i^{th} central moment [39]. The skewness measures the degree of asymmetry of a probability distribution, and it is equal to zero for a Gaussian distribution. If the skewness is positive, then the distribution is skewed to the right, i.e., the distribution has a long right tail. If it is negative, then the distribution is skewed to the left [40]. On the other hand, the kurtosis indicates the degree of peakedness of a distribution, and it is equal to 3 for a Gaussian distribution. The kurtosis "excess", i.e., the kurtosis subtracted by 3, is usually considered when the reference function is the Gaussian distribution. Therefore, distributions with kurtosis "excess" positive, also called leptokurtic distributions, are normally more peaked than the normal distribution, while distributions with kurtosis "excess" negative, also called leptokurtic, are more flat topped [40].

We have calculated, for each simulation, the skewness and the kurtosis excess of both the real and imaginary parts of the field. Both parameters are represented as a function of the distance in Fig. 5.9–a) and Fig. 5.9–b), respectively. From these results, we observe that the distributions represented in Figs. 5.6 and 5.7 have skewness and kurtosis excess values around zero, with small absolute values. For the case represented in Fig. 5.8, where important deviations from the Gaussian statistics were observed for the two field components, the skewness and kurtosis excess values are significant.

In order to simplify the graphical representation of these two statistical parameters, we have calculated the modulus of both parameters, as $\sqrt{|\gamma_i^{\text{Re}}|^2 + |\gamma_i^{\text{Im}}|^2}$, with $i = 1, 2$. The skewness modulus is represented in Fig. 5.9–c) and the kurtosis excess modulus in Fig. 5.9–d). From the analysis of the skewness values we conclude that the asymmetry

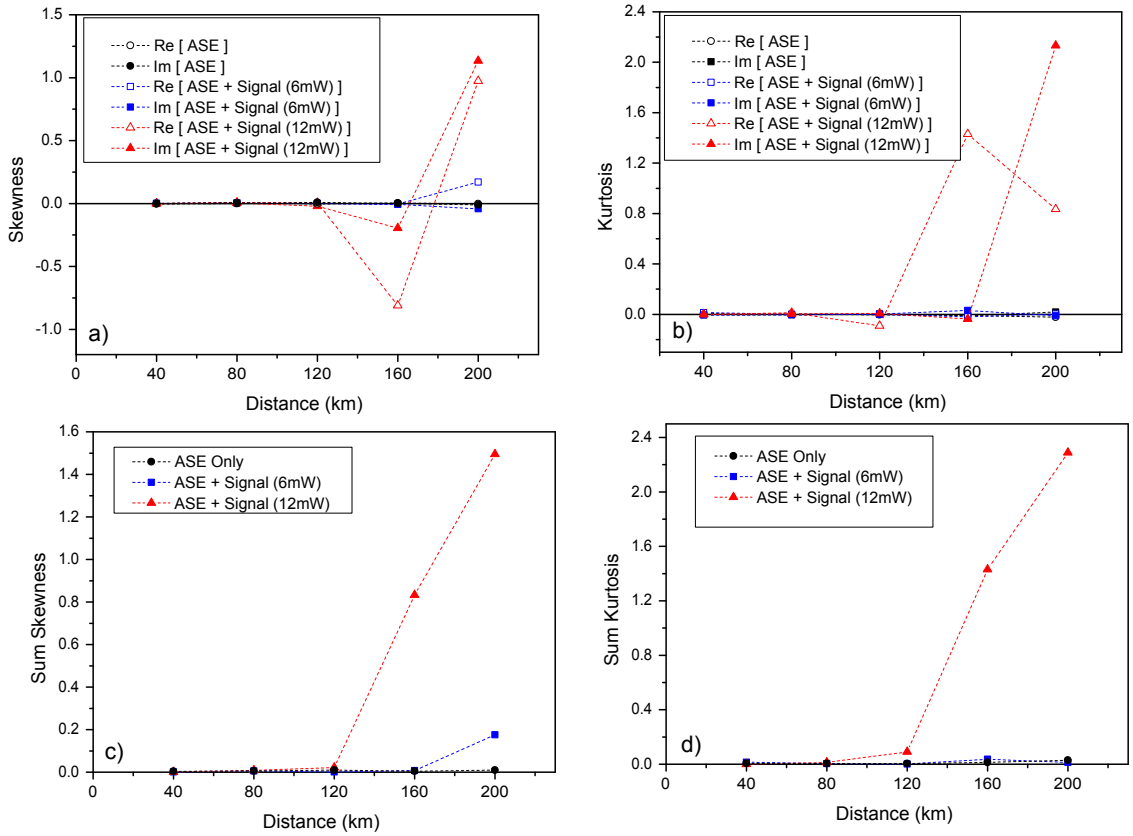

Figure 5.9: a) – Skewness, and b) – kurtosis excess for real and imaginary parts of the electric field. c) – Total skewness, and d) – total kurtosis excess for real and imaginary parts of the field.

of the distributions increases with the distance and with the signal power. The analysis of the kurtosis excess values also shows that the noise distributions deviate from the Gaussian statistics with the increase of the propagation distance and signal power. These results clearly indicate that the nonlinear interaction between signal and noise is relevant even for moderate distances and signal powers, and it needs to be taken into account for an accurate description of the field propagation.

Figure 5.10 summarizes the total skewness and kurtosis excess dependence on the propagation distance and signal power. Maps represented in Figs. 5.10–a) and 5.10–b) reveal that, for low signal powers, noise is in a regime of Gaussian statistics. Weak changes are observed with the increment of the propagation distance. On the other hand, for signal powers higher than 6 mW, the noise regime is highly dependent on the propagation distance. That means that for small propagation distances the statistics are close to Gaussian, whereas for propagation distances longer than 120 km considerable changes on the noise statistics are observed.

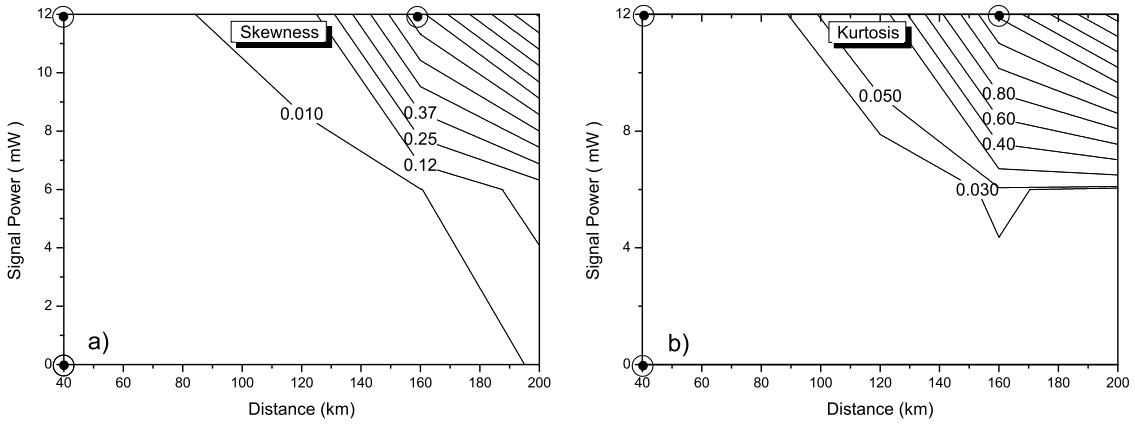

Figure 5.10: a) – Total skewness, and b) – kurtosis excess, as a function of the propagation distance and signal power. Symbols ⊙ show the map localization of the pdfs represented in Figs. 5.6, 5.7 and 5.8.

5.5 Summary

We have presented a numerical model that accurately describes the ASE noise in optical fiber systems with distributed Raman amplification. Our numerical results for the ASE noise power spectrum were validated by means of experimental data obtained for different pump powers (100 and 203 mW) and propagation distances (40 and 80 km).

The evolution of the noise statistics was analyzed considering the co-propagation of ASE noise with a CW signal. We have considered propagation distances up to 200 km and signal powers up to 12 mW. The calculation of the parameters skewness and kurtosis excess has permitted to quantify the deviations of the noise distributions from the Gaussian statistics. We have found that the noise preserves the Gaussian statistics along the fiber for regimes where the interaction between signal and noise due to fiber nonlinearities can be neglected. Nevertheless, for distances longer than 120 km and signal powers $\geq$ 6 mW, the nonlinearities induce a change on the noise distribution and the Gaussian statistics assumption becomes invalid.

This statistical information is quite relevant for an accurate estimation of performance key parameters, like the BER. Optical noise is usually approximated by Gaussian distributions, which reveals to be a wrong approximation for the regimes of high powers and long distances discussed in this work. In these regimes, the skewness values reveal that the noise distributions present a high degree of asymmetry. This kind of changes on the probability density of noise could be relevant for coherent amplitude modulated systems, namely in the context of multilevel quadrature-amplitude modulated systems.

References

[1] I. P. Kaminow, T. Li, and A. E. Willner, *Optical Fiber Telecommunications V-B Systems and Networks*. Academic Press, San Diego, 2008.

[2] G. P. Agrawal, *Lightwave Technology: Telecommunication Systems*. John Wiley & Sons, New Jersey, USA, 2005.

[3] M. Islam, "Raman amplifiers for telecommunications," *IEEE J. Sel. Top. Quantum Electron.*, vol. 8, no. 3, pp. 548–559, 2002.

[4] C. Headley III and G. P. Agrawal, *Raman Amplification in Fiber Optical communication Systems*. Academic Press, EUA, 2004.

[5] B. Neto, A. Teixeira, N. Wada, and P. André, "Efficient use of hybrid genetic algorithms in the gain optimization of distributed Raman amplifiers," *Opt. Express*, vol. 15, no. 26, pp. 17 520–17 528, December 2007.

[6] A. M. Rocha, B. Neto, and P. André, "Study of Raman amplification with low cost incoherent pumps," *Microw. Opt. Technol. Lett.*, vol. 50, no. 2, pp. 301–303, Feb. 2008.

[7] J. Bromage, "Raman amplification for fiber communications systems," *IEEE/OSA J. Lightwave Technol.*, vol. 22, no. 1, pp. 79–93, Jan. 2004.

[8] G. P. Agrawal, *Fiber-Optic Communication Systems, 3rd edition*. John Wiley & Sons, New York, USA, 2002.

[9] J. P. Gordon and H. A. Haus, "Random walk of coherently amplified solitons in optical fiber transmission," *Opt. Lett.*, vol. 11, no. 10, p. 665, 1986.

[10] A. N. Pinto, G. P. Agrawal, and J. R. F. da Rocha, "Effect of soliton interaction on timing jitter in communication systems," *IEEE/OSA J. Lightwave Technol.*, vol. 16, no. 4, pp. 515–519, 1998.

[11] A. N. Pinto, J. R. F. da Rocha, Q. Lin, and G. P. Agrawal, "Optical versus electrical dispersion compensation: Role of timing jitter," *IEEE/OSA J. Lightwave Technol.*, vol. 24, no. 1, p. 387, 2006.

[12] A. N. Pinto and G. P. Agrawal, "Nonlinear interaction between signal and noise in optical amplifiers," *IEEE/OSA J. Lightwave Technol.*, vol. 26, no. 13, pp. 1847–1853, 2008.

[13] H. Kidorf, K. Rottwitt, M. Nissov, M. Ma, and E. Rabarijaona, "Pump interactions in a 100-nm bandwidth Raman amplifier," *IEEE Photonics Technol. Lett.*, vol. 11, no. 5, pp. 530–532, May 1999.

[14] B. Min, W. J. Lee, and N. Park, "Efficient formulation of Raman amplifier propagation equations with average power analysis," *IEEE Photonics Technol. Lett.*, vol. 12, no. 11, pp. 1486–1488, Nov. 2000.

[15] V. Perlin and H. Winful, "Optimizing the noise performance of broad-band WDM systems with distributed Raman amplification," *IEEE Photonics Technol. Lett.*, vol. 14, no. 8, pp. 1199–1201, Aug. 2002.

[16] X. Liu and Y. Li, "Optimizing the bandwidth and noise performance of distributed multi-pump Raman amplifiers," *Opt. Communications*, vol. 230, no. 4-6, pp. 425–431, 2004.

[17] M. Fugihara and A. N. Pinto, "Low-cost Raman amplifier for CWDM systems," *Microw. Opt. Technol. Lett.*, vol. 50, pp. 297–301, Feb. 2008.

[18] P. Xiao, Q. Zeng, J. Huang, and J. Liu, "A new optimal algorithm for multipump sources of distributed fiber Raman amplifier," *IEEE Photonics Technol. Lett.*, vol. 15, no. 2, pp. 206–208, 2003.

[19] X. Liu and Y. Li, "Efficient algorithm and optimization for broadband Raman amplifiers," *Opt. Express*, vol. 12, no. 4, pp. 564–573, 2004.

[20] W. Zhang, X. Feng, J. Peng, and X. Liu, "A simple algorithm for gain spectrum adjustment of backward-pumped distributed fiber Raman amplifiers," *IEEE Photonics Technol. Lett.*, vol. 16, no. 1, pp. 69–71, Jan. 2004.

[21] C. Headley III and G. Agrawal, "Noise characteristics and statistics of picosecond stokes pulses generated in optical fibers through stimulated Raman scattering," *IEEE J. Quantum Electron.*, vol. 31, no. 11, pp. 2058–2067, Nov. 1995.

[22] G. P. Agrawal, *Nonlinear Fiber Optics, 3rd ed.* Academic Press, San Diego, USA, 2001.

[23] M. G. Raymer and J. Mostowski, "Stimulated Raman scattering: Unified treatment of spontaneous initiation and spatial propagation," *Phys. Rev. A*, vol. 24, no. 4, pp. 1980–1993, Oct. 1981.

[24] D. Marcuse, "Single-channel operation in very long nonlinear fibers with optical amplifiers at zero dispersion," *IEEE/OSA J. Lightwave Technol.*, vol. 9, no. 3, pp. 356–361, Mar. 1991.

[25] J. P. Gordon and L. F. Mollenauer, "Phase noise in photonic communications systems using linear amplifiers," *Opt. Lett.*, vol. 15, no. 23, pp. 1351–1353, 1990.

[26] A. Mecozzi, "Limits to long-haul coherent transmission set by the Kerr nonlinearity and noise of the in-line amplifiers," *IEEE/OSA J. Lightwave Technol.*, vol. 12, no. 11, pp. 1993–2000, Nov. 1994.

[27] E. Vanin, G. Jacobsen, and A. Berntson, "Nonlinear phase noise separation method for on-off keying transmission system modeling with non-Gaussian noise generation in optical fibers," *Opt. Lett.*, vol. 32, no. 12, pp. 1740–1742, 2007.

[28] M. P. Dlubek, A. J. Philliphs, and E. C. Larkins, "Nonlinear evolution of Gaussian ASE noise in ZMNL fiber," *IEEE/OSA J. Lightwave Technol.*, vol. 26, no. 8, pp. 891–898, 2008.

[29] G. P. Agrawal, *Applications of Nonlinear Fiber Optics.* Academic Press, San Diego, USA, 2002.

[30] C. Headley III and G. P. Agrawal, "Unified description of ultrafast stimulated Raman scattering in optical fibers," *J. Opt. Soc. Am. B*, vol. 13, no. 10, p. 2170, 1996.

[31] Q. Zhang and M. Hayee, "Symmetrized split-step fourier scheme to control global simulation accuracy in fiber-optic communication systems," *IEEE/OSA J. Lightwave Technol.*, vol. 26, no. 2, pp. 302–316, Jan. 2008.

[32] N. J. Muga, M. C. Fugihara, Mário F. S. Ferreira, and A. N. Pinto, "Non-Gaussian ASE noise in Raman amplification systems," *IEEE/OSA J. Lightwave Technol.*, vol. 27, no. 16, pp. 3389–3398, 2009.

[33] A. Papoulis, *Probability, random variables, and stochastic processes.* McGraw-Hill, New-York, 1991.

[34] N. J. Muga, M. C. Fugihara, Mário F. S. Ferreira, and A. N. Pinto, "Non-white noise generation method for ASE noise simulation in systems with Raman amplification," in *International Conf. on Transparent Optical Networks - ICTON*, vol. 1, Ponta Delgada - Azores, Portugal, Jun. 2009, p. WeA1.6.

[35] N. J. Muga, M. C. Fugihara, Mário F. S. Ferreira, and A. N. Pinto, "ASE noise simulation in Raman amplification systems," in *Proc Conf. on Telecommunications - ConfTele2009*, vol. 1, Santa Maria da Feira, Portugal, May 2009, pp. 347–350.

[36] M. C. Jeruchim, P. Balaban, and K. S. Shanmugan, *Simulation of Communication Systems: Modeling, Methodology and Techniques.* Kluwer Academic Publishers, New-York, 2000.

[37] G. Li, "Recent advances in coherent optical communication," *Advances in Optics and Photonics*, vol. 1, pp. 279–307, 2009.

[38] D. N. Joanest and C. A. Gill, "Comparing measures of sample skewness and kurtosis," *Journal of the Royal Statistical Society. Series D. (The Statistician)*, vol. 47, pp. 183–189, 1998.

[39] W. H. Press, *Numerical recipes in C: the art of scientific computing, 2nd ed.* Cambridge University Press, 1997.

[40] C. Forbes, M. Evans, N. Hastings, and B. Peacock, *Statistical Distributions, 4rd edition.* John Wiley & Sons, New Jersey., USA, 2001.

Chapter 6

Broadband Polarization Pulling Using Raman Amplification

All-optical polarization control and repolarization of unpolarized light processes are analyzed in this Chapter. We explore the Raman amplification in a scheme where a pump wave is co-propagated with a weak signal. Using a broadband model, we show that the preferred amplification of one particular polarization component of the signal allows an effective signal polarization pulling over a wavelength range of 60 nm (7.5 THz). We map parameters like the degree of polarization (DOP), the mean angle between the output signal state of polarization (SOP) and the output pump SOP, the mean gain and its standard deviation for the entire Raman gain bandwidth. We show that in the undepleted regime (signal input power ~ 1 μW), the signal DOP at the fiber output, corresponding to an unpolarized input signal, increases with the pump power for the entire Raman gain band. In the depleted regime (signal input power $\gtrsim 1$ mW), this behavior is observed only when the signal wavelength is far away from the Raman gain peak. For signal wavelengths near to the Raman gain peak (in a range of approximately 25 nm) the pump can be depleted, which means that there is an optimum pump power leading to a maximum DOP.

6.1 Introduction

All-optical polarization control schemes can found a large variety of applications in areas like all-optical signal processing and high-speed optical communication systems [1, 2]. Such polarization controllers provide a very fast response time, overcoming an important drawback of polarization control schemes based on optoelectronic elements [3–6]. Besides that, the theoretical possibility to convert unpolarized to polarized light with unit efficiency, represents a huge advantage over the standard polarizers that waste 50% of the unpolarized light [7]. The lossless repolarization was originally proposed in the context of the noninstantaneous and incoherent (phase insensitive) photorefractive effect [8], and of the instantaneous and coherent four-wave mixing (FWM) process [9].

The all-optical polarization control has been explored in optical fibers through FWM

and stimulated Raman scattering (SRS) effects [10–12]. Based on the FWM effect, the SOP control has been achieved by launching two intense counterpropagating waves in an optical fiber [11, 13]. On the other hand, the SOP control through the SRS effect has been obtained by copropagating or counterpropagating a pump wave with a weak signal. In this case, the polarization control is assisted by signal amplification [12]. In fact, the pump wave can lead to a preferred amplification of one particular polarization component of the propagating signal [14], giving rise to the pulling of the signal SOP.

In recent years, some works were been presented focusing the polarization-dependency property of Raman gain and its application to pull the polarization inside an optical fiber with random birefringence. Note that this solution allows an all-optical and passive SOP control, mixed with a broadband optical gain source. Raman induced polarization pulling was experimentally verified in [15], using a Raman pump co-propagated with a weak signal in a dispersion-shifted fiber. Fiber optic Raman polarizers were analyzed theoretically in copropagating [12] and counterpropagating [16] schemes, considering a two beam interaction through Kerr and Raman effects. More recently, an analysis of pump depletion effect on the performance of the polarization pulling process was presented in [17]. All these analyzes consider a single signal-pump frequency difference (13.2 THz) corresponding to the maximum Raman gain.

Here, we consider the effect of detuning the signal from the peak of the Raman gain in a copropagating scheme. We show that the preferred amplification of one particular polarization component of the signal can lead to an effective polarization pulling over a wide wavelength range. We map parameters like the DOP, the mean angle between the output signal SOP and the output pump SOP, the mean gain and its standard deviation for the entire Raman gain bandwidth. Both undepleted and depleted pump regimes are analyzed.

6.2 Broadband Propagation Model

The evolution along the fiber of the pump and signal Stokes vectors, $\vec{P}$ and $\vec{S}$, respectively, can be described by the following pair of coupled differential vector equations in the Stokes space [14, 18]

$$\frac{d\vec{P}}{dz} = -\alpha(\omega_p)\vec{P} - \frac{\omega_p}{2\omega_s} g_R(\Omega)(|\vec{P}|\vec{S} + |\vec{S}|\vec{P}) + (\omega_p\vec{b} + \gamma_p\vec{W}_p^{\mathrm{NL}}) \times \vec{P}, \tag{6.1}$$

and

$$\frac{d\vec{S}}{dz} = -\alpha(\omega_s)\vec{S} + \frac{1}{2} g_R(\Omega)(|\vec{S}|\vec{P} + |\vec{P}|\vec{S}) + (\omega_s\vec{b} + \gamma_s\vec{W}_s^{\mathrm{NL}}) \times \vec{S}, \tag{6.2}$$

respectively, where $\alpha(\omega_p)$ and $\alpha(\omega_s)$ are the fiber losses, at pump, ω_p, and signal, ω_s, frequencies, respectively, $g_R(\Omega)$ is the parallel Raman gain coefficient for a pump-signal frequency difference equal to $\Omega = \omega_p - \omega_s$, γ_p and γ_s are the pump and signal nonlinear coefficients, respectively, $\vec{b}$ is the ratio between the linear birefringence vector and the

angular frequency, and $|\vec{P}|$ and $|\vec{S}|$ represent the pump and signal powers, respectively. In (6.1) and (6.2), the terms containing $\vec{b}$ describe the linear polarization rotation of signal and pump waves, whereas the vectors $\vec{W}_p^{\mathrm{NL}}$ and $\vec{W}_s^{\mathrm{NL}}$ account for the nonlinear polarization rotation suffered by pump and signal waves, respectively, and are given by

$$\vec{W}_p^{\mathrm{NL}} = \frac{2}{3}[-2S_1, -2S_2, P_3]^t, \tag{6.3}$$

and

$$\vec{W}_s^{\mathrm{NL}} = \frac{2}{3}[-2P_1, -2P_2, S_3]^t, \tag{6.4}$$

where P_i, and S_i, with $i = 1, 2, 3$, are the components of the pump and signal Stokes vectors, respectively.

In this model, we neglect the Raman gain for orthogonally polarized beams because of its small magnitude [19]. Notice that the ratio between the perpendicular and parallel Raman gain coefficients has a value of approximately 0.012 for silica fibers at the Raman gain peak [20]. Besides that, we modeled pump and signal as continuous waves, which means that fiber chromatic dispersion is neglected. This approximation is discussed later, at the end of Section 6.4.

6.2.1 Birefringence

Experimental results verified that in most cases the birefringence present in optical fibers is linear [21]. Therefore, and as discussed in Section 2.2, the birefringence vector can be written as

$$\vec{\beta} = \omega\vec{b} = [\beta_1, \beta_2, 0]^t. \tag{6.5}$$

The two non-null components, β_1 and β_2, are obtained from the birefringence random modulus model [22, 23], i.e., they are modeled as a Langevin process. Hence, both components $\beta_1(z)$ and $\beta_2(z)$ vary independently according to the following Langevin equations

$$\frac{d\beta_1}{dz} = -\rho\beta_1 + \sigma\eta_1, \tag{6.6}$$

and

$$\frac{d\beta_2}{dz} = -\rho\beta_2 + \sigma\eta_2, \tag{6.7}$$

where η_1 and η_2 are two independent Gaussian white noise functions with zero mean and variance equal to 1. The parameters σ and ρ, present in (6.6) and (6.7), can be written

as functions of characteristic fiber lengths [23]

$$\sigma = \frac{2\pi}{L_B\sqrt{L_C}}, \tag{6.8}$$

and

$$\rho = 1/L_C, \tag{6.9}$$

where L_B and L_C represent the beat and correlation lengths, respectively, for the angular frequency ω. The PMD coefficient can also be expressed as a function of these two characteristic lengths [23]

$$D_p = \frac{16\sqrt{L_C}}{\sqrt{3}\omega L_B}. \tag{6.10}$$

Using (6.6) and (6.7), in conjugation with the three previous equations, we can generate the birefringence vector for the entire fiber length, given L_C and L_B.

6.2.2 Raman Gain and Fiber Losses

The shape of the Raman gain $g_R(\Omega)$ can be described with the sum of some Gaussian curves [24], whose details can be found in Chapter 5, see (5.20).

The frequency dependence of fiber losses was obtained following the model presented in [25]. That model accounts for different frequency-dependent losses contributions. The total fiber losses, $\alpha(\omega)$, are written as

$$\alpha(\omega) = \alpha_R(\omega) + \alpha_{\mathrm{OH}}(\omega) + \alpha_{\mathrm{WG}}(\omega) + \alpha_{\mathrm{IR}}(\omega) + \alpha_{\mathrm{UV}}(\omega), \tag{6.11}$$

where the first, second, third, fourth and fifth terms on the right hand side correspond, respectively, to the Rayleigh scattering, ion OH^- absorption, waveguide imperfections, infrared absorption, and ultraviolet absorption contributions to fiber losses.

6.3 Numerical Simulation

The resolution of the coupled differential equations (6.1) and (6.2) requires a previous calculation of the birefringence vector for the considered fiber length. For each simulation, (6.6) and (6.7) were numerically integrated by means of the Heun's method [26], using an integration step size of 40 cm. This length is much smaller than the evolution scale of any effect considered in the model. Figure 6.1 shows the evolution of the linear birefringence vector assuming $\vec{\beta}(z=0) = [\beta_1, \beta_2, 0]^t = \vec{0}$, correlation length $L_C = 10$ m, and beat length $L_B = 354$ m. Figure 6.1–a) shows the evolution of the birefringence on the "$\beta_1 - \beta_2$" plane, whereas Fig. 6.1–b) shows the individual evolution of the two non-null components with the distance.

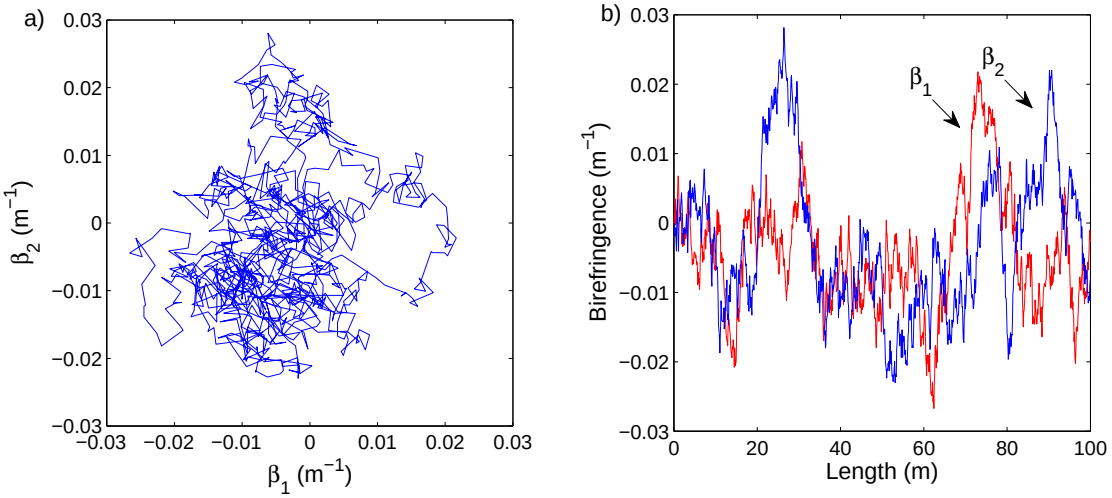

Figure 6.1: Evolution of the birefringence vector $\vec{\beta} = [\beta_1, \beta_2, 0]^t$ obtained from the numerical integration of (6.6) and (6.7) with a step size equal to 40 cm, assuming a correlation length equal to 10 m, and a beat length equal to 354 m: a) – 2D representation; b) – evolution with the distance of the components β_1 and β_2, represented as red and blue lines, respectively.

After obtaining the birefringence vector for each simulation step, (6.1) and (6.2) were solved using the fifth-order Runge-Kutta method. The following general parameters were used in this work: fiber length $L = 2$ km, correlation length $L_C = 10$ m, beat length $L_B = 354$ m (which gives $D_p = 0.0021$ ps/km$^{1/2}$ at 1550 nm), and nonlinear parameter $\gamma_p \sim \gamma_s = 2$ W^{-1}km^{-1}. The Raman gain shape is described by $N = 14$ Gaussian functions, whose parameters can be found in Table 5.1.

The pump wavelength and pump input SOP were kept fixed, with values $\lambda_p = 1450$ nm and $\hat{p} = [0, 1, 0]^t$, respectively, for all the simulations. On the other hand, the signal wavelength λ_s was swept from 1510 to 1570 nm. For each signal wavelength, we modeled an unpolarized input signal through the generation of $M = 50$ random points over the Poincaré sphere. After solving the coupled differential equations, given by (6.1) and (6.2), for each input signal SOP, we have calculated the DOP of the signal, the mean signal gain, the respective standard deviation, and the mean angle between the signal and pump output Stokes vectors (all obtained from the ensemble of signal input SOPs). The calculation of the DOP was based on the definition presented in (2.24). Hence, the output signal DOP can be written as

$$\text{DOP} = \left(\langle s_1 \rangle^2 + \langle s_2 \rangle^2 + \langle s_3 \rangle^2\right)^{1/2}, \tag{6.12}$$

where $\langle s_i \rangle$, $i = 1,2,3$, represents the average over the ensemble of input signal SOPs, i.e.,

$$\langle s_i \rangle = \frac{1}{M} \sum_{j=1}^{M} \frac{(S_i)_j}{(S_0)_j}, \tag{6.13}$$

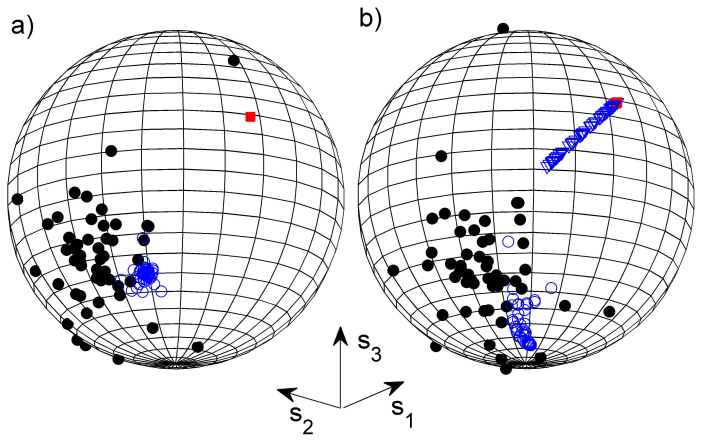

Figure 6.2: a) – Undepleted regime (signal input power equal to 1μW): output pump SOP is represented as a red filled square. b) – Depleted regime (signal input power equal to 1mW): output pump SOPs are represented as red filled squares (for $\lambda_s = 1510$ nm) and blue empty triangles (for $\lambda_s = 1550$ nm). Output SOPs corresponding to unpolarized input signals (SOPs uniformly distributed over the Poincaré sphere) at wavelengths $\lambda_s = 1510$ nm and $\lambda_s = 1550$ nm are represented as black filled and blue empty circles, respectively. Pump at wavelength $\lambda_p = 1450$ nm, input SOP equal to $[0,1,0]^t$, and optical power equal to 8 W.

where $(S_0)_j$ represents the output signal power for the j realization. Notice that with this definition the DOP equals 1 when all the output Stokes vectors have the same locus on the Poincaré sphere. On the other hand, SOPs uniformly distributed over the Poincaré sphere correspond to a DOP equal to 0.

6.4 Results

Two pump regimes were considered in the analysis of the Raman gain based SOP pulling process. In the first case, we analyzed the attraction process using a signal with input power equal to 1 μW in order to avoid saturation of the Raman gain. In the second case, we used an input signal power equal to 1 mW. For this higher signal power the pump depletion effect can be observed, with consequences in terms of the SOP pulling process efficiency.

6.4.1 Undepleted Pump Regime

Different signal-pump wavelength separations result in different SOP pulling efficiencies. This outcome can be observed in Fig. 6.2–a), where two ensembles of output signal SOPs

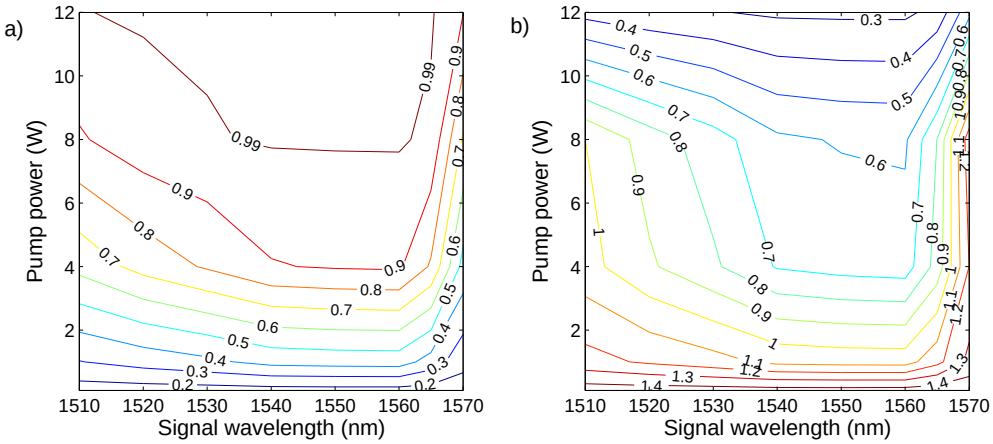

Figure 6.3: a) – Signal output DOP contour map. b) – Contour map of the mean angle in radians between the signal and pump output Stokes vectors. Signal input DOP equal to 0, signal input power equal to 1 μW, and pump wavelength equal to 1450 nm.

are presented, corresponding to two different signal wavelengths. Results show a stronger SOP pulling for the wavelength where the Raman gain is higher, i.e., $\lambda_s = 1550$ nm.

A detailed characterization is obtained if we calculate the DOP for the different pump powers and signal wavelengths. Figure 6.3–a) shows the signal output DOP contour map as a function of the input pump power and signal wavelength. Results show that the DOP increases with the pump power, reaching values close to 1 over the entire wavelength range considered (from 1510 to 1570 nm). Nevertheless, these high DOP values are more difficult to reach for signal wavelengths far away from the maximum Raman gain. In such cases, higher pump powers are required.

The mean angle between the output signal and pump Stokes vectors presents a behavior different to the one presented by the DOP. The contour map presented in Fig. 6.3–b) shows that the smallest mean angle values occur for the highest pump powers: for input pump powers ≥ 9 W and signal wavelengths around 1550 nm the mean angle takes values smaller than 0.5 rad.

Figures 6.4–a) and 6.4–b) show, respectively, the mean signal gain and the respective standard deviation. We should note that in this scenario, i.e., low polarization-mode dispersion (PMD), Raman gain is quite high because signal tends to be co-polarized with respect to the pump. We observe from Fig. 6.4–a) that the mean gain increases with the pump power, presenting a well-known spectrum shape. The highest gain deviations are observed for wavelengths near the maximum mean gain, see Fig. 6.4–b). In terms of pump power, the gain deviation saturates for input pump powers equal to 4 W. Figure 6.5 shows the gain values for the different input signal SOP and different signal wavelengths, assuming a input pump power equal to 4 W.

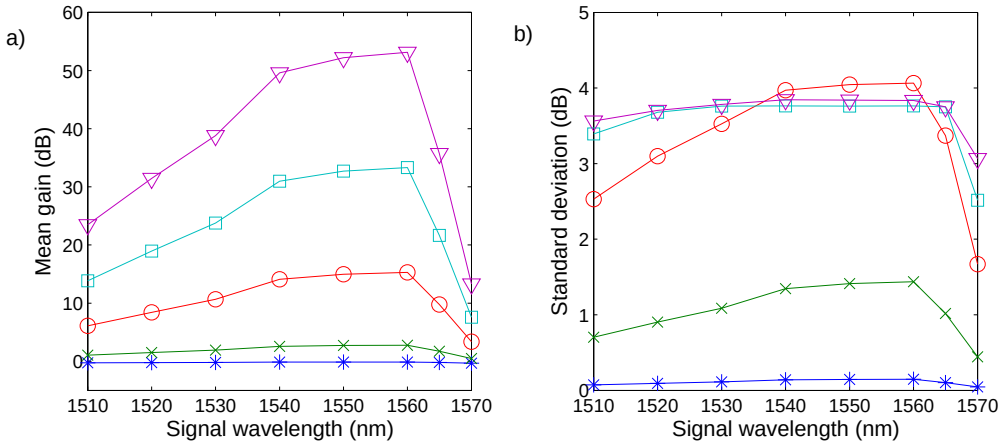

Figure 6.4: a) – Mean signal gain. b) – Standard deviation gain. Input signal power equal to 1 μW, pump wavelength equal to 1450 nm, and pump powers equal to 0.1, 1, 4, 8 and 12 W (asterisks, crosses, circles, squares and triangles, respectively).

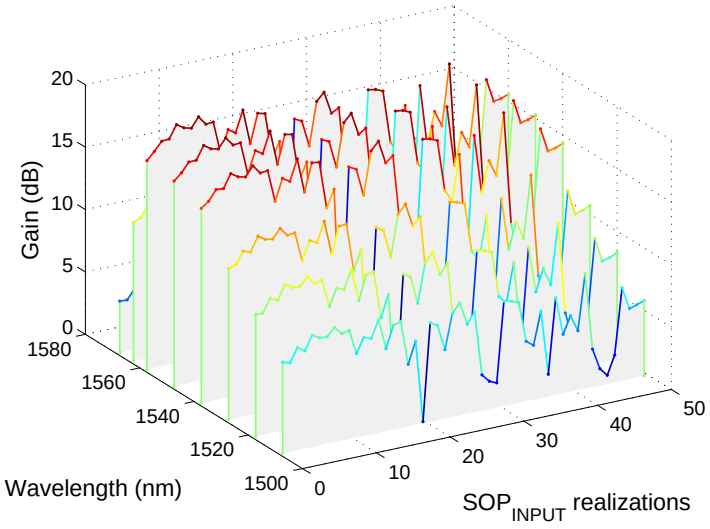

Figure 6.5: Gain map as a function of the signal pump wavelength separation and input signal SOP for a particular pump power $P_p = 4$ W.

6.4.2 Depleted Pump Regime

In order to explore the Raman induced SOP pulling process in a depleted regime, we increased the signal power to 1 mW. For this new scenario, the pulling SOP process is quantitative and qualitatively different of that observed in the previous case, where the input signal power was 1 μW. We found that for pump powers $\geq$ 8 W and high Raman gains the output pump SOP becomes dependent on the input signal SOP. Figure 6.2–b) shows the pump and signal output SOPs, considering a pump power equal to 8 W. For $\lambda_s = 1510$ nm the output pump SOP remains fixed, whereas for $\lambda_s = 1550$ nm it takes

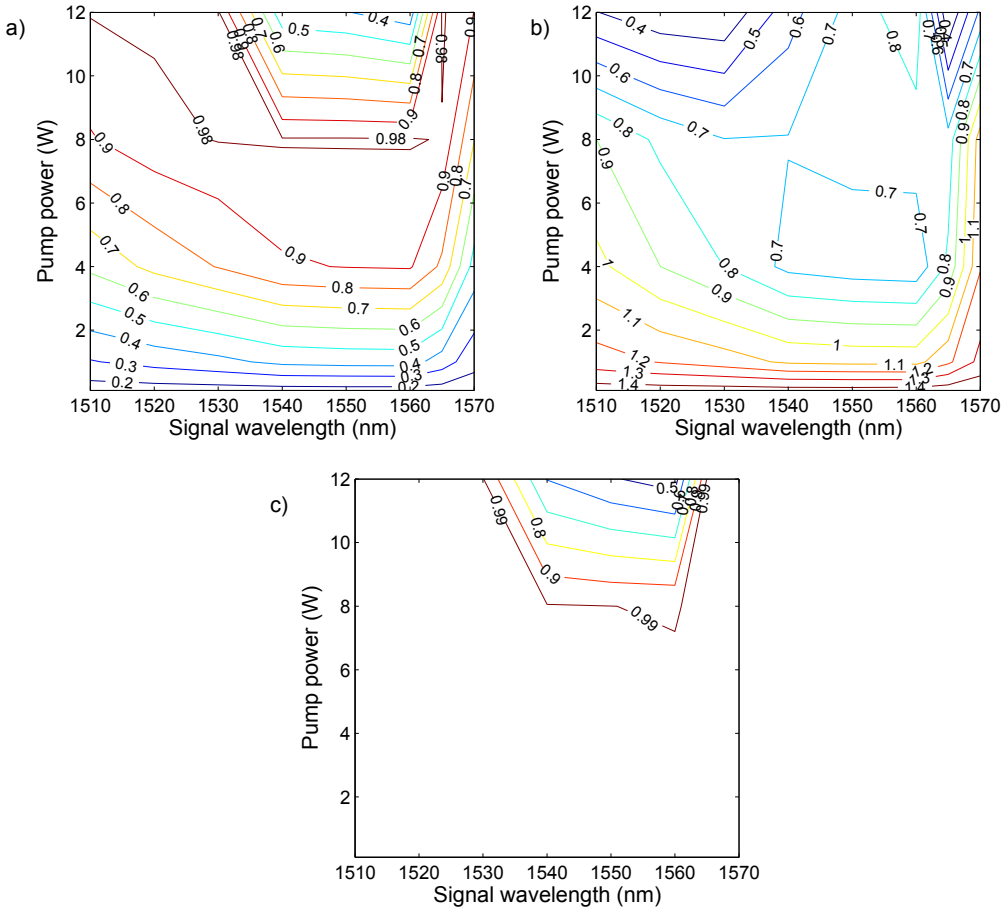

Figure 6.6: a) – Signal output DOP contour map. b) – Contour map of the mean angle in radians between the signal and pump output Stokes vectors. c) – Pump output DOP contour map. Signal input DOP equal to 0, signal input power equal to 1 mW, pump input DOP equal to 1, and pump wavelength equal to 1450 nm.

different values for different input signal SOPs.

Figure 6.6–a) shows the signal output DOP contour map as a function of the input pump power and signal wavelength. Results show that the highest DOP values are no more observed for the highest pump powers. For signal wavelengths between 1535 and 1560 nm, the highest DOP values are observed around 8 W. Figure 6.6–c) shows that the pump DOP becomes smaller than one for pump powers higher than 8 W and signal wavelengths between 1535 and 1560 nm. This result is in agreement with [17], where the same pump power threshold is reported for pump depolarization. From Figs. 6.6–a) and 6.6–c), we can conclude that the reduced SOP pulling efficiency observed for the highest pump powers around the Raman gain peak is related with the pump depolarization. The small mean angle values occur for high pump powers but for signal wavelengths around 1525 nm, see Fig. 6.6–b).

Due to pump depletion, the signal gain at the highest pump powers is smaller than that observed in the previous case (see Figs. 6.7–a) and 6.4–a), respectively). On the

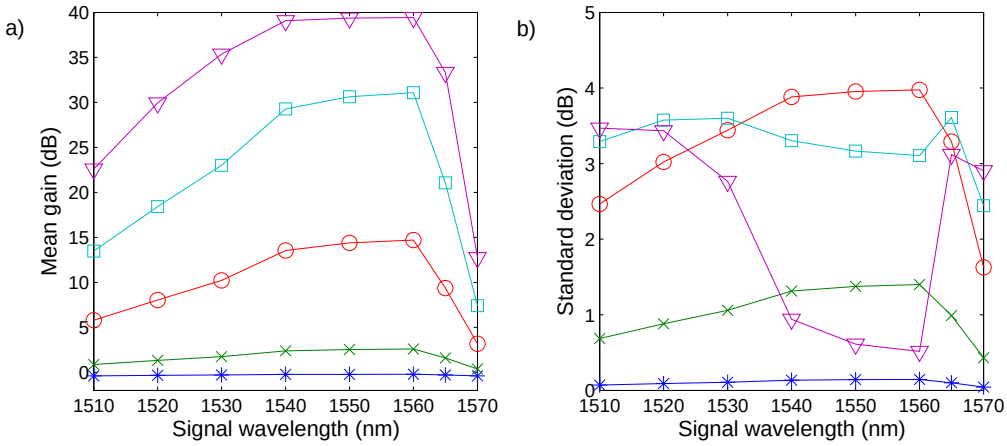

Figure 6.7: a) – Mean signal gain. b) – Standard deviation gain. Signal input power equal to 1 mW, pump wavelength equal to 1450 nm, and pump powers equal to 0.1, 1, 4, 8 and 12 W (asterisks, crosses, circles, squares and triangles, respectively).

other hand, Fig. 6.7–b) shows that the standard deviations around 1550 nm and for pump powers higher than 4 W are smaller when compared with the undepleted case (see Fig.6.4–b)). This means that pump depletion makes the signal gain independent of the input signal SOP.

Although not presented here, we have carried out simulations for $L_B = 35$ m (which gives $D_p = 0.022$ ps/km$^{1/2}$ at 1550 nm) in both depleted and undepleted pump regimes. Our results showed that the Raman pulling process efficiency remains stable into the considered range of PMD values, i.e., from 0.002 up to 0.02 ps/km$^{1/2}$, for both pump regimes.

We modeled pump and signal as continuous waves, neglecting the walk-off effect between pump and signal. Nevertheless, the signal DOP will certainly be influenced by pump power fluctuations. Our signal DOP maps, presented in Figs. 6.3–a) and 6.6–a), show that the domains of smallest gradients (along the y direction - pump power) tend to correspond to the highest DOP values. Therefore, systems operating with a Raman pump in such power range will tend to present an enhanced signal DOP tolerance with respect to pump power fluctuations. Therefore, the signal DOP dependence of pump power fluctuations can in principle be mitigated by choosing an appropriate pump power.

6.5 Summary

We showed that all-optical polarization control based on Raman scattering can be obtained over a wavelength range of 60 nm. This result represents an important advantage of this process over the other all-optical polarization techniques.

In the undepleted regime, the efficiency of the pulling process is higher close to the Raman gain peak, where the DOP is roughly constant for a wavelength range of 15 nm.

For shorter and longer wavelengths, higher pump powers are required in order to assure maximum efficiencies. For instance, a DOP equal to 0.9 is obtained at 1550 nm for a pump power around 4 W, whereas the double power is needed in order to obtain the same DOP at 1510 nm, considering $\lambda_p = 1450$ nm.

In spite of the random pump SOP evolution along the propagation, we also showed that the mean angle between the output signal and pump Stokes vectors becomes smaller when the signal output DOP is close to 1. The output pump SOP information can therefore be used in order to operate on the output signal SOP.

Different results were found in the depleted regime, where the highest DOP values are no more observed for the highest pump powers. For signal wavelengths between 1535 and 1560 nm, the highest DOP values occur for a optimum pump power, which in our case was 8 W. For powers higher than the optimum value, the polarization pulling effect becomes less efficient due to the decrease of the pump DOP.

References

[1] G. P. Agrawal, *Nonlinear Fiber Optics, 4rd ed.* Academic Press, San Diego, USA, 2007.

[2] M. F. Ferreira, *Nonlinear Effects in Optical Fibers.* John Wiley & Sons, Inc, 2011.

[3] M. Martinelli and R. Chipman, "Endless polarization control algorithm using adjustable linear retarders with fixed axes," *IEEE/OSA J. Lightwave Technol.*, vol. 21, no. 9, pp. 2089–2096, Sept. 2003.

[4] M. Martinelli, P. Martelli, and S. M. Pietralunga, "Polarization stabilization in optical communications systems," *IEEE/OSA J. Lightwave Technol.*, vol. 24, no. 11, pp. 4172–4183, 2006.

[5] Y. Liu, H. Chi, X. Zhang, X. Jin, and S. Zheng, "A novel control scheme for four-plate retardation polarization controller," *Microw. Opt. Technol. Lett.*, vol. 51, no. 1, pp. 124–128, 2009.

[6] N. J. Muga, Mário F. S. Ferreira, and A. N. Pinto, "QBER estimation in QKD systems with polarization encoding," *IEEE/OSA J. Lightwave Technol.*, vol. 29, no. 3, pp. 355–361, 2011.

[7] J. N. Damask, *Polarization optics in telecomunications.* Springer, New York, EUA, 2005.

[8] J. E. Heebner, R. S. Bennink, R. W. Boyd, and R. A. Fisher, "Conversion of unpolarized light to polarized light with greater than 50% efficiency by photorefractive two-beam coupling," *Opt. Lett.*, vol. 25, no. 4, pp. 257–259, Feb. 2000.

[9] S. Pitois, A. Picozzi, G. Millot, H. R. Jauslin, and M. Haelterman, "Polarization and modal attractors in conservative counterpropagating four-wave interaction," *EPL Europhys. Lett.)*, vol. 70, no. 1, p. 88, 2005.

[10] E. Assémat, S. Lagrange, A. Picozzi, H. R. Jauslin, and D. Sugny, "Complete nonlinear polarization control in an optical fiber system," *Opt. Lett.*, vol. 35, no. 12, pp. 2025–2027, Jun. 2010.

[11] J. Fatome, S. Pitois, P. Morin, and G. Millot, "Observation of light-by-light polarization control and stabilization in optical fibre for telecommunication applications," *Opt. Express*, vol. 18, no. 15, pp. 15 311–15 317, Jul. 2010.

[12] V. V. Kozlov, J. N. no, J. D. A.-C. nón, and S. Wabnitz, "Theory of fiber optic Raman polarizers," *Opt. Lett.*, vol. 35, no. 23, pp. 3970–3972, Dec. 2010.

[13] S. Pitois, J. Fatome, and G. Millot, "Polarization attraction using counter-propagating waves in optical fiber at telecommunication wavelengths," *Opt. Express*, vol. 16, no. 9, pp. 6646–6651, Apr. 2008.

[14] Q. Lin and G. P. Agrawal, "Statistics of polarization dependent gain in fiber-based Raman amplifiers," *Opt. Lett.*, vol. 28, pp. 227–229, Aug. 2003.

[15] M. Martinelli, M. Cirigliano, M. Ferrario, L. Marazzi, and P. Martelli, "Evidence of Raman-induced polarization pulling," *Opt. Express*, vol. 17, no. 2, pp. 947–955, Jan. 2009.

[16] V. V. Kozlov, J. Nuno, J. D. Ania-Castanon, and S. Wabnitz, "Theoretical study of optical fiber Raman polarizers with counterpropagating beams," *IEEE/OSA J. Lightwave Technol.*, vol. 29, no. 3, pp. 341–347, 2011.

[17] L. Ursini, M. Santagiustina, and L. Palmieri, "Raman nonlinear polarization pulling in the pump depleted regime in randomly birefringent fibers," *IEEE Photonics Technol. Lett.*, vol. 23, no. 4, pp. 254–256, Feb. 2011.

[18] Q. Lin and G. P. Agrawal, "Vector theory of stimulated Raman scattering and its application to fiber-based Raman amplifiers," *J. Opt. Soc. Am. B*, vol. 20, pp. 1616–1631, 2003.

[19] J. Bromage, "Raman amplification for fiber communications systems," *IEEE/OSA J. Lightwave Technol.*, vol. 22, no. 1, pp. 79–93, Jan. 2004.

[20] R. Hellwarth, J. Cherlow, and T.-T. Yang, "Origin and frequency dependence of nonlinear optical susceptibilities of glasses," *Phys. Rev. B*, vol. 11, pp. 964–967, 1975.

[21] A. Galtarossa, L. Palmieri, M. Schiano, and T. Tambosso, "Measurement of birefringence correlation length in long, single-mode fibers," *Opt. Lett.*, vol. 26, no. 13, pp. 962–964, Jul. 2001.

[22] P. K. A. Wai and C. R. Menyuk, "Polarization mode dispersion, decorrelation, and diffusion in optical fibers with randomly varying birefringence," *IEEE/OSA J. Lightwave Technol.*, vol. 14, no. 2, pp. 148–157, 1996.

[23] A. Galtarossa, L. Palmieri, M. Santagiustina, and L. Ursini, "Polarized backward Raman amplification in randomly birefringent fibers," *IEEE/OSA J. Lightwave Technol.*, vol. 24, no. 11, pp. 4055–4063, Nov. 2006.

[24] M. Fugihara and A. N. Pinto, "Low-cost Raman amplifier for CWDM systems," *Microw. Opt. Technol. Lett.*, vol. 50, pp. 297–301, Feb. 2008.

[25] M. Fugihara and A. N. Pinto, "Attenuation fitting functions," *Microw. Opt. Technol. Lett.*, vol. 51, pp. 2294–2296, Oct. 2009.

[26] M. S. Miguel and R. Toral, *"Stochastic effects in physical systems", in Instabilities and Nonequilibrium Structures IV.* Ed. E. Tirapegui and W. Zeller, Kluwer Academic, 1997.

Chapter 7

Polarization-Encoded QKD Systems

A model for quantum bit error rate (QBER) estimation in polarization-encoded quantum key distribution (QKD) systems with state of polarization (SOP) control is presented in this Chapter. Both time-division multiplexing (TDM)- and wavelength-division multiplexing (WDM)-based SOP control schemes are analyzed. It is shown that the TDM-based scheme presents some important advantages when compared with the WDM-based scheme. The polarization decorrelation between reference and data signals is identified as an intrinsic and very limitative impairment in the WDM-based SOP control scheme. The contribution of this effect to the QBER depends on the fiber polarization-mode dispersion (PMD), and increases with the propagation distance. It is also shown that the polarization decorrelation does not affects the operation of the TDM-based SOP control scheme. In this kind of SOP control, other issues, like single-photon detector dark counts, afterpulse detections or the feedback polarization control system performance, are identified has important technical impairments. Moreover, we show that for long distances the fiber losses represent the main contribution to the total QBER. For distances shorter than 70 km and frequencies higher than 5 MHz, the afterpulse detections provide an important contribution to the total QBER.

7.1 Introduction to QKD systems

QKD uses the laws of quantum mechanics in order to assure an unconditional secure distribution of secret keys between two parties (Alice and Bob) [1]. The first QKD protocol was developed in 1984 by Bennet and Brassard [2] and, eight years later, Bennett *et al.* [3] have reported the first QKD experiment using a 32-cm free-space transmission line. Since that pioneer work, several new experiments were presented and nowadays it is possible to share quantum information through telecom fibers for distances longer than 100 km [4, 5].

The implementation of the QKD protocols (for instance the protocol developed by Charles Bennett and Gilles Brassard in 1984 (BB84) [2], or that developed by Charles Bennett in 1992 (B92) [6]) can be performed encoding quantum bits into the polarization of single photons [1, 7–12]. Notice, however, that the photon SOP evolution is highly

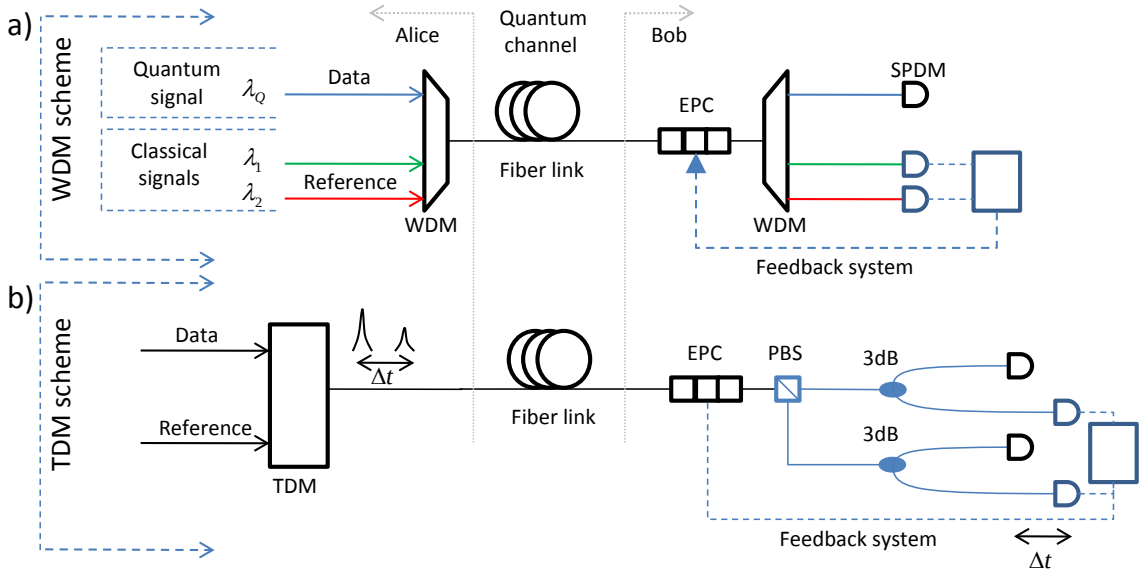

Figure 7.1: Schematic representation of TDM- and WDM-based dynamic polarization control schemes for polarization-encoded QKD systems in optical fibers: a) – WDM-based SOP controller scheme, two non-orthogonal classical signals at different wavelengths are used as reference signals; b) – TDM-based SOP controller scheme, data and reference pulses are multiplexed in the time domain. EPC – Electronic polarization controller, SPDM – Single-photon detector module, and PBS – polarization beam splitter.

dependent on the environmental conditions and on the physical characteristics of the optical channel, in particular PMD [13]. As stated in Chapter 2, the SOP evolution has a random behavior in time and frequency domains [14, 15]. Nevertheless, if the effects of polarization-dependent losses (PDL) are negligible, the relation between the SOP at the fiber input and at the fiber output is unitary [16]. This means that the SOP changes can be reversed by compensating two non-orthogonal SOPs [16–18].

In order to make polarization-encoded QKD feasible, both WDM- and TDM-based SOP control schemes can be used as practical solutions [8, 18–22]. Figure 7.1 shows a schematic representation of this kind of SOP control schemes. In the WDM-based scheme, two non-orthogonal classical signals at different wavelengths are used as reference signals, see Fig. 7.1–a), while in the TDM-based SOP control scheme data and reference pulses are multiplexed in the time domain, see Fig. 7.1–b). Notice that the influence of the SOP compensation system on the quantum channel should be avoided or, at least, minimized. This is an important aspect to evaluate the global performance of a SOP control system [1]. When co-propagating into the fiber, reference and data signals should be uncorrelated, otherwise any eavesdropping of the reference pulses will affect the security of the communication.

An active full polarization control scheme using two classical signals at different wavelengths is reported in [20]. Using an improved WDM control scheme, the same authors demonstrated a QKD system over 16 km of optical fiber [22]. The SOP control can also

be performed using the same wavelength for both reference and data signals, and in such case the system should be able to alternate between data communication and the reference signals (TDM-based SOP control scheme). Following that technique, a method and device for readjusting the polarization drift in the QKD systems was already patented [18]. These setups can be implemented using classical signals [18], where a switch alternates between the transmission of polarization-encoded signals and the SOP control system, or using pulses with a low mean number of photons per pulse [8, 19]. In [21], it is presented an incremental real-time polarization control scheme where the reference and signal pulses are time delayed. These systems assure a continuous transmission of quantum data information with real-time polarization control. A maximum transmission distance of 50 km is reported.

Here, we present a model for QBER estimation in polarization-encoded QKD systems with TDM- and WDM-based polarization control schemes. In both cases, we analyze the different contributions to the total QBER, and compare the results of our model with the experimental data presented in the literature. For the WDM-based scheme implementation, the decorrelation between the reference and data signal reveals to be a fundamental impairment. In the TDM-based scheme, we analyze the time autocorrelation function (ACF) of the Stokes vector, the cross-talk between reference and data signals, and the afterpulse probability detection.

7.2 WDM-Based SOP Control Scheme

In a WDM-based SOP control scheme the three wavelengths, corresponding to two reference signals and the quantum signal, can be combined into the fiber using an optical multiplexer (MUX). After propagation, they can be separated using an optical de-multiplexer (DMUX) (see Fig. 7.1–a)). However, the polarization decorrelation between the different wavelengths is an important drawback of such schemes. In this Section, we present a theory able to describe the WDM control scheme performance.

7.2.1 Wavelength Polarization Correlation

Generally, when two signals with different wavelengths are launched into an optical fiber their SOPs evolve differently [14]. The correlation along propagation between the SOPs of two signals depends on their wavelength separation. One way to assure a strong SOP correlation is to use a narrow wavelength separation between them [23, 24]. However, the use of very narrow wavelength separations presents problems in terms of channels isolation, requiring also a good performance in terms of the laser line stability. If we aim to build an experimental SOP control setup using standard telecom components, the choice of the signal wavelengths should account for the standard wavelength separation values. In the following we assume a wavelength separation equal to 0.8 nm [25].

The SOP of a light beam can be represented in the 3D Stokes space through a Stokes vector. As stated in Section 2.4, the degree of correlation along propagation between two Stokes vectors at different frequencies, ω_1 and ω_2, can be characterized by the respective

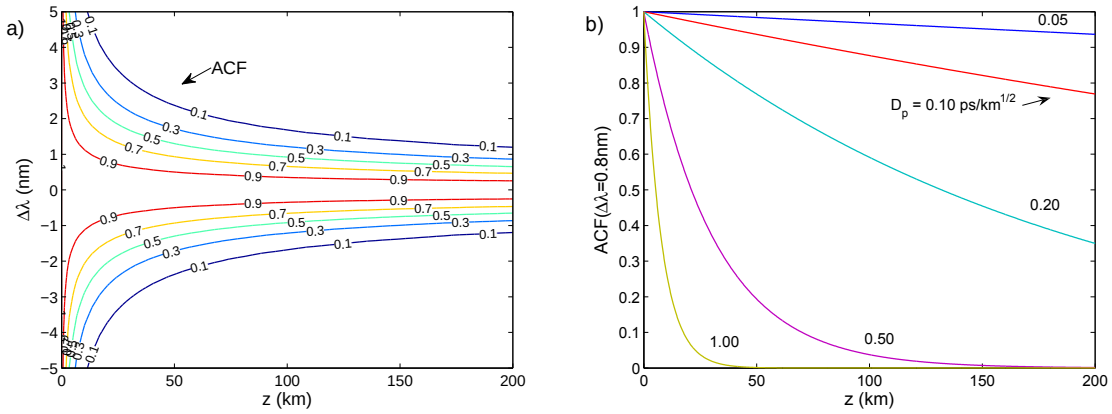

Figure 7.2: a) – Frequency ACF map of the Stokes vector $\hat{s}$ as a function of the wavelength separation and the propagation distance, assuming a PMD equal to $D_p = 0.2$ ps/km$^{1/2}$. b) – Frequency ACF of the Stokes vector as a function of the distance assuming a wavelength separation equal to 0.8 nm, for different D_P values.

ACF [14]. The ACF defined in (2.66) can be expressed explicitly as a function of the distance z as follows

$$\mathrm{ACF}(z, \Delta\omega) = \langle \hat{s}(z, \omega_1) \cdot \hat{s}(z, \omega_2) \rangle = \exp\left(\frac{-D_p^2 \, z \, \Delta\omega^2}{3} \right), \tag{7.1}$$

where $\Delta\omega = \omega_2 - \omega_1$ is the frequency separation, $\hat{s}(z, \omega_1)$ and $\hat{s}(z, \omega_2)$ are the SOPs at ω_1 and ω_2, respectively, and D_p is the PMD coefficient. If two signals are launched into an optical fiber their ACF assumes the maximum value at the fiber input (equal to 1), and as the signals propagate their ACF tends to zero due to the statistically independent SOPs evolution. Concerning the frequency, this function tells how large a frequency separation is necessary for two signal SOPs become statistically uncorrelated.

The ACF map represented in Fig. 7.2–a) shows the correlation between two Stokes vectors as a function of the wavelength separation, $\Delta\lambda$, and the propagation distance, z, assuming a particular PMD value ($D_p = 0.2$ ps/km$^{1/2}$). The level curves show that the correlation decreases quickly with the propagation distance and the wavelength separation. For distances longer than 20 km the high degree of correlation events only occurs for narrow wavelength separations (much smaller than 0.8 nm). Figure 7.2–b) shows the ACF of the SOP as a function of the distance for different values of D_P, and assuming a wavelength separation equal to 0.8 nm. Results show that for this wavelength separation the correlation decreases quickly, namely for the highest PMD values. In fact, even for a fiber with $D_p = 0.1$ ps/km$^{1/2}$, the maximum distance for which the polarization of two signals separated by 0.8 nm will be highly correlated (ACF$\geq$90%) is 80 km.

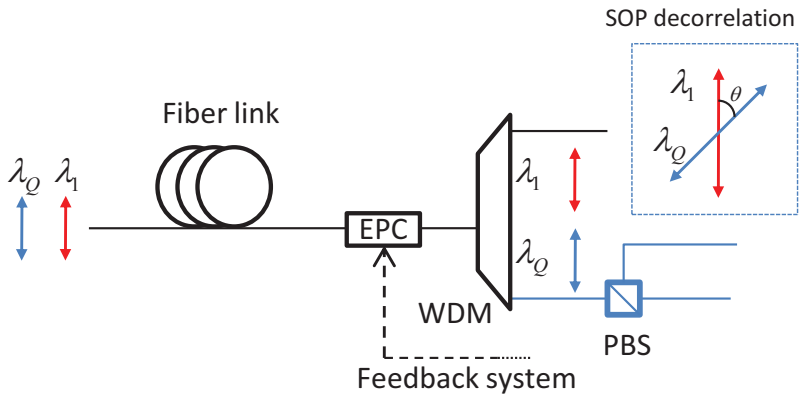

Figure 7.3: Schematic diagram of a WDM-based SOP control scheme for QKD systems with polarization encoding. The quantum and reference signals are represented by λ_Q and λ_1, respectively (only one reference signal is represented).

7.2.2 QBER Model

The receiver (Bob) of a general WDM based SOP control scheme for QKD system is presented in Fig. 7.3. We are going to assume that the active control scheme is able to perform an ideal SOP control of the reference signals. Therefore, the electronic polarization controller (EPC) placed at the receiver will be able to completely reverse the SOP rotation suffered by the two reference signals at wavelengths λ_1 and λ_2 (see Fig. 7.3, where only one reference signal is represented for convenience). In order to explain the model, we consider that the reference signal at λ_1 has a vertical linear polarization. If all signals are ideally correlated, then the quantum signal SOP evolution is also completely compensated. Nevertheless, the reference and quantum signals are launched at different wavelengths and therefore their SOPs present a degree of correlation lower than 100%. Therefore, the full control of the reference signal SOP cannot assure an absolute control of the quantum signal SOP.

The ACF of the SOP, given by (7.1), can be used to estimate the angle between the two vectors and then the QBER contribution due to the decrease on the polarization correlation. Using the definition of the inner product, and since the Stokes vectors $\hat{s}(z,\omega_1)$ and $\hat{s}(z,\omega_Q)$ are unit vectors, the ACF can be written as:

$$\mathrm{ACF}(z,\Delta\omega) = \langle \hat{s}(z,\omega_1)\cdot\hat{s}(z,\omega_Q)\rangle = \langle\cos\phi\rangle, \tag{7.2}$$

where ϕ represents the angle between the two SOP vectors in the 3D Stokes space [26]. As we are assuming that reference signal SOP, $\hat{s}(\lambda_1)$, is completely compensated, then it is well defined. On the other hand, equation (7.2) defines an ensemble of the most probable quantum signal SOP, $\hat{s}(\lambda_Q)$. The Stokes vectors verifying (7.2) define on the Poincaré sphere a circumference centered on the axis defined by the Stokes vector of the reference signal (which in this case is given by $\hat{s}(\lambda_1) = [-1,0,0]^t$). The most probable Stokes vectors of the quantum signal have the same value of the first Stokes parameter $s_1(\lambda_Q)$;

this means that in the 2D space their polarization ellipsis have the same projection on the horizontal and vertical axis.

Photons with a general polarization can be described by [27]

$$|\psi_g\rangle = \sin\theta \mathrm{e}^{i\psi_x}|x\rangle + \cos\theta \mathrm{e}^{i\psi_y}|y\rangle, \tag{7.3}$$

where $|x\rangle$ and $|y\rangle$ represent the states of the photons that exit through the horizontal and vertical polarization beam splitter (PBS) ports, respectively, θ is related with the polarization ellipsis projection, and ψ_x and ψ_y are the phases of the horizontal and vertical components, respectively. Such photons have the probability

$$p_h = |\langle x|\psi_g\rangle|^2 = 1 - \cos^2\theta, \tag{7.4}$$

to follow through the horizontal PBS port, and the probability

$$p_v = |\langle y|\psi_g\rangle|^2 = \cos^2\theta, \tag{7.5}$$

to follow through the vertical PBS port. Note that these probabilities are only dependent on θ, which means that all quantum signal SOP verifying (7.2) have indeed the same probability to follow to the wrong port of the PBS. In order to use the information given by the ACF into the calculation of p_h and p_v we should find a relationship between "$\langle\cos\phi\rangle$" and the term "$\cos^2\theta$" appearing in (7.4) and (7.5). Knowing that angles in the 2D Jones and in the 3D Stokes spaces are related by a factor of two, i.e. $\theta = \phi/2$, we can use the following double angle trigonometric identity

$$\cos 2u = 2\cos^2 u - 1. \tag{7.6}$$

After applying the average operator on (7.6), and solving it in order to $\langle\cos^2\theta\rangle$, we have

$$\langle\cos^2\theta\rangle = \frac{1}{2}(1 + \langle\cos\phi\rangle). \tag{7.7}$$

Using (7.1) and (7.2) into (7.7), we obtain

$$\langle\cos^2\theta\rangle = \frac{1}{2} + \frac{1}{2}\exp\left(\frac{-D_p^2\, z\, \Delta\omega^2}{3}\right). \tag{7.8}$$

For strongly correlated SOPs we have $\langle\cos^2\theta\rangle = 1$, whereas for SOPs completely uncorrelated we have $\langle\cos^2\theta\rangle = 1/2$. Therefore, the probability of a photon to follow through the wrong PBS port can be written as

$$p_{\mathrm{fACF}} = \frac{1}{2} - \frac{1}{2}\exp\left(\frac{-D_p^2\, z\, \Delta\omega^2}{3}\right). \tag{7.9}$$

The QBER is defined as the ratio between the number of wrong detections, N_{wrong},

and total detections, $N_{\text{total}} = N_{\text{right}} + N_{\text{wrong}}$. In terms of rates, we have [1]

$$\text{QBER} = \frac{N_{\text{wrong}}}{N_{\text{right}} + N_{\text{wrong}}} = \frac{R_{\text{error}}}{R_{\text{sift}} + R_{\text{error}}}, \tag{7.10}$$

where R_{error} represents the rate of error and R_{sift} is the rate of the sifted key. Due to the incompatible choice of bases $R_{\text{sift}} = 1/2R_{\text{raw}}$, where R_{raw} is the rate corresponding to the raw key. The raw key rate can be written as [1]

$$R_{\text{raw}} = f_{\text{rep}} \langle n \rangle t_{\text{link}} \eta_{\text{det}}, \tag{7.11}$$

where f_{rep} is the pulse rate, $\langle n \rangle$ is the mean number of photons per pulse, η_{det} is the detector efficiency, and $t_{\text{link}} = 10^{-\alpha z/10}$ is the transmission efficiency (α and z are the fiber losses and length, respectively). The total error rate can be written as

$$R_{\text{error}} = R_{\text{fACF}} + R_{\text{dc}}, \tag{7.12}$$

where R_{fACF} represents the error rate contribution due to the frequency decorrelation between reference and data SOPs, and R_{dc} represents the contribution due to dark counts. The contribution due to the decorrelation is given by

$$R_{\text{fACF}} = R_{\text{sift}} p_{\text{fACF}}, \tag{7.13}$$

where p_{fACF} is the probability of a photon to be detected in the wrong detector, given by (7.9). The R_{dc} contribution is given by [1]

$$R_{\text{dc}} = \frac{1}{4} f_{\text{rep}} P_{\text{dc}} n_{\text{det}}, \tag{7.14}$$

where n_{det} is the number of detectors, P_{dc} is the dark count probability, and the 1/4 factor is related with the choice of incompatible bases, which contributes with one half, and with the chance of occurring in the correct detector, which contributes with another one half. Using the last four equations into (7.10), we obtain [28]

$$\text{QBER} = \text{QBER}_{\text{fACF}} + \text{QBER}_{\text{dc}} \tag{7.15}$$

$$\begin{aligned} =& \frac{1 - \exp\left(\dfrac{-D_p^2 z \, \Delta\omega^2}{3}\right)}{3 - \exp\left(-\dfrac{D_p^2 z \, \Delta\omega^2}{3}\right) + \dfrac{P_{\text{dc}}}{\langle n \rangle t_{\text{link}}}} \\ &+ \frac{P_{\text{dc}}}{\langle n \rangle t_{\text{link}} \left[3 - \exp\left(-\dfrac{D_p^2 z \, \Delta\omega^2}{3}\right)\right] + P_{\text{dc}}}. \end{aligned} \tag{7.16}$$

Figure 7.4 shows a map of the total QBER, given by (7.16), as a function of the distance, z, and of the PMD coefficient, D_p, assuming a wavelength separation equal to

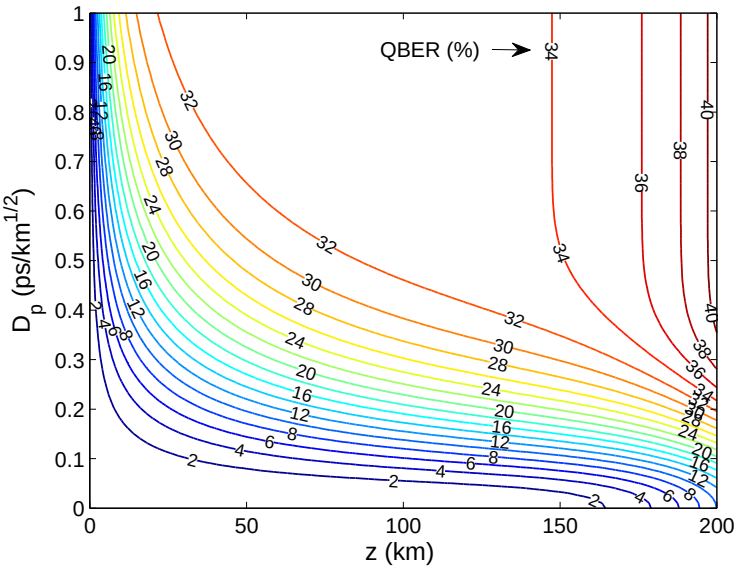

Figure 7.4: QBER estimation map for WDM-based SOP control scheme as a function of the distance and PMD coefficient, D_p, assuming a wavelength separation equal to 0.8 nm.

0.8 nm. Our model shows that errors are strongly dependent on D_p. For high D_p values (≥ 0.5 ps/km$^{1/2}$), the QBER grows quickly, reaching values higher than 30% for relatively short distances ($\sim$60 km). Between 60 km and 150 km, the QBER is almost constant, nevertheless, for distances longer than 150 km it starts to increase. In this regime, the transmission efficiency is strongly reduced by fiber losses, making the QBER_{dc} dominant. For PMD coefficients smaller than 0.1 ps/km$^{1/2}$, the QBER presents low values for short distances, however for long distances the transmission efficiency decreases and the QBER_{dc} contribution induces also an exponential increment on the total QBER. When the QBER_{dc} contribution is small, the PMD coefficient plays an important role if we aim to increase the length of the quantum channel.

Assuming for instance a fiber length equal to 8.4 km and a $D_p = 0.2$ ps/km$^{1/2}$ (values corresponding to the experimental conditions reported in [20]), the QBER given by (7.16) takes the value 2.1%, whereas assuming a fiber length equal to 16 km and a $D_p = 0.076$ ps/km$^{1/2}$ (values corresponding to the experimental conditions reported in [22]) the QBER takes the value 0.6%. Note that the use of a fiber with the $D_p = 0.2$ ps/km$^{1/2}$ for a distance equal to 16 km will double (from 2.1% to $\sim$4%) the QBER value obtained for 8.4 km. This is in agreement with the experimental results reported in [20] and [22]. Indeed, our results show that the loss of correlation between reference and data signals due to the increment of distance cannot be compensated with an improved WDM-based SOP control system.

From de above discussion, we can conclude that the use of fibers with low PMD values is mandatory if we aim to design a system with a low QBER, based on a WDM SOP control scheme.

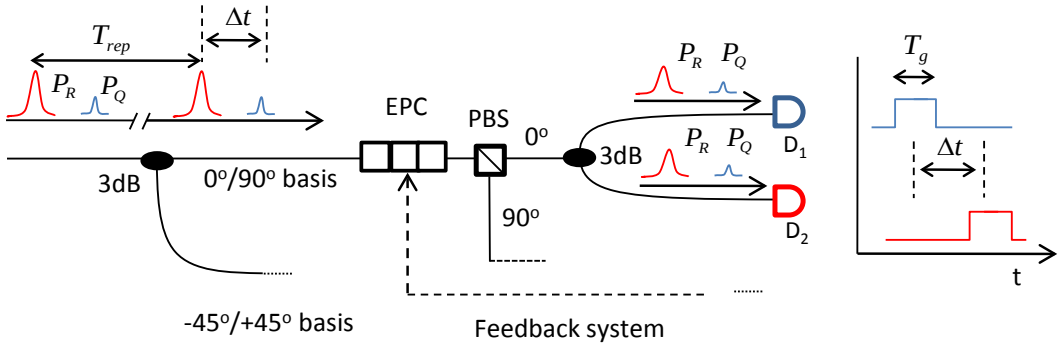

Figure 7.5: Schematic representation of the TDM-based SOP control scheme. Reference and quantum signals are time multiplexed: after passing through the PBS, the signals are split and are both present in the data (D_1) and reference (D_2) arms. Data and reference gates are delayed by Δt, which corresponds to the data and reference pulses delay.

7.3 TDM-Based SOP Control Scheme

In this section, we present a model for the estimation of the QBER, taking in account the main impairments of TDM-based SOP control scheme. The receiver (Bob) of a general QKD control scheme based on TDM is illustrated in Fig. 7.5. Reference and data signals are time multiplexed and separated by Δt (the time multiplexing can be preformed for instance using an asymmetric Mach-Zehnder interferometer, or using a parallel and synchronized reference pulses source). A correct synchronization of detector gates assures that data and reference pulses are detected at D_1 and D_2, respectively. The feedback system uses the count records of D_2 to actuate on the EPC in order to align the input photons with vertical polarization with the vertical port of the PBS.

7.3.1 Time Polarization Correlation

Generally, when two pulses with the same wavelength are launched into an optical fiber at different time instants their SOPs evolve differently [14, 29]. The correlation between the two SOPs depends on its time separation. As stated in Section 2.4, the time ACF is defined as the average dot product between two Stokes vectors, representing the polarization of the same wave, at a position z inside the fiber, separated by a time interval δt [14]. The time ACF defined in (2.65) can be expressed explicitly as a function of the distance z,

$$\mathrm{ACF}(z,\delta t) = \langle \hat{s}(z,t_1)\cdot\hat{s}(z,t_2)\rangle = \exp\left(\frac{-3\omega^2 D_p^2\, z\,|\delta t|}{2t_0}\right). \tag{7.17}$$

The ACF assumes the maximum value at the fiber input, and as the signal propagates the ACF tends to zero. This function tells how large a time separation between two pulses must be in order to make their SOP uncorrelated after propagation over a distance z.

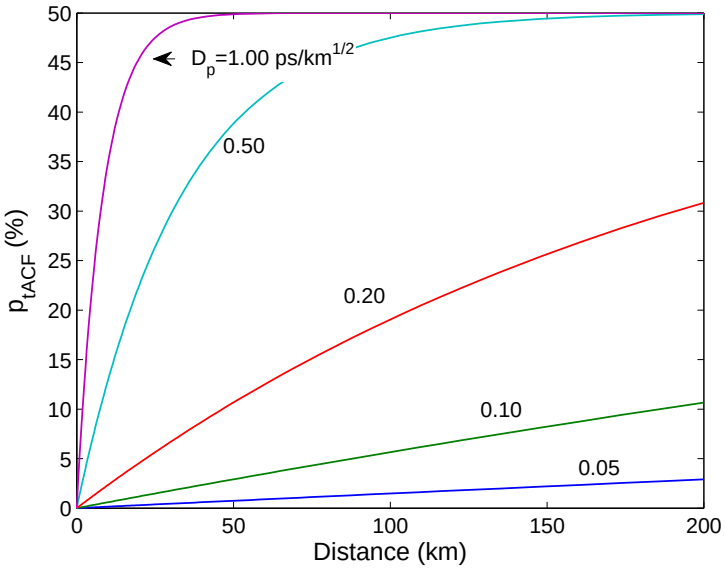

Figure 7.6: QBER in a system with a TDM-based SOP control scheme due to the SOP decorrelation as a function of the distance, assuming different values of D_p and a time delay equal to 1 μs.

Therefore, for a particular value of t_0, the changes on the SOP will be faster for longer fibers and higher PMD coefficients.

Since the data pulses arrive first at the PBS (see Fig. 7.5), the time delay at this point between the last reference pulse and the next data pulse will be $\delta t = T_{\text{rep}} - \Delta t$, where $T_{\text{rep}} = 1/f_{\text{rep}}$. Then, after passing through the EPC, reference photons will follow the correct port of the PBS. On the other hand, data photons will present a nonzero probability to follow through the wrong port that depends on the time ACF. The reference and data Stokes vectors will present an angle ϕ between them, verifying the following expression

$$\langle \cos\phi \rangle = \exp\left(\frac{-3\omega^2 D_p^2\, z\, |\delta t|}{2t_0}\right). \tag{7.18}$$

Using the previous expression in conjugation with (7.7) into (7.4), we obtain the probability of a photon follow through the wrong port due to time decorrelation between reference and data pulses

$$p_{\text{tACF}} = \frac{1}{2} - \frac{1}{2}\exp\left(\frac{-3\omega^2 D_p^2\, z\, |\delta t|}{2t_0}\right). \tag{7.19}$$

Figure 7.6 shows the error contribution given by (7.19) as a function of the distance, for different values of D_p. The stronger penalties in terms of QBER occur for the highest PMD coefficients. Results also show that, within the plotted distance range, systems

with low PMD present a QBER that grows linearly with the distance.

7.3.2 Feedback SOP Control Model

In contrast with the WDM-based control scheme, where a large number of photons can be used in the control system, the TDM-based control scheme uses a low number of photons. Besides that, the reference and data signals are time multiplexed, making the performance of the feedback SOP control system dependent of the pulse rate [21]. We account for this aspect by modeling the angle between the obtained and the target SOP in the Stokes space as

$$\theta = \Theta(1 - \exp(-gT_{\text{rep}})), \tag{7.20}$$

where Θ is the angle without the feedback SOP control, and $1/g$ is the characteristic time decay of the obtained SOP to Θ. For high values of pulse rates the SOP at the EPC output will be close to the target value, i.e. $\theta \to 0$, whereas for low rates the SOP will present a random value in the Poincaré sphere, i.e. $\theta \to \Theta$. Note that for a uniform distribution of SOPs over the sphere $\Theta = \pi/2$ rad [30]. Using (7.20) into (7.4), we obtain the following expression for the errors due to the imperfect operation of the feedback SOP control

$$p_{\text{SOP}} = 1 - \cos^2\left[\frac{1}{2}\Theta(1 - \exp(-gT_{\text{rep}}))\right]. \tag{7.21}$$

The error probability given by (7.21) is illustrated in Fig. 7.7 assuming $\Theta = \pi/2$. Results show that, independently of the g value, the QBER contribution due to the feedback SOP control can be minimized if a high pulse rate is used.

7.3.3 Cross-Talk Between Reference and Data Signals

TDM-based SOP control schemes can also lead to the leakage of photons from the reference to data pulses. In this scheme, reference and quantum signals are time multiplexed, and both signals are present in the data and reference arms (see Fig. 7.5). Therefore, in order to select the correct pulse, detectors D_1 and D_2 have the respective gates delayed by Δt, i.e. the time separation between quantum and reference pulses. The probability of photons traveling in the reference pulse being detected at D_1 due to the cross-talk, p_{leak}, will be dependent on the reference pulse shape, data gate width, and temporal separation, Δt, between the reference and data signals. We can write

$$p_{\text{leak}} = \eta_{\text{det}} t_{\text{link}} \langle n_g \rangle, \tag{7.22}$$

where $\langle n_g \rangle = A\langle n_r \rangle$ is the mean number of reference photons per pulse leakage to the data detector gate, with $\langle n_r \rangle$ being the mean number of reference photons per pulse, and the parameter A the fraction of photons that are leakage to the wrong detector.

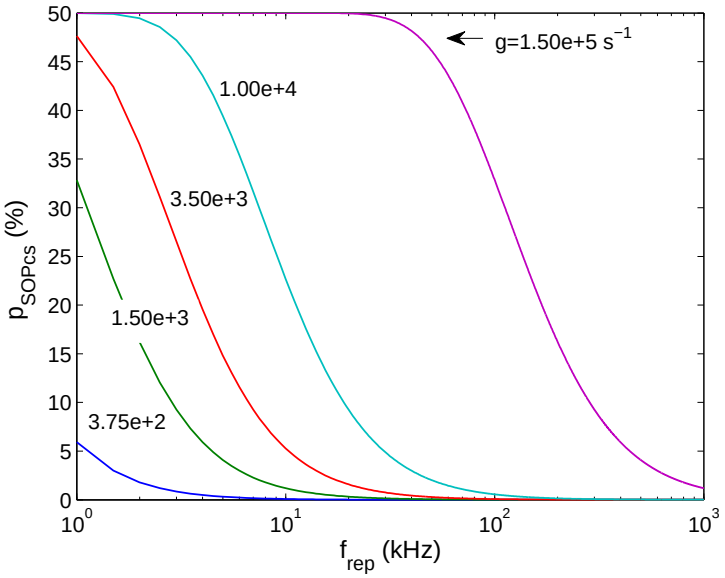

Figure 7.7: Feedback SOP control QBER contribution as a function of the pulse rate, for different values of the characteristic parameter g and assuming $\Theta = \pi/2$.

Considering a data gate width equal to T_g, and that the center of the data gate and the center of the reference pulse are separated by Δt, the coefficient A is given by

$$A = \int_{\Delta t - T_g/2}^{\Delta t + T_g/2} |f(t)|^2 \, dt, \tag{7.23}$$

where $\int_{t_1}^{t_2} |f(t)|^2 \, dt$ represents the probability of a photon be detected in the interval $t_1 - t_2$, and $f(t)$ is related with the pulse shape. Note that $f(t)$ should be a normalized function, i.e., if $t_1 \to -\infty$ and $t_2 \to +\infty$ then $\langle n_g \rangle \to \langle n_r \rangle$. Assuming a Gaussian pulse shape $f(t) = 1/(T_p\sqrt{\pi})^{1/2} \exp(-t^2/(2T_p^2))$, then A is given by

$$A = \frac{1}{2}\left[\text{erf}\left(-\frac{(2\Delta t - T_g)}{2T_p}\right) + \text{erf}\left(\frac{(2\Delta t + T_g)}{2T_p}\right)\right], \tag{7.24}$$

where T_p is the half-width at $1/e$-intensity of $f(t)$, which is related with the pulse full width at half maximum (FWHM) by $T_{\text{FWHM}} = 2\sqrt{\ln 2}T_p$. In order to account for the pulse broadening due to chromatic dispersion, we should replace T_p in (7.24) by

$$T_p(z) = T_p\left[1 + (z/L_D)^2\right]^{1/2}, \tag{7.25}$$

where $L_D = T_p^2/|\beta_{\omega\omega}|$ is the dispersion length [13]. In the case of $f(t)$ shape being represented by a hyperbolic secant function, then A is given by

$$A_{\text{sh}} = \frac{1}{2}\left[\tanh\left(\frac{2\Delta t + T_g}{2X}\right) - \tanh\left(\frac{2\Delta t - T_g}{2X}\right)\right], \tag{7.26}$$

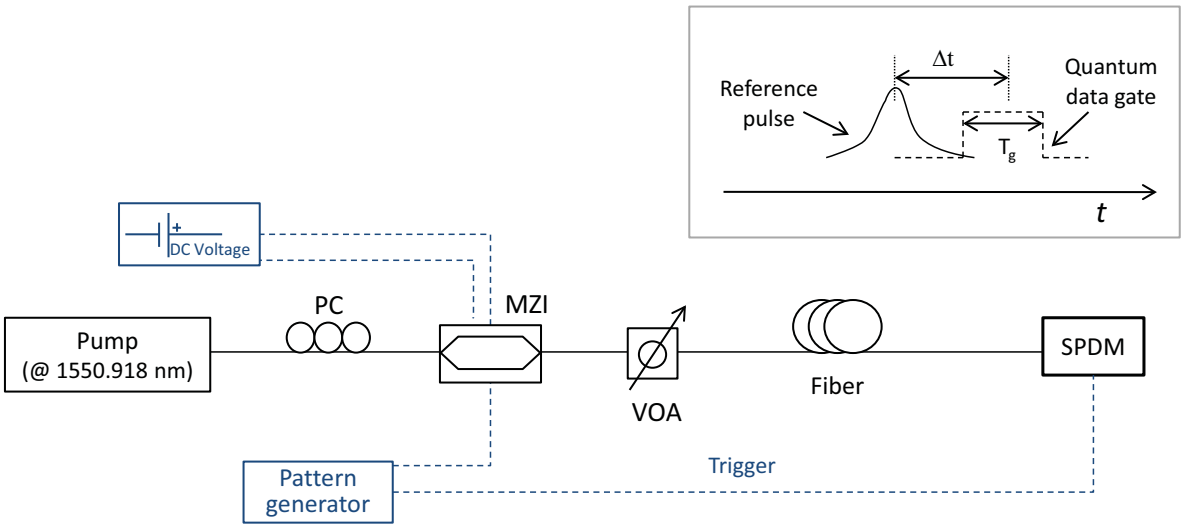

Figure 7.8: Experimental setup used to measure the leakage of reference photons to the gate of the data detector: PC – polarization controller, MZI – Mach-Zehnder interferometer, VOA – variable optical attenuator, and SPDM – single-photon detector module. A reference pulse and the data detector gate are schematically represented in the inset.

with

$$X = \frac{T_{\mathrm{FWHM}}(f^2)}{2\ln(1+\sqrt{2})}, \tag{7.27}$$

where $T_{\mathrm{FWHM}}(f^2)$ represents the FWHM of $(f(t))^2$.

Experimental validation

Assuming, for instance, that the quantum pulse is removed, then the total number of counts on the quantum data detector due to reference pulse leakage is given by [31]

$$N = f_{\mathrm{rep}} P_{\mathrm{click}} = f_{\mathrm{rep}}(p_{\mathrm{leak}} + P_{\mathrm{dc}} - p_{\mathrm{leak}} P_{\mathrm{dc}}), \tag{7.28}$$

where P_{click} is the click probability, and p_{leak} is given by (7.22).

In order to analyze the separation between reference pulses and polarization-encoded photons we have used the experimental setup schematically represented in Fig. 7.8. Reference pulses were obtained through a continuous wave (CW) source, centered at 1550.918 nm, whose light was pulsed using a Mach–Zehnder interferometer (MZI). At the MZI output a variable optical attenuator (VOA) reduces the mean number of photons per pulse to a value lower than 1 [32]. An accurately triggered single-photon detector module (SPDM), operating in a gated Geiger mode [33], is used to measure the photon counts.

The photon-counts given by (7.28) are represented in Fig. 7.9 as a function of time

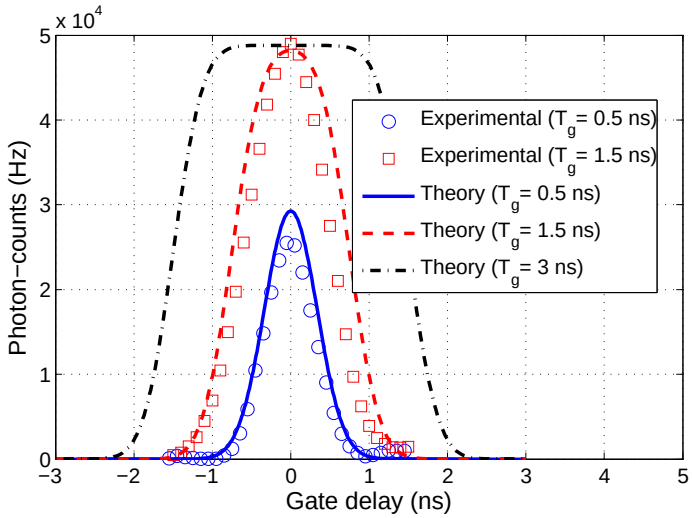

Figure 7.9: Experimental and theoretical photon-counts in a data detector due to the reference pulse leakage, considering a pulse with rate of 1.22 MHz, and a full width at half maximum equal to 0.7 ns. Three gate widths equal to 0.5 ns (blue solid line), 3 ns (red dashed line), and 3 ns (black dashdot line) are theoretically considered. Experimental results are represented as blue circles (T_g =0.5 ns) and red squares (T_g =1.5 ns).

separation between the center of the reference pulse and the center of the gate, Δt, considering different gate widths, in a back-to-back scenario ($z = 0$). Results show that for small time delays the photon-counts on the data detector coming from the reference pulse start to increase. Considering the particular gate width $T_g = 3$ ns we observe that this occurs for $\Delta t \approx 2$ ns. We also observe that for large gate widths the maximum photon-counts saturates. This occurs when the gate completely overlaps the pulse.

Figure 7.9 also shows the experimental data obtained with the SPDM from IDQuantique (id201). The detector has a dark count probability $P_{\text{dc}} = 2.55 \times 10^{-5}$, and a quantum detection efficiency $\eta_{\text{det}} = 10$ %. We used pulses with $T_{\text{FWHM}} = 0.7$ ns (and shape close to Gaussian), a mean number of photons $\langle n_r \rangle = 0.4$, and a repetition rate $f_{\text{rep}} = 1.22 \times 10^6$ Hz. We have performed the measurements using id201 gate widths equal to 2.5 ns and 5 ns. Note that although we have selected gate widths equal to 2.5 ns and 5 ns, these gate widths correspond to effective gates widths [34] of typically 0.5 ns and 1.5 ns, respectively. Broader gates will be incompatible with maximum id201 gate delay.

Results presented in Fig. 7.9 show that our model is in good agreement with the experimental data. This model can therefore be used in order to estimate the minimum separation between reference and data pulses that assures an isolation between the two kind of signals. Results show that pulses separations larger than 5 ns assure a very low number of counts.

7.3.4 Afterpulse Probability

The power of reference pulses is a setup parameter that can also be optimized [35]. Notice, however, that high power reference pulses can induce afterpulse detections. The afterpulse probability results from the trapping of charge carriers during an avalanche or due to photons impinging outside the gate [33]. We will assume that this probability depends on the arrival time before the gate as follows,

$$P_{\text{af}} = \frac{g_{\text{af}}}{T_{\text{af}}}, \tag{7.29}$$

where g_{af} is a characteristic constant of the detector, and T_{af} is the difference between the time arrival of the reference pulse and the next data gate opening, i.e., $T_{\text{af}} = T_{\text{rep}} - \Delta t$. Using the experimental data presented in [33] we have found the following value for the characteristic constant of the detector $g_{\text{af}} = 2.79 \times 10^{-12}$ s.

7.3.5 Total QBER

According to the analysis presented above, the total error rate in a QKD system with TDM-based SOP control can be written as

$$R_{\text{error}} = R_{\text{tACF}} + R_{\text{SOP}} + R_{\text{leak}} + R_{\text{af}} + R_{\text{dc}}, \tag{7.30}$$

where R_{tACF} represents the contribution due to the time decorrelation between reference and data SOPs, given by

$$R_{\text{tACF}} = R_{\text{sift}} p_{\text{tACF}}, \tag{7.31}$$

in which p_{tACF} is a probability given by (7.19). The term R_{SOP} represents the contribution due to the feedback SOP control system, and can be written as

$$R_{\text{SOP}} = R_{\text{sift}} p_{\text{SOP}}, \tag{7.32}$$

where p_{SOP} is a probability given by (7.21). The contribution due to the leakage of photons from the reference pulse to the data gate, is given by

$$R_{\text{leak}} = \frac{1}{4} f_{\text{rep}} p_{\text{leak}}, \tag{7.33}$$

in which p_{leak} is a probability given by (7.22). The 1/4 factor in the above equation is related with the transmitter and the receptor choice of incompatible bases [1], which contributes with one half, and with the probability of the leak photon to coincide with a correct data qubit, which contributes with another half. The contribution due to the afterpulse probability related with the photons impinging outside the gate, is given by

$$R_{\text{af}} = \frac{1}{2} f_{\text{rep}} t_{\text{link}} \langle n_r \rangle P_{\text{af}}, \tag{7.34}$$

Table 7.1: List of parameters used to plot the QBER map, represented in Fig. 7.10, corresponding to a QKD system with TDM-based SOP control.

Parameter	Value	Unities
α	0.22	dB/km
$\beta_{\omega\omega}$	-20	ps^2/km
Δt	100	ns
D_p	0.2	$\text{ps}/\text{km}^{1/2}$
g	0.5×10^{2}	s^{-1}
g_{af}	2.79×10^{-12}	s
η_{det}	10	%
$\langle n_r\rangle$	4	-
$\langle n_q\rangle$	0.1	-
P_{dc}	1×10^{-6}	-
Θ	$\pi/2$	rad
t_0	8.5×10^{7}	s
T_0	1	ns
T_g	2	ns

where P_{af} is given by (7.29). The term R_{dc} represents the contribution due to dark counts, given by (7.14).

Using the previous results into (7.10), we obtain the following expression for the total QBER in a QKD system with TDM-based SOP control [28]

$$\text{QBER} = \text{QBER}_{\text{tACF}} + \text{QBER}_{\text{SOP}} + \text{QBER}_{\text{leak}} + \text{QBER}_{\text{af}} + \text{QBER}_{\text{dc}} \tag{7.35}$$

$$\begin{aligned} =&\frac{1}{4} - \frac{1}{4}\exp\left(\frac{-3\omega^2 D_p^2 z\,|T_{\text{rep}} - \Delta t|}{2t_0}\right) + 1 - \cos^2\left(\frac{1}{2}\Theta(1-\exp(-gT_{\text{rep}}))\right) \\ &+ \frac{1}{2}\frac{\langle n_r\rangle A}{\langle n\rangle} + \frac{\langle n_r\rangle g_{\text{af}}}{\langle n\rangle\eta_{\text{det}}(T_{\text{rep}}-\Delta t)} + \frac{1}{2}\frac{P_{\text{dc}} n_{\text{det}}}{\langle n\rangle t_{\text{link}}\eta_{\text{det}}}. \end{aligned} \tag{7.36}$$

Some contributions to the QBER in (7.36) depend on the propagation distance. In the case of QBER_{dc}, it occurs because the detector dark-counts are constant, whereas R_{sift} decreases with t_{link} (see (7.11)). The contribution due to the pulse leakage, $\text{QBER}_{\text{leak}}$, is dependent on the propagation distance, since for narrow pulses chromatic dispersion can induce pulse broadening. With that, and since reference signal is also present in the data arm, the probability of photons be detected into the data detector, A, increases. Since the typical drift time t_d is dependent on the PMD, the $\text{QBER}_{\text{tACF}}$ will increase with

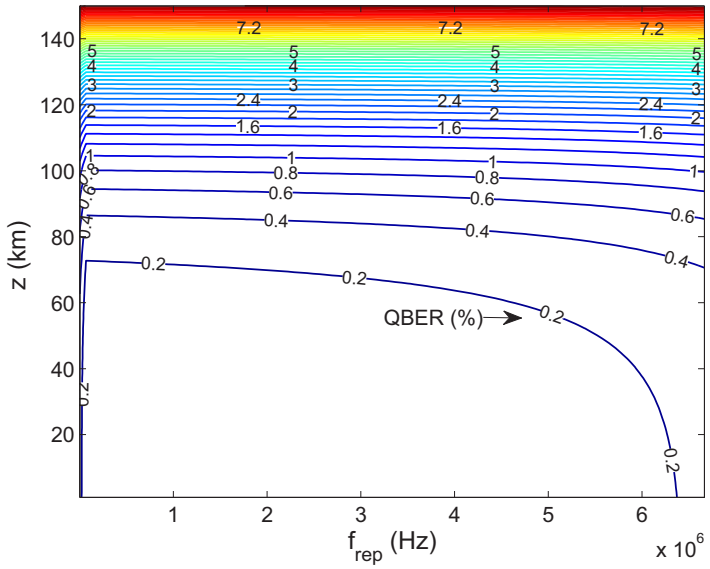

Figure 7.10: QBER estimation map for TDM-based SOP control scheme as a function of the distance z and pulse rate f_{rep}. The parameters used to plot the map are given in Table 7.1.

the distance. Concerning the frequency, we observe that only $\text{QBER}_{\text{leak}}$ and QBER_{dc} are frequency independent. On the other hand, both QBER_{SOP} and $\text{QBER}_{\text{tACF}}$ contributions decrease with the frequency. In the first case, that occurs because as more photons are received at the SOP controller system, smaller will be the deviations from the target SOP at the EPC output. In the second case, the QBER contribution decreases because as higher the frequency is, smaller will be the separation between the reference and data pulses, which means a stronger correlation between their SOP. The QBER_{af} contribution increases with frequency since T_{af} decreases with the increment of f_{rep}.

Figure 7.10 shows a map of the total QBER, given by (7.36), as a function of pulse rate, f_{rep}, and propagation distance, z. The parameters values used in order to plot the map are presented in Table 7.1. Our model shows that in this setting the QBER increases with the frequency for distances smaller than 70 km. In fact, the QBER system is dominated by the afterpulse contribution QBER_{af}. This process limits the maximum frequency rate for small distances, where fiber losses are not the main impairment. The fiber losses become dominant for distances longer than 100 km. In such case, the QBER increases exponentially and reaches values higher than 7% for distances longer than 140 km. For low frequencies (< 1 kHz) the QBER can present high values if the SOP control system is characterized by a high value of the parameter g (see Fig. 7.7).

The QKD experiment over 50 km of fiber with a TDM control scheme presented in [21] reports a QBER of 5.3%. The authors identify two main contributions to the total QBER: a contribution of 3.3% resulting from the dark noise detections, and 2% from the SOP control imperfections. They claim that the effectiveness of the SOP control

can be improved if higher pulse rates are used, which is in agreement with the results presented here. Nevertheless, we show that for high pulse rates the afterpulse detections can become an important impairment, and therefore a good balance between $\mathrm{QBER}_{\mathrm{dc}}$, $\mathrm{QBER}_{\mathrm{SOP}}$ and $\mathrm{QBER}_{\mathrm{af}}$ contributions is needed.

7.4 Summary

We have presented an analytical model able to estimate the QBER in QKD systems based on polarization encoding with SOP control schemes. The novel QBER expressions, given by (7.16) and (7.36), are in agreement with experimental results reported in the literature.

We have shown that the decorrelation between the reference and data signals is the fundamental impairment in the implementation of WDM-based SOP control schemes. This makes mandatory the use of low PMD fibers in order to achieve large distances with a low QBER. In the TDM-based SOP control scheme, we have identified some limitative technical aspects, likewise the single-photon detector dark counts, the afterpulse detections or the feedback SOP control system performance. However, our results show that for long distances fiber losses are the major impairment, presenting a main contribution to the total QBER. For distances shorter than 70 km and frequencies higher than 5 MHz the afterpulse probability reveals an important contribution to the QBER.

The results presented here can be used in order to understand the performance of these kind of SOP control schemes and they can lead to the optimization of polarization-encoded QKD systems.

References

[1] N. Gisin, G. Ribordy, W. Tittel, and H. Zbinden, "Quantum cryptography," *Rev. Mod. Phys.*, vol. 74, no. 1, pp. 145–195, Mar. 2002.

[2] C. H. Bennett and G. Brassard, "Quantum cryptography: Public key distribution and coin tossing," *in Proceedings of the IEEE International Conference on Computers, Systems, and Signal Processing, Bangalore, India*, pp. 175–179, 1984.

[3] C. Bennett, F. Bessette, G. Brassard, L. Salvail, and J. Smolin, "Experimental quantum cryptography," *J. Cryptology*, vol. 5, pp. 3–28, 1992.

[4] E. Diamanti, H. Takesue, C. Langrock, M. M. Fejer, and Y. Yamamoto, "100 km differential phase shift QKD experiment with low jitter up-conversion detectors," *Opt. Express*, vol. 14, no. 26, pp. 13 073–13 082, 2006.

[5] H. Takesue, S. W. Nam, Q. Zhang, R. H. Hadfield, T. Honjo, K. Tamaki, and Y. Yamamoto, "Quantum key distribution over a 40-dB channel loss using superconducting single-photon detectors," *Nat. Photonics*, vol. 1, no. 6, pp. 343–348, 2007.

[6] C. H. Bennett, "Quantum cryptography using any two nonorthogonal states," *Phys. Rev. Lett.*, vol. 68, no. 21, pp. 3121–3124, May 1992.

[7] K. Gordon, V. Fernandez, G. Buller, I. Rech, S. Cova, and P. Townsend, "Quantum key distribution system clocked at 2 GHz," *Opt. Express*, vol. 13, no. 8, pp. 3015–3020, 2005.

[8] P. Cheng-Zhi, Z. Jun, Y. Dong, G. Wei-Bo, M. Huai-Xin, H. Yin, H.-P. Zeng, Y. Tao, W. Xiang-Bin, and P. Jian-Wei, "Experimental long-distance decoy-state quantum key distribution based on polarization encoding," *Phys. Rev. Lett.*, vol. 98, no. 1, p. 010505, Jan. 2007.

[9] A. N. Pinto, Álvaro J. Almeida, N. A. Silva, N. J. Muga, and L. M. Martins, "Optical quantum communications: An experimental approach," in *International Conference on Applications of Optics and Photonics - AOP2011, Braga, Portugal*, vol. 1, Apr. 2011.

[10] Á. J. Almeida, S. R. Carneiro, N. A. Silva, N. J. Muga, and A. N. Pinto, "Polarization-entangled photon pairs using spontaneous four-wave mixing in a fiber loop," in *EUROCON2011 & CONFTELE2011, Lisbon, Portugal*, 2011.

[11] Á. J. Almeida, N. A. Silva, N. J. Muga, and A. N. Pinto, "Single-photon source using stimulated FWM in optical fibers for quantum communication," in *International Conference on Applications of Optics and Photonics, Braga, Portugal*, 2011.

[12] Á. J. Almeida, S. R. Carneiro, N. A. Silva, N. J. Muga, and A. N. Pinto, "Time coincidence of entangle photon pairs using spontaneous four-wave mixing in a fiber loop," in *Proceedings of VIII Symposium On Enabling Optical Networks and Sensors, Porto, Portugal*, 2010.

[13] G. P. Agrawal, *Nonlinear Fiber Optics, 3rd ed.* Academic Press, San Diego, USA, 2001.

[14] M. Karlsson, J. Brentel, and P. Andrekson, "Long-term measurement of PMD and polarization drift in installed fibers," *IEEE/OSA J. Lightwave Technol.*, vol. 18, no. 7, pp. 941–951, Jul. 2000.

[15] H. Zbinden, N. Gisin, B. Huttner, A. Muller, and W. Tittel, "Practical aspects of quantum cryptographic key distribution," *J. Cryptology*, vol. 13, no. 2, pp. 207–220, Dec. 2000.

[16] B. Huttner, A. Muller, J. D. Gautier, H. Zbinden, and N. Gisin, "Unambiguous quantum measurement of nonorthogonal states," *Phys. Rev. A*, vol. 54, no. 5, pp. 3783–3789, Nov. 1996.

[17] M. Martinelli, P. Martelli, and S. M. Pietralunga, "Polarization stabilization in optical communications systems," *IEEE/OSA J. Lightwave Technol.*, vol. 24, no. 11, pp. 4172–4183, 2006.

[18] A. Poppe, "Method and device for readjusting a polarization drift," *United States Patent, no. US2008/0310856 A1*, Dec. 2008.

[19] J. Chen, G. Wu, Y. Li, E. Wu, and H. Zeng, "Active polarization stabilization in optical fibers suitable for quantum key distribution," *Opt. Express*, vol. 15, no. 26, pp. 17 928–17 936, 2007.

[20] G. B. Xavier, G. V. de Faria, G. P. T. ao, and J. P. von der Weid, "Full polarization control for fiber optical quantum communication systems using polarization encoding," *Opt. Express*, vol. 16, no. 3, pp. 1867–1873, 2008.

[21] J. Chen, G. Wu, L. Xu, X. Gu, E. Wu, and H. Zeng, "Stable quantum key distribution with active polarization control based on time-division multiplexing," *New J. Phys.*, vol. 11, no. 6, pp. 17 928–17 936, 2009.

[22] G. B. Xavier, N. Walenta, G. V. de Faria, G. P. Temporão, N. Gisin, H. Zbinden, and J. P. von der Weid, "Experimental polarization encoded quantum key distribution over optical fibres with real-time continuous birefringence compensation," *New J. Phys.*, vol. 11, no. 4, p. 045015, 2009.

[23] N. A. Silva, N. J. Muga, and A. N. Pinto, "Effective nonlinear parameter measurement using FWM in optical fibers in a low power regime," *IEEE J. Quantum Electron.*, vol. 46, no. 3, pp. 285–291, 2010.

[24] N. A. Silva, N. J. Muga, and A. N. Pinto, "Measurement of the effective nonlinear parameter using FWM in random polarization optical fibers," in *Proc European Conf. on Networks and Optical Communications and Conf. on Optical Cabling and Infrastructure - NOC/OC*, vol. 1, Faro, Portugal, Jun. 2010, pp. 185–190.

[25] ITU-T G. 694.1, "Spectral grids for WDM applications: DWDM wavelength grid," 2002.

[26] J. N. Damask, *Polarization optics in telecomunications.* Springer, New York, EUA, 2005.

[27] H.-A. Bachor and T. C. Ralph, *A Guide to Experiments in Quantum Optics*, 2nd ed. Wiley-VCH, 2003.

[28] N. J. Muga, Mário F. S. Ferreira, and A. N. Pinto, "QBER estimation in QKD systems with polarization encoding," *IEEE/OSA J. Lightwave Technol.*, vol. 29, no. 3, pp. 355–361, 2011.

[29] N. J. Muga, N. A. Silva, M. Ferreira, and A. N. Pinto, "Evolution of the degree of copolarization in high-birefringence fibers," *Opt. Commun.*, vol. 283, no. 10, pp. 2125–2132, 2010.

[30] N. J. Muga, A. N. Pinto, M. Ferreira, and J. R. F. da Rocha, "Uniform polarization scattering with fiber-coil based polarization controllers," *IEEE/OSA J. Lightwave Technol.*, vol. 24, no. 11, pp. 3932–3943, 2006.

[31] N. J. Muga, Á. J. Almeida, M. Ferreira, and A. N. Pinto, "Optimization of polarization control schemes for QKD systems," in *International Conference on Applications of Optics and Photonics - AOP2011*, vol. 1, Braga, Portugal, Apr. 2011.

[32] N. A. Silva, N. J. Muga, and A. N. Pinto, "Single-photon generation," in *Proc Conf. on Telecommunications - ConfTele2009*, vol. 1, Santa Maria da Feira, Portugal, May 2009.

[33] G. Ribordy, N. Gisin, O. Guinnard, D. Stuck, M. Wegmuller, and H. Zbinden, "Photon counting at telecom wavelengths with commercial InGaAs/InP avalanche photodiodes: Current performance." *J. Mod. Opt.*, vol. 51, no. 9, pp. 1381–1398, 2006.

[34] IDQuantique, *id201 datasheet*, www.idquantique.com, 2010.

[35] N. J. Muga, Á. J. Almeida, M. Ferreira, and A. N. Pinto, "Critical issues in polarization encoded quantum key distribution systems," in *Proc EUROCON2011 and 8ª Conf. on Telecommunications - ConfTele2011*, vol. 1, Lisboa, Portugal, May 2011, pp. 11–11.

Chapter 8

Conclusions and Future Directions

In this thesis several polarization effects in optical fibers were analyzed, covering both classical and quantum fiber-optic communication fields. In the framework of this work, we have obtained new analytical models which have been validated through experimental results or through numerical results when detailed numerical models were available. In this Chapter, we overview the developed work, summarize the main conclusions, and present suggestions for future work.

8.1 Conclusions

Our approach to scatter the light state of polarization (SOP), presented in Chapter 3, was based in a detailed study of the fiber-coil based polarization controller (PC). The proposed model for the fiber-coil based PC allows to deterministically calculate the PC configuration in order to transform the light polarization between any two SOPs [1]. Besides that, the expression obtained for the mean square values of the Stokes parameters when several fiber-coil based PCs devices are concatenated shows that with three concatenated PCs a uniform polarization scattering is obtained [2, 3]. These results demonstrate the suitability of this SOP scattering method to be used into the design of polarization-mode dispersion (PMD) emulators. In fact, we showed that first- and second-order PMD statistics are accurately generated when fifteen polarization-maintaining fibers (PMFs) are interconnected with fourteen polarization scattering sections. We concluded that for a high number of polarization scattering sections, the generated PMD statistics become less dependent of the number of PCs used in each scattering section.

The propagation of two signals at different wavelengths inside an high-birefringence (HiBi) optical fiber was analyzed in Chapter 4. The analytical model developed in that Chapter accurately describes the degree of co-polarization between two continuous wave (CW) signals [4–6]. We observed that, for small fiber lengths or narrow wavelength separations, launching two signals into a HiBi fiber with orthogonal polarizations can result in a highest degree of co-polarization when compared with the initially parallel SOPs scheme. On the other hand, we identified a long-distance regime where the degree of co-polarization for the parallel scheme is always equal or higher than that presented by

the orthogonal case. The degree of co-polarization model was experimentally validated in a long-distance regime through measurements of the efficiency of the four-wave mixing (FWM) process in a dispersion-shifted HiBi fiber. The results presented in Chapter 4 can be used in order to accurately understand the behavior of some polarization dependent physical effects involving more than one signal [4, 7–9]. We believe that they could lead to the optimization or implementation of new all-optical signal processing devices based on special fibers with high birefringence and nonlinear response.

The subject of amplified spontaneous emission (ASE) noise in optical communication systems with Raman amplification was addressed in Chapter 5. We developed a numerical model to describe the interaction between the signal and noise mediated by the Kerr effect [10]. The numerical results for the ASE noise power spectrum were compared with experimental data, and a good agreement was observed for different pump powers and propagation distances [11–13]. We used the proposed model in order to analyze the evolution of the noise statistics in a scenario where the ASE noise is co-propagated with a CW signal. The deviations of the noise distributions from the Gaussian statistics were evaluated through the calculation of the skewness and kurtosis excess parameters. We have shown that the noise preserves the Gaussian statistics along the fiber for regimes where the interaction between signal and noise due to fiber nonlinearities can be neglected. Nevertheless, for distances longer than 120 km and signal powers higher than 6 mW, the nonlinearities induce a change on the noise distribution and the Gaussian statistics assumption becomes invalid. The detailed knowledge of the noise statistics can be important in the estimation of some performance parameters in coherent amplitude modulated systems which are recently attracting renewed attention.

The all-optical polarization control based on stimulated Raman scattering (SRS) was explored in Chapter 6. We have considered the effect of detuning the signal from the peak of the Raman gain in a copropagating scheme, showing that the efficiency of the pulling process is higher close to the Raman gain peak, where the degree of polarization (DOP) is roughly constant for a wavelength range of 15 nm [14]. For shorter and longer wavelengths, higher pump powers are required in order to assure maximum efficiencies. For instance, a DOP equal to 0.9 can be obtained at 1550 nm for a pump power around 4 W, whereas the double power is needed in order to obtain the same DOP at 1510 nm (considering a pump wavelength at 1450 nm and an ensemble of input signal SOPs uniformly distributed over the Poincaré sphere, i.e., an input DOP equal to zero). Our results showed that, in spite of the random pump SOP evolution along the propagation, the mean angle between the output signal and pump Stokes vectors can be made very small. Therefore, the output pump SOP information can be used in order to operate on the output signal SOP. Different results were found in the depleted regime, where the highest DOP values are no more observed for the highest pump powers. For signal wavelengths between 1535 and 1560 nm, the highest DOP values occur for a optimum pump power, which in our case was 8 W (considering again a pump wavelength at 1450 nm and an input signal DOP equal to zero). For powers higher than the optimum value, the polarization pulling effect becomes less efficient due to the decrease of the pump DOP.

Standard single-mode fibers (SSMFs) are often used as a communication channel in all fiber-based implementations of quantum cryptography systems. Chapter 7 provided

an analysis of the polarization control process applied to polarization-encoded quantum key distribution (QKD) systems. We have showed that the time-division multiplexing (TDM)-based SOP control scheme presents important advantages when compared with the wavelength-division multiplexing (WDM)-based scheme. Indeed, we have derived novel analytical expressions to estimate the quantum bit error rate (QBER) in polarization-encoded QKD systems with both kind of SOP control schemes [15]. We demonstrated that the decorrelation between the reference and data signals is the fundamental impairment in the implementation of WDM-based SOP control scheme. This result clearly shows that, in order to achieve large distances with a low QBER, the use of low PMD fibers becomes mandatory [16, 17]. In the TDM-based control scheme, we have identified some limitative technical aspects, likewise the single-photon detector dark counts, after pulse detections, or the feedback SOP control system performance. Besides that, we showed that for long distances fiber losses are the major impairment, presenting a main contribution to the total QBER. For distances shorter than 70 km and frequencies higher than 5 MHz the after pulse probability reveals an important contribution to the QBER.

8.2 Future Directions

We consider that the results presented in this thesis are valuable and useful, and we believe that some subjects can be explored more thoroughly. Thus, from this work, several investigations can be conducted.

The analysis performed in Chapter 3 shows how to scatter the light SOP through the concatenation of fiber-coil based SOP controllers. It is also shown how to deterministically transform the light polarization between any two SOPs. We believe that it will be interesting to extend that work to electronic polarization controllers (EPCs).

The analytical model accurately describing the evolution of the relative state of polarization (rSOP) presented in Chapter 4 was only partially validated. Hence we believe that an experimental validation of the short-distance regime will provide a valuable contribution to the optimization or implementation of new all-optical signal processing devices based on special fibers. A photonic crystal fiber will be a good candidate to be used in such experiments due their high nonlinear response and high-birefringence. Note that in this regime the highest degree of co-polarization values can occur when signals are launched with orthogonal SOPs.

The model characterizing the interaction between signal and noise could be generalized for a counter-propagating pump scheme and for pulsed signals. Besides that, it would be very useful to find a technique to measure experimentally the noise statistics properties reported here.

Regarding the topic of the Raman polarization pulling process, we consider that our broadband analysis could be extended to the counter-propagation scheme. Notice that using a counter-propagation scheme the pump SOP at the fiber end is selected by the user, which means that the signal out SOP will be well defined. This behavior is in con-

trast with that presented by the co-propagating scheme, where the birefringence defines both the pump and signal output SOPs. Besides that, the polarization pulling effect could be explored in research fields as optic regeneration or all-optical processing. Such applications can benefit from the new fibers/microfibers produced from new materials, presenting enabling properties, including, high confinement, robustness, high nonlinear response, robustness, and compactness.

Concerning the subject of QBER estimation in polarization encoded QKD systems with dynamic SOP control schemes, we also consider that an experimental validation of the presented QBER expressions will represent a valuable contribution to QKD systems. The main goal of SOP control systems is to compensate drift changes on the SOP, nevertheless it should be assured that the influence of compensation schemes on the quantum channel is avoided or, at least, minimized. This a characteristic to be considered when evaluating the overall performance of a QKD system.

References

[1] N. J. Muga, A. N. Pinto, M. Ferreira, and J. R. F. da Rocha, "Uniform polarization scattering with fiber-coil based polarization controllers," *IEEE/OSA J. Lightwave Technol.*, vol. 24, no. 11, pp. 3932–3943, 2006.

[2] N. J. Muga, A. N. Pinto, and M. Ferreira, "Polarization scattering property of cascaded polarization controllers," *ETRI Trans.*, vol. 29, no. 6, pp. 838–840, 2007.

[3] N. J. Muga, A. N. Pinto, and M. Ferreira, "Polarization controller: Angles configuration and scattering properties," in *Proc Conf. on Telecommunications - ConfTele2007*, vol. IM.1, Peniche, Portugal, May 2007, pp. 243–246.

[4] N. J. Muga, N. A. Silva, M. Ferreira, and A. N. Pinto, "Evolution of the degree of copolarization in high-birefringence fibers," *Opt. Commun.*, vol. 283, no. 10, pp. 2125–2132, 2010.

[5] N. J. Muga, N. A. Silva, M. Ferreira, and A. N. Pinto, "Generalized analysis of the polarization evolution in high-birefringence fibers," in *Proc International Conf. on Transparent Networks – ICTON*, vol. Mo.P.2, Munich, Germany, Jun. 2010.

[6] N. J. Muga, N. A. Silva, M. Ferreira, and A. N. Pinto, "Relative state-of-polarization in high-birefringence fibers," in *Proc European Conf. on Networks and Optical Communications and Conf. on Optical Cabling and Infrastructure - NOC/OC*, vol. 1, Faro, Portugal, Jun. 2010, pp. 121–126.

[7] N. A. Silva, N. J. Muga, and A. N. Pinto, "Influence of the stimulated Raman scattering on the four-wave mixing process in birefringent fibers," *IEEE/OSA J. Lightwave Technol.*, vol. 27, no. 22, pp. 4979–4988, Nov. 2009.

[8] N. A. Silva, N. J. Muga, and A. N. Pinto, "Effective nonlinear parameter measurement using FWM in optical fibers in a low power regime," *IEEE J. Quantum Electron.*, vol. 46, no. 3, pp. 285–291, 2010.

[9] N. A. Silva, N. J. Muga, and A. N. Pinto, "Evolution of first-order sidebands from multiple FWM processes in HiBi optical fibers," *Opt. Commun.*, vol. 284, no. 13, pp. 3408–3415, 2011.

[10] N. J. Muga, M. C. Fugihara, Mário F. S. Ferreira, and A. N. Pinto, "Non-Gaussian ASE noise in Raman amplification systems," *IEEE/OSA J. Lightwave Technol.*, vol. 27, no. 16, pp. 3389–3398, 2009.

[11] N. J. Muga, M. C. Fugihara, Mário F. S. Ferreira, and A. N. Pinto, "Modeling of ASE noise in broadband systems with Raman amplification," in *Proc Symp. on Enabling Optical Networks - SEON*, Porto, Portugal, Jul. 2008, pp. 145–146.

[12] N. J. Muga, M. C. Fugihara, Mário F. S. Ferreira, and A. N. Pinto, "Non-white noise generation method for ASE noise simulation in systems with Raman amplification," in *International Conf. on Transparent Optical Networks - ICTON*, vol. 1, Ponta Delgada - Azores, Portugal, Jun. 2009, p. WeA1.6.

[13] N. J. Muga, M. C. Fugihara, Mário F. S. Ferreira, and A. N. Pinto, "ASE noise simulation in Raman amplification systems," in *Proc Conf. on Telecommunications - ConfTele2009*, vol. 1, Santa Maria da Feira, Portugal, May 2009, pp. 347–350.

[14] N. J. Muga, M. F. S. Ferreira, and A. N. Pinto, "Broadband polarization pulling using Raman amplification," *Opt. Express*, vol. 19, no. 19, pp. 18 707–18 712, Sept. 2011.

[15] N. J. Muga, Mário F. S. Ferreira, and A. N. Pinto, "QBER estimation in QKD systems with polarization encoding," *IEEE/OSA J. Lightwave Technol.*, vol. 29, no. 3, pp. 355–361, 2011.

[16] N. J. Muga, Á. J. Almeida, M. Ferreira, and A. N. Pinto, "Critical issues in polarization encoded quantum key distribution systems," in *Proc EUROCON2011 and 8ª Conf. on Telecommunications - ConfTele2011*, vol. 1, Lisboa, Portugal, May 2011, pp. 11–11.

[17] N. J. Muga, Á. J. Almeida, M. Ferreira, and A. N. Pinto, "Optimization of polarization control schemes for QKD systems," in *International Conference on Applications of Optics and Photonics - AOP2011*, vol. 1, Braga, Portugal, Apr. 2011.

Appendix A

Equivalent Representations on Jones and Stokes Spaces

This Appendix presents a list of equivalent mathematical representations on Jones and Stokes spaces of several states of polarization (SOPs), elementary rotations, and some optical elements.

Table A.1: Equivalent representations of different SOPs in the Jones and Stokes spaces. In the Jones space, SOPs are represented as 2D ket vectors, whereas in the Stokes space, SOPs are represented as 3D vectors [1].

SOP	**Jones space**	**Stokes space**
Linear horizontal	$\begin{bmatrix} 1 \\ 0 \end{bmatrix}$	$\begin{bmatrix} 1 \\ 0 \\ 0 \end{bmatrix}$
Linear vertical	$\begin{bmatrix} 0 \\ 1 \end{bmatrix}$	$\begin{bmatrix} -1 \\ 0 \\ 0 \end{bmatrix}$
Linear at +45°	$\frac{1}{\sqrt{2}}\begin{bmatrix} 1 \\ 1 \end{bmatrix}$	$\begin{bmatrix} 0 \\ 1 \\ 0 \end{bmatrix}$
Linear at -45°	$-\frac{1}{\sqrt{2}}\begin{bmatrix} 1 \\ 1 \end{bmatrix}$	$\begin{bmatrix} 0 \\ -1 \\ 0 \end{bmatrix}$
Right-handed circular	$\frac{1}{\sqrt{2}}\begin{bmatrix} 1 \\ i \end{bmatrix}$	$\begin{bmatrix} 0 \\ 0 \\ 1 \end{bmatrix}$
Left-handed circular	$\frac{1}{\sqrt{2}}\begin{bmatrix} 1 \\ -i \end{bmatrix}$	$\begin{bmatrix} 0 \\ 0 \\ -1 \end{bmatrix}$

Table A.2: Equivalent matricial representations of several optical elements in Jones and Stokes spaces. In the Jones space, optical elements are represented as 2×2 matrices, whose entries can be either complex or real, whereas in the Stokes space, optic elements are represented as 4×4 matrices, with real entries [2].

Optical element	**Jones matrix**	**Mueller matrix**
Linear polarizer (x axis)	$\begin{bmatrix} 1 & 0 \\ 0 & 0 \end{bmatrix}$	$\frac{1}{2}\begin{bmatrix} 1 & 1 & 0 & 0 \\ 1 & 1 & 0 & 0 \\ 0 & 0 & 0 & 0 \\ 0 & 0 & 0 & 0 \end{bmatrix}$
Linear polarizer (y axis)	$\begin{bmatrix} 0 & 0 \\ 0 & 1 \end{bmatrix}$	$\frac{1}{2}\begin{bmatrix} 1 & -1 & 0 & 0 \\ -1 & 1 & 0 & 0 \\ 0 & 0 & 0 & 0 \\ 0 & 0 & 0 & 0 \end{bmatrix}$
Linear polarizer (angle $\frac{\theta}{2}$)	$\begin{bmatrix} \cos^2\frac{\theta}{2} & \cos\frac{\theta}{2}\sin\frac{\theta}{2} \\ \cos\frac{\theta}{2}\sin\frac{\theta}{2} & \sin^2\frac{\theta}{2} \end{bmatrix}$	$\frac{1}{2}\begin{bmatrix} 1 & \cos\theta & \sin\theta & 0 \\ \cos\theta & \cos^2\theta & \cos\theta\sin\theta & 0 \\ \sin\theta & \cos\theta\sin\theta & \sin^2\theta & 0 \\ 0 & 0 & 0 & 1 \end{bmatrix}$
QWP (fast-axis vertical)	$\begin{bmatrix} 1 & 0 \\ 0 & i \end{bmatrix}$	$\begin{bmatrix} 1 & 0 & 0 & 0 \\ 0 & 1 & 0 & 0 \\ 0 & 0 & 0 & -1 \\ 0 & 0 & 1 & 0 \end{bmatrix}$
HWP (fast-axis vertical)	$\begin{bmatrix} 1 & 0 \\ 0 & -1 \end{bmatrix}$	$\begin{bmatrix} 1 & 0 & 0 & 0 \\ 0 & 1 & 0 & 0 \\ 0 & 0 & -1 & 0 \\ 0 & 0 & 0 & -1 \end{bmatrix}$

Table A.3: Elementary rotations of the Stokes vectors in the Stokes space around the 1, 2, and 3 axes of the Poincaré sphere [1].

Rotation axis	**Jones matrix**	**Stokes space rotation**
1	$U_1 = \begin{bmatrix} e^{i\varphi/2} & 0 \\ 0 & e^{-i\varphi/2} \end{bmatrix}$	$R_1 = \begin{bmatrix} 1 & 0 & 0 \\ 0 & \cos\varphi & -\sin\varphi \\ 0 & \sin\varphi & \cos\varphi \end{bmatrix}$
2	$U_2 = \begin{bmatrix} \cos\varphi/2 & i\sin\varphi/2 \\ i\sin\varphi/2 & \cos\varphi/2 \end{bmatrix}$	$R_2 = \begin{bmatrix} \cos\varphi & 0 & \sin\varphi \\ 0 & 1 & 0 \\ -\sin\varphi & 0 & \cos\varphi \end{bmatrix}$
3	$U_3 = \begin{bmatrix} \cos\varphi/2 & -\sin\varphi/2 \\ \sin\varphi/2 & \cos\varphi/2 \end{bmatrix}$	$R_3 = \begin{bmatrix} \cos\varphi & -\sin\varphi & 0 \\ \sin\varphi & \cos\varphi & 0 \\ 0 & 0 & 1 \end{bmatrix}$

References

[1] J. P. Gordon and H. Kogelnik, "PMD fundamentals: Polarization mode dispersion in optical fibers," *PNAS*, vol. 97, no. 9, pp. 4541–4550, 2000.

[2] D. Goldstein, *Polarized Light, Second edition.* CRC Press, New York, EUA, 2003.

Appendix B

Uniform Distribution Over the Poincaré Sphere

This Appendix derives the statistics of each Stokes vector component, s_i, respecting to a uniform distribution of Stokes vectors over the Poincaré sphere.

We start this derivation by calculating the area element of a surface revolution obtained around the s_3 axis. It can be written as

$$dS = 2\pi r ds, \tag{B.1}$$

where ds represents a curve element, and r is the distance between the s_3 axis and the sphere surface, see Fig. B.1. The ds curve element can be written as

$$ds^2 = dr^2 + ds_3^2, \tag{B.2}$$

where dr and ds_3 are infinitesimal increments on r and s_3, respectively. Taking the square root of (B.2), we obtain

$$ds = \sqrt{1 + \left(\frac{dr}{ds_3}\right)^2} ds_3. \tag{B.3}$$

Assuming a sphere radius equal to one, the distance r can be written as function of the coordinate s_3 as

$$r(s_3) = \sqrt{1 - s_3^2}. \tag{B.4}$$

Equations (B.4) and (B.3) can be used to obtain ds. Taking the derivative of r in order to s_3, and using it in (B.3), we obtain the following expression for ds,

$$ds = \frac{ds_3}{\sqrt{1 - s_3^2}}. \tag{B.5}$$

Using (B.5) and (B.4) in (B.1) we obtain finally the relation between the area dS and the coordinate s_3

$$dS = 2\pi ds_3. \tag{B.6}$$

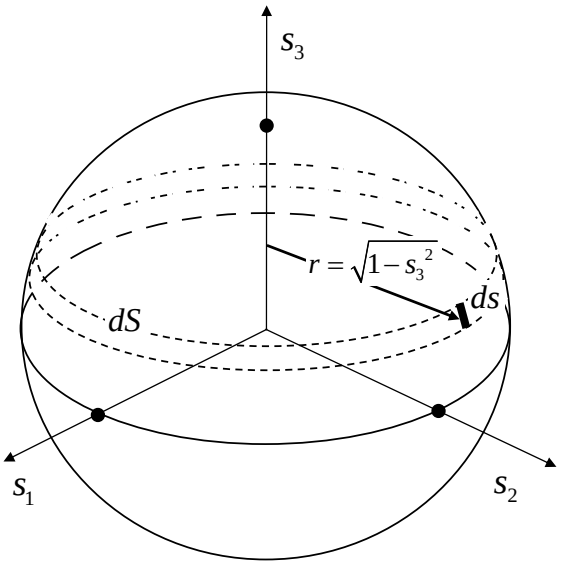

Figure B.1: Poincaré sphere representation of the area element of the surface of revolution.

We can therefore calculate the area S comprised between $s_3 = a$ and $s_3 = b$ as

$$S = 2\pi \int_a^b ds_3. \tag{B.7}$$

The solution of (B.7) is just $2\pi h$, with $h = b - a$, i.e., the area is a constant, independent of s_3.

This proof also works for the s_1 and s_2 axes. Using this result, we can conclude that if we have a uniform distribution of points over the sphere surface, the respective projections are also uniformly distributed between -1 and 1. Therefore, observing the normalization condition, i.e.,

$$\int_{-1}^{1} g_{s_i} \equiv 1, \tag{B.8}$$

the three coordinate probability density functions, g_{s_i}, have the constant value $1/2$.

As the mean value of each coordinate is zero, the variances, σ_i, are given by the mean squares

$$\sigma_i = \left\langle s_i^2 \right\rangle = \int_{-1}^{1} g_{s_i} s_i^2 ds_i. \tag{B.9}$$

Using $g_{s_i} = 1/2$ into (B.9), we then obtain for the $1/3$ value for variance of each Stokes vector component.